



**HAL**  
open science

# Non linear interaction of self-accelerating light beams

Thomas Bouchet

► **To cite this version:**

Thomas Bouchet. Non linear interaction of self-accelerating light beams. Pattern Formation and Solitons [nlin.PS]. Université de Lorraine, 2019. English. NNT : 2019LORR0312 . tel-02998405

**HAL Id: tel-02998405**

**<https://hal.univ-lorraine.fr/tel-02998405>**

Submitted on 10 Nov 2020

**HAL** is a multi-disciplinary open access archive for the deposit and dissemination of scientific research documents, whether they are published or not. The documents may come from teaching and research institutions in France or abroad, or from public or private research centers.

L'archive ouverte pluridisciplinaire **HAL**, est destinée au dépôt et à la diffusion de documents scientifiques de niveau recherche, publiés ou non, émanant des établissements d'enseignement et de recherche français ou étrangers, des laboratoires publics ou privés.



## AVERTISSEMENT

Ce document est le fruit d'un long travail approuvé par le jury de soutenance et mis à disposition de l'ensemble de la communauté universitaire élargie.

Il est soumis à la propriété intellectuelle de l'auteur. Ceci implique une obligation de citation et de référencement lors de l'utilisation de ce document.

D'autre part, toute contrefaçon, plagiat, reproduction illicite encourt une poursuite pénale.

Contact : [ddoc-theses-contact@univ-lorraine.fr](mailto:ddoc-theses-contact@univ-lorraine.fr)

## LIENS

Code de la Propriété Intellectuelle. articles L 122. 4

Code de la Propriété Intellectuelle. articles L 335.2- L 335.10

[http://www.cfcopies.com/V2/leg/leg\\_droi.php](http://www.cfcopies.com/V2/leg/leg_droi.php)

<http://www.culture.gouv.fr/culture/infos-pratiques/droits/protection.htm>

# NON LINEAR INTERACTION OF SELF-ACCELERATING LIGHT BEAMS

## THÈSE

---

Présentée et soutenue publiquement le 20 décembre 2019  
pour l'obtention du titre de

DOCTEUR DE L'UNIVERSITE DE LORRAINE

Mention : "Physique"

par Thomas BOUCHET

Membres du jury :

Directeur de thèse :	Pr. Delphine Wolfersberger	Professeur, CentraleSupélec
Co-encadrant de thèse :	Dr. Nicolas Marsal	Maître de Conférence, CentraleSupélec
Rapporteurs :	Dr. Eric Louvergneaux	Maître de Conférence, Université Lille 1
	Pr. Pascal Kockaert	Professeur, Université Libre de Bruxelles
Examineurs :	Pr. Marc Sciamanna	Professeur, CentraleSupélec
	Pr. Fabrice Devaux	Professeur, Université de Franche-Comté



# TABLE OF CONTENTS

	<b>Page</b>
<b>1 General Introduction</b>	<b>1</b>
1.1 Photonics . . . . .	2
1.1.1 What is a Photon? . . . . .	2
1.1.1.1 The MASER and the LASER . . . . .	3
1.1.1.2 Fiber Optics . . . . .	4
1.2 Non conventional beams and nonlinear media . . . . .	7
1.2.1 Non-conventional beams . . . . .	7
1.2.2 Linear and nonlinear media . . . . .	10
1.2.2.1 Spatial solitons . . . . .	11
1.2.2.2 Airy beams in nonlinear media . . . . .	12
1.2.3 Imprinting in photorefractive media . . . . .	13
1.2.4 Outline . . . . .	15
<b>2 Experimental generation of Airy beams</b>	<b>17</b>
2.1 An overview of Airy beams . . . . .	18
2.1.1 What are Airy beams? . . . . .	18
2.1.2 How are Airy beams generated? . . . . .	24
2.2 Airy beam generation using LCOS SLM . . . . .	26
2.2.1 LCOS SLM Technology . . . . .	27
2.2.2 Influence of experimental conditions on the generation of Airy Beams	29
2.2.2.1 Border effects and pixelisation limit . . . . .	33
2.2.2.2 Parameter range . . . . .	37
2.3 Conclusions . . . . .	41
<b>3 Airy beam propagation in nonlinear media</b>	<b>43</b>
3.1 Physical concepts: Solitons and Photorefractive effect . . . . .	44
3.1.1 Solitons . . . . .	44

TABLE OF CONTENTS

---

3.1.2	Photorefractive crystals . . . . .	49
3.1.3	Photorefractive soliton . . . . .	54
3.2	Finite Airy beam propagation in photorefractive media . . . . .	57
3.2.1	Airy beams in photorefractive media . . . . .	58
3.2.2	Experimental propagation of 1D Airy beam . . . . .	62
3.2.3	Numerical analysis . . . . .	65
3.3	Conclusion . . . . .	71
<b>4</b>	<b>2D Airy beam propagation in photorefractive media</b>	<b>73</b>
4.1	Propagation dynamic and soliton formation in two-dimensional saturable nonlinear media . . . . .	74
4.1.1	Experimental observation of 2D Airy beam propagation in photorefractive media . . . . .	80
4.2	Self-bending of the OSS and time considerations . . . . .	85
4.3	2D Airy beam propagation behavior and soliton existence curve . . . . .	88
4.4	Conclusion . . . . .	90
<b>5</b>	<b>Counter propagating Airy beams in photorefractive medium</b>	<b>91</b>
5.1	Overview of beam interactions and interconnects in photorefractive media	91
5.2	Numerical Antisymmetric Airy beam propagation in nonlinear self-focusing conditions . . . . .	100
5.2.1	Antisymmetric Airy beams interactions scheme . . . . .	100
5.2.2	Optical interconnections for a transverse shift $d=1$ . . . . .	102
5.3	Stability of the photoinduced waveguides to input positions . . . . .	107
5.4	Conclusion . . . . .	111
<b>6</b>	<b>Conclusion and Perspectives</b>	<b>113</b>
6.1	Conclusion . . . . .	113
6.2	Perspectives . . . . .	116
6.2.1	The use of nonconventional beams . . . . .	116
6.2.1.1	Diverse ways to propagate light . . . . .	116
6.2.1.2	Challenging the existing theoretical and numerical models	117
6.2.1.3	Transition dynamics from linear to nonlinear propagation	118
6.2.2	Off-shooting Soliton stability . . . . .	119
6.2.3	Instability of counterpropagating waveguides . . . . .	119
6.2.4	Experimental waveguiding of probe beams . . . . .	120

6.2.5 Greater control of the focusing conditions . . . . .	121
<b>Résumé en Français</b>	<b>125</b>
<b>Bibliography</b>	<b>133</b>



## GENERAL INTRODUCTION

The communication of ideas and the sharing of knowledge is one of the core concepts of human societies, from imprinted prehistoric pictorial symbols to printers, and from books to magnetic tapes. From the calculations with a tally stick to the abacus, from electromechanic systems and Turing's machine to modern computers, humans have efficiently externalized a part of their memory and computation processes. The first three industrial revolutions allowed manpower to be surpassed by successively mechanical, electrical and electronic systems. This multiplied our capabilities in terms of sheer power and speed thus increasing our communication and computational capabilities. A large part of modern society's communications, storage and computations are based on electronic devices today. However a fourth revolution has started, and it began with the rise of internet, lasers and fiber optics. This technology is based on the physics of photonics, and is the next step in information processing and transmission. Photonics is replacing or aiding electronics in our devices today and plays a major role in research and development. This thesis typically searches for new ways to route information using photonics. To do so we look at interactions between light and matter knowing that a better understanding is the key to future breakthroughs. In this general introduction we will shortly present what is the field of photonics and two major breakthroughs, the laser and the optical fiber. We will then introduce more specific notions regarding the subject of this thesis: non-conventional light beams and nonlinear photorefractive media.

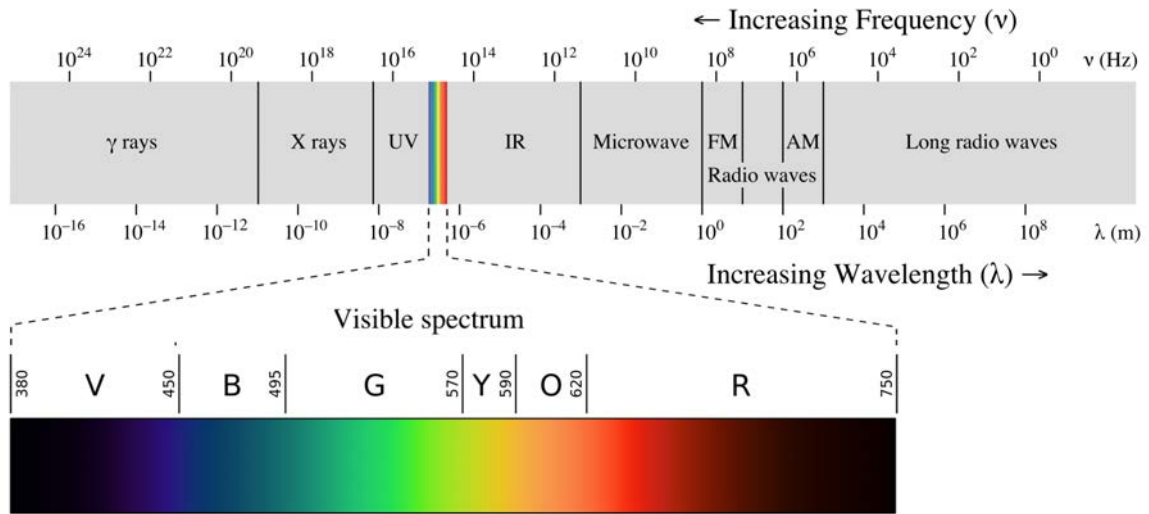


Figure 1.1: Electromagnetic spectrum with visible spectrum highlighted

## 1.1 Photonics

Photonics is defined as the physical science of light, it is a field of physics that studies the emission, transmission, processing and sensing of photons. In other words, it consists of using photons instead of electrons for the realization of similar functions such as switches, amplifiers, modulators, sensors and so on.

### 1.1.1 What is a Photon?

A photon is an elementary particle traveling at the speed of light. It is also the quantum (ie. the smallest indivisible measure) of electromagnetic waves. Which means that the electromagnetic wave is a sum of multiple indivisible photons. Light represents only a small fraction of electromagnetic waves, of wavelengths between 390nm and 750nm (see figure 1.1). As can be seen in figure 1.1 the electromagnetic wave can be defined by either a wavelength or a frequency since they are the inverse of one another ( $\lambda = c/\nu$  with  $\lambda$  the wavelength,  $\nu$  the frequency and  $c$  the speed of light.) The energy level of the photon defines the wavelength (or frequency) of the electromagnetic wave using the relation  $E = h\nu$  ( $E$  the energy,  $h$  the Planck constant and  $\nu$  the electromagnetic wave's frequency). The higher the frequency is, the higher the energy level of the photon is and the easier it is to observe the behavior of individual photons forming the electromagnetic wave. It is

therefore often easier to observe at higher frequencies both the particle nature and the wave nature of the electromagnetic waves, then at lower frequencies when the individual photons are of low energy, and the wave nature is predominantly observed.

All matter reacts differently to electromagnetic waves depending on the frequency (or wavelength) of the wave. In the case of light for example, some objects appear opaque, transparent, and/or of different colors. An object is transparent when the wave passes through the object unimpeded. An object is opaque if the object absorbs or reflects the wave. Colors can be associated with wavelengths and/or energy levels of photons. The different ways objects react to the light spectrum defines their color, transparency or brightness when we look at them. This kind of behavior exceeds the domain of light and concerns the infinite electromagnetic spectrum. What differentiates the electromagnetic waves is more often how we use them, such as radio waves for which most objects are transparent or on the contrary, microwaves for which metals are like mirrors and water, grease and sugar are absorbent. The field of photonics is vast and is closely related to the field of electronics since the electromagnetic wave interacts with matter notably through electrons absorbing and emitting photons. For example, the laser is an electronic photon emitter, the photovoltaic panels are photon to electron converters, optic fibers are photon transmitters etc...

#### **1.1.1.1 The MASER and the LASER**

The modern field of photonics starts in the 1950s and the invention of the MASER (Microwaves Amplification by Stimulated Emission of Radiations) in 1953 by Charles H. Townes, James P. Gordon, and Herbert J. Zeiger [1]. The maser itself was based on the principle of stimulated emission proposed by Albert Einstein in 1917. When a photon of energy  $h\nu$  is absorbed by an atom it will reach an excited state as in figure 1.2(a). In reverse, an excited atom can spontaneously emit a photon to reach its ground state as in figure 1.2(b). The difference of energy level between excited and ground state will correspond to the energy of the photon  $\Delta E = h\nu$ . In the case of stimulated emission, a photon of energy  $h\nu$  will cause an excited atom (of energy  $h\nu$  above its ground state) to emit a photon of same energy  $h\nu$ . The two photons will be in phase and produce a coherent light wave as seen in figure 1.2(c). By placing this amplifier in a resonant cavity as in figure 1.2(d), the wave will keep amplifying itself by going back and forth in the cavity. This will produce a powerful coherent (one wavelength) electromagnetic wave. Using the exact same principle of an amplification medium inside a resonant cavity, the LASER (Light Amplification by Stimulated Emission of Radiation) was developed using

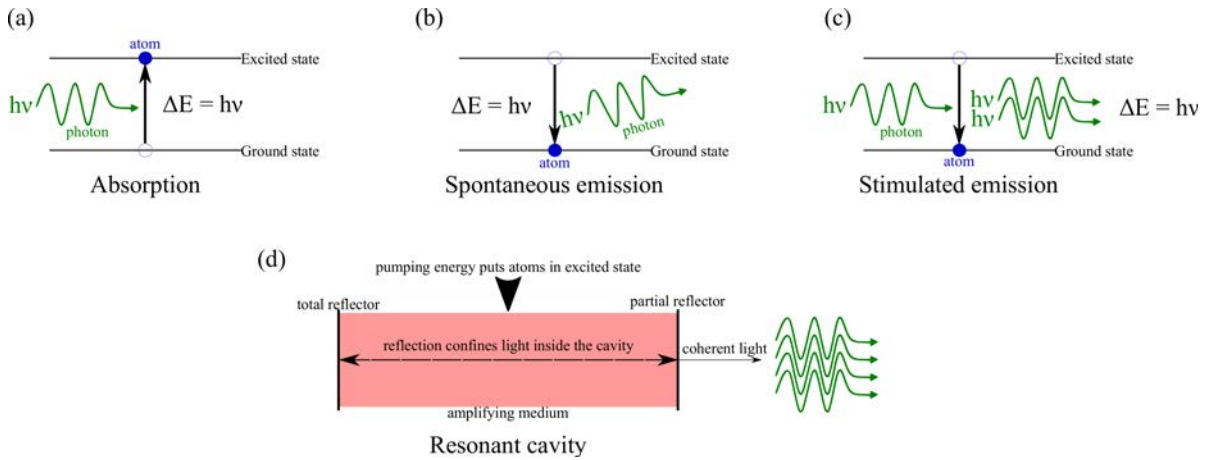


Figure 1.2: Schematic of (a) absorption, (b) spontaneous emission, (c) stimulated emission of a photon. (d) Schematic of a MASER or LASER.

a ruby crystal, by Theodore H. Maiman in 1960 based on the work of Charles H. Townes and Arthur L. Schawlow [2]. The difference lies in the shorter wavelengths, pertaining to the visible spectrum, produced by the laser compared to the microwaves produced by the maser. The use of lasers soared due to the fact that the active region inside the laser cavities could be replaced by a cheap semiconductor (p-n junction) instead of a crystal [3]. Charles H. Townes, Nikolai G. Bassov, and Alexandre M. Prokhorov shared the Nobel prize in 1963 "for fundamental work in the field of quantum electronics, which has led to the construction of oscillators and amplifiers based on the maser-laser principle". Lasers have found use in a number of applications in telecommunications, in scientific research, in military devices, in medical treatments and devices, in cars and more.

### 1.1.1.2 Fiber Optics

Another milestone in photonics is the first low loss optical fiber for telecommunications in 1970. The light propagates through the core of the optical fiber made of glass and of relatively high refractive index surrounded by a cladding of relatively low refractive index. The light is confined within due to internal reflection preventing the beam from escaping. Total internal reflection takes place when a beam propagating in a material of relatively high refractive index arrives with grazing incidence at the interface with a material of relatively low refractive index, as depicted in figure 1.3.

Before 1970, propagation through glass lead to an attenuation of 1000 dB/km. In 1970, based on the work of Charles K. Kao and George A. Hockham [4] that defined the principles for attaining very low attenuation, Corning Glass Works reduced the attenuation to

17 dB/km. In 2009, Charles K. Kao was awarded the Nobel prize "for groundbreaking achievements concerning the transmission of light in fibers for optical communication". This meant that fiber optics could be used for long distance communications. The first generation of fiber optics operated at 45Mbit/s, with repeaters that would re-emit the reconstructed signal spaced to up to 10km. In 1987, at the end of the second generation of fiber optics the systems operated at 1.7Gbit/s with repeaters every 50km. By the late 1980s, the third generation fibers operated at 2.5Gbit/s with repeaters every 100km. The revolution, occurred with the fourth generation of fiber optics in 1992 and the emergence of optical amplifications and wavelength-division multiplexing (WDM). The optical amplifiers increased the strength of a light signal without first converting it to some other form enabling the replacement of some repeaters and the propagation of signals over great distances. The WDM used different wavelengths in the same fiber to propagate different information on each wavelength, increasing the transmission capacity of each fiber. This revolution was accompanied by the rise of internet, strongly boosted by the abundance of bandwidth that doubled every 6 months [5]. In 2016 commercially operated submarine cables carry 5-10Tbit/s but the state of the art transmission speeds go up to 100 Tbit/s. The fifth generation may include the concept of optical solitons first suggested in 1973 by Akira Hasegawawas [6]. The optical temporal solitons exists in optical fibers due to the nonlinear effect of fibers compensating dispersive spreading of wave packets [6]. The optical temporal soliton was first observed in 1980 by Linn Molenhauer, and in 1988 soliton pulses were transmitted over a distance of 4000 kilometers, and three years later, transmitted at 2.5 gigabits per second over more than 14000 kilometers by a Bell labs research team [7]. Using temporal solitons in the fifth generation could greatly

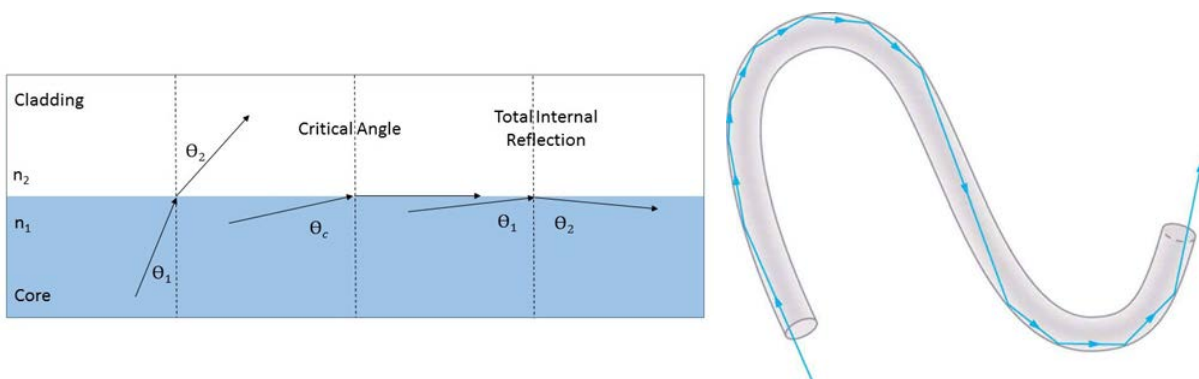


Figure 1.3: (Left) Refraction, critical angle and reflection at the interface of the core ( $n_1$ ) and the cladding ( $n_2$ ) of an optical fiber ( $n_1 > n_2$ ). Source *fluxlight.com* (Right) Example of light propagation inside an optical fiber Source *lumenlearning.com*.

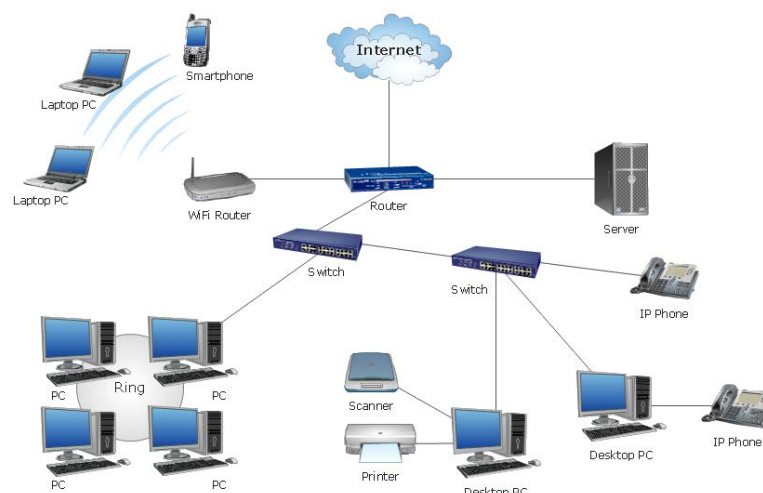


Figure 1.4: Typical office network requiring a router to distribute information between different devices. Source *conceptdraw.com*

enhance the propagation distances and further reduce the number of repeaters.

The reasons for the success of fiber optics over preexisting copper wire networks used for telegraphs and phone lines are numerous. They have much higher bandwidth, the data travels very long distances without requiring as much amplifications and repeaters, the fiber is immune to electrical interference and corrosion giving the fiber a longer lifespan, it is lighter, it is more difficult to tap giving better security and it consumes less energy. All of these reasons explain the progressive shift from electronics to photonics in telecommunications and other applications. Lasers and sensors have accompanied the evolution of the fiber optics however the routers and relays remain for the most part electronic. A routing device reads incoming data from different input channels and redistributes the data in the correct output channels. Figure 1.4 shows a schematic of typical router and switch connections to common appliances at the office or at home.

In order to fluidize traffic around the routers, nodes of our telecommunication networks, we believe that most computational electronics can be replaced by faster, more robust, energy efficient photonic devices. Given the actual climate change, low power, efficient and long lifespan devices are the key to the rising demands around the world of cloud services, internet of things, data storage, and computation power. In our lab we are intent in finding new possibilities for all-optical routers and computing devices. In 2008, using infrared-red beams in iron doped indium phosphide semiconductors (InP:Fe), very fast and steady state self-focusing was observed [8]. It was demonstrated in 2010 that by using two soliton beams and changing their relative phase it is possible to

switch between the condition of fusion and repulsion of these beams, thus giving the opportunity of addressing optical signal in an all-optical way with a very short response time[9]. Furthermore the role of the dopant, temperature and the background lighting have been studied and used to control the type of soliton propagation observed [10]. Finally, in 2014, the use of non-conventional Airy beams has revealed more numerous and complex waveguiding structures [11] for the realization of more complex routers. This thesis builds on our labs previous studies and focuses on the nonlinear behavior of non-conventional Airy beams in photorefractive crystals and the different resulting waveguiding possibilities for future routing applications.

## 1.2 Non conventional beams and nonlinear media

In this section we will detail and introduce more specific notions regarding this thesis such as non-conventional beams, nonlinear media, spatial solitons and imprinting in photorefractive crystals.

### 1.2.1 Non-conventional beams

In geometrical optics, the propagation of light is seen as series of rays propagating in straight lines from an emitting light source and through different optical devices that can change the direction of individual rays. From this standpoint, we can explain many

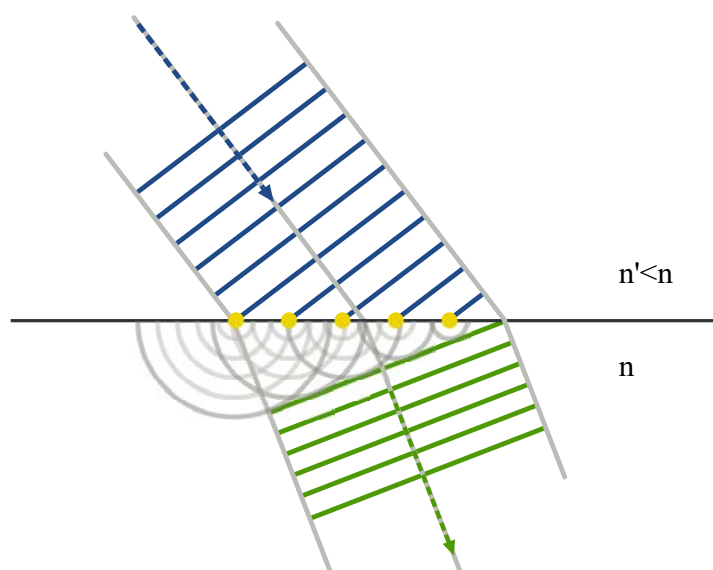


Figure 1.5: Refraction using the Huygens-Fresnel principle. Source *wikipedia*

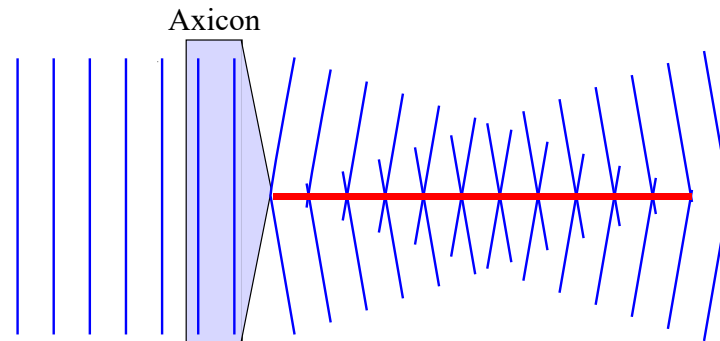


Figure 1.6: Bessel beam formed (in red) using an axicon to make two plane waves interfere.

properties such as mirrors, lenses, total internal-reflection or the formation of rainbows. This works as long as the illuminated objects are much larger than the wavelength of the illuminating beam. If an object is of the size of the wavelength, diffraction occurs and interesting phenomena can take place. The Huygens-Fresnel principle states that every point of the wavefront is itself the source of spherical wavelets that interfere to form the propagating wavefront. In figure 1.5, the wavefront propagates in a medium of refractive index  $n'$  (blue), at the speed  $v = c/n'$ . At the interface, by considering every point of the wavefront as an emitter of spherical waves, the wavefront is reconstructed in the medium of refractive index  $n$  (green). The angle is due to the difference of propagating speed of the wave between the two media. The speed is slower in the second medium  $v = c/n$ , so the reconstructed wavefront is tilted.

Using complex diffraction patterns, the transverse profile of a propagating wavefront can be reorganized and structured. In doing so we can create what is called non-conventional beams that give the impression of being *diffraction-free* because they preserve their profile along propagation. Bessel beams, Mathieu beams and Airy beams are examples of non-diffracting beams [12]. Figure 1.6 shows a plane wavefront traversing an axicon. The axicon divides the wavefront in two new wave fronts propagating at an angle. These two wavefronts interfere constructively in the red area creating a Bessel beam. The Bessel beam preserves its profile along propagation and its propagation length depends on the plane waves transverse size. A common way to generate complex diffraction patterns is by using a spatial light modulator (SLM). This device formed by a matrix of small cells can be remotely controlled to change the wavefront of an incoming light beam. The beam will illuminate the SLM and by reflection or transmittance, the wavefront can be shaped to our choosing. This *phase modulation* can be different for each pixel of the SLM. Therefore, the resolution of the SLM will determine the number

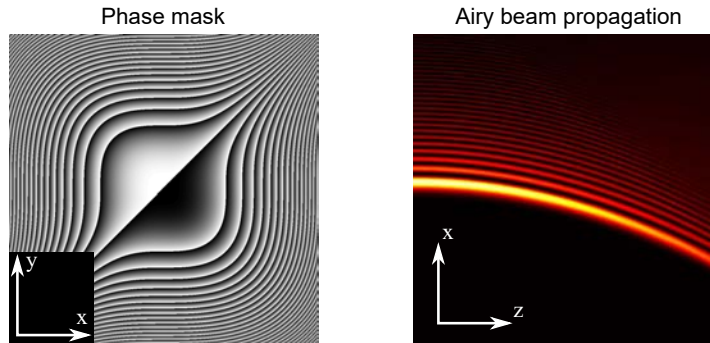


Figure 1.7: (Left) Phase mask on the SLM that creates an Airy beam after diffraction. (Right) Airy beam propagating along the  $z$ -axis.

of points we use to reconstruct the wavefront using the Huygens-Fresnel principle.

Our group has taken interest in the most recent non-conventional beam, the Airy beam seen in figure 1.7. This beam has been extensively studied in the last twelve years since their first experimental observation in 2007 [13, 14]. The idea of the Airy beam originates from the field of quantum mechanics in 1979 with the work of Berry and Balazs [15]. The Airy beam has three interesting properties [16]; it is *diffraction-free*, propagates along a parabolic *self-accelerating* trajectory, and has *self-healing* properties [17]. Our work consists in studying the Airy beam, their generation, their nonlinear propagation and interactions in photorefractive crystal and possible applications such as waveguiding devices. In our case the advantage of studying non conventional beams is threefold. First they offer diverse ways to propagate light, for example inside a nonlinear photorefractive crystal, and can create complex waveguiding structures. Secondly they challenge the theoretical and numerical models used in anisotropic photorefractive media, challenging our understanding of nonlinear effects. Finally they can help understand the transition dynamics from linear to nonlinear propagation. The Airy wave function is a *spatial* solution of the wave equation but it is also a *temporal* solution of the wave equation. By considering spatiotemporal dynamics, different beams that propagate undistorted in a 3D space-time environment can be derived from the Airy beam such as the Airy-Bessel beam [13, 18], or Airy light bullets [19, 20], and more [21, 22]. The combinations of temporal or spatial Airy beams or other non-conventional beams have greatly widened the possible applications for Airy beams in the field of photonics.

## 1.2.2 Linear and nonlinear media

When light illuminates a material, the light's electric wave induces a movement of the electron charges inside the medium which results in the creation of dipoles and/or modifications of existing dipoles  $p(t) = qd(t)$  (with  $q$  the displaced charge and  $d(t)$  the distance of displacement over time). Under the influence of the electric field, the dipoles oscillate and radiate their own electromagnetic field. For example, if the dipoles move in accordance with the light's electric wave (ie. they oscillate at the same frequency and are in phase), they have no impact on the light's electric field and the medium is considered transparent. On the contrary, if the electric field oscillates at a speed that the dipoles have difficulty matching, their oscillation amplitude is dampened, and the electric field is absorbed, the media appears opaque.

In optics, the terms linear and nonlinear media refers to the way polarization density  $p$  responds to the light's electric field  $E$  inside the media. In the case of a linear response, the polarization density can be expressed  $p(t) = \epsilon_0\chi^{(1)}E(t)$ . In the case of a nonlinear response, the polarization density is more complex:

$$p(t) = \epsilon_0\chi^{(1)}E(t) + \epsilon_0\chi^{(2)}E(t)^2 + \epsilon_0\chi^{(3)}E(t)^3 \dots$$

With  $\epsilon_0$  the electric permittivity of free space and  $\chi$  the electric susceptibility which characterizes the interactions of the nonlinear material. In the case of isotropic materials the susceptibility is the same in all direction. However, in the case of birefringent materials, the susceptibility will be related to preferential axes in the material, and be instead a susceptibility tensor. This is notably the case of photorefractive materials discussed further on.

In nonlinear media, if  $\chi^{(2)} \neq 0$ , the second term to the right of the equation representing interactions of the order of the electric field squared can be considered. Therefore, by injecting two different light electric fields, their product will be able to interact within the crystal. This interaction is called three wave mixing. In function of the two electric field's wavelengths, we obtain second-harmonic generation, sum-frequency generation or difference-frequency generation. This leads to applications such as optical parametric oscillators or phase-conjugated mirrors.

The response of the material in the linear case is often embodied in the more common expression, the refractive index  $n_0 = \sqrt{1 + \chi^{(1)}}$ . When the response is nonlinear, the refractive index varies inside the crystal depending on the electric field distribution:

$$n = n_0 + \Delta n$$

If  $\chi^{(2)} \neq 0$  (respectively  $\chi^{(3)} \neq 0$ ),  $\Delta n$  is proportional to  $E$  (respectively  $E^2$ ) and the induced nonlinear effect is called the Pockels effect (respectively the Kerr effect). The fact that the refractive index variation varies with the electric field means that the refractive index will only change where light propagates. If the variation is positive (respectively negative) the propagation will undergo self-focusing (respectively defocusing).

### 1.2.2.1 Spatial solitons

In particular, if the focusing effect cancels out the diffraction of the propagating beam, self-trapped beams can propagate. These beams are called *solitons* and given the right nonlinear conditions, they preserve their profile when propagating over infinite distances. The name soliton was given to describe their particle-like nature, notably the way these solitary waves remained unchanged after collision [23]. They were first observed in 1966 in carbon disulfide [24] and the first observation of spatial solitons in dielectric media were done by Barthelemy et al. in 1985 in carbon disulfide (Kerr media) using high power light beams ( $\sim GW\ cm^{-2}$ ) [25]. It had been established in 1965 that, in the case of Kerr circular solitons, over-focusing would tend to change the beam into filaments [26]. To avoid destructive over self-focusing of the propagating beam Barthelemy reduced the problem from three dimension to two dimensions. Instead of a three dimensional circular beam soliton he considered a two dimensional steady plane soliton, or (1+1)D soliton. The first spatial soliton in solid-state material was observed in 1990 using a single-mode planar glass waveguides [27] and in 1993 the first photorefractive soliton was observed, requiring less power to generate and propagate itself than the Kerr soliton [28, 29].

Due to the *saturable* nonlinear nature of photorefractive media, the photorefractive soliton contrarily to Kerr solitons can be stable in the two transverse dimensions enabling (2+1)D solitons to propagate. Due to saturation of the nonlinear focusing effect, the over-focusing observed in Kerr media is avoided in photorefractive media. The displaced charges relocate and the lensing effect instead of becoming stronger becomes wider [30, 31]. Therefore in photorefractive media, the particle-like interactions and collisions of soliton beams occur in three dimensions, and spatial solitons can spiral around each other [32]. The interactions in photorefractive media are therefore more rich and complex than in Kerr media where the interactions are in-plane attraction and repulsion [33]. Additionally, saturable nonlinearity means that inelastic collisions can be observed leading to soliton fusion or fission [30, 31]. The low power required to observe strong nonlinear effect, and the saturable nature of photorefractive crystals have made it our crystal of choice to study beam propagation.

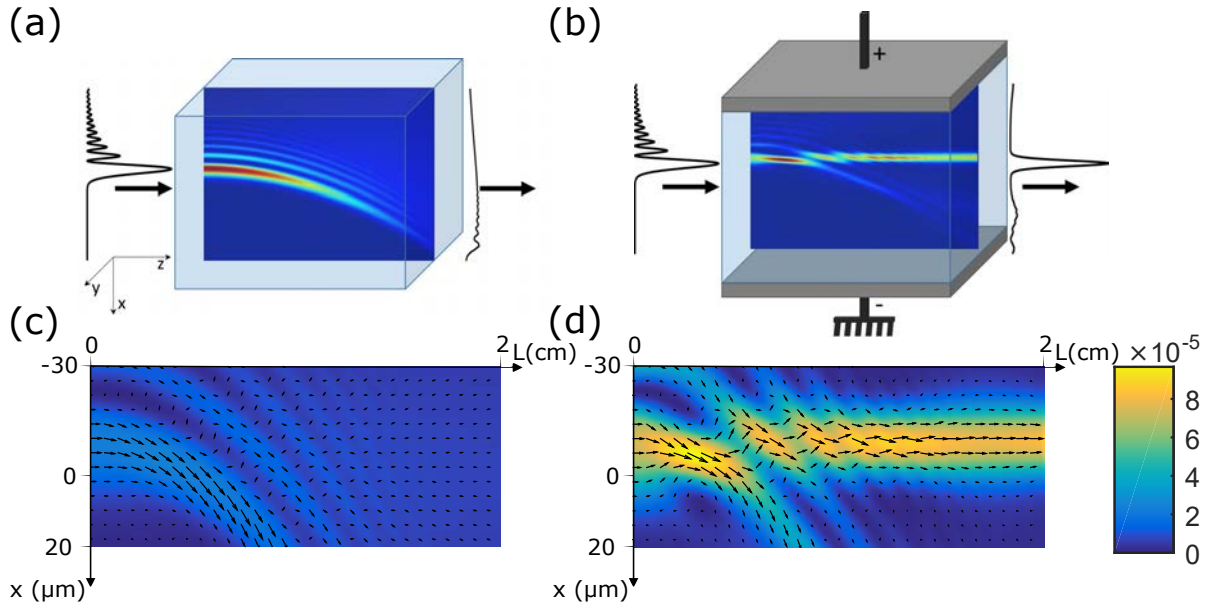


Figure 1.8: Propagation of a 1D Airy beam in a photorefractive crystal at steady state. (a) Linear propagation. (b) Nonlinear propagation in the presence of an external electric field leading to an OSS. (c), (d) Distribution of the refractive index change corresponding to (a) and (b) respectively. Arrows represent the Poynting vector.

### 1.2.2.2 Airy beams in nonlinear media

The propagation of non-conventional Airy beams in nonlinear media has been studied extensively in both Kerr media [34–36] and photorefractive media [35, 37–41] and to lesser extent in thermal nonlinear media [42]. The Airy beams in biased nonlinear media have interesting dynamics such as soliton-like behaviors [35, 37, 39–41] and interactions of co- and counter-propagating Airy beams [39–41]. With a refractive index gradient modifying the deflection of the propagating beam, in nonlinear medium, the deflection or acceleration of the Airy beam can be enhanced, reduced, or canceled [43]. Other interesting dynamics can be obtained using more complex index variations inside the photorefractive medium such as induced photonic lattices [44, 45].

Under focusing nonlinear conditions the Airy beam may split into a weak accelerating structure and a structure that has been named "off-shooting soliton" (OSS) and that propagates along the medium without transverse acceleration [46]. The first experimental OSS was observed by Wiersma *et al* and the interactions between the photoinduced OSS and the accelerating beam have been studied [41], resulting in attraction, deflection and tightening effects of the OSS and interesting analogies with gravitational lensing and tidal forces.

Figure 1.8 shows the propagation behavior of an Airy beam through a photorefractive crystal for (a) linear and (b) non-linear conditions. Figure 1.8(c-d) show the photo-induced refractive index variation of the medium and the arrows represent the Poynting vector or energy transfer of propagating light. For high enough nonlinearity strength, most of the beam turns into a so-called "off-shooting soliton", while a small fraction of the power remains a self-accelerating linear packet [41, 46]. The linear Airy beam is a stationary solution of the *linear* Schrödinger equation that is used to describe the evolution of propagating beams in linear media. When a nonlinear effect is applied on the photorefractive crystal the Airy beam propagates through a nonlinear media, and the propagation is described by the *nonlinear* Schrödinger equation. The Airy beam propagation is no longer a stationary solution of this equation. A stationary solution of the *nonlinear* Schrödinger equation is a family of soliton beams. The Airy beam profile injected in nonlinear media changes shape along propagation and converges to a stationary soliton profile. The emergence of the OSS when injecting an Airy beam in nonlinear media can therefore be considered as the transition from the linear Airy solution to the nonlinear soliton one. Interestingly this transition is slow enough for the coexistence of a linear self-accelerating wave packet and an OSS structure allowing interesting interactions and waveguiding possibilities. However one question remained and has been answered in this thesis: is the Airy beam off-shooting soliton a spatial soliton? Furthermore, as very few studies exist, we will take an interest on two dimensional Airy beam propagation in nonlinear media and the two dimensional OSS.

### 1.2.3 Imprinting in photorefractive media

The photorefractive effect was discovered as "optical damage" in 1966 by Ashkin et al. [47]. The degradation occurred when the beam was linearly polarized along the c-axis direction of the crystal. The c-axis is the preferred direction of diffusion of free-charges inside the birefringent photorefractive crystal. This degradation quickly turned into an interesting electro-optic feature however, as Chen et al. proposed to use photorefractive crystals (PR) as storage media for optical holography [48].

The photoinduced hologram is a refractive index structure written in three dimensions inside the crystal without any other form of processing. The refractive index structure appears at very low optical powers ( $\mu W$ ) due to the Pockels effect, making photorefractive media a promising candidate for low power consumption optical information processing. In writing mode, an information is stored inside the photorefractive crystal as an imprinted interference pattern called *hologram*. In reading mode, the diffraction

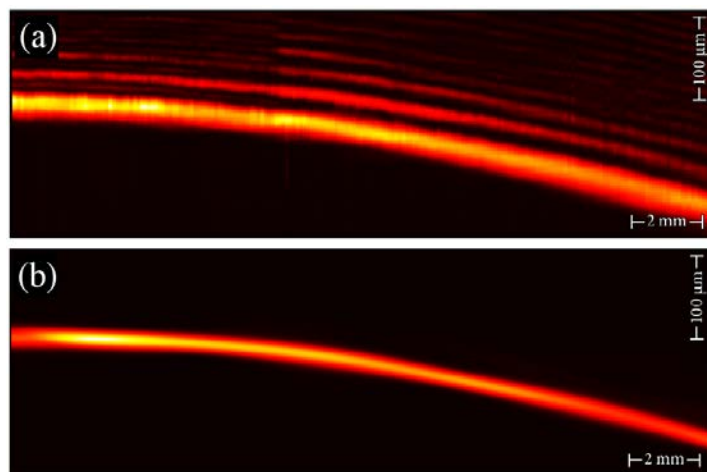


Figure 1.9: Airy beam induced guiding. (a) Airy beam accelerating intensity profile in longitudinal direction. (b) Numerical simulation of a guided beam during propagation. Extracted from [38].

image of the hologram returns the initially stored information. In addition, the read and write functions must be operated with the same reference beam in terms of wavelength and angle of incidence. Therefore, using different reference beams, multiple images can be stored in the same crystal.

Since the natural diffraction of light beams in photorefractive crystals can be compensated by self-induced nonlinear focusing effects creating a spatial solitons, waveguides that share the same properties as the soliton, particularly an unchanging profile along propagation can be created [49].

Instead of using Gaussian soliton beams to imprint waveguides in photorefractive medium, other non-conventional beams such as Airy beams can be used. The waveguiding structure can then present interesting properties of the Airy beam, such as a multilobed structure or a curved trajectory. In 2013, Airy beams were presented as a possibility for optical routing [38]. In figure 1.9, the Airy beam's main lobe is used as the waveguiding structure and different output positions can be obtained by varying the Airy beam's acceleration. Furthermore, an optically induced splitter was obtained by switching between two waveguiding configurations at a quicker speed than the response time of the crystal thus enabling two or more waveguiding structures to superimpose themselves. Additionally, multiple Airy beams can be used in nonlinear conditions to leverage interactions and off-shooting solitons as waveguiding structures [11]. These results show that Airy beams can be used in all-optical routing setups and enable multiple channel configurations.

### 1.2.4 Outline

In this thesis we study the propagation of non-conventional Airy beams in photorefractive media, and the resulting waveguiding possibilities. We demonstrate the soliton nature of the Airy beam off-shooting soliton, the focusing mechanics of the Airy beam in anisotropic biased photorefractive media, and new waveguiding possibilities.

In the first chapter we take an interest in the experimental generation of the Airy beam. We provide insight on the reasons for strangely shaped experimental Airy beams and the way to obtain correct experimental finite Airy beams, in accord with numerical and theoretical results. We look at parameters such as the initial Gaussian beam size and shape, the phase shift on the mask, and misalignment. This allows to understand the influence of these experimental parameters on the Airy beam size, number of lobes and integrity.

In the second and third chapter, we explore the nonlinear propagation of the Airy beams.

Chapter 3 tackles one transverse dimension Airy beam propagation in order to underline the similar nature of the photorefractive Airy beam off-shooting soliton and the (1+1)D photorefractive soliton. We observe that for fixed nonlinear conditions inside a photorefractive crystal, there exists a range of intensity values for which the off-shooting soliton property is the closest to the ideal theoretical soliton.

Chapter 4.6 tackles two transverse dimension Airy beam nonlinear propagation. These observations show that the anisotropy of the crystal and asymmetry of the applied electric field results in a two-stepped focusing dynamic of the Airy beam into an off-shooting (2+1)D soliton. Therefore, by changing the nonlinearity strength we can tune the propagation from linear Airy beam profile to nonlinear off-shooting beam profile allowing different waveguiding structures to exist between the two configuration with the use of a single Airy beam.

Finally, we look at multiple waveguiding structures inside a saturable nonlinear media using two counter-propagating Airy beams in anti-symmetric configuration. We test the waveguiding structure using a Gaussian probe beam and look at the effects of Airy beam truncation, shift between the Airy beams and nonlinear strength on the waveguiding structures. We find configurations giving multiple outputs for multiple input positions with large output-to-input shifts.

Thanks to this three year thesis, we demonstrate that the Airy beam offers solutions for all-optical routing. The non-diffracting, self-healing and accelerating nature of the Airy beam combined with tunable nonlinear propagation allows large, curved, multi-channel, modular, optically induced waveguides to interconnect or separate an optical signal into multiple beams. Additionally, the use of multiple counterpropagating Airy beams and their nonlinear interaction, increases the possibilities of optical interconnections and routing. Therefore the results presented in the following chapters confirm the promising implementation of Airy beams in all-optical computing.

## EXPERIMENTAL GENERATION OF AIRY BEAMS

**T**his thesis presents both experimental and numerical results of a propagating Airy beam in a nonlinear medium. We will first give the reader an understanding of what is an Airy beam, where do they come from and how to generate them experimentally. We will start with an analytic approach to understand the amount of control we can have on the experimental Airy beam. We will then take an interest in the effect that specific experimental parameters have on the shape of the Airy beam. Numerical simulations and experimental images will illustrate our study.

## 2.1 An overview of Airy beams

### 2.1.1 What are Airy beams?

Conventionally, we imagine the propagation of light as a beam along a straight trajectory that diffracts and diverges. In fact, the intensity centroid of the light beam propagates along a straight trajectory in homogeneous media, in accordance with Ehrenfest's theorem and diffraction generally scatters the light intensity. However, the transverse profile can be reorganized and structured along the propagation axis. In doing so we can create *diffraction-free* beams that preserve their profile along propagation. Bessel beams, Mathieu beams and Airy beams are examples of non-diffracting beams [12]. The Airy beam is the most recent non-conventional beam and they have been extensively studied in the last twelve years since their first experimental observation in 2007 [13, 14]. The idea of the Airy beam originated from the domain of quantum mechanics in 1979 with the work of Berry and Balazs [15]. They found a wave packet  $\psi(x, t)$  whose probability density  $|\psi(x, t)|$  was shape-preserving and self-accelerating along the transverse x-axis. The term *self-accelerating* indicates that the wave is accelerating without the need of an external potential. At time  $t=0$  the wave packet is

$$(2.1) \quad \psi(x, 0) = Ai(Bx/\hbar^{2/3}),$$

with  $B$  an arbitrary constant,  $\hbar$  the Planck constant and  $Ai$  the Airy function. The "Airy packet" is a solution to the potential-free Schrödinger equation

$$(2.2) \quad -\frac{\hbar^2}{2m} \frac{\partial^2 \psi}{\partial x^2} = i\hbar \frac{\partial \psi}{\partial t}$$

with  $m$  the mass of the particle.

The solution is of the form:

$$(2.3) \quad \psi(x, t) = Ai \left[ \frac{B}{\hbar^{2/3}} \left( x - \frac{B^3 t^2}{4m^2} \right) \right] \exp \left( i \frac{B^3}{2m\hbar} t \left[ x - \left( \frac{B^3}{6m^2} t^2 \right) \right] \right)$$

The probability density  $|\psi(x, t)|^2$  remains unchanged in form, it has the shape of the Airy function squared, but it accelerates with a velocity of  $\frac{B^3 t^2}{4m^2}$ .

This result remained unnoticed from 1979 to 2007, probably due to the difficulty of generating quantum particles in an Airy state or due to the Airy wave function's infinite norm.

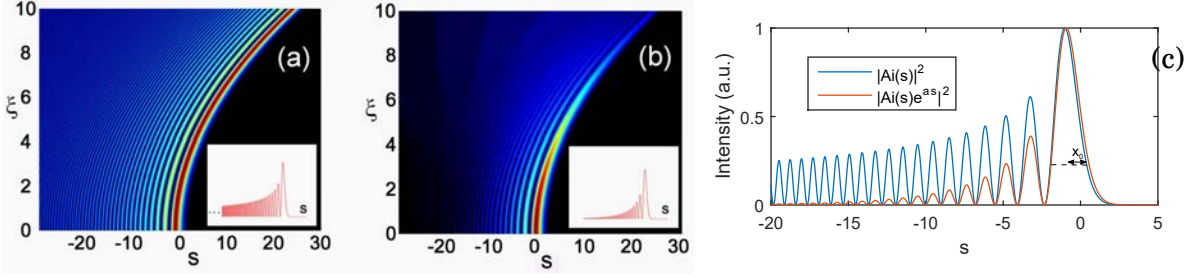


Figure 2.1: Propagation dynamics of (a) a diffraction-free infinite-power Airy beam and (b) a finite-power Airy beam when  $a=0.05$ . Extracted from [14] (c) Transverse profile of the infinite-power Airy beam and finite-power Airy beam at  $\xi = 0$

The breakthrough occurred in 2007 in the field of optics. Indeed, the paraxial wave equation is a mathematical equivalent of the Schrödinger potential-free equation,

$$(2.4) \quad -\frac{1}{2} \frac{\partial^2 \phi}{\partial s^2} = i \frac{\partial \phi}{\partial \xi}$$

where  $\phi$  is the electric field envelope,  $s = x/x_0$  is the transverse scale normalized by an arbitrary  $x_0$ ,  $\xi = z/k_0 x_0^2$  is a normalized propagation distance with  $k_0 = 2\pi n/\lambda_0$  the wave vector,  $\lambda_0$  the wavelength and  $n$  the refractive index of the propagative medium.

Therefore there is a solution to the equation 2.4 that is similar to equation 2.3 that applies in optics, the infinite-power Airy beam solution:

$$(2.5) \quad \phi(\xi, s) = Ai\left(s - \frac{\xi^2}{4}\right) e^{i\left(\frac{1}{2}s\xi - \frac{1}{12}\xi^3\right)}$$

The Airy function presents an infinite tail, which makes it impossible to create experimentally as that would require an infinite amount of energy. The finite power Airy beam is obtained by considering its exponentially decaying version,

$$(2.6) \quad \phi(s, \xi = 0) = Ai(s) e^{as}$$

with  $a > 0$  the decay factor. The corresponding exponentially truncated Airy beam solution is :

$$(2.7) \quad \phi(\xi, s) = Ai\left(s - \frac{\xi^2}{4} + ia\xi\right) e^{as - \frac{a}{2}\xi^2 + i\left(\frac{s}{2}\xi + \frac{a^2}{2}\xi - \frac{1}{12}\xi^3\right)}$$

$a = 0$  corresponds to the ideal infinite power Airy beam.

Figure 2.1(a) (respectively (b)) shows an infinite-power (respectively finite-power) Airy beam propagating along the  $\xi$  axis. The initial ( $\xi = 0$ ) transverse profile, along the transverse s-axis, is plotted in red in figures 2.1(a-b) and they are plotted in blue and red in figure 2.1(c). Without truncation, in figure 2.1(a), the Airy beam intensity profile does not change along propagation, but only shifts along the s-axis at an accelerating pace while propagating. With truncation, in figure 2.1(b), the intensity profile of the Airy beam slowly fades while propagating, so the truncation has the effect of tarnishing the diffraction-free nature of the Airy beam. However, the lateral accelerating shift of the Airy beam along propagation is not impacted by truncation.

The Airy beam has therefore three interesting properties [16], illustrated in figure 2.2. It is *diffraction-free* (2.2(a)), the amplitude profile is invariant in the transverse plane when propagating. The beam shifts on the transverse axis, along a parabolic *self-accelerating* trajectory. This allows the beam to circumvent obstacles as in figure 2.2(c). Finally, the beam has *self-healing* properties allowing it to regenerate its transverse profile after being blocked by an obstacle [17]. Figure 2.2(d) shows an Airy beam with the main lobe blocked. After propagating 11cm, the profile in figure 2.2(e) has partially regenerated. This behavior can be analyzed by using optics ray description illustrated in figure 2.2(b). The main lobe results of a parabolic caustic, giving it the characteristic curved trajectory and if part of the main lobe is blocked it will be regenerated by the other rays forming the caustic.

The parabolic trajectory of the Airy beam has been studied [51, 52] and so have other families of accelerating beams such as Weber accelerating beams or half-Mathieu beams [16, 53], showing that the trajectory can be controlled and modified, allowing to circumvent obstacles as in figure 2.2(c). Due to the fact that many interactions with light are based on the peak intensity and not the intensity centroid of the beam, the fact that the peak intensity of the beam accelerates transversely while the centroid of the beam remains unchanged [54] leads to a number of applications where an intense parabolic light beam is needed [50], such as curved plasma channel generations [55], particle manipulation [56], plasmons [57], material processing [58] or all-optical routing [11, 38, 59].

Figure 2.3(1) shows the Airy beam used a 'snowblower'. The particles are pushed in the same direction as the Airy beam's accelerating trajectory. In figure 2.3(1.a) the particles are pushed in the down-left purple quadrant whereas in figure 2.3(1.b) the Airy beam is rotated  $180^\circ$  and the particles are pushed in the opposite direction to the green quadrant. Figure 2.3(2) shows the Airy beam used in material processing. The machining

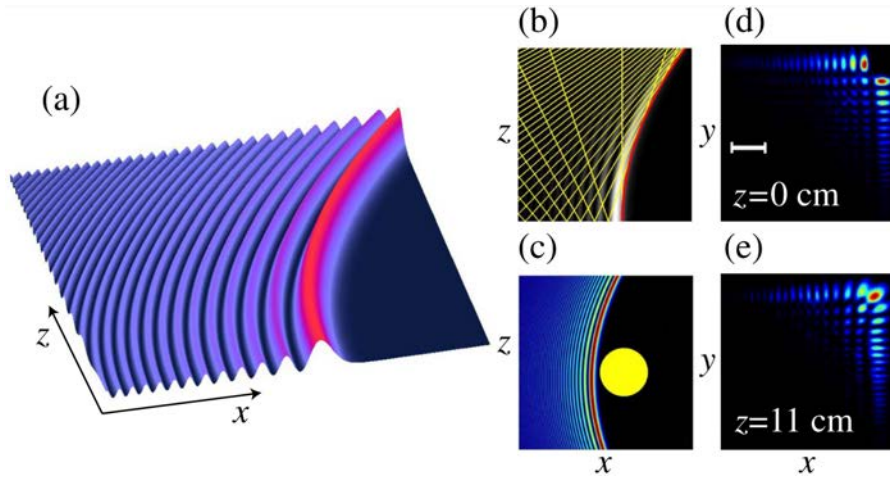
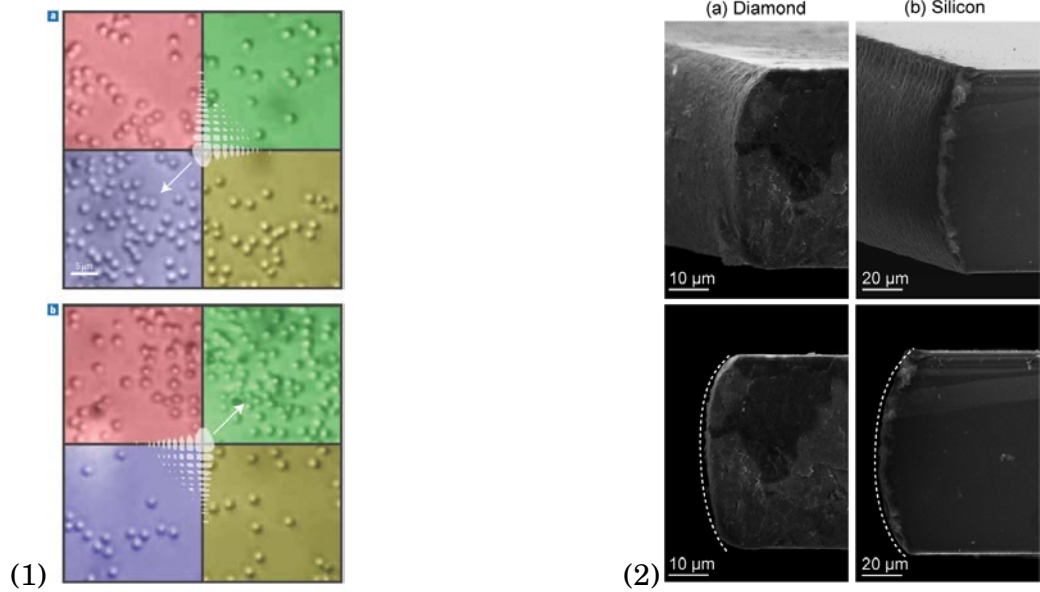


Figure 2.2: Airy beam along with its diffraction-free, self-bending, and self-healing properties. In (a), the propagation dynamics of an accelerating diffraction-free Airy beam is depicted. A optics ray description is shown in (b), with the rays presented as yellow lines and the parabolic caustic trajectory shown with a red curve. (c) Due to its curved parabolic trajectory, the Airy beam is able to circumvent obstacles. The experimental generation of a 2D Airy beam is shown in (d) and (e). (d) On the input plane the main lobe of the Airy beam is blocked. (e) Due to self-healing, the main lobe is then reconstructed during propagation. The scaling bar in (d) and (e) is  $200 \mu\text{m}$ . Extracted from references [17, 50, 51]

of diamond (a) and silicon (b) using an accelerating beam allows the etched surface to be curved, matching the accelerating trajectory of the etching beam.

A different kind of application for Airy beams is light-sheet microscopy; the interest in this case is to excite the fluorescence of a sample. The non-diffracting nature of beams like the Bessel or Airy beams enhances the field of view, and the asymmetry of the Airy beam gives better results [60] as can be seen in figure 2.4. In figure 2.4, the first row corresponds to a conventional circular Gaussian beam, the second row is obtained by using a diffraction-free Bessel beam and the third row is obtained using a diffraction-free asymmetric Airy beam. The image resolution is systematically better using the Airy beam.

In the previous example of application of the Airy beam to manipulate microparticles (figure 2.3(1)), the Airy beam transverse profile is two dimensional, ie. the beam has an Airy function shape along both transverse axis. Indeed, many beams have been derived from the one-dimensional Airy beam solution. By applying the solution in a cylindrical coordinate system for example, we can obtain circular Airy beams and abruptly auto-focusing waves [61–63] that leverage the parabolic trajectories of multiple 1D-Airy beams



The micrometre-scale 'snowblower' at work. The white arrow indicates the deflection of the beam's main spot during propagation. (b) Subsequently to the micrograph shown in (a) the Airy beam was rotated by 180°. Extracted from reference [56]

Machining of (a) diamond and (b) silicon using circular accelerating beams. In the bottom row is compared the form of the machined surface with the expected profile. Extracted from reference [58]

Figure 2.3: Examples of applications of Airy beams : the micromanipulation of microparticles and material processing.

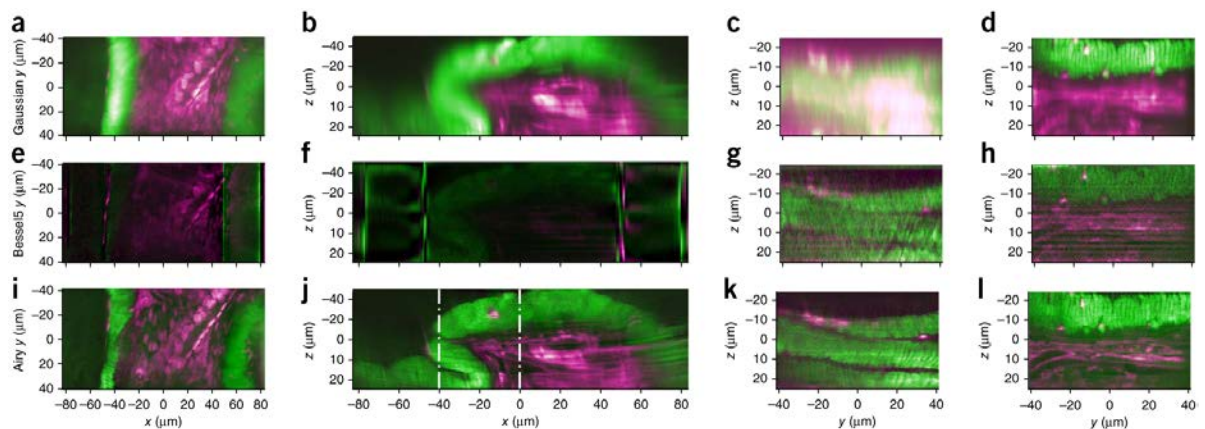


Figure 2.4: Light-sheet microscopy scan of a juvenile amphioxus. (a-l) Three volumetric images were acquired using Gaussian (a-d), Bessel (e-h) and Airy (i-l) illumination beams, respectively. Extracted from reference [60]

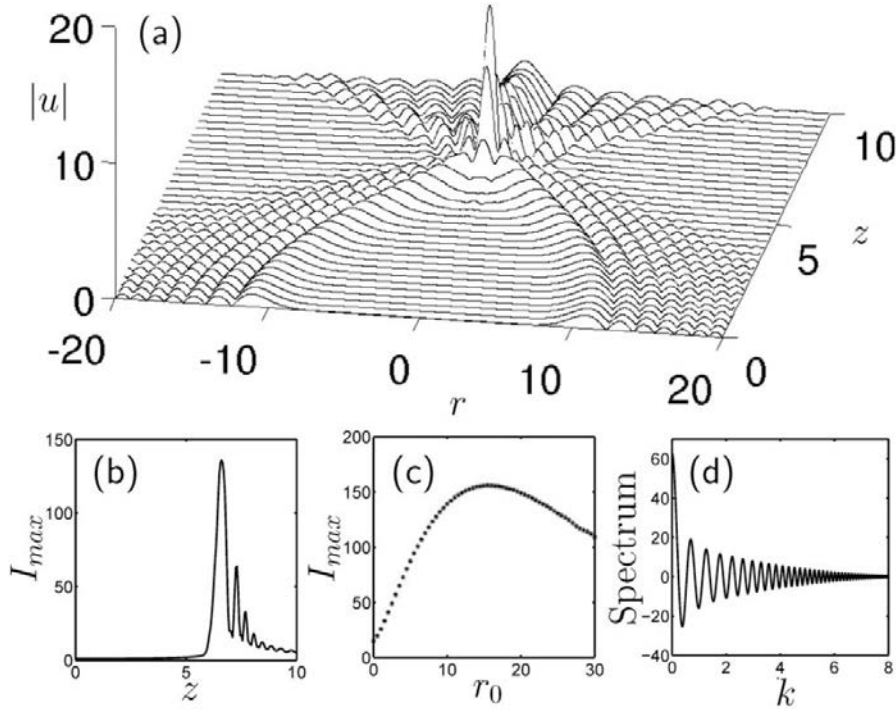


Figure 2.5: Dynamics of radially symmetric Airy beams for  $a = 0.05$ ,  $r$  is the normalized transverse scale,  $z$  is the normalized propagation scale,  $I$  is the intensity,  $r_0$  is the initial radius of the main ring, and  $I_{max}(z = 0) = 1$ . (a) Detailed plot of the central part of the propagation dynamics. (b) Maximum intensity as a function of  $z$ . (c) Maximum intensity that the Airy beam reaches during propagation for different values of the initial radius  $r_0$ . (d) Hankel transform<sup>1</sup> of the initial condition. Extracted from [61]

to maximize the peak intensity in one point of space as seen in figure 2.5.

The Airy wave function is a *spatial* solution of the wave equation but it is also a *temporal* solution of the wave equation: the Airy impulse. When considering spatiotemporal dynamics other kind of beams that propagate undistorted in a 3D space-time environment can be derived from the Airy beam such as the Airy-Bessel beam [13, 18]. The generation of an Airy-Bessel beam is shown in figure 2.6. By using a cubic spectral phase, a Gaussian beam is transformed into a Gaussian shaped Airy pulse. The Airy pulse then travels through an axicon that changes the Gaussian spatial profile into a Bessel beam profile thus creating an Bessel shaped Airy pulse. Other combinations are possible such as the Airy-Airy-Airy beams that combine a two spatial dimension Airy beam with an Airy pulse in time [19–21], or the Airy-Hermite-Gaussian and Airy-Helical-

<sup>1</sup>The Hankel transform, also known as the Fourier–Bessel transform, expresses any given function  $f(r)$  as the weighted sum of an infinite number of Bessel functions of the first kind. It is similar to the Fourier transform, but using Bessel functions.

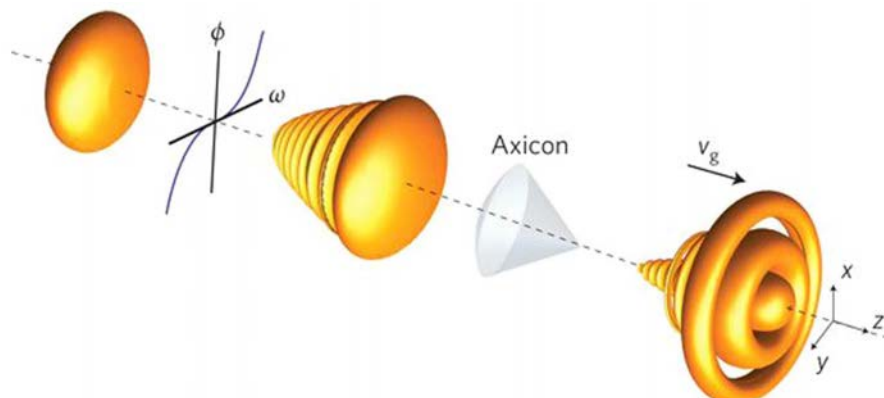


Figure 2.6: Experimental generation of an Airy-Bessel light bullet. 3D plots comprising iso-intensity contour plots of Gaussian-Gaussian (initial profile), Airy-Gaussian (after adding a large cubic spectral phase) and Airy-Bessel (after the axicon) wave packets.  $\phi$ ,  $\omega$ , and  $v_g$  are phase, optical frequency and group velocity respectively. Extracted from [18]

Hermite-Gaussian beams [22]. The combinations of spatial or temporal Airy beams and other non-conventional beams have greatly widened the possible applications for Airy beams.

### 2.1.2 How are Airy beams generated?

The Airy beam is not a "natural" light beam in the sense that it has to be engineered in order to be observed. Light is an electromagnetic *wave*; similarly to waves in the ocean, at a given time and space these waves can be in phase and reinforce each other or out of phase and cancel each other out. This phenomenon is commonly called interference, the areas in phase give light whereas the areas out of phase are dark. This creates an interference pattern that will depend on the phase, direction and resulting interference of multiple light beams. The Huygens-Fresnel principle states that every point on a wavefront is itself the source of spherical wavelets. Therefore, by engineering the wavefront of electromagnetic waves we can decide where there will be light and reorganize light in interference patterns. The Airy beam is an interference pattern, much like the Bessel beam [64].

G. Siviloglou et al. noticed in 2007 [13] that the Fourier transform  $\Phi_0(k)$  of the finite energy Airy beam is proportional to:

$$(2.8) \quad \Phi_0(k) \propto \exp(-ak^2)\exp(ik^3/3)$$

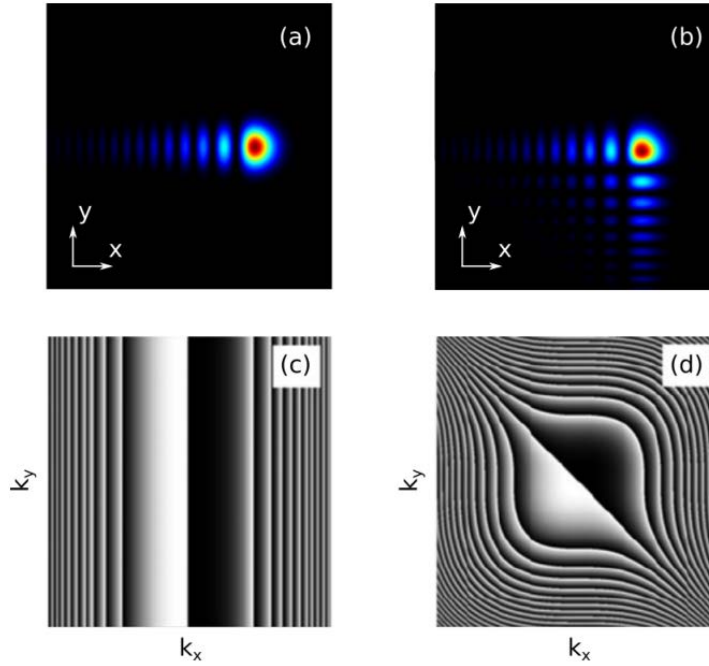


Figure 2.7: Transverse intensity distribution of a (a) 1 D-Airy beam and (b) 2 D-Airy beam. Phase mask on the spatial light modulator for the generation of a (c) 1 D-Airy beam and (d) 2 D-Airy beam. [14]

this expression's first product  $\exp(-ak^2)$  describes a Gaussian and the second product  $\exp(ik^3/3)$  defines a cubic phase. This entails that a Gaussian beam with a cubic modulated phase going through a Fourier transformation device (a lens in optics) will give an Airy beam [14].

To insert a cubic phase mask in the Fourier plane of a propagating Gaussian beam a spatial light modulator (SLM) can be used. SLMs can modulate the phase, amplitude or polarization of light and there exists various kinds of devices ; multiple quantum well SLM, ferroelectric liquid crystal SLM, magneto-optic SLM, charge-transfer-plate membrane-mirror SLM to name a few [65]. Figure 2.7 shows a one dimensional Airy beam (a), a two dimensional Airy beam (b) and the corresponding phase masks displayed on the SLM underneath (c) and (d). In the one dimensional case the phase mask is a cubic function to which is applied the modulo operator in order to confine the phase between 0 and  $2\pi$ . This results in black and white fringes, black being zero and white  $2\pi$ . In the two dimensional case, the cubic phase is along both orthogonal axes, and it results in an onion shaped phase mask. When modulating a Gaussian beam with a one dimensional phase mask, the Airy beam is one dimensional, in our case the Airy profile is along the x-axis (figure 2.7(a)), whereas the profile along the orthogonal y-axis remains

Gaussian. In the two dimensional case, the illuminating Gaussian beam is modulated in both transverse dimensions, along the x-axis and the y-axis, and results in an two dimensional Airy beam (figure 2.7(b)), with an Airy beam profile along both the x-axis and the y-axis.

It is worth mentioning for future applications, that there exists other ways to generate Airy beams, such as the Airy beam lasers [66] that uses a reflection diffraction grating on one end of a laser cavity; the grating both reflects light inside the laser cavity and shapes the output light according to the grating's profile. This makes it a more compact way to generate Airy beams since the lasers output beam does not need any externally applied phase modulation; however the grating cannot be changed once manufactured making it a less flexible solution than a SLM solution. Another solution uses arrayed waveguides [67] that force light into the Airy beam modes, which guaranties stability and easy handling but remains a less flexible solution than SLMs due to similar reasons as diffraction gratings. Another way to obtain Airy beams is completely passive, the cubic phase profile is obtained using the aberrations of the lens that performs the Fourier transform [68]. A final example of Airy beam generation uses nonlinear quadratic crystals [69], illustrated in figure 2.8. The Airy beams are generated by three-wave mixing (TWM) processes; the nonlinear quadratic crystals are asymmetricly modulated and induce a cubic phase front. Similarly to other methods, the Airy beam is obtained by Fourier transform of the TWM output. This method allows the creation of Airy beams at various wavelengths thanks to TWM as well as high intensities thanks to the robustness of nonlinear crystals to light intensity.

Due to our research purposes we value flexibility over robustness and will use a SLM; indeed the phase mask can be easily modified in order to adapt to different experimental setups. Furthermore, we want to test different type of Airy beams in our setup (different size, number of lobes, truncation). Future use could also be to fashion the light distribution even further, for example the creation of so-called "super-Airy beams" [70]. However, it is noteworthy that for other applications, other Airy beam generation methods may be more suitable.

## **2.2 Airy beam generation using LCOS SLM**

We decide to use a SLM in order to modulate the phase of a Gaussian beam and generate an Airy beam similarly to reference [13]. Current SLM-based systems use either optical MEMS (microelectromechanical system, [71]) or LCD (liquid crystal display) technology

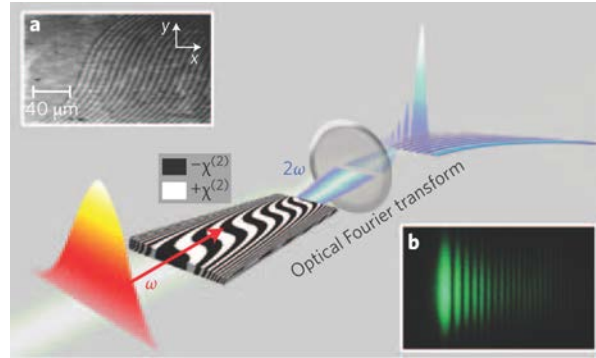


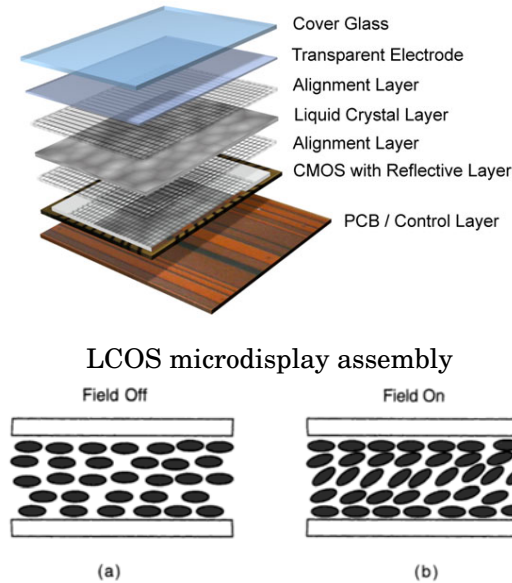
Figure 2.8: Nonlinear generation of Airy beams using a Gaussian pump, second-harmonic generation and an asymmetric nonlinear photonic crystal.  $\omega$  is the angular frequency of the Gaussian pump beam. (a) Microscope photograph of the quadratic crystal, after selective etching (which reveals the inverted domain pattern). The x- and y-axes were rescaled for viewing purposes and are not comparable. (b) Profile photograph of the green second-harmonic Airy beam. Extracted from [69]

[72]. The major advantages of MEMS are frame rate, spectral range, and an efficient use of nonpolarized light, however phase modulators and other optical implementations are rare and expensive [73]. Since LC-based technology is able to modulate intensity, phase, and/or polarization we will use a LCOS (liquid crystal on silicon) SLM, that enables almost analogue phase modulation.

There are possible limitations to this kind of generating method and it is useful to determine the right range of parameters for our experimental setup. This will help us to understand Airy beam shape defaults and ascertain that our experimental observations are authentic.

### 2.2.1 LCOS SLM Technology

The SLM is made up of multiple pixels (one cell is represented in figure 2.9) of liquid crystals (LC). They can each modify individually the phase of an incoming beam and create a complex wavefront that result in complex interference patterns. A LC is made up of molecular dipoles in a state between crystal and solid. It has liquid properties because the molecules are mobile and their positions in space are not rigid; but it has also crystal properties because the direction of the molecular dipoles tend to self-orient in a given direction due to intermolecular attractive forces. The mobility enables to actively change the direction of the molecular dipoles and their self-orientation causes anisotropy, both properties explaining its use in SLMs. Figure 2.9 shows the LC is confined between two polarizers, themselves confined between two electrodes. The illuminating light must



The alignment layer is treated to orient the liquid crystal molecules parallel to the surfaces, while the electric field tends to align the director perpendicular to the surfaces. (a) field below threshold value. (b) field above threshold value. Extracted from [74]

Figure 2.9: SLM liquid crystal cell and liquid crystal behavior

be polarized according to the SLM's polarizers, in our case a horizontal polarization. The light traverses the LC and its phase is delayed due to the LC refractive index. The apparent refractive index of the LC cell can be modified by rotating the LC molecules due to their anisotropy. The degree of rotation of the LC depends on the value of the applied field to the cell; on and off cases are shown in figure 2.9(a-b).

On the SLM is displayed a phase mask (example in figure 2.7). A certain gray level represents a defined average voltage across the LC cell. This voltage leads to a variable tilt of the LC molecules due to their *electrical* anisotropy. Since the LC molecules also show *optical* anisotropy this tilt changes the refractive index of the LC molecules (given the right incident polarization) which causes a modified optical path length within the LC cell. The addressed gray level therefore corresponds to a phase value.

Each gray level of a frame is encoded by a series of binary pulses in the kilohertz range. The pulses interact with the LC molecules individually but due to the rotational viscosity of the liquid crystals the response of the LC will depend on the series of binary pulses. This enables the different gray levels to be represented almost analogically

[73]. However, this leads to a slight superimposed phase flicker which will lead to the generated Airy beam to flicker as well.

The SLM we use is a phase only SLM (PLUTO-VIS of Holoeye), it must be illuminated with a horizontal polarization and modulates through reflection.

PLUTO - Spatial Light Modulator - Microdisplay Features	
Display Type	Reflective LCOS (Phase Only)
Resolution	1920 x 1080
Pixel Pitch	8.0 $\mu m$
Fill Factor	87%
Active Area	15.36 x 8.64 mm (0.7" Diagonal)
Addressing	8 Bit (256 Grey Levels)
Input Frame Rate	60 Hz
Wavelength Range	420-700 nm

### 2.2.2 Influence of experimental conditions on the generation of Airy Beams

The use of different experimental conditions can lead to various results in terms of Airy beam intensity profile and thus Airy beam propagation. Figure 2.10 shows a schematic of the experimental setup used to generate an Airy beam. A horizontally polarized Gaussian beam illuminates the cubic phase mask on the SLM to generate a specific wavefront. The SLM is placed in the object focal plane of a lens of short focal length (75.6mm) and the Fourier transform of the generated wavefront is obtained in the image focal plane. As depicted in figure 2.10, the propagating beam can be a 1D Airy beam or a 2D Airy beam depending on the phase mask displayed on the SLM. If the SLM is blank, it acts as a mirror and the Gaussian beam will propagate, which is useful for aligning purposes. Experimentally the SLM reflects many diffraction orders<sup>2</sup> so a linear phase is added to the cubic phase on the displayed mask in order to separate the different orders of diffraction. To obtain the corresponding Gaussian beam propagation, only the linear phase needs to be displayed on the SLM. A spatial filter selects the first order diffracted Airy beam blocking out other orders of diffraction. The 1D Airy beam will accelerate along one direction (horizontal in figure 2.10) whereas the 2D Airy beam acceleration is the cumulative acceleration along both the horizontal and vertical axis.

<sup>2</sup>The SLM's pixel matrix acts as a diffraction grating. An Airy beam is formed for each order of diffraction and they can overlap.

To analyze the Airy beam generation we use results from reference [76]. The scalar field  $u_0$  in the object focal plane at  $z = 0$  is of the form:

$$(2.9) \quad u_0(x, y, 0) = \exp\left(-\frac{x^2 + y^2}{w_0^2}\right) \exp\left(ic_0^3 \frac{x^3 + y^3}{3}\right)$$

where the first product corresponds to the incident Gaussian beam of waist  $w_0$ , while the second corresponds to the cubic phase imposed on the beam by the SLM (as seen in equation 2.8).  $x$  and  $y$  are the transverse horizontal and vertical axis respectively.  $c_0 = \sqrt[3]{6\Theta}/l$ , with  $l$  the side length of the phase mask and  $\Theta$  the maximal phase shift across the mask.

The size of the Airy beam after Fourier transform depends on the focal length  $f_{\mathcal{L}}$  of the lens used in figure 2.10 [76] :

$$(2.10) \quad x_0 = \frac{c_0 f_{\mathcal{L}}}{k_0}$$

and the truncation parameter  $a$  of the Airy beam depends on the Gaussian beam waist  $w_0$  and on the normalized maximal phase shift of the phase mask  $c_0$ .

$$(2.11) \quad a = \frac{1}{c_0^2 w_0^2}$$

We can then numerically determine the Airy beam shape and size versus the choice of parameters  $f_{\mathcal{L}}$ ,  $w_0$ ,  $c_0$ .

Figure 2.11(a-d) shows a series of numerical simulations of Airy beam generation using different parameter values  $w_0$  and  $c_0$ . Simulations (a) and (b) use the same phase

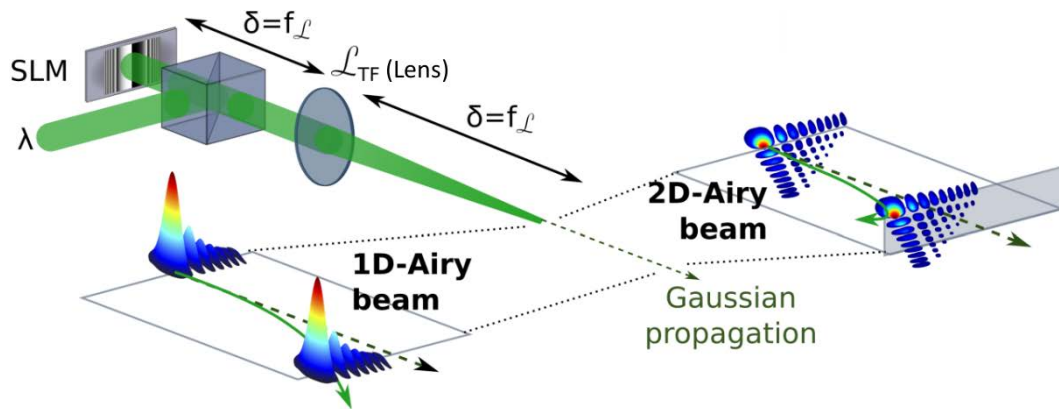


Figure 2.10: Experimental setup to generate 1 D- or 2 D-Airy beams using a SLM-modulation in Fourier space. Extracted from reference [75]

mask  $c_0 = 1400m^{-1}$  but with a differently sized Gaussian beam, respectively  $w_0 = 3.5mm$  and  $w_0 = 1.5mm$ . Simulations (c) and (d) use the same beam size as simulation(a) but with different phase masks, respectively  $c_0 = 600m^{-1}$  and  $c_0 = 3000m^{-1}$ . For each simulation we image the Gaussian beam illuminating the phase mask, the phase mask, the scalar field  $u_0$  that results of the illuminated phase mask and the resulting Airy beam in the image plane of the lens ( $f_{\mathcal{L}} = 75.6mm$ ). When the size of the illuminating beam is reduced from figure 2.11(a) to figure 2.11(b), the size of the Airy beam is unchanged ( $x_0 = 3.0\mu m$ ), but the number of lobes is reduced due to stronger truncation (from  $a = 0.04$  to  $a = 0.2$ ). When the phase mask's maximal phase shift is increased from figure 2.11(c) to figure 2.11(d), the size of the Airy beam is increased (from  $x_0 = 1.7\mu m$  to  $x_0 = 8.3\mu m$ ), and the number of lobes is increased as well, due to weaker truncation (from  $a = 0.2$  to  $a = 0.009$ ). We see that if the Gaussian beam is too small compared to the phase mask (figure 2.11(b)) or if the phase mask is too large for the Gaussian beam (in figure 2.11(c)), the resulting scalar field lacks high spatial frequencies and the Fourier transform yields a strongly truncated Airy beam  $a = 0.2$  in accordance with equation 2.11. We can therefore obtain different shaped Airy beams; their size or number of lobes can be controlled to a certain extent by modifying the Gaussian beam waist  $w_0$  or the phase mask's maximum phase shift  $c_0$ .

When illuminating the phase mask, if the Gaussian beam is not circular or if the beam is not centered on the SLM defaults can appear, as can be seen in the last column of figure 2.12. Figure 2.12(a-b) shows two simulations of deformed Airy beam generation, in figure 2.12(a) a misaligned Gaussian beam and in figure 2.12(b) a non circular Gaussian beam (1 to 3 ratio). For each simulation we image the Gaussian beam illuminating the phase mask, the phase mask, the scalar field  $u_0$  that results of the illuminated phase mask and the Airy beam obtained in the image plane of the lens ( $f_{\mathcal{L}} = 75.6mm$ ). In both cases the Airy beam will be of the same size  $x_0 = 3.9\mu m$  but present more lobes along the x-axis. The size of both Airy beams are the same because they use the same phase mask to form. The fact they present more lobes along the x-axis than the y-axis is due to the illumination along the x-axis of the phase mask of areas farther from the center of the mask. The Airy beam will be less truncated in the direction the Gaussian beam has sided (figure 2.12(a)) or along the direction corresponding to the Gaussian beams wider width (figure 2.12(b)). Between the two simulations, the main difference observed in the Airy beam is the blur of the secondary lobes when the beam is misaligned. Due to misalignment, the illumination of the phase mask is asymmetric which partially destroys the interference pattern and creates the blur. However, misalignment of the

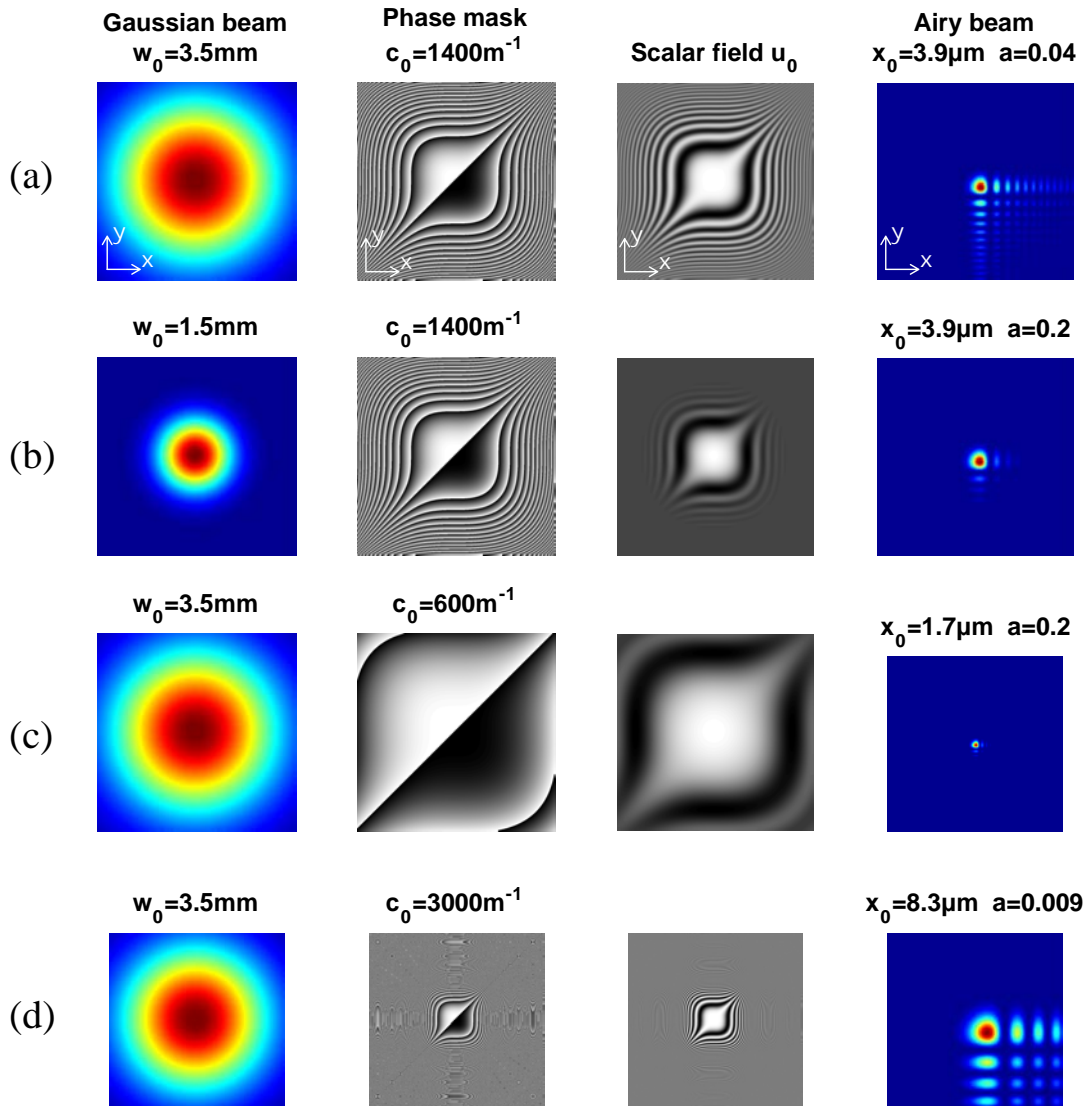


Figure 2.11: Numerical simulations of Airy beam generation. First column: Gaussian beam illuminating the phase mask. Second column: Illuminated phase mask on the SLM. Third column: Scalar field in the object plane of the Fourier transform lens. Fourth column: Transverse intensity profile of the resulting Airy beam in the image focal plane of the Fourier transform lens.

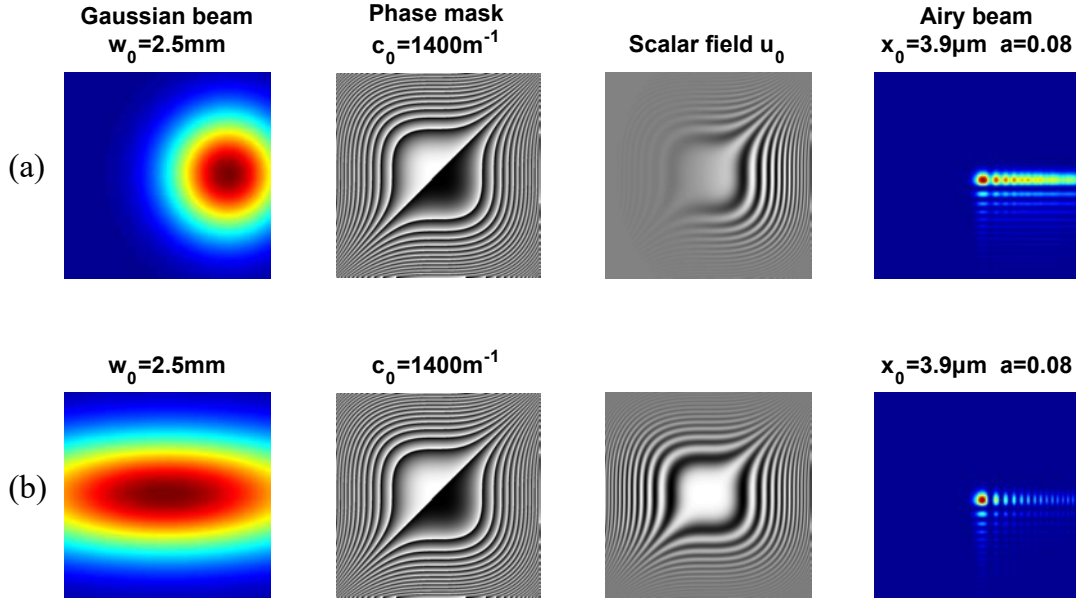


Figure 2.12: Numerical simulations of Airy beam with Gaussian misalignment (a) and Gaussian deformation (b). The resulting Airy beam has more lobes along the x-axis but only the case of misalignment presents additional blur. Columns are similar to figure 2.11.

Gaussian beam and the phase mask can be done purposefully in order to control the ballistic motion of the Airy beam [52].

We have seen in these few examples that the illumination of the phase mask will affect the shape of the Airy beam in terms of size, number of lobes and eventually blur. In the following, we will restrict ourselves to a properly aligned, circular Gaussian beam and focus on the phase mask parameter  $c_0$  and the size of the Gaussian beam  $w_0$ .

### 2.2.2.1 Border effects and pixelisation limit

In this section we will determine the parameter values, regarding the phase mask parameter  $c_0$  and the size of the Gaussian beam  $w_0$ , to obtain Airy beams of proper shape. The two main deformations observed that we will discuss are aliasing<sup>3</sup> and the discontinuity of the intensity peaks in the tail of the Airy beam (respectively seen in figure 2.13 and figure 2.14).

As seen in figure 2.11, the size of the Airy beam and the number of lobes can be controlled to a certain extent by varying the phase mask and Gaussian size parameters.

<sup>3</sup>Aliasing is visible or audible distortion introduced into digital information, such as images or audio signals, caused when a continuous line or transition is not smoothly captured or represented because of the low resolution or sampling rate of a digital medium.

Typically, by increasing the maximal phase shift of the phase mask we can obtain larger Airy beams. However according to Shannon's theorem there is a limit due to the sample-rate of our SLM (1 pixel per  $8\mu m$ ). The highest spatial frequency of our phase mask  $\phi_{SLM}(x, y) = c_0^3 \frac{x^3 + y^3}{3}$  is situated at the edge of the displayed area. Between two pixels  $\Delta x_{pixel} = 8\mu m$  at the edge  $x_{edge} = 4.32mm$  of our phase mask, the phase variation  $\Delta\phi_{SLM}$  must be lower than  $\pi$  to avoid under sampling:

$$(2.12) \quad \Delta\phi_{SLM}(x_{edge}, y = 0) < \pi$$

$$(2.13) \quad c_0^3 x_{edge}^2 \Delta x_{pixel} < \pi$$

$$(2.14) \quad c_0 < \left( \frac{\pi}{x_{edge}^2 \Delta x_{pixel}} \right)^{\frac{1}{3}}$$

$$(2.15) \quad c_0 < 2700m^{-1}$$

For values  $c_0$  over  $2700m^{-1}$ , there is a risk of spatial aliasing due to the low sampling rate of the SLM which can lead to Airy beam profile degradation (example in figure 2.13(a)). The error increases with  $c_0$  as high spatial frequencies converge to the center of the phase mask where there is the maximum illumination. Indeed an under-sampled pixel will contribute more to the Airy beam generation if it is brightly illuminated. To reduce aliasing, while keeping the same phase mask, the waist of the Gaussian beam must be reduced in order to avoid lighting these areas. Since 95% of the Gaussian beam intensity is situated in a radius of  $1.224w_0$  to the beam's center, we can choose :

$$(2.16) \quad \boxed{w_0 < \frac{1}{1.224} \sqrt{\frac{\pi}{\Delta x_{pixel} c_0^3}}}$$

Figure 2.13 shows two simulations of Airy beam generation. The two Airy beams are the same size  $x_0 = 11\mu m$ , generated by using the same phase mask  $c_0 = 4000m^{-1}$ , but with two differently sized Gaussian beams  $w_0 = 3.5mm$  (figure 2.13(a)) and  $w_0 = 2mm$  (figure 2.13(b)). For each simulation we image the Gaussian beam illuminating the phase mask, the phase mask, the scalar field  $u_0$  that results of the illuminated phase mask and finally the Airy beam obtained in the image plane of the lens ( $f_{\mathcal{L}} = 75.6mm$ ). The Airy beam generated in simulation (a) presents aliasing whereas the Airy beam generated in simulation (b) does not.

Due to the high value  $c_0 = 4000 > 2700$  there is a possibility for aliasing as seen in the case of the larger Gaussian beam (figure 2.13(a)). This is due to the phase mask's high spatial frequencies that the resolution of the SLM cannot render. In figure 2.13(b), the

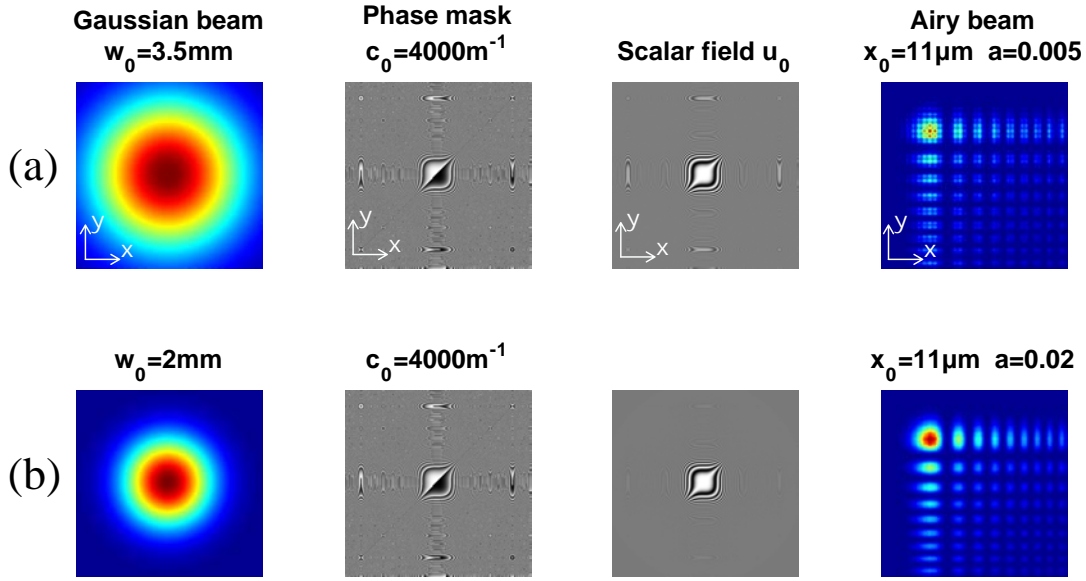


Figure 2.13: Numerical simulation of Airy beam aliasing. Columns are similar to figure 2.11. Simulation (a) shows an aliased Airy beam due to a high value  $c_0 = 4000$ . Simulation (b) shows the aliasing is reduced by adapting the Gaussian beam size.

aliasing is reduced by adapting the Gaussian beam size in accordance to equation 2.16. The errors in the high spatial frequencies of the scalar field have decreased in amplitude and the resulting Airy beam is smoother.

Another defect can arise if the Gaussian beam is too large compared to the phase mask because the phase mask itself will become a square aperture. In figure 2.14 are shown two simulations of Airy beam generation. Simulation (a) uses a Gaussian beam of size  $3.5\text{mm}$  whereas simulation (b) uses an infinitely large plane wave. For each simulation we image the scalar field  $u_0$  that results of the illuminated phase mask, the Airy beam obtained in the image plane, and the transverse profile along the x-axis with the expected analytic result. The tail of the Airy beam generated with a plane wave (figure 2.14(b)) does not fit with the expected analytic result, and the peak intensities of the secondary lobes tend to oscillate. The difference between the two scenarios is the illuminated borders of the phase mask. Figure 2.14(a) shows an Airy beam generation where the Gaussian beam of waist  $3.5\text{mm}$  is smaller than width of the phase mask ( $width_{mask} = 8.64\text{mm}$ ); the resulting numerical Airy beam profile matches the analytic profile. Figure 2.14(b) shows a case where the Gaussian beam has been replaced by a plane wave that fully illuminates the phase mask. The mask now plays the role of an aperture that diffracts, and the change in the Airy beam profile is notable. The secondary lobe peaks are discontinuous, the envelope of the tail oscillates due to the aperture and

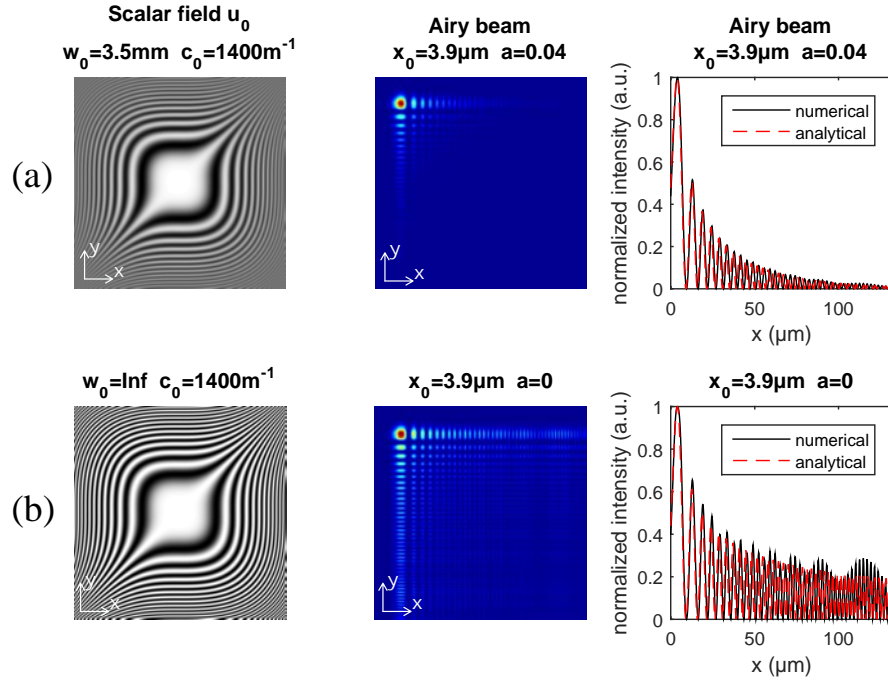


Figure 2.14: Numerical simulation of Airy beam generation showing border effects of the phase mask. (a) the phase mask of size  $8.64\text{mm} * 8.64\text{mm}$  is illuminated by a Gaussian beam of waist  $w_0 = 3.5\text{mm}$ , and the numerical wave function matches with the analytic wave function. (b) the phase mask is illuminated by an infinitely large plane wave, and the numerical Airy beam function envelope shows oscillating patterns due to the square aperture of the SLM screen.

the resulting numerical Airy beam does not match the analytic Airy function. To avoid this aberration, the size of the Gaussian beam cannot exceed the size of the phase mask on the SLM. This restriction can be written :

$$(2.17) \quad w_0 < \frac{1}{1.224} \frac{\text{width}_{\text{mask}}}{2}$$

This numerical study has allowed us to anticipate possible aberrations in the experimental Airy beam profile and understand how to fix them. In order to avoid aliasing or unwanted SLM border effects, the Gaussian beam illuminating the phase mask on the SLM must be small enough to respect both conditions:

$$w_0 < \frac{1}{1.224} \sqrt{\frac{\pi}{\Delta x_{\text{pixel}} c_0^3}} \quad \text{and} \quad w_0 < \frac{1}{1.224} \frac{\text{width}_{\text{mask}}}{2}$$

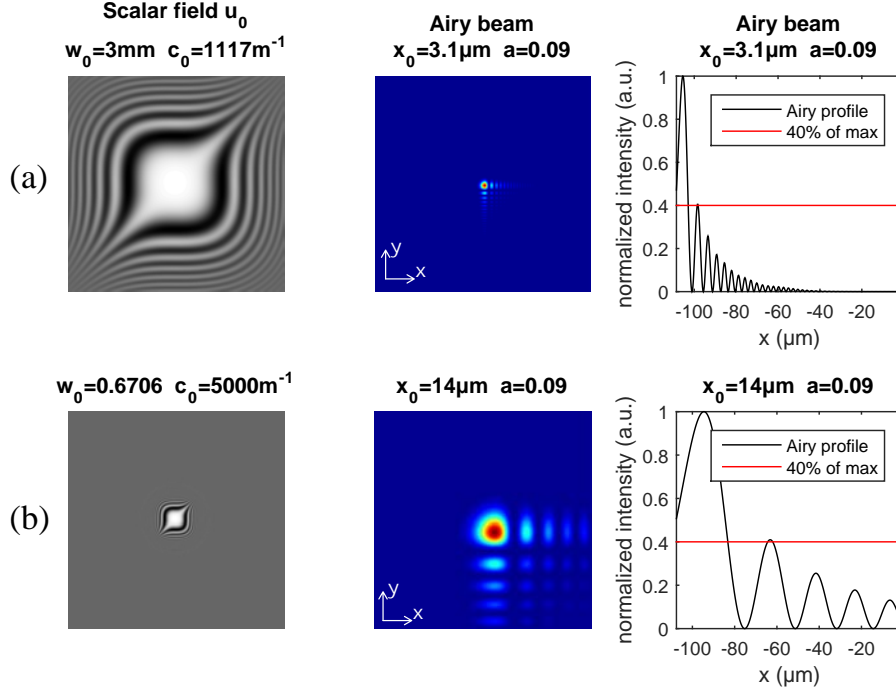


Figure 2.15: Two Airy beams of different size, each with a secondary lobe peak intensity equal to 40% of the main peak intensity.  $w_0$  and  $c_0$  are chosen as limit cases of condition 2.20.

### 2.2.2.2 Parameter range

We can now determine a range of parameter values for which the Airy beam is closest to the analytic wave form. Equations 2.16 and 2.17 determines a maximum value for the Gaussian beam waist. However the Gaussian beam waist must be sufficiently large compared to the phase mask in order to have significant secondary lobes. We arbitrarily decide that a secondary lobe exists if its peak value is at least 40% of the main lobes peak value. This corresponds to a certain illumination of the mask: we have found that the phase mask must be illuminated over a surface area representing at least a variation of  $4\pi$  :

$$(2.18) \quad \phi_{SLM}(x = w_0, y = 0) - \phi_{SLM}(x = 0, y = 0) > 4\pi$$

$$(2.19) \quad \frac{c_0^3 w_0^3}{3} > 4\pi$$

$$(2.20) \quad w_0 > \frac{(12\pi)^{\frac{1}{3}}}{c_0}$$

Figure 2.15 shows two simulations of Airy beam generation in the limit case conditions of equation 2.20, where the secondary lobe peak intensity of the Airy beams

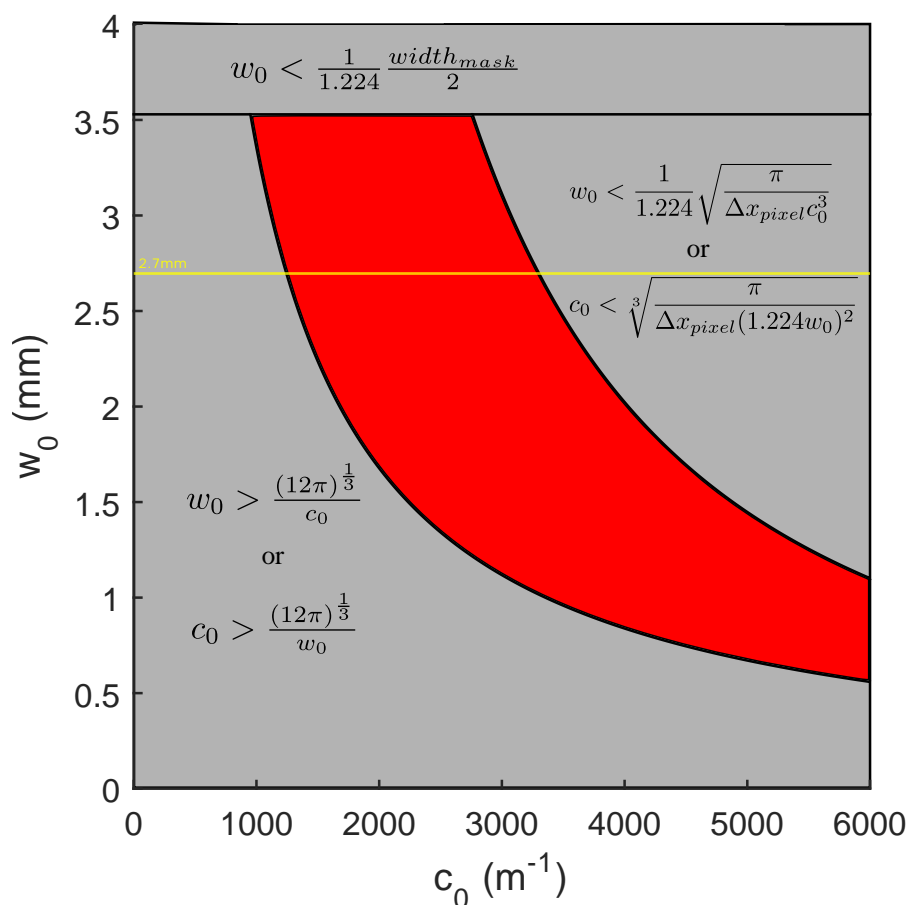


Figure 2.16: Plot representing in red the parameter range for the generation of analytical like Airy beams.  $w_0$  is the Gaussian beam waist illuminating the phase mask and  $c_0$  represents the phase shift within the mask.

are equal to 40% of the Airy beam's main lobe peak intensity. The two different Airy beam shapes are similar, with a truncation  $a = 0.09$ . Indeed by adapting the mask's phase shift  $c_0$  and Gaussian beams waist  $w_0$  to one another, the resulting scalar fields are identical but at different scales (first column of figure 2.15). The difference in scale however results in the change of the Airy beams size from  $x_0 = 3.1\mu m$  (figure 2.15(a)) to  $x_0 = 14\mu m$  (figure 2.15(b)).

This last condition in equation 2.20, in addition to the previous conditions of equations 2.17 and 2.16, all link  $w_0$  to  $c_0$ . They allow us to determine a parameter range value for which the Airy beams have the expected Airy beam properties. Figure 2.16 shows the area of interest in red, which is of use when realizing experimental measures.

Figure 2.17 tests experimentally our previous numerical and analytic work. The Gaussian beam is polarized horizontally to interact correctly with the SLM and its

waist  $w_0$  is fixed and measures  $w_0 = 2.7mm$  (first column). It illuminates, in the object focal plane, a phase mask that can be easily changed experimentally (second column, phase shift ranging from  $c_0 = 800m^{-1}$  to  $5000m^{-1}$ ). The resulting Airy beam's transverse intensity profile is formed in the image focal plane and is represented in the third column; as the phase shift increases, the Airy beam size increases as expected from equation 2.10 and the truncation parameter reduces as expected from equation 2.11. We fit the transverse profile along the x-axis with the expected analytic Airy beam profile (fourth column). For figure 2.17(a), the phase mask is not sufficiently illuminated, it does not respect the condition 2.20 so the secondary peaks are not clearly visible. In figure 2.17(b) the phase shift within the mask has been increased to be at the limit case scenario of condition 2.20 and we observe an Airy beam that matches nicely with our analytic expectations. Figure 2.17(c) represents the generation of a beam satisfying all our previously set conditions that matches well with the analytic profile. In figure 2.17(d) the phase shift has increased to the limit case scenario of condition 2.16; we can see slight aliasing of the Airy beam, but its profile follows the same trend as the analytic profile. Finally, figure 2.17(e) shows a case where the phase shift has increased and exceeded condition 2.16 resulting in strong aliasing of the Airy beam. The analytic profile does not match the experimental profile but rather envelopes its. The five experimental configurations of figure 2.17 can be foreknown using figure 2.16. Indeed  $w_0 = 2.7mm$  does not change so we draw a line from left to right (yellow line in figure 2.16). We start in the grey area to the left (under illumination), stop at the first curve (first limit case scenario), go through the red area (all conditions are met), stop at the next curve (aliasing limit case scenario) and finish in the gray area at the right side of the plot (aliasing of the Airy beam).

The conditions that have been set to properly illuminate the phase mask on the SLM and that allow to obtain a similar profile to the analytic Airy beam profile are not restricted to our SLM. Indeed conditions 2.17 and 2.20 apply to any kind of phase mask since they are due to respectively the masks aperture and the mask's sufficient illumination. The condition 2.16 however is due to pixel size; reducing the pixel size  $\Delta x_{pixel}$  can widen the red area. An analog phase mask could even absolve this condition altogether.

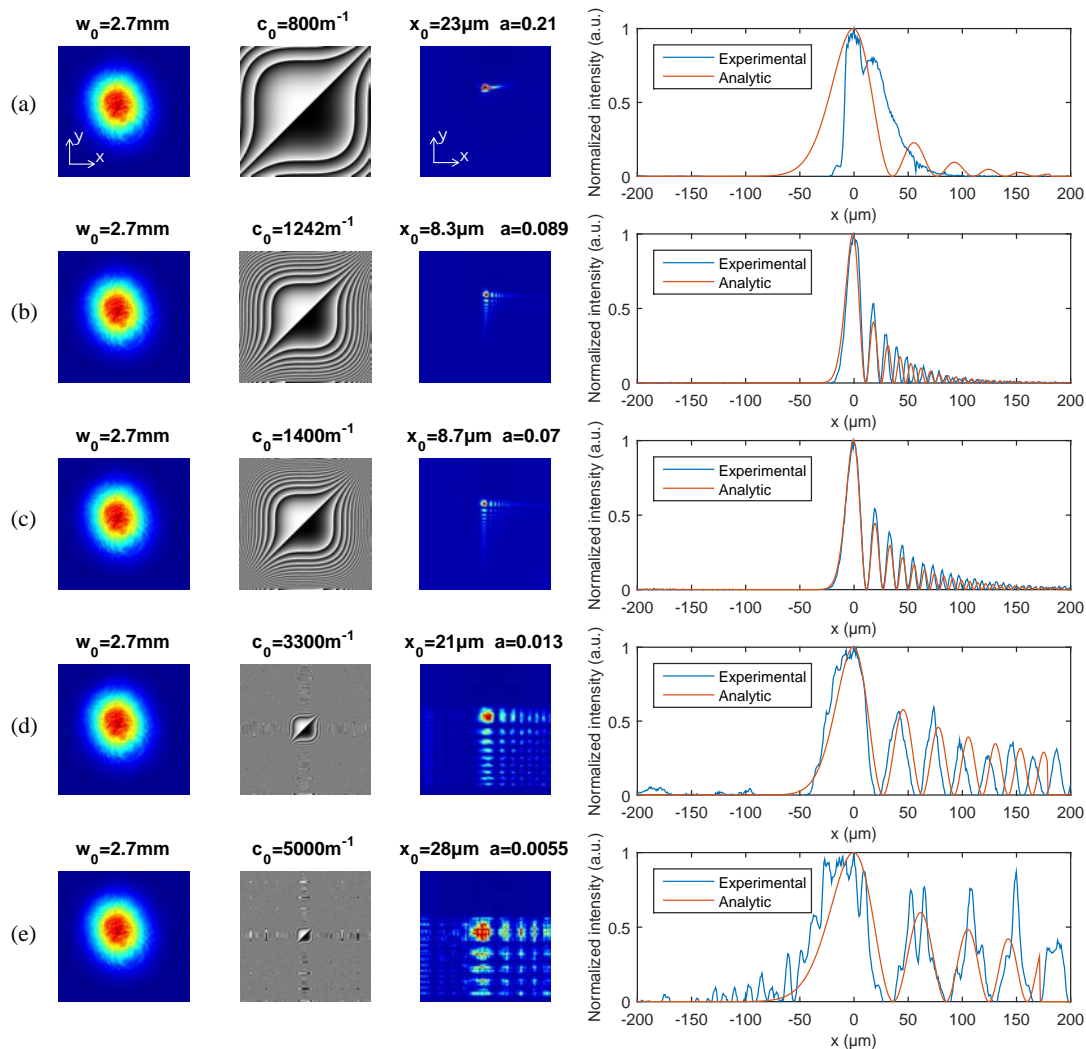


Figure 2.17: Experimental generation of Airy beams with  $w_0 = 2.7\text{mm}$ . The phase mask's phase shift  $c_0$  is increased one row to the next. (a) phase shift too low to yield an Airy beam with secondary lobes. (b) limit case scenario when the Airy beam's secondary lobes are significantly formed (deduced from equation 2.20). (c) example of an Airy beam generated in the red parameter range from figure 2.16. (d) limit case scenario when the Airy beam starts showing aliasing (deduced from equation 2.16). (e) high phase shift leads to aliasing of the Airy beam. *First column*: Gaussian beam illuminating the phase mask. *Second column*: Illuminated phase mask on the SLM. *Third column*: Transverse intensity profile of the resulting Airy beam in the image focal plane of the Fourier transform lens. *Fourth column*: Intensity profile of the experimental Airy beam along the horizontal x-axis vs the Airy beam analytic profile.

## 2.3 Conclusions

We have seen that Airy beams are generated using a cubic phase mask illuminated by a Gaussian beam, which is then Fourier transformed using an optical lens. We have assessed that changing the beam size does not affect the Airy beam lobe size but its number of lobes through the truncation parameter. Furthermore, increasing the phase shift on the mask increases simultaneously the size of the Airy beam lobes and their number. We have then found the limits of these control parameters analytically and verified these conditions both numerically and experimentally. Finally we have drawn a plot resuming these conditions and representing appropriate Airy beams in red. The numerical tool is a powerful one as it allows us to quickly foreknow the Airy beam profile as well as anticipate errors due to possible shifts or deformation of the incident Gaussian beam. Finally we will remind that this study is based on the use of an SLM to generate an Airy beam; the method and conditions developed in this chapter can apply to other technology based phase masks and similar studies can be lead on other kind of beams.



## AIRY BEAM PROPAGATION IN NONLINEAR MEDIA

**T**he Airy beam propagation has been extensively studied in free space. Even though the Airy beam is a non-diffracting beam it still diffracts slightly, however nonlinear media can compensate the diffraction of light. In this chapter we are interested in the behavior of the Airy beam propagation in nonlinear media. To do so we will have to explain what are solitons and nonlinear media, specifically photorefractive materials that we have chosen to study here. We will then study the solitonic characteristics of the Airy beam propagation by comparing experimental beam profiles versus photorefractive spatial soliton theory. Finally we will extend the study by using numerical simulations to understand the propagation behavior inside the crystal.

The context of this chapter is related to the following publication and can be found at the end of this thesis: Bouchet, T., Marsal, N., Sciamanna, M., & Wolfersberger, D. (2018). Solitonic characteristics of Airy beam nonlinear propagation. *Physical Review A*, 97(5), 051801

## 3.1 Physical concepts: Solitons and Photorefractive effect

We have seen that the Airy beams, like Bessel beams or Mathieu beams are non-diffracting beams. Another way to obtain non-diffracting beams is to compensate diffraction with another opposite phenomenon. For example, in nonlinear media, there are specific beams that, given the right profile, propagate endlessly without changing profile: they are called *solitons*. Photorefractive crystals can be used as nonlinear media. In this section we will define the physical concepts of solitons, photorefractive media and afterwards analyze in particular the photorefractive soliton.

### 3.1.1 Solitons

Generally a soliton is described as a wave that has a permanent form during propagation, that is localized within a region and that emerges from collisions with other solitons unchanged. Tidal waves or tidal bore, tsunamis [77] and morning glory clouds [78] are a few examples of soliton propagation in nature (see figure 3.1). Figure 3.1(a) shows a tidal bore soliton wave heading upstream and figure 3.1(b) shows morning glory clouds or atmospheric solitons.

In 1834 Scottish engineer John Scott Russel is the first to report the observation of



(a) Tidal bore soliton wave heading upstream

(b) Morning glory clouds in the Gulf of Carpentaria in Northern Australia

Figure 3.1: Example of Solitons in nature. (a) Tidal bore in Morecambe Bay, the tidal effect and the shallow waters result in a soliton wave propagating upstream. Source *Wikipedia - Arnold Price*. (b) Morning glory clouds in the Gulf of Carpentaria in Northern Australia; convection dynamics resulting in atmospheric solitons. Source *Wikipedia - Mick Petroff*

such a wave :

*I was observing the motion of a boat which was rapidly drawn along a narrow channel by a pair of horses, when the boat suddenly stopped-not so the mass of water in the channel which it had put in motion; it accumulated round the prow of the vessel in a state of violent agitation, then suddenly leaving it behind, rolled forward with great velocity, assuming the form of a large solitary elevation, a rounded, smooth and well-defined heap of water, which continued its course along the channel apparently without change of form or diminution of speed. I followed it on horseback, and overtook it still rolling on at a rate of some eight or nine miles an hour (14 km / h), preserving its original figure some thirty feet (9 m) long and a foot to a foot and a half (30-45 cm) in height. Its height gradually diminished, and after a chase of one or two miles (2-3 km) I lost it in the windings of the channel. Such, in the month of August 1834, was my first chance interview with that singular and beautiful phenomenon which I have called the Wave of Translation. [79]*

From Russel's first observation in August 1834 to Rayleigh's calculation of the profile in 1876 the term *wave of translation* changed to *solitary wave*. There was controversy and doubt in the existence of Russel's solitary wave as it could not exist in a linear system [80]. Joseph Boussinesq in 1877 and the Dutchmen Diederick Johannes Korteweg and Gustave de Vries in 1895 answered this problem by giving the *Korteweg-de Vries equation* (KdV): a nonlinear equation describing wave propagation in shallow water and the corresponding solitary wave solution [81, 82]. This nonlinear equation is used to describe tidal waves, tidal bore and tsunami dynamics.

Normally, a solitary wave disperses when it propagates. Dispersion occurs because harmonic waves of different wavelengths propagate at different speeds. In deep water for example, the speed of a harmonic wave is proportional to the square root of the wavelength: the longer the wave is, the quicker it propagates. Since a solitary wave is formed by the superposition of an infinite number of harmonic waves of different wavelengths and speeds, the harmonic waves dissociate themselves and disperse when propagating resulting in the solitary wave's loss of amplitude and flattening out. In the case of shallow water, the speed of all wavelengths become proportional to depth and amplitude. Therefore if the depth decreases for example when approaching the shoreline, the first waves will slow allowing other waves to catch up and build up, creating a focusing effect; the energy of many waves can accumulate in a short span of space and time creating one great wave or tsunami. In the case of a solitary wave, the dispersion effects and focusing effects cancel each other out; the wave can then propagate without deformation or change of speed over long distances.

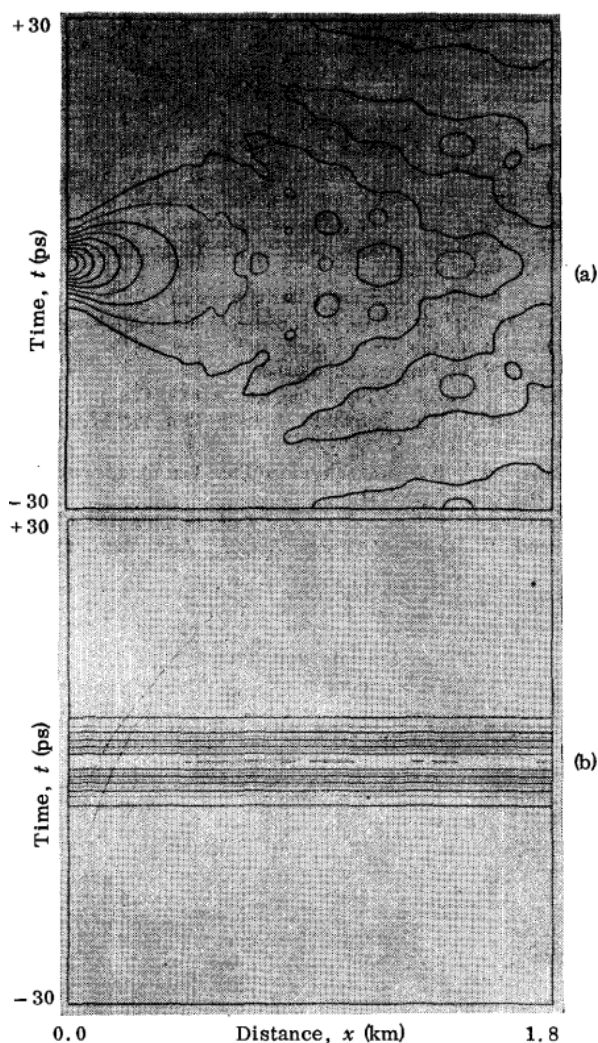


Figure 3.2: Propagation of a  $3\text{ ps}$  optical pulse in glass fiber. The pulse profile is represented vertically and its evolution over propagation distance is represented horizontally. Comparison of linear (a) and stationary nonlinear (b). Extracted from [6]

Seventy years later, numerical tools rekindled interest in the field. Indeed Norman Zabusky and Martin Kruskal published their numerical solutions of the KdV equation showing that the solitary waves remained unchanged after collision and invented the term *soliton* to describe this particle-like nature [23]. Ensued a small revolution in the domain of mathematics with the *inverse scattering method* developed by the mathematicians Clifford Gardner, John Greene, Martin Kruskal, and Robert Miura in 1967 [83, 84], this method consists in an explicit nonlinear transformation between solutions of related nonlinear partial equations. Using this method, they established that the asymptotic state to any initial condition of the KdV equation is a finite set of solitons [84]. In 1972,

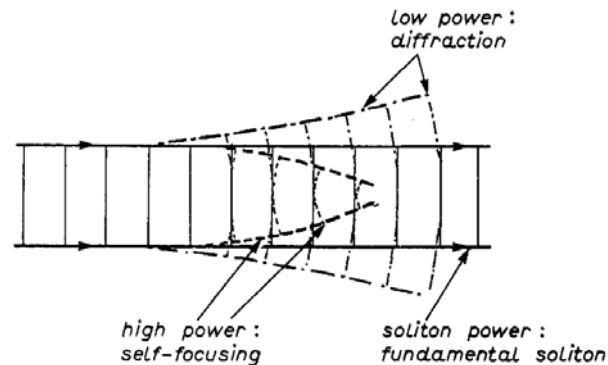


Figure 3.3: Propagation of a limited plane wave in nonlinear Kerr medium. At low power the beam spreads under diffraction. At high power the beam self-focuses. At soliton power the beam propagates without variation of the transverse dimension. Extracted from [33].

Vladimir Zakharov and Alexei Borisovich Shabat, using the inverse scattering method as well, solved the nonlinear Schrödinger equation and demonstrated the existence of soliton solutions [85]. Similarly to what we have seen in chapter 2 the nonlinear Schrödinger equation can model the nonlinear propagation of light. In 1973 Akira Hasegawawa suggested that optical temporal solitons could exist in optical fibers, due to the nonlinear effect of fibers compensating dispersive spreading of wave packets [6]. Similarly to hydrodynamics, electromagnetic waves of longer wavelengths propagate quicker in most media than electromagnetic waves of shorter wavelengths. This causes the dispersion of wave packets, as can be seen in figure 3.2(a). However, a nonlinear effect causes the index of refraction of dielectric materials to vary with intensity i.e. the electric field amplitude squared. Since the speed of the wave is linked to the refractive index of the material it is propagating through, the speed of the wave decreases with the amplitude of the field, which is similar to the dynamics of waves in shallow water. It is therefore possible for an electromagnetic wave packet to propagate without deformation or change of speed over endless distances if the two effects cancel each other as can be seen in figure 3.2(b). The optical temporal soliton was first observed in 1980 by Linn Mollenhauer, and this has led to a number of applications, notably in telecommunications: in 1988 soliton pulses were transmitted over a distance of 4000 kilometers, and three years later, transmitted at 2.5 gigabits per second over more than 14000 kilometers by a Bell labs research team [7].

In 1964, at the same time as numerical tools were developed to solve the KdV equation, arose the idea to self-trap an optical beam *spatially* [86]. Indeed, in materials where the refractive index (or dielectric constant) increases with field intensity it is possible for an electromagnetic beam to produce its own dielectric waveguide; a beam propagating in

a high index medium will undergo total internal reflection if surrounded by low index medium. Instead of compensating dispersion, the nonlinear effect compensates diffraction and the beam propagates without changing shape. The nonlinear effect can be referred to as nonlinearly induced self-lensing or self-focusing effects. If the nonlinear effects strength is adapted we can obtain optical spatial solitons that are self-trapped beams of light as illustrated in figure 3.3. In figure 3.3, the nonlinear effect is proportional to the intensity of the optical beams. Three cases are distinguished: high power resulting in self-focusing, low power resulting in diffraction of the beam and 'soliton' power resulting in unchanging propagation.

The first observations of self-trapped optical beams were done in 1966 in carbon disulfide [24] and self-trapped beams were observed afterwards in other kinds of media: for example in lead glass due to thermal effects in 1968 [87] or sodium vapor in 1974 [88]. The first observation of spatial solitons in dielectric media, by Barthelemy *et al* in 1985 were carried out in carbon disulfide (Kerr media) using high power light beams ( $\sim GW.cm^{-2}$ ) [25]. Indeed, the nonlinear Kerr effect induces a local index change proportional to the local light power. In Kerr-like media, it was established in 1965 that the intensity of the self-focused region tends to be anomalously large and change the beam into filaments [26]. To avoid destructive over self-focusing of the propagating beam Barthelemy reduced the problem from three dimensions to two dimensions: the propagating axis and only one transverse axis. Instead of a three dimensional circular beam soliton he considered a two dimensional plane soliton. The nonlinear Shrödinger equation reduced to two dimensions has a stable (1+1)D spatial soliton solution similar to the temporal soliton where time has been replaced by a transverse spatial axis.

In 1990 the first observation of spatial solitons in solid-state material was performed using single-mode planar glass waveguides [27]. In 1992 Mordechai Segev had the idea to use photorefractive nonlinearity to create solitons requiring less power to generate and propagate themselves [28], and they were observed experimentally in 1993 [29]. Photorefractive solitons are very interesting for experimental implementations, as weak continuous sources lasing at a weak power (a few mW) are sufficient to reach and explore the solitonic physics and its applications [89]. The first solitons experimentally observed in photorefractive media however were of transient nature (so called "quasisteady state") and existed only within a narrow temporal window. To reach the steady-state regime, an external background illumination enabled to adjust the soliton formation and its dynamics [90]. Furthermore, the photorefractive solitons contrarily to Kerr solitons can be stable in the two transverse dimensions enabling (2+1)D solitons to propagate.

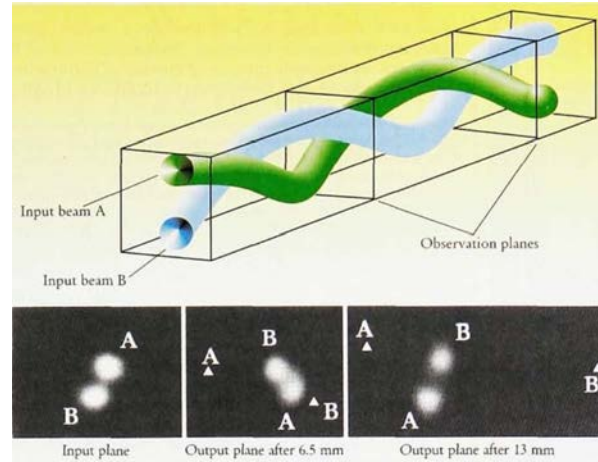


Figure 3.4: Spiraling of two colliding photorefractive screening solitons with initial trajectories that do not lie in the same plane. Shown are photographs of the optical beams. Left: Beams A and B about  $14\mu\text{m}$  apart at the input plane. Middle: The spiraling soliton pair after  $6.5\text{mm}$  of propagation. Right: The spiraling pair after  $13\text{mm}$  of propagation. The triangles indicate the centers of the corresponding diffracting beams. After  $6.5\text{mm}$  the solitons have spiraled about each other by  $270^\circ$ ; after  $13\text{mm}$  the spiraling angle doubles to  $540^\circ$ . Note that the spiraling is in elliptical orbits. Extracted from reference [30–32].

This was typically the case of solitons in sodium vapor in 1974 [88], and it is due to *saturable* nonlinear media. Due to saturation of the nonlinear focusing effect, the over self-focusing observed in Kerr media can be avoided in photorefractive media: the lensing effect instead of becoming stronger becomes wider [30, 31]. Since they occur in three dimensions, the particle-like interaction or collision of soliton beams in photorefractive media are therefore more rich and complex than in Kerr media where the interactions are uni-dimensional attraction or repulsion [33]. For example figure 3.4 shows two (2+1)D spatial photorefractive solitons spiraling around each other [32], only possible in three dimensions. Additionally the saturable nonlinearity means that inelastic collision experiments can be observed leading to soliton fusion or fission [30, 31].

### 3.1.2 Photorefractive crystals

Since we will be working with photorefractive crystals and photorefractive effects we have to explain the physical phenomena occurring in this particular crystal. The photorefractive effect was discovered in 1966 by A. Ashkin in  $\text{LiNbO}_3$  [47]. The injection of focused or unfocused laser beams produced an inhomogeneity in their crystal, and this was seen initially as highly detrimental to the optics of nonlinear devices. This degrada-

tion occurred when the beam polarization was aligned with the c-axis of the crystal <sup>1</sup>. However it turned out to be the basis for three main applications: holograms [48, 91], phase conjugated mirrors [92] and optical solitons. As the photorefractive effect appears for very low optical powers ( $\mu W$ ), photorefractive media have become very attractive and their physical mechanisms have been extensively explored. A variety of materials have been explored such as inorganic insulators like ferroelectrics ( $LiNbO_3$ ,  $BaTiO_3$ ,  $KnBO_3$ ,  $KTN$ ,  $SBN$ ) or sillenite crystals ( $BSO$ ,  $BGO$  and  $BTO$ ) and semiconductors (GaAs, InP, CdTe, CdZnTe) but also organic compounds [93, 94]. The band transport model of Kukhtarev [95] is the most widely used and explains the following. The photorefractive effect can be divided into three physical phenomenons that affect free-charge carriers (electrons or holes) inside the media :

- Photo-excitation of free charge carriers in the illuminated areas.
- Charge transport of the free charge carriers due to diffusion, drift and photovoltaic effects.
- Recombination of the excited charge carriers into a trapped state.

Figure 3.5 shows a schematic of what happens inside an illuminated photorefractive crystal. When a photorefractive crystal is illuminated, donor sites in the illuminated areas absorb the energy of incoming photons and ionize themselves. An ionized donor unleashes for example, an excited electron at an energy level inside the conduction band. The free electron in the conduction band can then be transported elsewhere due to drift, diffusion or photovoltaic effects. The electron will finally recombine with an ionized donor or acceptor at its new location. The recombination of excited charge carriers takes place everywhere in the crystal, however photo-excitation takes place only in the lighted areas. This creates an accumulation of charges in darker areas and this gradient of charges results in an electric field inside the crystal called *space charge field*.

In the context of holographic writing in photorefractive media, Kukhtarev *et al.* solved the complete set of material equations for electro-optic crystals, these equations are

---

<sup>1</sup>The c-axis corresponds to the preferential polarization axis of the crystal

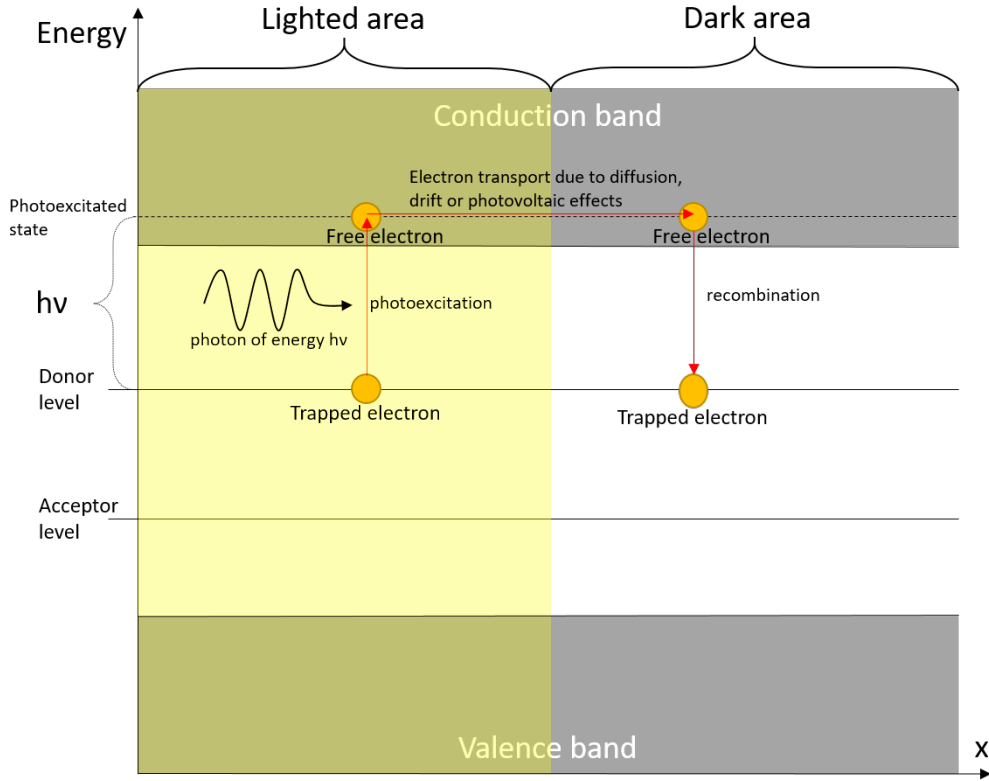


Figure 3.5: Schematic of the one band Kukhtarev transport model. A photon of energy  $h\nu$  excites an electron that frees itself of its donor. The free electron is subject to transportation effects. The free electron recombines with another donor. The vertical axis represents energy levels, the horizontal axis represents spatial coordinates

referred to as the Kukhtarev band transport model [95] :

$$(3.1) \quad \frac{dn}{dt} = \frac{dN_D^+}{dt} - \frac{1}{e} \nabla \mathbf{j}$$

$$(3.2) \quad \frac{dN_D^+}{dt} = (sI + \beta)(N_D - N_D^+) - \gamma_r n N_D^+$$

$$(3.3) \quad \mathbf{j} = e\mu n \left( \mathbf{E} - \frac{k_b T}{e} \nabla \ln(n) \right) + pI \mathbf{e}_c$$

$$(3.4) \quad \nabla(\epsilon_0 \mathbf{E}) = e(n + N_A - N_D^+)$$

with:

$E$	electric field	$n$	free electron charges number
$I$	light intensity	$N_D^+$	density of ionized donors number
$j$	current density	$N_D$	total density of donors number
$pI$	photovoltaic current	$N_A$	total density of acceptors number
$e$	electron charge	$s$	cross section of photoionization
$k_b$	Boltzman's constant	$\beta$	rate of thermal generation
$\epsilon_0$	static dielectric constant	$\gamma_r$	recombination constant
$\mu$	permeability	$T$	Temperature
$\mathbf{e}_c$	unit vector along the c-axis		

The first equation 3.1 ensures the continuity of charges since the variation of charges  $n$  and  $N_D^+$  over time must coincide with the charges' flow  $j$ . The second equation 3.2 indicates the evolution of ionized donors  $N_D^+$  over time, which depends on the probability of a remaining donor ( $N_D - N_D^+$ ) to ionize ( $s$  for photoionization and  $\beta$  for thermal excitation) subtracted by the probability of a ionized donor  $N_D^+$  and electron  $n$  to recombine (constant  $\gamma_r$ ). The third equation 3.3 expresses the current density  $j$  resulting from the transport of charges. The drift effect  $e\mu nE$  is proportional to the electric field,  $\mu nk_b T \nabla \ln(n)$  results from the diffusion effect and  $pI$  is the photovoltaic effect along the c-axis direction of the photorefractive crystal (vector  $\mathbf{e}_c$ ). The fourth equation 3.4 is Poisson's equation that relates the electric field  $E$  to the actual resulting charge density ( $n + N_A - N_D^+$ ).

We have seen that the space charge field distribution in the crystal is a result of the light distribution creating an accumulation of charges. In a photorefractive material however, the space charge field is also going to influence the light distribution itself through the linear electro-optic effect known as the Pockels effect in honor of F. Pockels who studied the effect in 1893. Photorefractive crystals are birefringent which means light does not propagate through it similarly in function of direction or orientation. To describe the influence of the crystal structure on the propagation of electromagnetic waves, we have to consider a three-dimensional object (since the electromagnetic wave can oscillate in any direction in 3D) propagating in three-dimensions. Linearization of this problem yields  $3^3 = 27$  coefficients in a tensor called the eletro-optic tensor. Thankfully, by taking into account the symmetry, the polarization of the electromagnetic wave, and the alignment of the electromagnetic wave with the strongest response coefficients of the crystal, we can simplify the problem and consider only one coefficient. The local variation of the refractive index  $\Delta n$  by the Pockels effect can be expressed in function of the local space charge field  $E_{sc}$ , the electro-optical coefficient  $r_{eff}$  and the extraordinary

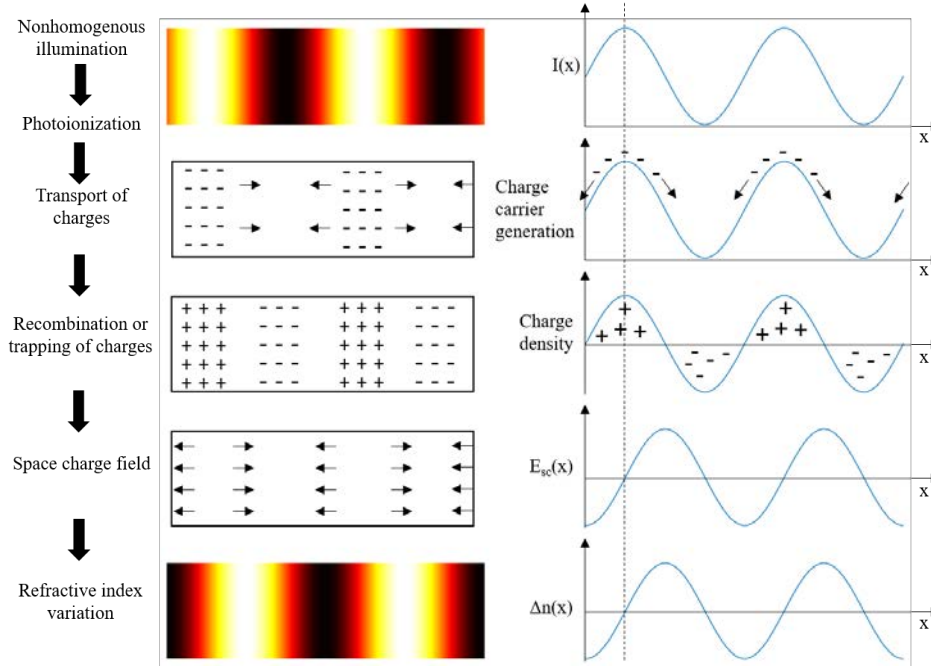


Figure 3.6: Schematic of the photorefractive effect in a crystal illuminated by light fringes.

refractive index  $n_e$  :

$$(3.5) \quad \Delta n = \pm \frac{1}{2} n_e^3 r_{eff} E_{sc}$$

and the refractive index  $n$ , can be written :

$$(3.6) \quad n = n_e + \Delta n$$

Figure 3.6 illustrates the different steps going from nonhomogeneous illumination to a refractive index variation. The fringes of light photoionize the donors in the lighted region. The free electron charges are transported to darker areas and the charge distribution results in a space charge field. The space charge field modifies the refractive index, creating areas with strong refractive indices between areas with weaker refractive indices. This creates a waveguiding structure resembling the initial light distribution but slightly shifted.

A single beam can create similarly its own waveguide (a strong refractive index surrounded by weaker surrounded index) resulting in self-trapping and spatial solitons as illustrated in figure3.7. It is worth emphasizing that unlike other nonlinear optical effects, the photorefractive nonlinear effect is nonlocal (shift between light distribution

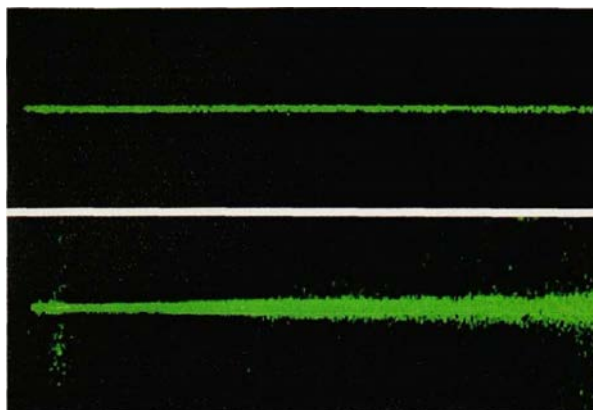


Figure 3.7: Comparison of a spatial soliton and ordinary beam. Top: Photograph of a  $10\ \mu\text{m}$  wide spatial soliton propagating in a photorefractive crystal. Bottom: Beam in the same crystal diffracting naturally when the nonlinearity is turned off. Extracted from [30]

and refractive index distribution) and non instantaneous (due to the time response of the crystal). However, similarly to other electro-optic effects, the nonlinearity can be turned 'on' and 'off' by applying an external field to the crystal. When it is 'on' the externally applied field will greatly increase the mobility of the electrons and activate a stronger nonlinear effect. Additionally, it can cancel the phase shift between the light distribution and the photoinduced refractive index variation distribution.

The photoinduced refractive index variation distribution can act as a waveguide [49], and by engineering the light distribution inside a photorefractive media we can engineer complex waveguiding structure. For example, by using Airy beams [38], which will be discussed in chapter 5.

### 3.1.3 Photorefractive soliton

When we inject an Airy beam inside a nonlinear photorefractive media, solitonic structures can appear [46]. In order to settle the solitonic nature of these beams we must first take particular interest in the photorefractive soliton. This section will focus on the theory of the photorefractive soliton, notably its profile and the relation between its peak intensity and width.

In order for the photorefractive soliton to propagate without change, the resulting waveguide structure must be adapted to its initial beam profile: the focusing effect must compensate diffraction. We start with the equations of the Kukhtarev model in order

to determine the soliton profile. We will first obtain the space charge field required for spatial soliton propagation using the first four equations: by restricting the analysis to one transverse dimension, by neglecting the photovoltaic current and by considering a steady state, the equations of the Kukhtarev band model 3.1, 3.2, 3.3 and 3.4 become :

$$(3.7) \quad \frac{dj}{dx} = 0$$

$$(3.8) \quad \gamma_r n N_D^+ = (sI + \beta)(N_D - N_D^+)$$

$$(3.9) \quad j = e\mu n E - \mu k_b T \frac{dn}{dx}$$

$$(3.10) \quad \epsilon_0 \frac{dE}{dx} = e(n + N_A - N_D^+)$$

$$(3.11)$$

to which is added the boundary condition due to the applied external field [96]:

$$(3.12) \quad V = - \int_{l/2}^{l/2} E dx$$

with  $V$  the voltage applied on the sides of crystal of length  $l$ . Assuming that in the conditions of soliton propagation the light intensity distribution  $I$  is such that the resulting concentration of photo-excited electrons  $n$ , the concentration of acceptor impurities  $N_a$ , and the concentration of donor impurities  $N_d$  follow the scaling  $n \ll N_A \ll N_D$ , and that the soliton width is in the range of  $10\mu m$ , we can use the previous equations to express the dominant term of the space charge field  $E_{sc}$  [97]:

$$(3.13) \quad E_{sc} = \frac{V}{l} \frac{1}{1 + I/I_{eff}}$$

with  $I_{eff}$  the effective background intensity. The effective background intensity is defined as the sum of the background and dark intensities induced respectively by an external homogeneous illumination of the crystal and the intrinsic thermal excitation of charges inside the crystal.  $I_{eff} = I_b + I_d$  with  $I_d = \frac{\beta}{s}$  and  $I_b$  the homogeneous optical intensity that allows a finite crystal conductivity [96]. In our case  $I_b \gg I_d$  so we will consider  $I_{eff} = I_b$ . The space charge field is saturable due to the  $(1 + I/I_{eff})$  denominator, explaining the saturable nonlinearity of the photorefractive media.

$$(3.14) \quad \Delta n = \pm \frac{1}{2} n_e^3 r_{eff} \frac{V}{l} \frac{1}{1 + I/I_b}$$

The nonlinear monochromatic paraxial equation 3.15 can be used to describe the evolution along the z-axis of the optical electromagnetic beam  $E_{opt} = A(x, z)e^{ikz - i\omega t}$ :

$$(3.15) \quad \frac{\partial A(x, z)}{\partial z} - \frac{i}{2k} \frac{\partial^2 A(x, z)}{\partial x^2} = -\frac{ik}{n_e} \Delta n A(x, z)$$

$$\begin{array}{llll}
 I = |A(x, z)|^2 & \text{light intensity} & \lambda & \text{wave length} \\
 k = \frac{2\pi n_e}{\lambda} & \text{wave vector} & c & \text{speed of light} \\
 \omega = \frac{2\pi c}{n_e \lambda} & \text{angular frequency} & n_e & \text{extraordinary refractive index}
 \end{array}$$

Solutions can be found using the self-consistency method [97]: the solution has an unchanging profile  $u(x)$  when propagating along the  $z$ -axis, so its expression is of the form

$$(3.16) \quad A(x, z) = u(x)e^{i\Gamma_z z} \sqrt{I_b}$$

Where  $\Gamma_z$  is the propagation constant. Injection of equation 3.16 into 3.15 yields a one dimensional equation of the transverse amplitude profile  $u$  [97]:

$$(3.17) \quad \frac{d^2 u(\xi)}{d\xi^2} = \pm \left( \frac{\Gamma_z}{b} - \frac{1}{1+u(\xi)^2} \right) u(\xi)$$

with  $\xi = \frac{x}{d}$  the normalized transverse spatial scale and  $d = (\pm 2kb)^{-1/2}$  the nonlinear length scale, and the constant  $b = \frac{1}{2}kn_e^2 r_{eff} \frac{V}{\Gamma}$

The sign in front of the right term of the equation 3.17 depends on the sign of  $b$  or rather  $\Delta n$ . We chose to look at bright soliton formed by a self focusing effect so  $\Delta n > 0$ . The opposite case would correspond to defocusing conditions and the observation of dark solitons. [97]

Experimentally we can have access to the nonlinear parameter  $b$  and the peak intensity normalized by the background intensity  $u_0^2 = \frac{I(0)}{I_b}$ . An equation requiring only these parameters can predict the corresponding soliton profile. The number of parameters of equation 3.17 can be reduced using the relation [97]

$$\frac{\Gamma_z}{b} = \frac{\ln(1+u_0^2)}{u_0^2}$$

Finally, a one-dimensional steady state bright screening soliton profile is described by the following reduced wave equation [98]:

$$(3.18) \quad \frac{d^2 u}{d\xi^2} + \frac{u}{u_0^2} \ln(1+u^2) - \frac{u}{1+u^2} = 0$$

whose first integral is

$$(3.19) \quad \boxed{\frac{du}{d\xi} = [\ln(1+u^2) - \frac{u^2}{u_0^2} \ln(1+u_0^2)]^{1/2}}$$

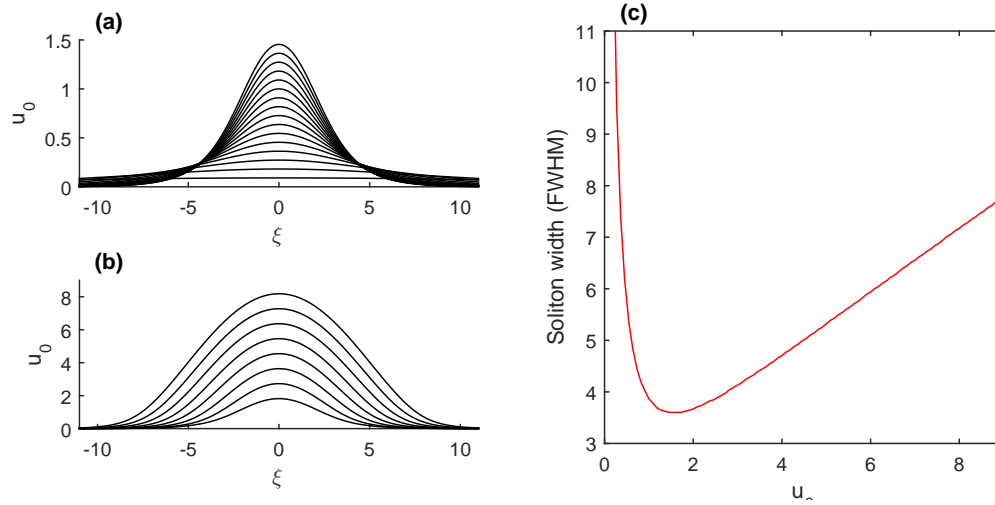


Figure 3.8: Photorefractive spatial soliton profiles for values of  $u_0 < 1.5$  (a) and  $u_0 > 1.5$  (b). Soliton existence curve (c), plots the corresponding width of the soliton in function of its peak amplitude in normalized transverse scale.

Equation (3.19) can be solved using a Runge-Kutta method in order to obtain numerically the theoretical soliton profile. Figure 3.8(a) and (b) shows different soliton profiles for increasing values of normalized maximum amplitude  $u_0$ . Figure 3.8(c) plots the soliton existence curve [98], i.e. the full width at half maximum (FWHM) of the soliton profiles in function of their normalized maximum amplitude  $u_0$ . When the amplitude increases, the existence curve decreases for values  $u_0 < 1.5$ , giving evidence of a tightening of the soliton profile that can be seen in figure 3.8(a). On the contrary the existence curve increases for values  $u_0 > 1.5$ , giving evidence of a broadening soliton profile as can be seen in figure 3.8(b).

Using this model and given the experimental conditions, we can fit the profile of a theoretical soliton on an experimental one as was done in references [98, 99]. We will use this fitting method to analyze the solitonic nature of the output laser beams in photorefractive crystal in this chapter.

## 3.2 Finite Airy beam propagation in photorefractive media

In this section we study and analyze both experimentally and theoretically the nonlinear propagation of a 1D-Airy beam in an SBN photorefractive crystal. We have seen in chapter 2 that the finite Airy beam is a truncated form of the ideal Airy wave func-

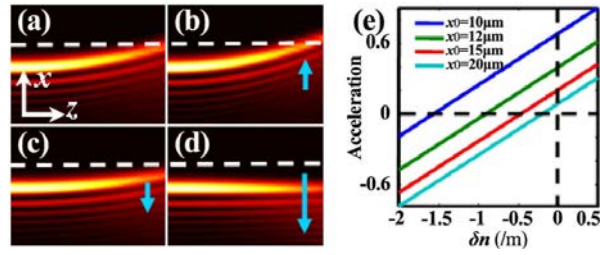


Figure 3.9: Theoretical results of 1D Airy beams propagating in a medium with different index gradients  $\Delta n$ . (a) Normal propagation at  $\Delta n = 0$ . (b) Enhanced and (c) reduced acceleration at  $\Delta n > 0$  and  $\Delta n < 0$ , respectively; (d) Airy beam acceleration canceled. (e) Plot of acceleration as a function of  $\Delta n$  under different  $x_0$ . The white dashed lines mark the position of the central lobe at the output in (a), and the arrows illustrate the index gradient. Extracted from reference [43]

tion, therefore the beam diffracts slightly. We have seen that in photorefractive media diffraction can be compensated by a nonlinear focusing effect, and notably create spatial solitons. What we are interested in is the propagation behavior of such a finite Airy beam in nonlinear photorefractive media in focusing conditions. In particular, the soliton nature of its off-shooting beams. We will begin with an overview of the Airy beam propagation in nonlinear media, notably photorefractive crystals, and then present our own experimental results and analysis of the soliton characteristics of the Airy beam nonlinear propagation.

### 3.2.1 Airy beams in photorefractive media

We have suggested in chapter 2 to engineer the Airy beam propagation by engineering the beam itself using the phase mask on the spatial light modulator (SLM), for example the so-called "super-Airy beams" [70], or by changing the illumination of the phase mask to change the parabolic trajectory [52]. However, the propagation behavior through a medium can also be engineered through control of the refractive index gradient inside the medium [43, 44, 100]. Figure 3.9 shows a propagating Airy beam in a nonlinear medium with a refractive index gradient modifying the deflection of the propagating beam. The deflection or acceleration of the Airy beam can be enhanced (figure 3.9(b)), reduced (figure 3.9(c)), or canceled (figure 3.9(d)). Other interesting dynamics can be obtained using more complex index variations inside the photorefractive medium such as induced photonic lattices [44, 45]. These dynamics require first a good understanding of the self-induced behavior of Airy beams in nonlinear media: in the following we will focus on self-induced waveguiding or focusing conditions.

The injection of non-conventional Airy beams in nonlinear media has been studied extensively in both Kerr media [34–36] and photorefractive media [35, 37–41] and to lesser extent in thermal nonlinear media [42]. The Airy beams in biased nonlinear media have interesting dynamics such as soliton-like behaviors [35, 37, 39–41] and interactions of co- and counter-propagating Airy beams [39–41].

A definition in terminology is required for Airy beam *self-trapping* and Airy beam *self-focusing*. Previously, with Gaussian beams and solitons, the self-trapping and self-focusing could be seen as equivalent as both refer to the propagation of an unchanging profile. In the case of the Airy beam *self-trapping* and the Airy beam *self-focusing* we will have to differentiate the case where the profile of the Airy beam propagates unchanged and the case where the Airy beam changes profile while propagating and refocuses in a soliton-like profile.

- *Airy beam self-trapping*: the multi-lobed Airy beam profile and curved trajectory remain unchanged.
- *Airy beam self-focusing*: the Airy beam changes profile and refocuses in a soliton-like profile.

When applying a small bias electric field to the nonlinear medium, the Airy beam self-traps and its main lobe is narrower while still accelerating [35]. When applying a larger bias electric field to the nonlinear medium, it is possible to induce spatial soliton-like beams through self-focusing of optical Airy beams [36, 41, 42, 46].

Figure 3.10 shows the propagation behavior of an Airy beam in linear conditions (figure 3.10(a)), under nonlinear focusing conditions (figure 3.10(b)) and nonlinear defocusing conditions (figure 3.10(c)). Numbers 1, 2 and 3 correspond to the shift of the cubic phase mask, the first column corresponds to no shift, columns two and three correspond respectively to small and great shifts. Under nonlinear defocusing conditions (figure 3.10(c)), the Airy beam main lobe becomes larger. Under nonlinear focusing conditions (figure 3.10(b)), the Airy beam can shed an off-shooting beam. In particular, in figure 3.10(b1), under nonlinear focusing conditions the Airy beam may split into a weak accelerating structure and a structure that has been named "off-shooting soliton" (OSS) and that propagates along the medium without transverse acceleration [46].

The first experimental analysis of the OSS and its interaction with the remainder of the self-accelerating beam was done by Wiersma *et al* [41] and is shown in figures 3.11 and 3.12. Figure 3.11(a) shows a schematic of the experimental setup: a Gaussian beam illuminates a one dimensional cubic phase mask on a SLM, and a lens plays the

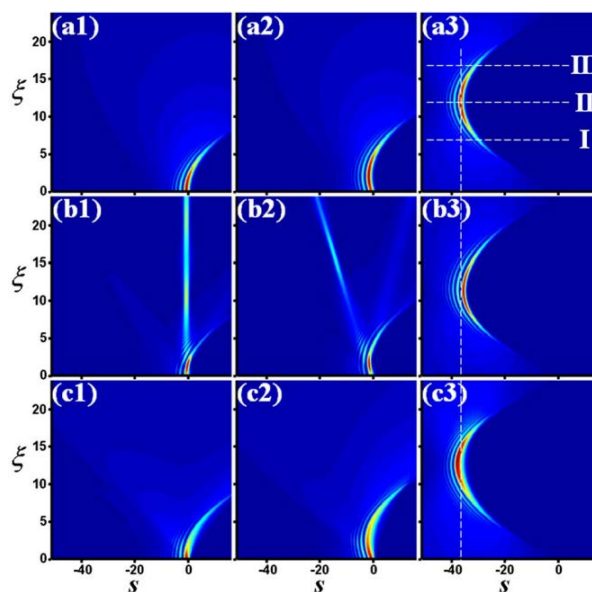


Figure 3.10: Propagation of an Airy beam under different conditions: (a) linear, (b) nonlinear self-focusing, and (c) nonlinear self-defocusing. The panels from left to right correspond to different shifting of the cubic phase mask. Extracted from [46]

role of a Fourier transform to shape the Airy beam. The Airy beam is injected inside the photorefractive crystal which is subject to background illumination. The output shape of the beam along time is shown in figures 3.11(b-h). The Airy beam partially loses its accelerating shape to refocus in one beam (figure 3.11(c-d)) propagating without transverse acceleration (the reference is represented by a red dotted line). The beam then relaxes, regaining a profile resembling the Airy beam profile in linear conditions. The study of the influence of the background intensity is shown in figure 3.12. We see that for greater values of dark intensity  $I_d$  (increased with background lighting), or for lower values of input intensity  $I$ , the transient and the final self-focusing beam are closer in size. This result will motivate our decision to work at low values of input beam intensity and sufficiently high background intensity. The interactions between the photoinduced OSS and the accelerating beam have resulted in attraction, deflection and tightening effects of the OSS and interesting analogies with gravitational lensing and tidal forces [41]. The propagation and interactions suggest that the OSSs share properties that are typically attributed to spatial solitons.

In spite of these recent achievements, one question remains of interest: *is the Airy beam OSS or nonlinear Airy beam propagation well described by the Kukhtarev model? In other words, is the Airy beam OSS of the same nature as other well known spatial solitons?*

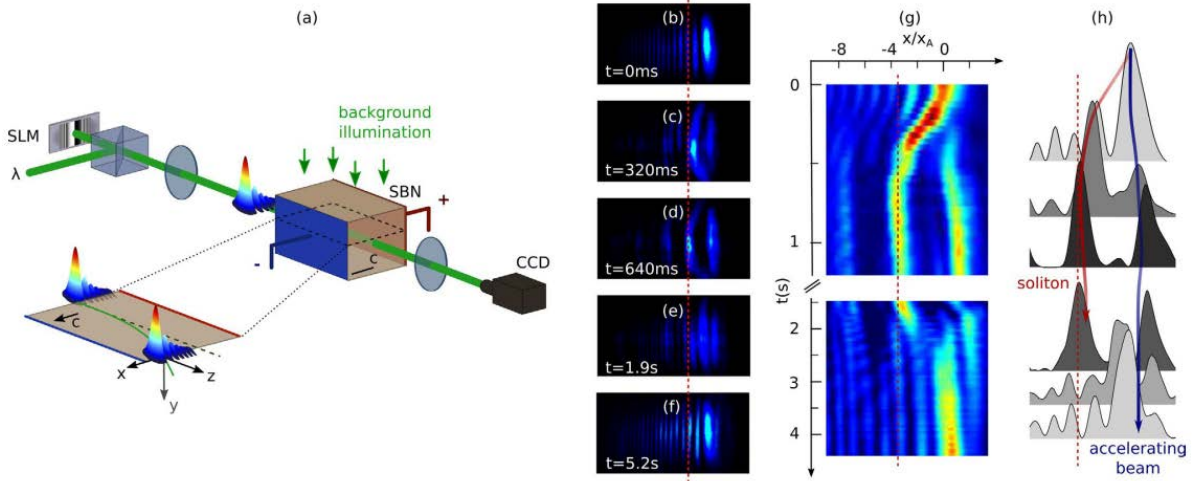


Figure 3.11: (a) Experimental setup. (b-f) Transverse intensity profile of the output beam under nonlinear focusing conditions for increasing times. (g) 1D intensity profile along time. (h) Top-view sketch of the accelerating beam interacting with the off-shooting soliton, superimposed with their intensity profiles along time. Extracted from [41]

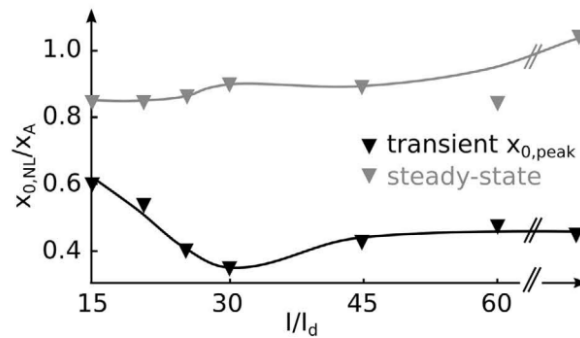


Figure 3.12: Influence of the background illumination on the transient and final self-focusing beam size  $x_0$  normalized by the Airy beam main lobe size  $x_A$ . Extracted from [41]

During this Phd we observed experimentally that the OSS matches with the theoretical soliton profile in terms of width and amplitude. We also prove that its profile remains unchanged during propagation. Finally, we analyze the OSS output position and width behavior versus its amplitude and show that its characteristics match with the existence curve of the theoretical spatial soliton.

### 3.2.2 Experimental propagation of 1D Airy beam

Our experiment consists in propagating a one-dimensional Airy beam into a biased photorefractive cerium doped (1%)  $Sr_{0.61}Ba_{0.39}Nb_2O_6$  (SBN:61) crystal with dimensions  $5\text{mm} \times 5\text{mm} \times 2\text{cm}$ . Figure 3.13 depicts our experimental setup. First, the vertically polarized laser beam goes through a half-wave plate in order for the polarization to become horizontal and illuminate the SLM correctly, the beam is also enlarged to  $2.7\text{mm}$  through a set of lenses (focal lengths of  $15\text{cm}$  and  $25\text{cm}$ ). The size of the illuminating beam on our SLM determines the possible phase shifts value  $1240 < c_0 < 3300$  as seen in the previous chapter. Then, Airy beams of different orders are generated using a one dimensional cubic phase mask combined with a diffraction grating on the SLM [13]. The first diffraction order Airy beam is obtained in the image focal plane of the Fourier transform lens  $f_L$ , where we also place a spatial filter in order to only keep the first order Airy beam and block all other light. The filtered Airy beam is then imaged at the input of our crystal through a set of lenses of same focal lengths ( $20\text{cm}$ ). To view the

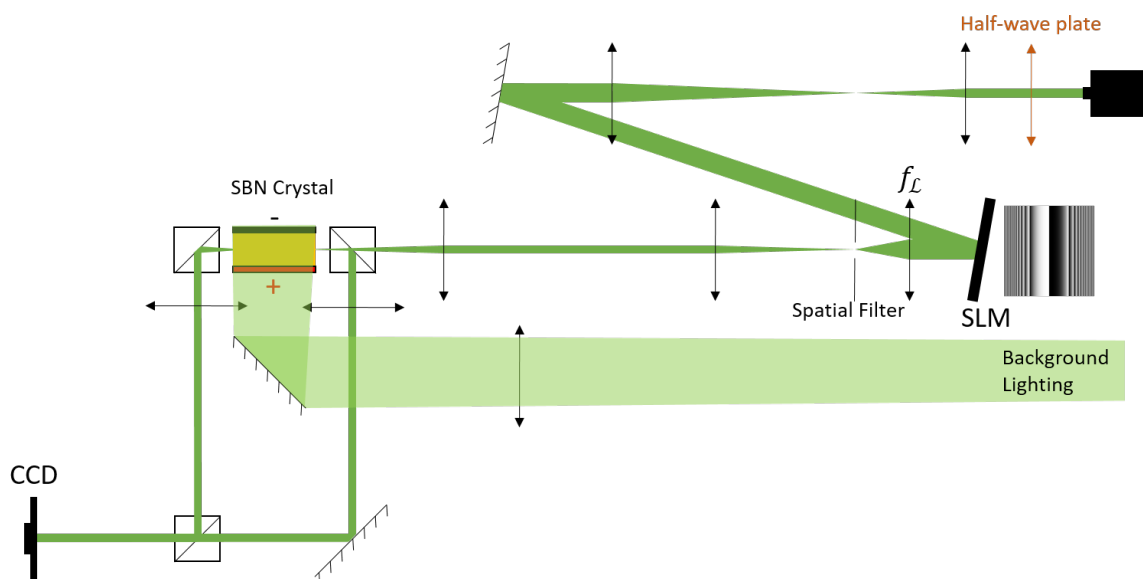


Figure 3.13: Schematic of the experimental setup

Airy beam injected inside the crystal we place a beam splitter before the crystal and image the input face of the crystal on the CCD camera (WinCamD-LCM) using a lens (focal length of  $14\text{cm}$ ) and a mirror. The output face of the crystal is imaged on the same CCD camera using a lens (focal length  $16\text{cm}$ ) and two beam splitters. We calibrate the measures using a  $90\mu\text{m}$  wide copper wire, corresponding to 113 pixels for the input face image and 72 pixels for the output face image, thus ensuring precision of the order of the  $\mu\text{m}$ . Finally background lighting  $I_b$  illuminates the crystal from the top and is controlled using a different laser.

In figure 3.14 we observe the profile of the Airy beam OSS at the output face of the crystal. Figure 3.14(a) is a simplified schematic of the experimental setup that sets the reference frame of our coordinate system. The Airy beam propagates along the z-axis and accelerates along the x-axis. The crystal's c-axis is the preferential axis of electron polarization in the crystal and is parallel to the x-axis. When a bias external electrical field is applied along the crystal c-axis, the optical Airy beam photoinduces a refractive index variation inside the crystal through the Pockels effect. For high enough nonlinearity strength, most of the beam turns into a so-called "off-shooting soliton", while a small fraction of the power remains a self-accelerating linear packet [41, 46]. Figure 3.14(b) shows the output beam profile when no voltage is applied. Figures 3.14(c-d) show the beam output captured on the camera with a bias electric field of  $200\text{V/cm}$  and  $400\text{V/cm}$ . The experimental transverse profile of both OSS are plotted in figure 3.14(e) and are extracted from the brightest areas of figures 3.14(c-d). We can note that the OSS width and amplitude can be controlled by changing the voltage applied to the crystal. The analysis of each profile and their comparison to a theoretical soliton profile is done using the equation 3.19, detailed in the previous section 3.1.3, used to draw the soliton existence curve (see figure 3.8) and used in reference [98]:

$$\frac{du}{d\xi} = [\ln(1 + u^2) - \frac{u^2}{u_0^2} \ln(1 + u_0^2)]^{1/2}$$

We use this equation to find numerically the profile corresponding to the values  $d = (k^2 n_e^2 r_{eff} V/l)^{-1/2}$  and  $u_0 = \sqrt{\frac{I(0)}{I_b}}$  from our experiment ( $n_e = 2.3$ ,  $r_{eff} = 235 \text{ pm/V}$ ,  $V = 100 \text{ V}$  or  $200 \text{ V}$  and  $l = 0.5 \text{ cm}$ ).  $I_b$  is the effective background intensity defined as the sum of the background and dark intensities induced respectively by an external homogeneous illumination of the crystal and the intrinsic thermal excitation of charges inside the crystal. However, the dark intensity is negligible compared to the background intensity so we can consider that the background intensity illuminating our crystal is the effective background intensity. We therefore have access to the theoretical soliton

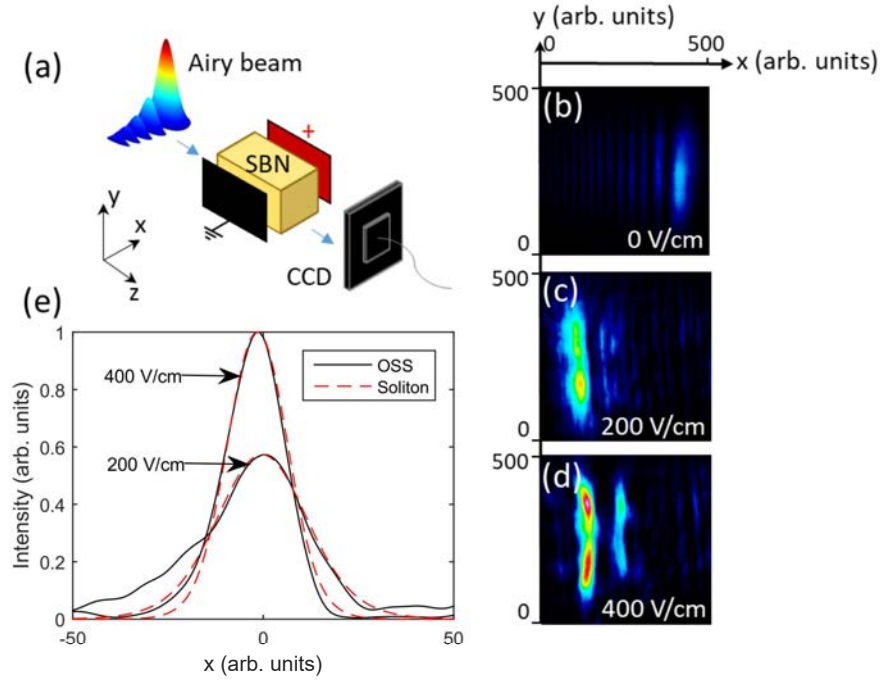


Figure 3.14: (a) Schematic of the experimental setup: 1D Airy beam propagating in a 2 cm long SBN crystal. ( $x_0 = 10$ ,  $a = 0,1$ ) (b) Observation of the Airy beam at the crystal output face on camera with no electric field  $E_{ext}$  applied. (c)-(d) Observation of the OSS at the crystal output face on the CCD camera ( $E_{ext} = V/l = 200$  and  $400 \text{ V/cm}$ ). (e) Corresponding experimental Airy beam OSS profile extracted from the camera and theoretical classic soliton fit ( $E_{ext} = 200$  or  $400 \text{ V/cm}$  and  $P_A = 50 \mu\text{W}$ ).

profile corresponding to our experiment. The theoretical soliton profile is superimposed in figure 3.14(e) with the transverse experimental profiles. We evidence that under focusing condition, the Airy beam sheds an OSS whose profile matches the theoretical soliton profile.

In certain focusing conditions, for a smaller apodization factor ( $a = 0.06$ ), the Airy beam may focus into more than one beam. In figure 3.15 multiple beams are observed at the output of the crystal when strong nonlinearity is used. Figure 3.15(a1) shows the Airy beam at the input face of the crystal. Figure 3.15(b1) shows the Airy beam at the output face of the crystal. Figure 3.15(c1) shows the output face of the crystal when background lighting is applied ( $35 \text{ mW}$ ) and figure 3.15(d1) when the external field is applied ( $E_{ext} = 800 \text{ V/cm}$ ). Figures 3.15(a2-d2) show the horizontal transverse profile of the above images. In figure 3.15(d2) we have plotted the profile of the expected soliton in these experimental conditions for each off-shooting beam. Alignment of the input

face and the output face has been done by combining the observation of the Gaussian soliton (when only the diffraction grating is used on the SLM) and the center of the two symmetric Airy beam. An Airy beam's symmetry is obtained by changing the phase mask value  $c_0 = 1500$  to its opposite  $c_0 = -1500$ . We notice that between figures 3.15(b1) and (c1) the background lighting has allowed the recovery of the diffracted Airy beam profile showing a form of *self-trapping*. Between figures 3.15(c1) and (d1) the increased nonlinearity due to the applied electric field has made the Airy beam shed an OSS which is referred to as *self-focusing* to differentiate from *self-trapping*. On the three beams obtained after self-focusing, the middle one is the OSS; it is of great intensity, in the position in  $x$  of the input Airy beam's main lobe and has a soliton profile. The beam on the left is expected as it has been observed that the Airy beam may shed multiple beams in nonlinear media [101]. Interestingly, it also has a soliton profile but it is not aligned with the input Airy beam's main lobe. We can consider this off-shooting beam a soliton propagating with a different direction than the OSS. The beam on the right does not fit the profile as well as the other two: it is slanted on its left and a secondary lobe can be distinguished. This beam is the residual linear Airy beam profile.

Please note that the two experimental profiles from figure 3.14 are obtained using the same Airy beam but different applied electric fields on the crystal. Therefore we can control the output width and amplitude of the OSS by changing the electric field applied on the crystal. To obtain additional off-shooting beams of soliton-like profile we can reduce the apodization factor as seen in figure 3.15. Therefore we can control the presence of secondary off-shooting beams by changing the phase shift  $c_0$  on the phase mask generating the Airy beam (see chapter 2) which is of interest in the case of optical interconnects detailed in chapter 5.

Although the experimental profile of the OSS fits with the theoretical soliton profile, it is worth mentioning that experimentally we only image the output and input faces of the crystal due to the non homogeneous refractive index that alters the imaging system inside the medium. In order to observe the formation and evolution of the OSS inside the crystal versus different parameters (crystal length or beam intensity for example), we use a numerical model to simulate the OSS propagation.

### 3.2.3 Numerical analysis

In what follows, we numerically propagate a 1+1D Airy beam in a photorefractive medium. The model is similar to the one presented in references [11, 40, 41, 102]. The

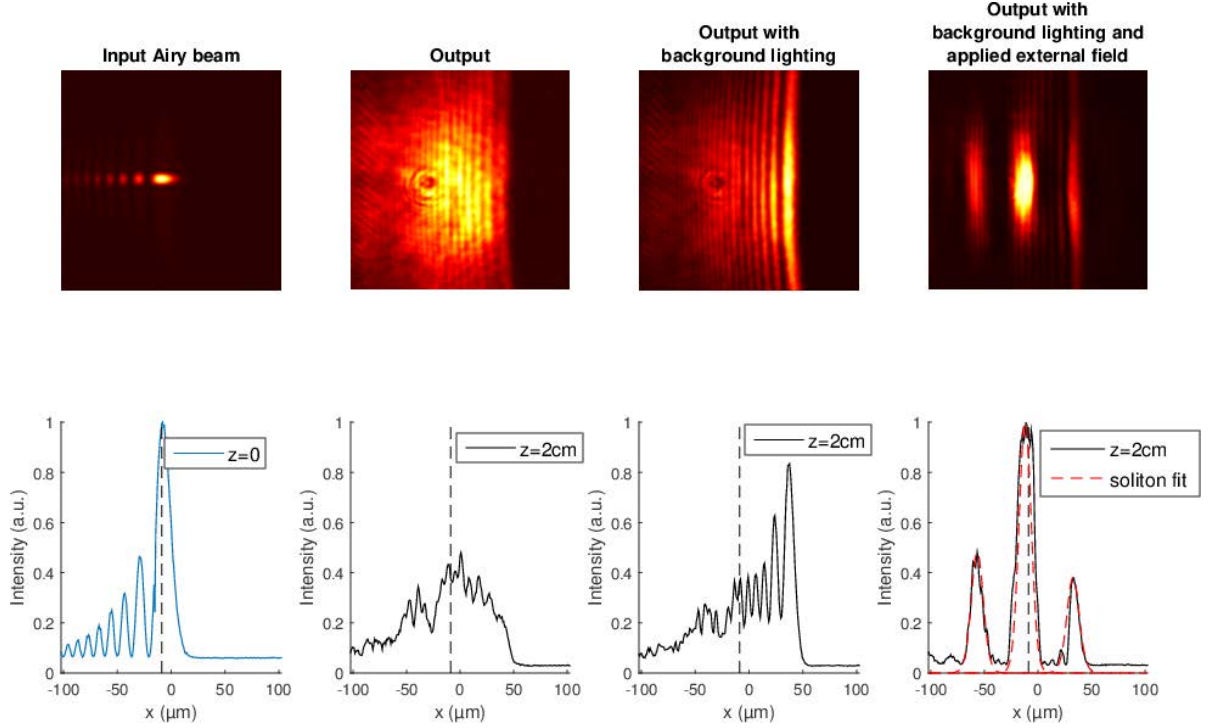


Figure 3.15: Input (a) and output (b-d) images of the transverse intensity profile of a  $2\mu\text{W}$  Airy beam ( $x_0 = 9.1\mu\text{m}$   $a = 0.06$ ), propagating through a 2cm SBN crystal. From (b) to (c) background lighting  $I_b = 35\text{mW}$  has been turned on. From (c) to (d) the externally applied field  $800\text{V/cm}$  has been turned on. The second row is the transverse profile along the horizontal axis.

normalized nonlinear Schrödinger equation reads:

$$(3.20) \quad i\partial_z F + \partial_x^2 F = \Gamma E_0 F$$

where  $F$  is the beam electric field amplitude,  $\Gamma = (kn_e x_0)^2 r_{eff} E_e$  is the nonlinear photorefractive coupling strength,  $E_e$  is the external electric field.  $E_0$  is the homogeneous part of the x-component of the photorefractive space-charge field normalized by the external electric field. The temporal evolution of the space-charge field  $E_0$  is considered with saturable nonlinearity and calculated using a relaxation-type dynamic:

$$(3.21) \quad \tau \partial_t E_0 + E_0 = -\frac{I_{num}}{1 + I_{num}}$$

where the normalized relaxation time of the crystal  $\tau$  is the relaxation time  $\tau_0$  divided by the total intensity  $\tau = \frac{\tau_0}{1+I}$ , and  $I_{num} = |F|^2 = \frac{I}{I_b}$  is the intensity normalized by the effective background intensity.

The beam propagates along the  $z$  axis, and has a truncated Airy beam transverse profile

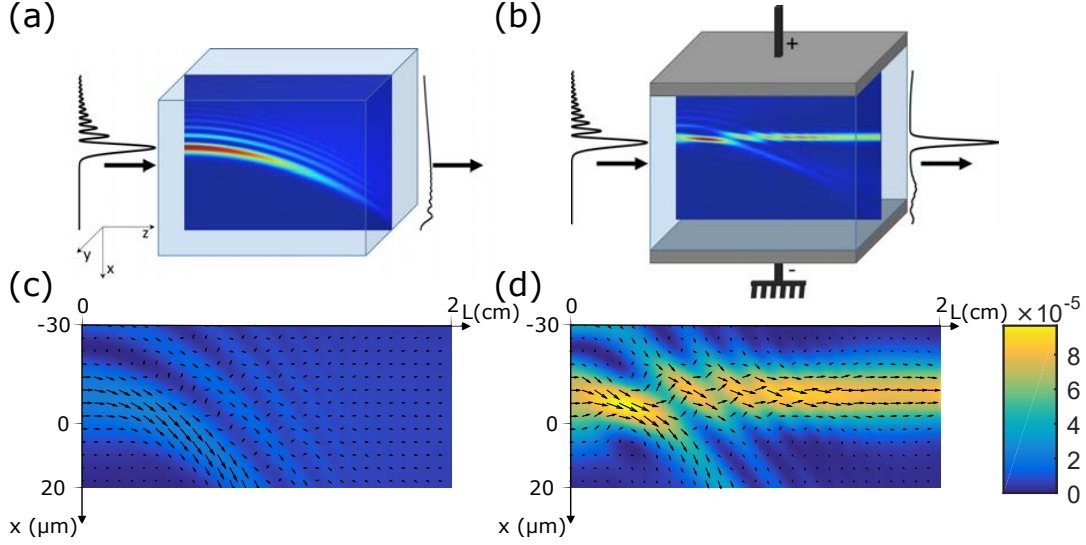


Figure 3.16: Propagation of a 1D-Airy beam in a 2cm long photorefractive crystal at steady state. (a) Linear propagation ( $\Gamma = 0$ ). (b) Nonlinear propagation in presence of an external electric field leading to an OSS. ( $\Gamma = 10$ ,  $F_0 = 1.95$ ,  $x_0 = 10\mu\text{m}$ ,  $a = 0.1$ ). (c-d) Distribution of the refractive index change versus  $x$  and  $z$  at steady state. Arrows represent the Poynting vector. (c)  $\Gamma = 3$ . (d)  $\Gamma = 10$ .

upon injection at  $z = 0$ :

$$(3.22) \quad F(x, z = 0) = F_0 Ai\left(\frac{x}{x_0}\right) e^{a \frac{x}{x_0}}$$

where  $F_0$  is the total amplitude of the Airy beam,  $Ai$  is the Airy function,  $x_0$  is the Airy beam's main lobe waist at  $1/e$  of its maximum intensity, and  $a$  is the truncation parameter or apodization factor.

Based on this model we numerically propagate a 1+1D Airy beam in a photorefractive medium using a beam propagation method within a temporal loop that recalculates the electric field inside the crystal at each time iteration. The study is done once steady state is reached (more than  $50 \tau$ ).

Figure 3.16(a) shows the linear propagation at steady state of the 1D-Airy beam along the  $z$ -axis of a photorefractive medium. Similar to reference [11] and in order to fit to the experiment presented in figure 3.14, the truncation and waist parameters are  $x_0 = 10\mu\text{m}$  and  $a = 0.1$ . As expected, we observe a curved trajectory for a 2cm propagation length inside the medium. Moreover, our numerical simulation reproduces qualitatively well our experimental result since similarly to the experiment in figure 3.14, when an external electric field is applied ( $\Gamma > 0$ ), we numerically observe the shedding of an OSS from the

original Airy beam [Fig. 3.16(b)]. It is worth noting that for a smaller apodization factor we observe numerically several off-shooting beams in different directions of propagation (similar to ref. [36] in Kerr media and our experiment in figure 3.15). In our study we decided to focus on the OSS which does not deviate from the propagation axis.

Figure 3.16(c) (respectively (d)) represents the photoinduced distribution of the refractive index change  $\Delta n = -\frac{n_e^3}{2} r_{eff} E_{sc}$  inside the crystal for  $\Gamma = 3$  (respectively  $\Gamma = 10$ ) versus  $x$  and  $z$ . To gain further insight we superimpose the time-averaged Poynting vector  $\langle \vec{S} \rangle$  using the following equation from references [103, 104]:

$$(3.23) \quad \langle \vec{S} \rangle = i\omega \frac{\epsilon_0}{2} (F_x \frac{\partial F_x^*}{\partial x} - F_x^* \frac{\partial F_x}{\partial x}) \vec{u}_x + \omega k \epsilon_0 |F|^2 \vec{u}_z$$

where  $\epsilon_0$  is the vacuum permittivity and  $\omega = ck$  with  $c$  the speed of light. Increasing the nonlinearity  $\Gamma$  leads to the creation of a photoinduced waveguide that modifies the beams propagation. The arrows show how energy is transferred from the main lobe to the second lobe which is then transferred to the next lobes hence explaining the creation of the OSS.

We now propose to compare the numerical OSS with the theoretical soliton and analyze its behavior versus  $u_0$ . We therefore link the two models using:

$$(3.24) \quad d = \frac{x_0}{\sqrt{\Gamma}}$$

and fix the maximum amplitude of the Airy beam OSS as  $u_0$ . Then we can solve equation (3.19) and compare the different profiles.

Figure 3.17(a) shows the OSS numerical amplitude profile versus  $x$  corresponding to Fig. 3.16(b) after a propagation of 2 cm at steady state. The amplitude does not reach the 0 value in the tails of the soliton-like profile because the diffraction of the Airy beam multi-lobe structure creates residual lighting on the numerical simulation [Fig. 3.17(b)]. The OSS numerical profile shows a transverse profile that matches a soliton-like profile. By using the model from ref. [98] [equations (3.18), (3.19)] and the expression (3.24), we can link our numerical simulations with the theoretical soliton model. We draw the theoretical soliton profile that would propagate in the crystal under the same conditions as our numerical simulation. Figure 3.17(a) demonstrates that the theoretical soliton profile fits nicely with the numerical profile of the OSS.

***Is the soliton-like profile of the OSS stable over long distances?*** To answer this question, we numerically propagate the OSS up to 12 cm inside the nonlinear medium (corresponding to more than twenty diffraction lengths). The profile illustrated in Figure

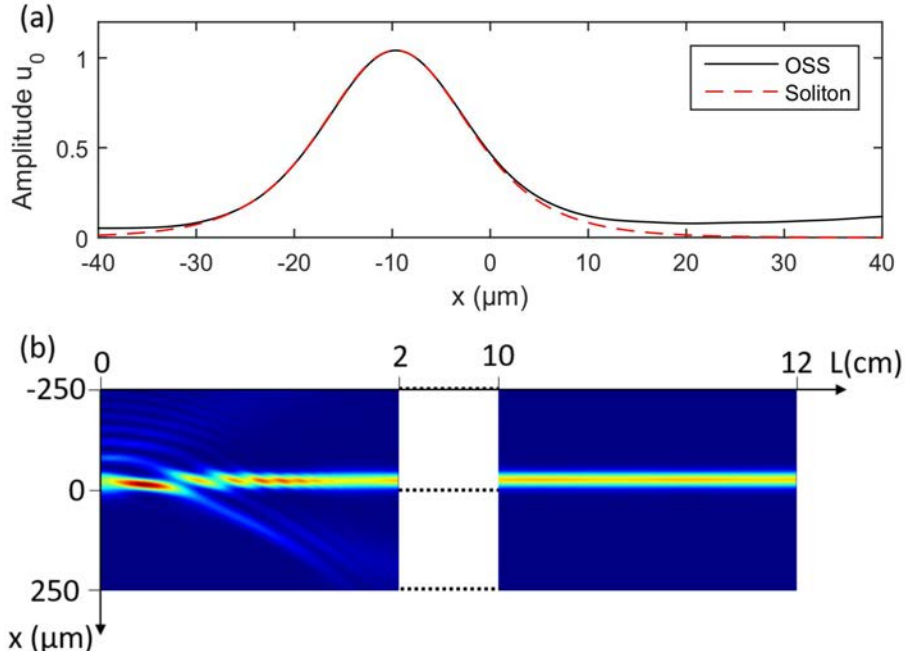


Figure 3.17: (a) Numerical profile of the Airy beam OSS in Fig. 3.16(b) and corresponding theoretical soliton at  $L=2\text{cm}$ . (b) Propagation of the OSS over long distances at steady state. ( $\Gamma = 10$ ,  $F_0 = 1.95$ ,  $x_0 = 10\mu\text{m}$ ,  $a = 0.1$ ,  $u_0 = 1.04$ ).

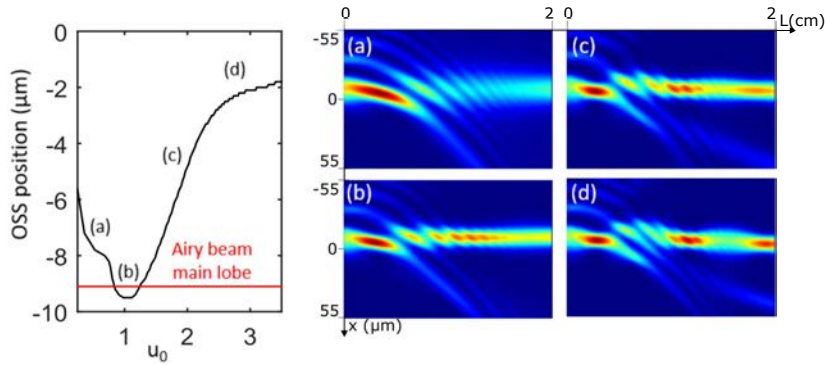


Figure 3.18: Position of the Airy beam OSS as function of OSS maximum amplitude for  $\Gamma = 10$ ,  $F_0 = 1$  to  $7.5$  or  $u_0 = 0.25$  to  $3.5$ ,  $x_0 = 10 \mu\text{m}$ ,  $a = 0.1$  and  $t_f = 20 \tau_0$ . (a to d) Corresponding numerical simulation inside the crystal for (a)  $u_0 = 0.5$ , (b)  $u_0 = 1.04$ , (c)  $u_0 = 1.9$ , (d)  $u_0 = 2.9$

3.17(b) shows a constant behavior over the 12 cm propagation length. The maximum amplitude between the OSS at 2 cm and the one at 12 cm of propagation differs only from 1% unveiling its soliton-like nature.

We can now fairly consider the Airy beam OSS as a spatial soliton even after 2cm of propagation inside the crystal. But as observed in [41], it is important to note that

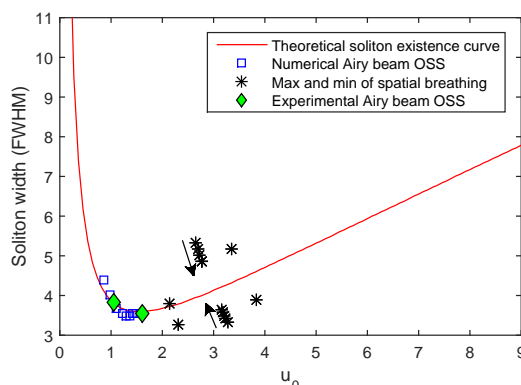


Figure 3.19: Full width at half maximum (FWHM) in dimensionless units ( $\xi$ ) in function of soliton amplitude. In red the theoretical curve from Ref. [98], in blue squares the Airy beam OSS at 2 cm propagation from our numerical model, in black stars the maximum and minimum of the observed spatial breathing and the arrows show the evolution when propagating greater distances. In green diamonds, the experimental OSS observed in Fig. 1.

the output position of the OSS varies slightly with the intensity of the Airy beam sent into the nonlinear medium. Figure 3.18 shows at steady state the evolution of the OSS position at the output face of the crystal as a function of the off-shooting beam's maximum amplitude. This curve is drawn by increasing numerically the total amplitude of the input Airy beam  $F$  from 1 to 7.5 which corresponds to the maximum amplitude  $u_0$  of the OSS going from 0.25 to 3.5. We notice that the OSS position is correlated to different propagation behaviors. For  $0.5 < u_0 < 2$  [Fig. 3.18(a)-3.18(c)] the position of the OSS at steady state is close ( $< 5\mu m$ ,  $< x_0/2$ ) to the position of the Airy beam's main lobe at the input of the crystal (red line in Fig. 3.18). We also checked that the OSS beam profile corresponds to that of a theoretical soliton in this region. When  $u_0 > 2$  [Fig.3.18(d)], the OSS trajectory is no longer perpendicular to the input face of the crystal, the solitonic profile is lost and we observe spatial breathing along the propagation axis. For Figs. 3.18(a) and 3.18(c) the trajectory of the OSS is not perpendicular to the input face of the crystal and the position of the OSS shifts along the x-axis at greater distances, whereas in the area close to the extremum of the curve [Fig. 3.18(b)] the position of the soliton does not change anymore at greater distances.

Referring to Figs. 3.18(a)-(d) we can observe variations of the intensity and width of the OSS at the output face of the medium. The theory of one-dimensional steady state screening solitons in bulk material states that a relation exists between the width and the intensity of the soliton: figure 3.19 depicts the theoretical existence curve of the

soliton full width at half maximum (FWHM) as a function of  $u_0$  from ref.[98]. The green diamonds represent the experimental Airy OSS seen in Fig 3.14 for the two different applied electric fields (200 V/cm and 400 V/cm). These experimental points are on the existence curve and confirm that the obtained OSS is indeed a soliton. Is also represented on this figure the Airy beam off-shooting FWHM for different values of  $u_0$ , all selected close to the extrema in Fig. 3.18, and obtained by solely modifying the input Airy beams amplitude. The values of  $u_0$  go from 0.8 to 1.5 and we measure the corresponding FWHM of the OSS. We see that our numerical OSS width and theoretical curve are in good agreement, further corroborating the similarity between OSS and a classical soliton. At greater values of  $u_0$ , where spatial breathing takes place, the maximum and minimum of the FWHM and corresponding  $u_0$  are included in fig. 3.19 as black stars. These points are on either side of the existence curve. Therefore the beam's profile oscillates around the soliton profile. Furthermore, the amplitude and FWHM of these spatial oscillations tend to converge towards the theoretical soliton existence curve at greater distances (arrows on Fig 3.19).

For a given Airy beam input profile the OSS fits with the theoretical plot for values of  $u_0$  from 0.8 to 1.5. The values of  $u_0$  from 0.8 to 1.5 correspond to the extrema in position of the OSS as function of  $u_0$  (seen in fig. 3.18). We conclude that the extrema in position versus  $u_0$  indicates the area for which the OSS is closest to a theoretical soliton (blue squares in fig.3.19). Furthermore, since there is a quasilinear relation between the Airy beam amplitude and the OSS amplitude we can also control the output OSS width and amplitude by changing the amplitude of the Airy beam. Therefore, unlike Gaussian beams, with one Airy beam we can create solitons of different widths when we change the nonlinearity in the crystal by modifying either the light intensity or the applied electric field.

### 3.3 Conclusion

In summary, we have evidenced the solitonic properties of Airy beam nonlinear propagation. Differently from Gaussian beams, the OSS coexists with a remaining self-accelerating structure and eventual off-shooting beams. Experimental and numerical profiles of the OSS fit nicely with the theoretical soliton profile. Numerical simulations confirm that the OSS propagates invariably on great distances (more than twenty diffraction lengths). We observed that for fixed nonlinear conditions inside a photorefractive

crystal, there exists a range of intensity values for which the OSS property is the closest to the ideal theoretical soliton. This work motivates further studies of 2D-Airy beams propagating in a photorefractive medium for testing the properties and the stability of the 2D-OSS. Furthermore, since the OSS profile is quite similar to previously observed solitons such as those arising from Gaussian beams, further studies can be envisioned in particular those analyzing interactions and applications of spatial solitons.

## 2D AIRY BEAM PROPAGATION IN PHOTOREFRACTIVE MEDIA

In the previous chapter we have looked at one-dimensional propagation of Airy beams in photorefractive nonlinear media and the formation of off-shooting solitons (OSS). In this chapter we wish to observe similarly two-dimensional Airy beams propagating in photorefractive media and the resulting OSS. We will also take this opportunity to widen the scope of our observation and consider other effects inherent to photorefractive media. To do so we will start by explaining the effect of anisotropy on beam propagation. We will then present our experimental observations of 2D Airy beam nonlinear propagation and the formation of two dimensional off-shooting solitons (OSS). Finally we will discuss the OSS self-bending and the OSS profile to the existence curve.

## 4.1 Propagation dynamic and soliton formation in two-dimensional saturable nonlinear media

We have seen in the previous chapter (section 3.2.2) that saturable nonlinearity allows for stable (2+1)D solitons to propagate. Indeed, due to saturation of the nonlinear focusing effect, the over self-focusing observed in other nonlinear media can be partially avoided in photorefractive media. The lensing effect becomes wider instead of becoming stronger [30, 31]. Different approaches have been used to describe the dynamics of soliton propagation in photorefractive anisotropic medium. The first one considers that the photorefractive-index change responsible for the formation of photorefractive spatial screening solitons and coherent collisions between them is primarily isotropic in nature, even though the photorefractive medium is inherently anisotropic [105]. This model is correct to a certain extent and has been used to explain experimental results such as circular photorefractive solitons [106, 107] and soliton interactions such as spiraling [108]. A second approach however takes into account the anisotropy and the spatially nonlocal nature of the nonlinear effect. Interestingly this analysis reveals the soliton in anisotropic medium is in fact an elliptically shaped soliton and it has also been observed experimentally [109]. If the injected Gaussian beam is too far from the profile of the elliptic soliton, complex spatial oscillations, including asymmetric filamentation into several beamlets can be observed [110]. Another advanced model, is a time-dependant three-dimensional model. It relies on calculations of the time dependence of the charges distribution in the photorefractive material. This determines the dynamical formation of the space charge electric field, which allows to compute the diameter and the bending of the self-focused beam for a given propagation distance [111]. This model was further refined in order to apply to materials where both electrons and holes participated in the photorefractive effect [112] and notably explained dynamics observed in  $InP : Fe$  and  $LiNbO_3$  crystals [113].

The anisotropy is due to the crystalline structure of the material. In the case of the SBN crystal, electron mobility naturally creates a polarization along the crystal's c-axis. This results in a different response of the material along that particular axis direction. By lighting the crystal perpendicularly to the c-axis, the crystal is birefringent (due to anisotropy). This means that the refractive index will be different if the polarization of light is along the preferential c-axis (extraordinary polarization) or perpendicular to both the c-axis and the propagation axis (ordinary polarization). The nonlinear photorefractive effect needs extraordinarily polarized light.

The anisotropic model has been compared to the isotropic model [114–116], and put to the test using nonconventional beams such as vortices [115, 116]. In the case of two solitons for example, in the isotropic model the two solitons will spiral around each other whereas for the anisotropic model they will stop spiraling after a rotation of  $\pi/2$  and start oscillating [115]. Experimentally, both models can explain certain beam configurations at the output face of a crystal. The propagation behavior inside the crystal can only be seen from the side of the crystal, by light dispersed orthogonally to the propagation axis of the beam. This dispersed light propagates through the complex refractive index variation distribution inside the crystal and this deforms any possible observation. Since inside the crystal, due to refractive index variations, we cannot properly observe propagation, models are important to understand the dynamic of the propagation and explain experimental observations at the output face of the crystal. To explain the photorefractive effect, the set of Kukhtarev equations is accepted as valid (see chapter 3.1.2) but the approximations required to solve these equations may differ, for example, if we are studying three wave mixing or self-focusing beams. The most accurate way to solve the equations seems to be A. Zozulya’s method [109], which solves the electrostatic potential first in order to find the space-charge field afterwards inside the crystal. F. Devaux and M. Chauvet solved a time-dependant electrostatic potential which explained the occurrence of beam bending as connected to the saturation of charges necessary to screen the effective electric field. The accuracy of these models relies on the validity of the approximations made to solve the equations. The approximations using the electrostatic potential are more accurate than the approximations used when solving the space charge field directly [115], and have been used to simulate propagating two dimensional Airy beams [117].

Figure 4.1(Left) shows analytical results of the elliptic nature of the soliton profile. On the left is plotted the curves of both transverse diameters of the elliptic soliton solution (solid lines) and their ratio (dashed line) versus the soliton’s maximum intensity. In terms of soliton profile evolution, the tendency of the solid curves resemble the soliton existence curve described in chapter 3.1.3 in the one dimensional case. When the intensity increases, the soliton beam profile tightens. After reaching an extrema, the increase of intensity causes the soliton beam profile to widen. However, the soliton profile is not the same along both transverse dimensions due to the photorefractive crystal’s anisotropy leading to an elliptic shaped soliton. Figure 4.1(Right) shows the diameter evolution of an initially round beam for both low intensity (solid line) and high intensity (dashed curve). For low intensity, the profile stabilizes for both transverse dimensions

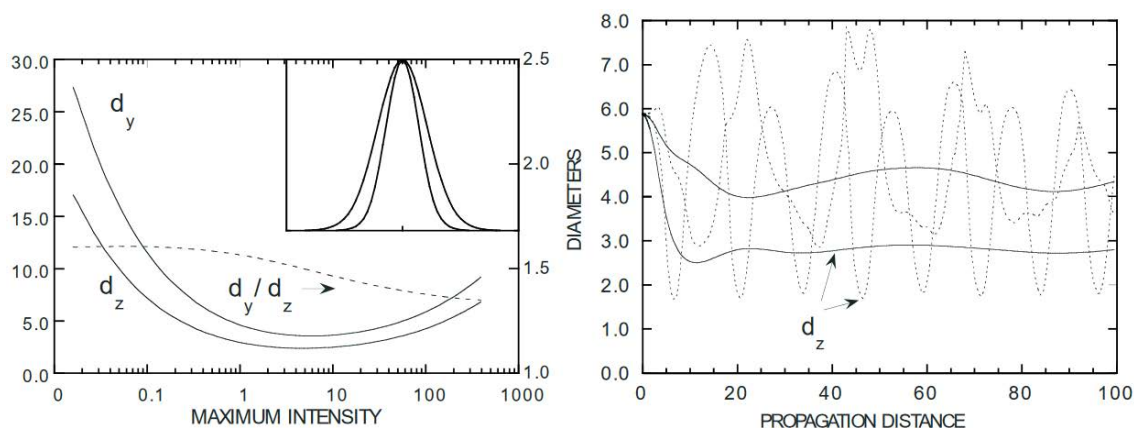


Figure 4.1: (Left) Both transverse diameters of the elliptic soliton solution (solid) and their ratio vs. its maximum intensity (dashed). The insert shows the soliton intensity cross-sections for maximum intensity equal to 5. (Right) Evolution of diameters of an initially round Gaussian beam for low intensity (solid) and high intensity (dashed curves). Extracted from reference [109].

leading to an elliptic soliton, whereas for high intensity the transverse profile does not seem to stabilize; the diameters oscillate and we observe a breathing soliton similarly to what is observed for numerical one-dimensional simulations carried out at high intensity reported at the end of chapter 3.2.3, and represented in the one-dimensional existence curve of figure 3.19.

Aside from the solitons being elliptically shaped in anisotropic photorefractive media, *self-bending* is also a commonly observed phenomenon. *Self-bending* occurs when there is a slight shift between the soliton profile and the refractive index variation. The soliton beam will shift direction due to the photo-induced refractive index waveguide being shifted. Since the refractive index variation and the soliton beam profile remain shifted along propagation, the soliton is constantly adapting its propagation direction to follow its self-induced waveguiding structure. This causes the beam trajectory to bend without any other additional exterior force and is called *self-bending*. Different causes have been identified that explain self-bending. If the beam size is in the range of the carrier diffusion length then the self-bending becomes significant enough to be observed [118]. The diffusion of charges along the crystal's preferential c-axis and the influence of beam intensity and bias electric field are reported in reference [118] and shown in figure 4.2.

Figure 4.2(a) and (b) show the beam bending distance in function of applied electric field and beam intensity respectively. In figure 4.2(a) the soliton forms for  $3.6kV/cm$  and the self-bending distance increases for increasing values of electric field. After reaching a

#### 4.1. PROPAGATION DYNAMIC AND SOLITON FORMATION IN TWO-DIMENSIONAL SATURABLE NONLINEAR MEDIA

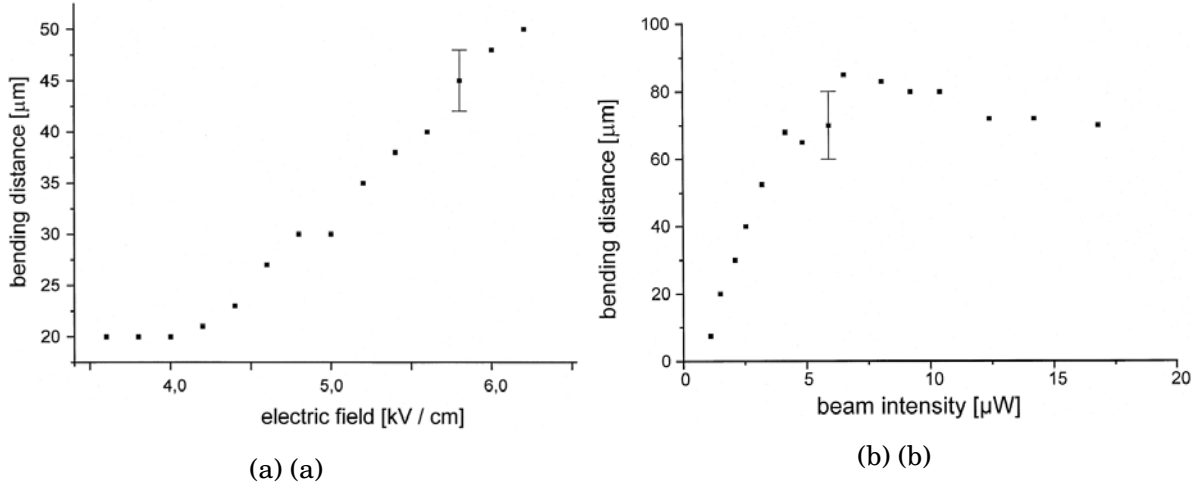


Figure 4.2: (a) Beam bending distance depending on the applied electric field. For a beam intensity of  $8.1\mu W$ , diameter  $17\mu m$  and  $I/I_b = 1$ . (b) Beam bending distance depending on the the beam intensity. Applied electric field of  $5.4kV/cm$ , beam diameter  $12\mu m$ . Extracted from [118].

maximum self-bending distance of 2.5 times its diameter, further increase of the electric field lead to filamentation dynamics [118]. In figure 4.2(b) the self-bending increases for increasing values of light beam intensity. Both the applied electric field and the beam intensity increase the nonlinear response of the crystal and increase the beam bending. In the case of the beam intensity, the self-bending distance slowly decreases past a certain point due to higher saturation and the widening of the beam [118].

We have reproduced previously mentioned beam propagation dynamics with our own set up in figures 4.3 and 4.4. An experimental transverse intensity distribution of an elliptic soliton can be seen in Figure 4.3. We have injected a  $2\mu W$  Gaussian beam in a  $2cm$  long and  $5mm$  wide cerium doped SBN:61 crystal. We apply an external electric field on the sides of the crystal, along the c-axis, perpendicular to the propagation direction. When the applied voltage is increased from  $0V/cm$  (figure 4.3(a)) to  $800V/cm$  (4.3(d)) the focusing effect is stronger along the horizontal c-axis of our crystal. The anisotropy of the crystal and the asymmetry due to the applied external field results in a highly elliptic shaped beam.

Figure 4.4 shows the evolution along time of a soliton for a greater applied voltage of  $2000V/cm$ . When we increase the applied electric field furthermore, the horizontal focusing saturates while the vertical focusing keeps increasing enabling quasi-circular solitons to take shape as can be seen in figure 4.4(a). Once vertical saturation is reached however, for strong applied electric fields, the soliton self-bends along the c-axis and

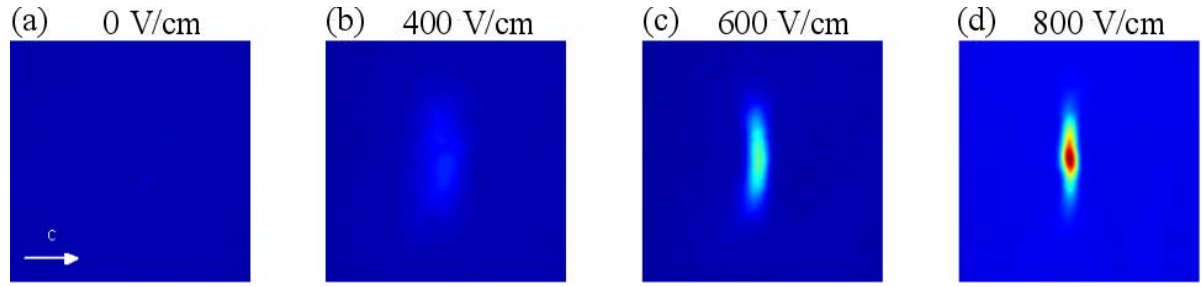


Figure 4.3: Experimental observation of soliton formation in a 2cm long SBN crystal for increasing applied electric voltages. Injected Gaussian beam of  $2\mu W$ ,  $I_b = 35mW$ .

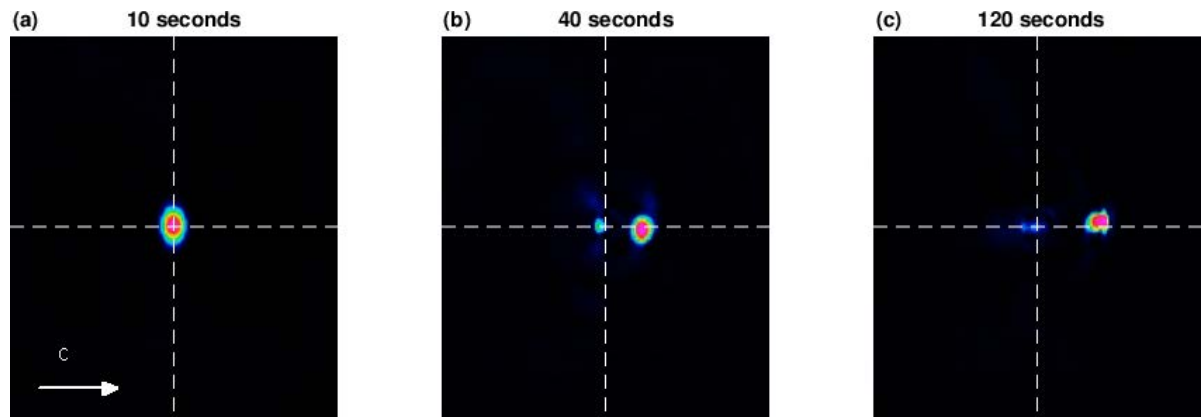
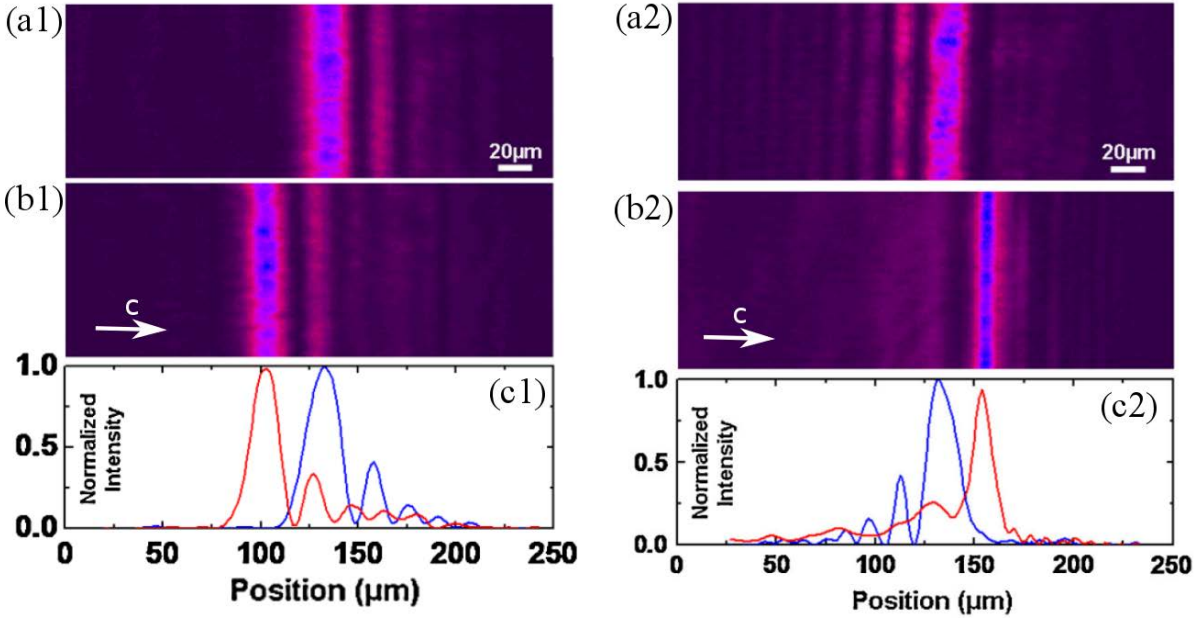


Figure 4.4: Transverse intensity distribution of a soliton over time propagating through a 2cm long SBN crystal and an externally applied voltage along the c-axis of the crystal of  $V = 2000V/cm$ . Injected Gaussian beam of  $2\mu W$ ,  $I_b = 35mW$ .

along the bias electric field direction due to a greater diffusion of the charge carriers as has been analyzed in reference [118]. In the numerical approach developed in the previous chapter, we chose to express only the dominant term of the space charge field  $E_{sc}$  (equation 3.13), also referred to as the screening term. There are additional terms that can be considered [97], notably two, the diffusion field and the coupling of the diffusion field with the screening field. These two terms are anti-symmetric and play a central role in photorefractive wave mixing. These terms are also the ones that in our case, lead to soliton self-bending.

To sum up, the anisotropy of the crystal and the asymmetry of the applied electric field induces different focusing strengths along the transverse axis. The horizontal c-axis, along which the voltage is applied, focuses more strongly than the vertical axis. Due to the saturation nature of the photorefractive effect, the focusing will saturate for both transverse axis but at different values of the applied electric fields. Before saturation is reached for both axis the beam is elliptic, once saturation is reached along both axis the

#### 4.1. PROPAGATION DYNAMIC AND SOLITON FORMATION IN TWO-DIMENSIONAL SATURABLE NONLINEAR MEDIA



(a) (a)

(b) Nonlinear Airy beam propagation for a  $350mW$  beam with extraordinary polarization (polarization along the crystal's  $c$ -axis). For (1) and (2) symmetric Airy beams with acceleration in the opposite direction (1) as the  $c$ -axis and in the same direction (b) as the  $c$ -axis. (a) Input Airy beam. (b) Output beam with (c) corresponding cross section. Extracted from [37].

soliton is circular. However, due to the strong applied electric field needed for saturation to be reached, the soliton also tends to self-bend in the direction of the applied electric field.

The effect of diffusion on the one-dimensional Airy beam propagation when no electric field is applied has also been studied in reference [37]. Figure 4.5b shows the nonlinear Airy beam propagation for a  $350mW$  beam with extraordinary polarization (polarization along the crystal's  $c$ -axis). The first case corresponds to an Airy beam accelerating opposite the  $c$ -axis direction. The second corresponds to an Airy beam accelerating in the direction of the  $c$ -axis. Figure 4.5b(a) shows the input 1D-Airy beam, figure 4.5b(b) shows the output beam and figure 4.5b(c) shows a cross section of the output beam. The shift in position of the main lobe from input (figure 4.5b(a)) to output (figure 4.5b(b)) corresponds to the acceleration direction of the curved propagating Airy beam. In the first case the Airy beam is *self-trapped*, meaning that the Airy beam profile is both preserved and more intense than in the case of a linear propagation (see reference [37]). In the second case due to diffusion the light of the beam refocuses in the main lobe of the Airy beam. When a strong electric field is applied Airy beam *self-focusing* occurs as observed in

the previous chapter section 3.2.2. By *self-focusing* we mean that the Airy beam profile refocuses into a soliton-like beam.

In this section we have seen typical dynamics of soliton propagation in anisotropic and nonlinear media. We have observed a 1D-Airy beam propagation when no electric field is applied in this section and when an electric field is applied in the previous chapter 3.2.2. We have not seen the dynamics for a 2D-Airy beams propagating with and without an applied electric field in anisotropic saturable nonlinear media.

### 4.1.1 Experimental observation of 2D Airy beam propagation in photorefractive media

In this section, we study the propagation behavior inside a photorefractive cerium doped strontium barium niobate (SBN:61) crystal of an experimental 2D Airy beam for different values of light intensity and externally applied electric field on the crystal.

Our experimental setup is the same as the one in the previous chapter 3.2.2 except the phase mask that has been changed in order to obtain a propagating 2D-Airy beam. A schematic of the experimental setup is shown in figure 4.6(e). The experimental study consists in propagating a two-dimensional Airy beam ( $\lambda = 532 \text{ nm}$ ) into a photorefractive SBN-crystal with dimensions  $5 \text{ mm} \times 5 \text{ mm} \times 2 \text{ cm}$  ( $n_{SBN} = 2.3$ ). The laser beam is widened ( $\omega_0 = 2.7 \text{ mm}$ ) to illuminate the spatial light modulator (SLM). The SLM displays a 2D quadratic phase ( $c_0 = 1400$ ) superimposed with a diffraction grating. A lens of short focal length forms the Airy beam in the plane of a spatial filter. Two lenses then image at the input of our SBN crystal the focal plane where the Airy beam is formed. The viewing system uses beam splitters to image the input and the output faces of the crystal on a CCD camera. A different light source is used as background lighting ( $I_b = 35 \text{ mW}$ ), illuminating the entire crystal from above.

Figure 4.6(a) shows the Airy beam injected inside the crystal. Figures 4.6(b-d) shows the output face of the crystal for different values of externally applied electric field, in white is circled the position of the OSS. Figures 4.6(f-g) shows the cross section of the transverse intensity profile at the output of the crystal at the Airy beam OSS position for applied fields of  $800 \text{ V/cm}$  and  $1200 \text{ V/cm}$ . After propagation through the SBN crystal, in figure 4.6(b), the Airy beam is slightly diffracted and shifted due to the acceleration of the Airy beam. When an external electric field is applied (figure 4.6(c-d)), the light focuses into an off-shooting soliton (OSS) that presents almost no shift in position when compared to the input Airy beam's main lobe position. This dynamic of spatial light

#### 4.1. PROPAGATION DYNAMIC AND SOLITON FORMATION IN TWO-DIMENSIONAL SATURABLE NONLINEAR MEDIA

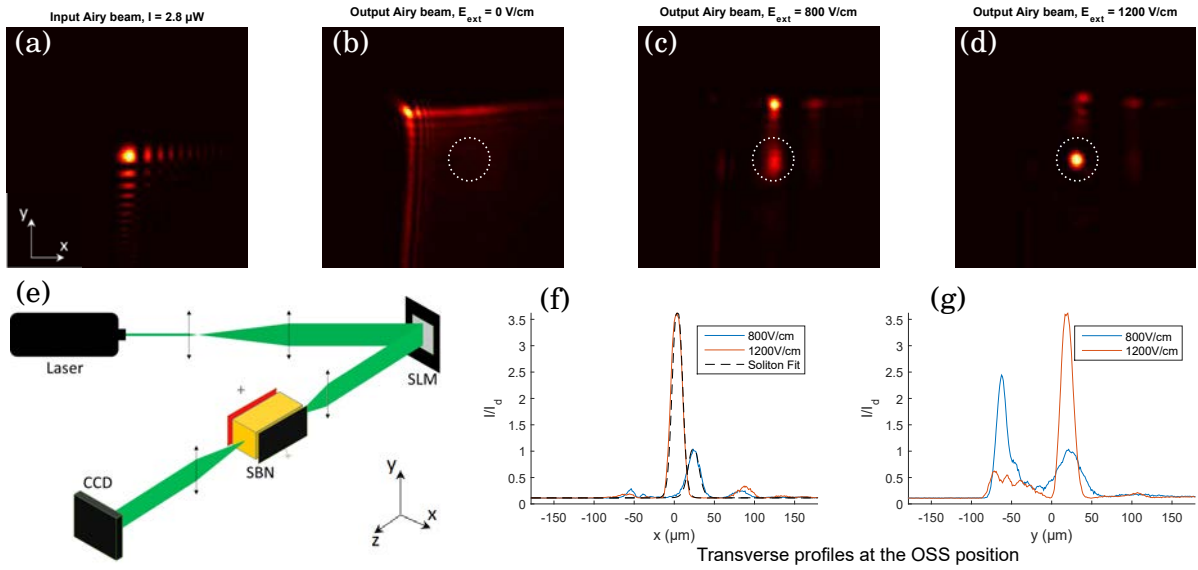


Figure 4.6: (a) Transverse intensity profile of the input Airy beam,  $2.8 \mu\text{W}$ . (b-d) Transverse intensity profile of the output for different applied external field (b)  $E_{ext} = 0 \text{ V/cm}$ , (c)  $E_{ext} = 800 \text{ V/cm}$ , and (d)  $E_{ext} = 1200 \text{ V/cm}$ , the OSS position is represented by a dotted white circle. (e) Schematic of the experimental setup. (f-g) Intensity profile cross sections along the x and y axis at the OSS position

distribution in a photorefractive media is due to the interaction of light and matter and can be explained using the Kukhtarev band transport model [95] detailed in chapter 3.1.2. Light locally photoexcites charges inside the crystal that are then displaced due to the externally applied field. The displacement of charges creates an electric field opposite the externally applied electric field and localized in the lighted areas. Due to the Pockels electro-optic effect, the refractive index is modified locally proportionally to the local space charge field. The refractive index variations affect the light propagation and light distribution inside the crystal which will change the space charge field distribution anew. This dynamic can result in a focusing effect that, if sufficiently strong (figure 4.6(c-d)), modifies the profile of the propagating beam into an OSS. In order to compare the Airy beam OSS profile to the theoretical soliton profile, we use the same method as reference [98]. The theory is developed for a one-dimensional steady state bright screening soliton profile and is detailed in chapter 3.1.3.

When increasing the external field, the transition from Airy beam to OSS at the output face of the crystal is a continuous process. However we can distinguish two steps. The first step is the focusing along the preferential c-axis which is collinear to the applied external field or the x-axis. In figure 4.6(c-d) the light has focused horizontally along the x-axis to form an OSS (figure 4.6(f)). However the linear Airy beam structure remains

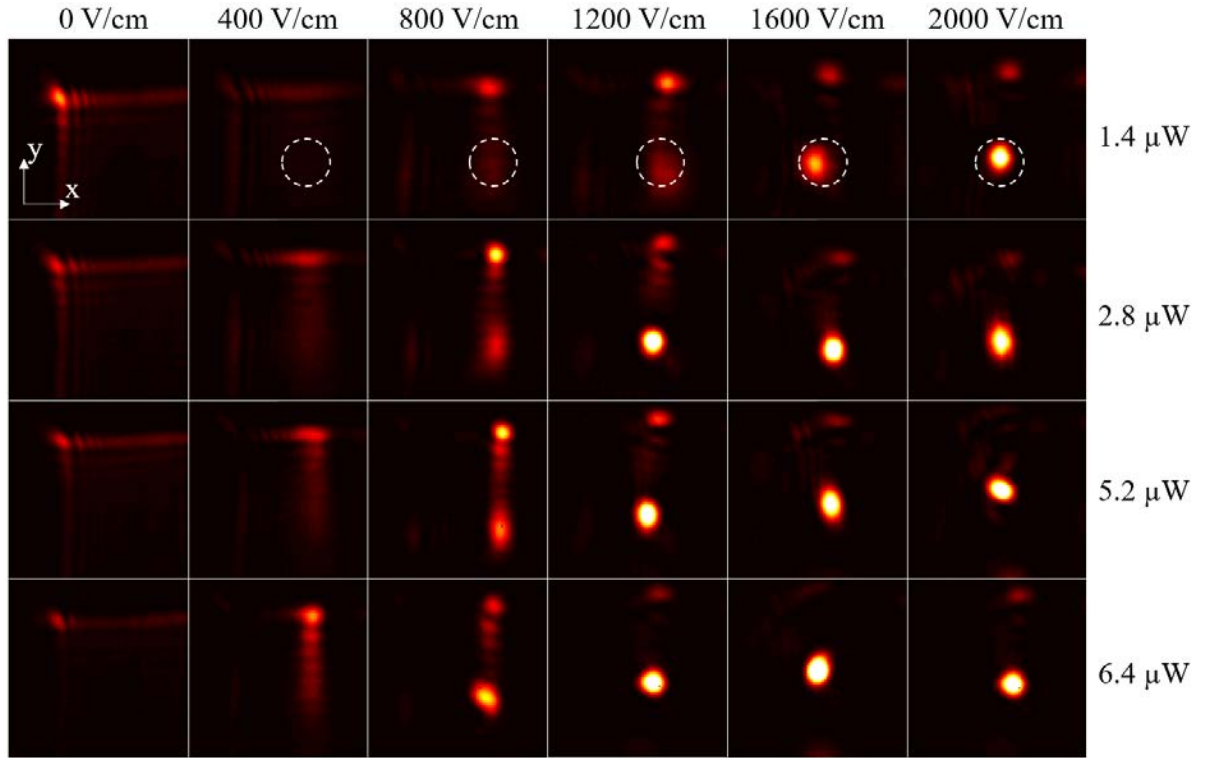


Figure 4.7: Intensity profiles of the beam at the output of a 2 cm SBN crystal for input intensity values  $I_{input} = 1.4$  to  $6.4 \mu\text{W}$  and applied external field  $E_{ext} = 0$  to  $2000\text{V}/\text{cm}$ . Airy beam acceleration negative along  $x$  and positive along  $y$ . The OSS position is represented by a dotted white circle.

along the vertical  $y$ -axis and is in competition with the OSS (figure 4.6(g)). The second step is focusing along the vertical  $y$ -axis and requires a stronger nonlinear effect to take place. When further increasing the applied electric field, the light previously confined in the linear Airy beam structure shifts to the nonlinear OSS structure as can be seen in figure 4.6(g)(red), and ultimately leads to the nonlinear OSS structure as the only structure.

The light structure at the output of the crystal when propagating a two dimensional Airy beam can have a two dimensional beam profile (figure 4.6(b)), a residual one dimensional Airy profile and an OSS profile (figure 4.6(c)) or a quasi-circular OSS (figure 4.6(d)). This was not the case when injecting a Gaussian beam in similar experimental conditions in figure 4.3 where the profile was elliptic or quasi-circular in figure 4.4. Other non-conventional beams could yield different output profiles.

We have looked at the behavior of the output profile for a range of beam intensities and bias electric field applied on the crystal. Figure 4.7 and figure 4.8 show a matrix of

4.1. PROPAGATION DYNAMIC AND SOLITON FORMATION IN TWO-DIMENSIONAL SATURABLE NONLINEAR MEDIA

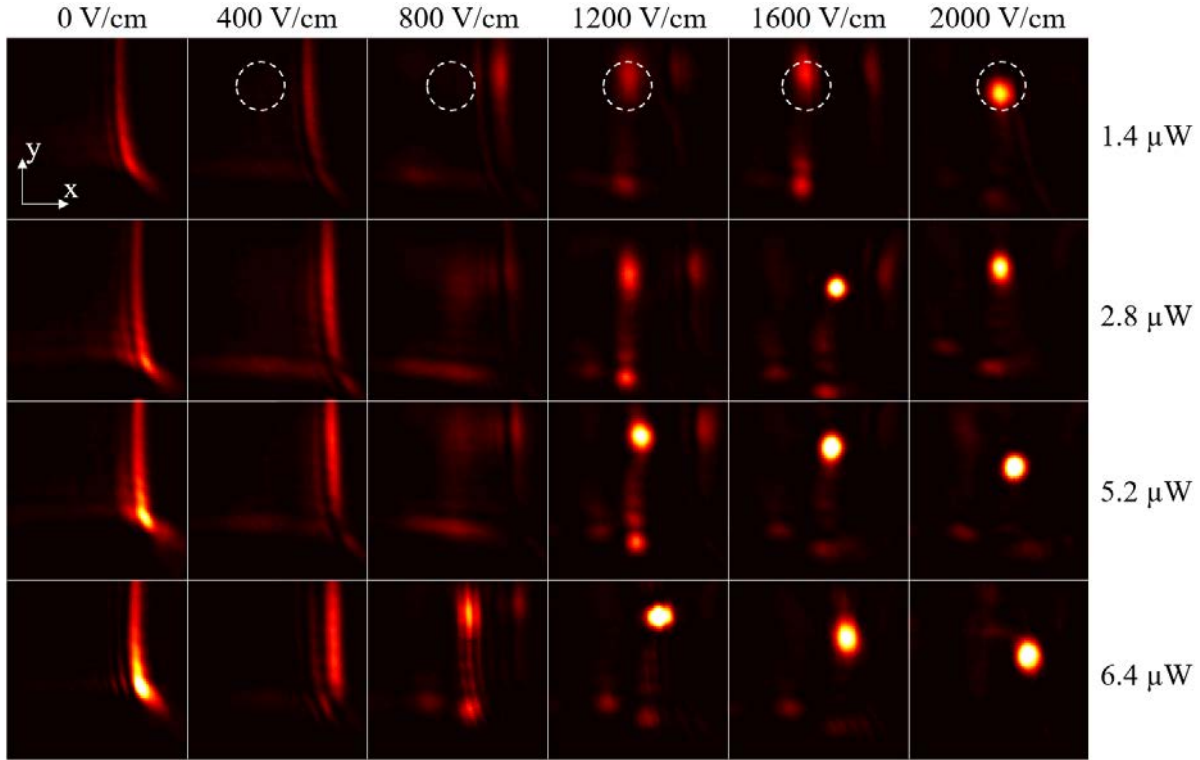


Figure 4.8: Intensity profiles of the beam at the output of a 2 cm SBN crystal for input intensity values  $I_{input} = 1.4$  to  $6.4 \mu\text{W}$  and applied external field  $E_{ext} = 0$  to  $2000\text{V}/\text{cm}$ . Airy beam acceleration positive along  $x$  and negative along  $y$ . The OSS position is represented by a dotted white circle.

different intensity profiles at the output of an SBN-crystal when injecting an Airy beam for different values of input intensity and externally applied electric field. For figure 4.7 we have injected an Airy beam with an acceleration negative along  $x$  and positive along  $y$ . Whereas for figure 4.8, we have injected the opposite, an Airy beam with an acceleration positive along  $x$  and negative along  $y$ . The input intensity ranges from  $1.4\mu\text{W}$  to  $6.4\mu\text{W}$ , the background lighting is constant at  $35\text{mW}$  and the applied electric field ranges from  $0\text{V}$  to  $2000\text{V}/\text{cm}$ . The same exposure time and attenuation in front of the camera is used for images of the same row, but different attenuation and exposure time are used for different rows. The OSS position is circled in white for the first row (light intensity of  $1.4\mu\text{W}$ ) for each figure 4.7 and 4.8.

In figure 4.7, when no electric field is applied, the 2D-Airy beam profile is unchanged. When an electric field of  $400\text{V}/\text{cm}$  is applied, the profile resembles a vertical 1D-Airy beam profile at the position in  $x$  where the OSS will form. Additionally, the 1D-Airy beam profile is better defined at higher intensities ( $6.4\mu\text{W}$ ). When an electric field of  $800\text{V}/\text{cm}$

is applied the residual vertical 1D-Airy beam is in competition with the OSS: for low values of intensities ( $1.4\mu W$ ) the profile resembles a vertical 1D-Airy beam, whereas for higher values of intensities ( $6.4\mu W$ ), both the 1D-Airy beam and OSS are clearly discerned. When an electric field of  $1200V/cm$  is applied the 1D-Airy beam is still in competition with the OSS: for a beam intensity of  $1.4\mu W$  both the 1D-Airy beam and OSS are discerned, whereas for a beam intensity of  $6.4\mu W$  the 1D-Airy profile has almost disappeared to the benefit of the intense OSS. When an electric field of  $1600V/cm$  or  $2000V/cm$  is applied the OSS is very intense and other few off-shooting beams (OSB) of low intensity are discerned.

In figure 4.8, when no electric field is applied, the 2D-Airy beam profile is already changed: all of the intensity has shifted to the main lobe along the x-axis. This is to be expected, as seen in figure 4.5b and explained in the corresponding reference [37], diffusion of carriers along the c-axis causes the light intensity to shift to the Airy beam's main lobe. When an electric field of  $400V/cm$  is applied, the light focuses more strongly in the Airy beam's main lobe. When an electric field of  $800V/cm$  is applied, light intensity starts to shift from the Airy beam's main lobe position in  $x$  to the OSS position. When light shifts to the position of the OSS position in  $x$ , for  $6.4\mu W$ , a residual vertical 1D-Airy beam is in competition with the OSS. When an electric field of  $1200V/cm$  is applied the light in the Airy beam's main lobe has refocused in an OSB and is in competition with the 1D-Airy beam and the OSS: for a beam intensity of  $1.4\mu W$  to  $5.5\mu W$ , three structure can be observed (Airy and OSS to the left, OSB to the right), whereas for a beam intensity of  $6.4\mu W$  the OSB is no longer visible. When an electric field of  $1600V/cm$  is applied the Airy beam, OSS and OSB are still in competition: the three structures are discerned for light intensities of  $1.4\mu W$  to  $2.8\mu W$  and only the OSS is very intense for light intensities of  $5.5\mu W$  and  $6.4\mu W$ . When an electric field of  $2000V/cm$  is applied only the OSS remains.

The nonlinear effect can be increased by increasing the value of the applied electric field or the value of light intensity injected in the crystal. In both figure 4.7 and Figure 4.8, increasing the nonlinear effect yields similar behaviors, the Airy profile disappears, replaced by a refocused and centered OSS. Indeed, for a given injected light intensity and when increasing the applied external field, the output light when propagating is focused first horizontally from  $400V/cm$  to  $1200V/cm$  and secondly is focused both horizontally and vertically from  $1200V/cm$  to  $2000V/cm$ . Similarly for a given externally applied electric field of  $1200V/cm$  for example, increasing the light intensity allows focusing that was solely along the x-axis at  $1.4\mu W$  to be focusing along both x and y axis at  $6.4\mu W$ .

As explained before, the c-axis of the SBN-crystal and the applied external field are both along the x-axis, explaining the stronger horizontal focusing effect and a two step focusing dynamic. Figures 4.7 and figures 4.8 present slightly different behaviors that can be due to different factors. The main identified factor is the diffusion effect as it is unidirectional and along the horizontal c-axis. It is best observed at  $0V/cm$  and the resulting profiles coincide with what can be expected in literature [37].

The propagation behavior of the Airy beam varies significantly when varying the externally applied electric field and the Airy beam's intensity. With low intensity and applied electric field, the Airy beam profile is preserved. With medium light intensity, the Airy beam and OSS coexist and with high nonlinearity only the OSS remains. On a theoretical standpoint, observation of these dynamics and comparison between experiment and theory could improve the models of anisotropic propagation in photorefractive media. On an application standpoint, these different configurations controlled by either a voltage or light intensity show promising applications in the domain of optical interconnects and waveguide imprinting.

## 4.2 Self-bending of the OSS and time considerations

We have said in this chapter's first section that for high nonlinear effect, the soliton self-bends [118]. The Airy beam OSS shows similar behavior. When the externally applied electric field or light intensity is strong, the drift effect increases and the OSS shifts position at the output of the crystal or "bends" similarly to previous works on Gaussian solitons [118, 119].

The bending effect is not apparent in figures 4.7 and 4.8 because the bending occurs

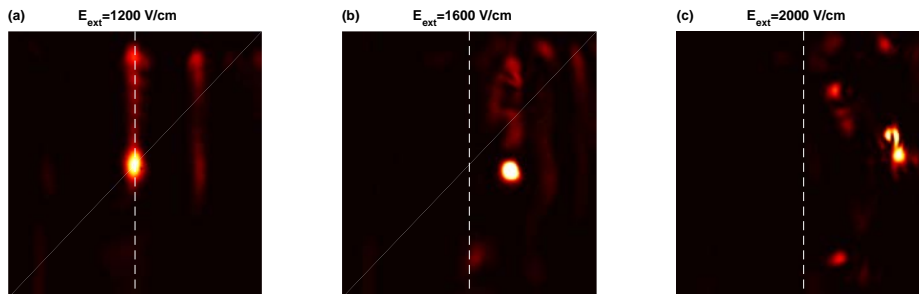


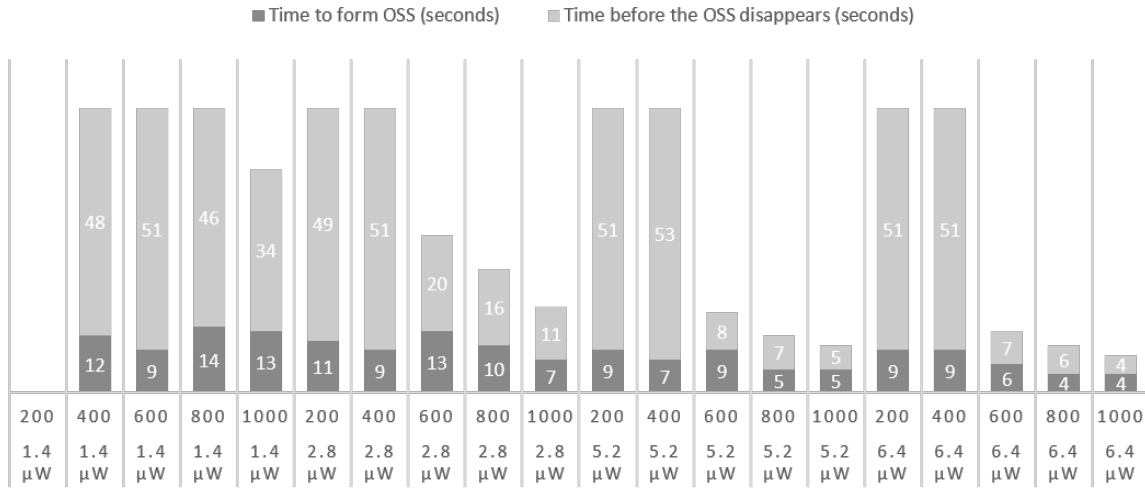
Figure 4.9: Self bending of the Airy beam OSS. Transverse intensity profiles at the output of the crystal for increasing values of externally applied electric field. Input Airy beam has an intensity of  $2.8 \mu W$ . (a)  $E_{ext} = 1200V$ , (b)  $E_{ext} = 1400V$  and (c)  $E_{ext} = 1600V$ .

after the OSS is formed, on a time scale ranging from a few dozen seconds to a few minutes. It seems that the linear Airy beam structures stabilizes the OSS because when the Airy beam profile disappears, bending occurs very suddenly at shifts superior to 2.5 beam diameters, quickly leading to overfocusing. Figure 4.9 shows the output face of the crystal after the bending occurs. The bending becomes substantial if the focusing effect has saturated in both transverse dimensions. For  $E_{ext} = 1200V/cm$  (figure 4.9(a)), the vertical focusing effect has not saturated since both the Airy profile and OSS profile coexist and the bending is unsubstantial. For  $E_{ext} = 1200V/cm$  (figure 4.9(b-c)), the vertical focusing effect has saturated and self-bending has occurred. Furthermore, the greater the applied external field the greater the self-bending effect, as expected from previous studies [118, 119]. Finally, when the self-bending effect is too strong, the OSS structure becomes compromised as can be seen in figure 4.9(c). Time measurements show that the bending is quickest when the light intensity or externally applied field is greatest.

The Airy beam OSS is unstable when the nonlinearity is too strong. When the light intensity or when the externally applied electric field increases, the Airy beam OSS moves or disappears more quickly. The histograms of figure 4.10 shows the time necessary for the formation, duration and disappearance of the OSS observed in figure 4.7. Measures are stopped after 1 min. The top set of histograms show the evolution of the OSS formation and duration versus applied electric field for different values of input Airy beam intensities, and the bottom set of histograms show the evolution of the OSS formation and duration versus input Airy beam intensities for different values of applied electric field. It appears that the variations of light intensity and applied external field play a similar role in the duration of the OSS. This is to be expected since the light intensity and the applied external field both increase the nonlinear effect. Therefore, under a certain nonlinear threshold, the OSS appears to be stable and takes at maximum 15 seconds to form. For greater values of nonlinearity the OSS is quicker to form however it is less stable and disappears also more quickly. The time response of the photorefractive crystal is proportional to light intensity, however the nonlinear behavior of propagating beams inside a photorefractive crystal depends on the ratio of the light beam intensity over the background light intensity. This means that by keeping the same ratio  $I/I_b$ , while increasing the intensity of the Airy beam  $I$  (therefore the background intensity  $I_b$  is increased as well), the same phenomenons can be observed at greater speed. We have chosen this low speed to better observe the OSS soliton but by doubling both the background intensity and the Airy beam intensity, we have been able

## 4.2. SELF-BENDING OF THE OSS AND TIME CONSIDERATIONS

### AIRY OFF-SHOOTING SOLITON FORMATION



### AIRY OFF-SHOOTING SOLITON FORMATION

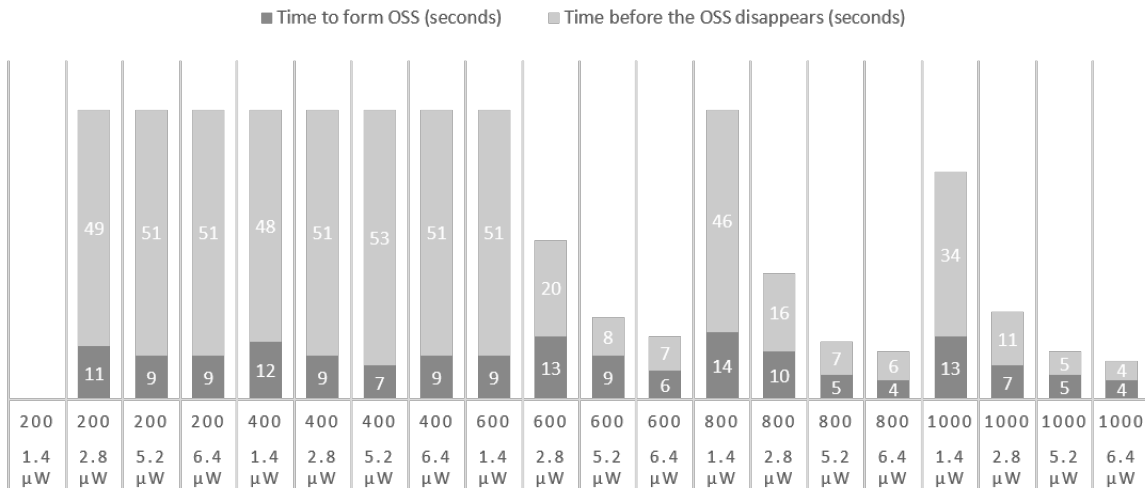


Figure 4.10: Histogram representing time formation, duration and disappearance of the OSS from fig 4.7. (Top) Evolution as a function of the applied external field for different input Airy beam power. (Bottom) Evolution as a function of the different input Airy beams for different applied external fields.

to increase the overall speed of the different propagation behaviors. In all cases with this input Airy beam profile, the instability occurs when the nonlinear effect refocuses all light into the OSS at the expense of the residual linear Airy beam. Therefore the sole OSS is the most unstable configuration and it is preferable to place oneself at the threshold of the event to maximize the OSS stability.

The aftermath is that by choosing a low ratio of beam intensity over background intensity we can maximise the OSS's stability, and by having high intensity values we can have a fast crystal response time. Finally, three configuration can be observed: lone Airy beam, residual Airy beam with OSS and lone OSS.

### 4.3 2D Airy beam propagation behavior and soliton existence curve

To further understand the dynamic of the Airy beam OSS behavior we can look at the OSS profile along the c-axis (x-axis) by plotting the full width at half maximum (FWHM) in function of maximum amplitude onto the theoretical soliton existence curve. The FWHM of the amplitude profile  $u(\xi)$  as a function of  $u_0$  is represented in figure 4.11 in red. The experimental horizontal FWHM of the Airy beam OSS and the corresponding max amplitude from Figure 4.7 are plotted as diamonds in figure 4.11. The experimental measures are scattered along the existence curve, and follow the same trend confirming the solitonic nature of the OSS. This curve is also a good indicator of the expected Airy beam OSS propagation behavior. Indeed experimental measures corresponding to  $u_0 < 1.5$  corresponds to unidimensional horizontal focussing, whereas experimental values corresponding to  $u_0 > 1.5$  correspond to two dimensional focusing. However, the experimental values far from the curve and the ones for  $u_0 > 3$  in general lead to overfocusing, strong drift effects and represent less stable OSS. Therefore, the one dimensionally focused OSS ( $u_0 < 1.5$ ) is very stable and the two dimensionally focused OSS is most stable for  $u_0$  closest to the effect's threshold ( $u_0 \approx 1.5$ ).

We were able to obtain steady state OSSs and OSBs in the case of a (1+1)D truncated Airy beam propagating in nonlinear photorefractive media in chapter 3. The (2+1)D Airy beam OSS is stable for a time (up to 34 seconds for  $E_{ext} = 2000V/cm$  and  $I = 1.4\mu W$ ) but remains transitional and it is unclear if it can be stabilized. When the Airy beam refocuses along both transverse dimensions to form an OSS, the newly formed OSS bends and shifts along the preferential c-axis. It is probable that the bending does not occur before due to the residual linear Airy beam profile. What is surprising is the relatively

### 4.3. 2D AIRY BEAM PROPAGATION BEHAVIOR AND SOLITON EXISTENCE CURVE

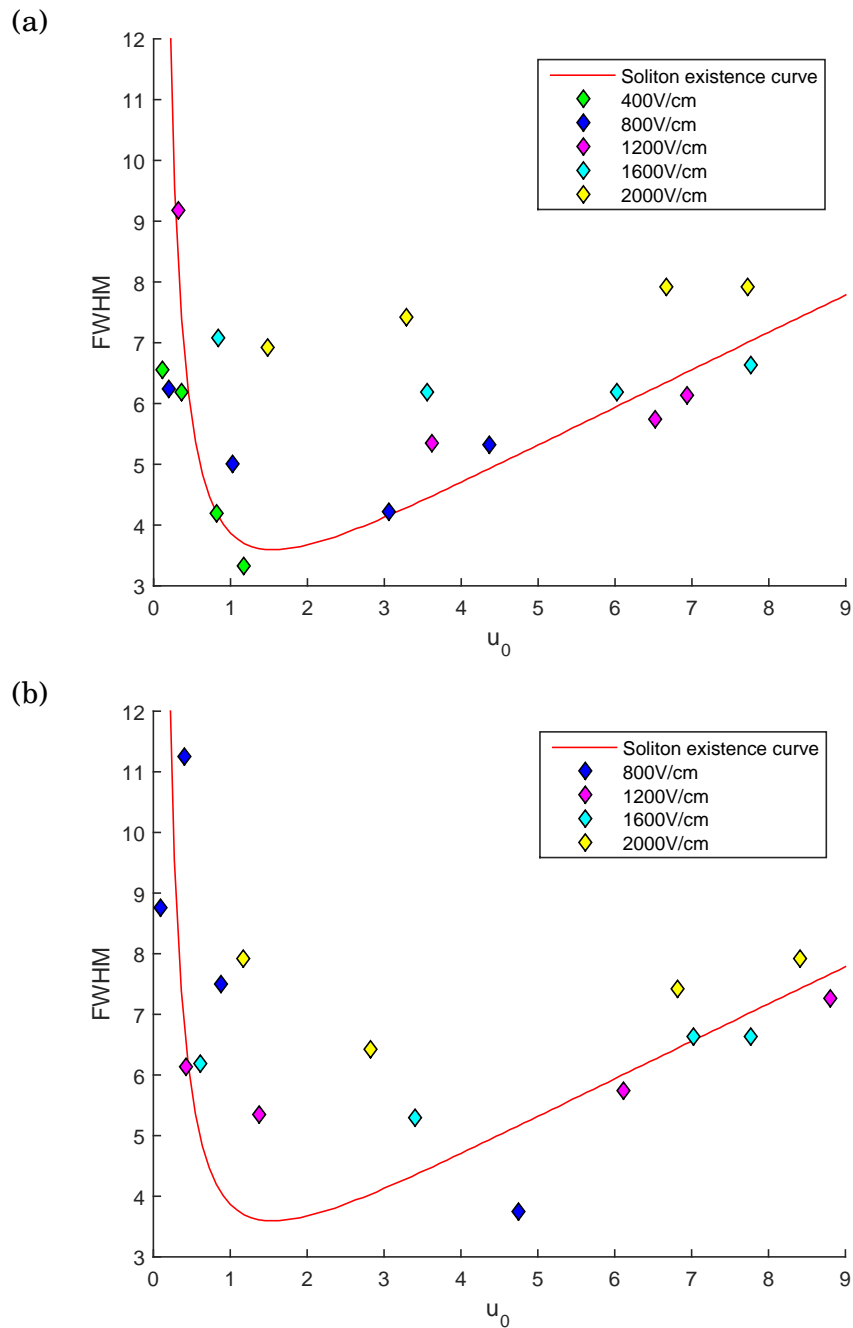


Figure 4.11: Theoretical soliton existence curve and experimental measures corresponding to Figure 4.7. (a) Airy beam of north-west acceleration. (b) Airy beam of south-east acceleration

sudden and strong bending effect that occurs after a certain nonlinear strength threshold value. The reason is that when the beam fully changes to an OSS, all the light intensity previously dispersed in the Airy beam profile refocuses into the OSS. The peak intensity of the newly formed OSS is much higher than what was previously observed causing a sudden and strong bending effect. The discontinuity of the phenomenon may not allow a stable sole (2+1)D OSS to be observed, even if the bending can be delayed by using low power beams.

## 4.4 Conclusion

We have seen in this chapter the propagation behavior of a two dimensional Airy beam in nonlinear photorefractive medium. The anisotropy of the crystal and asymmetry of the applied electric field along the c-axis of the crystal results in a two-stepped focusing dynamic. Interestingly both steps can be linked to the soliton existence curve, the first step when the soliton existence curve is decreasing and the second step when the soliton existence curve increases. This two step dynamic allows different types of propagation to take place:

- for low nonlinear strength we observe a 1D Airy beam profile at the output of the crystal,
- for medium nonlinearity, the 1D Airy beam is in competition with the OSS,
- for high nonlinearity only the OSS is observed.

It is also at higher nonlinearity that the output profile is most unstable as self-bending and over-focusing can occur. This encourages the sole OSS configuration to be obtained for the lowest but high enough nonlinearity strength possible.

The flexibility and control of the output profile using either light intensity or applied electric fields makes the use of 2D Airy beams an interesting approach in optical interconnects, enabling different waveguide configurations by controlling the nonlinear strength of the medium.

## COUNTER PROPAGATING AIRY BEAMS IN PHOTOREFRACTIVE MEDIUM

**W**e have mentioned the use of Airy beams and photorefractive media as a basis for creating optical interconnects. Leveraging the possibility to imprint waveguides in photorefractive material and multilobed, curved Airy beams to imprint them, optical interconnects are an interesting application to consider. In this chapter we will view soliton and Airy beam interactions in photorefractive media and the possible waveguides resulting from these interactions.

### 5.1 Overview of beam interactions and interconnects in photorefractive media

The photorefractive effect was discovered in 1966 by Ashkin et al. in lithium niobate ( $LiNbO_3$ ) and lithium tantalate ( $LiTaO_3$ ), where the effect was considered "optical damage". Indeed an optically-induced inhomogeneity in the refractive index was observed [47]. The degradation occurred when the beam was linearly polarized along the c-axis direction of the crystal, whereas a beam perpendicularly polarized to the c-axis undergoes conventional diffraction. The c-axis is the preferred direction of diffusion of free-charges inside the birefringent photorefractive crystal. This damage was quickly turned into an interesting electro-optic feature however, with the idea to use photorefractive crystals (PR) as storage media for optical holography suggested by Chen et al. [48]. The photoin-

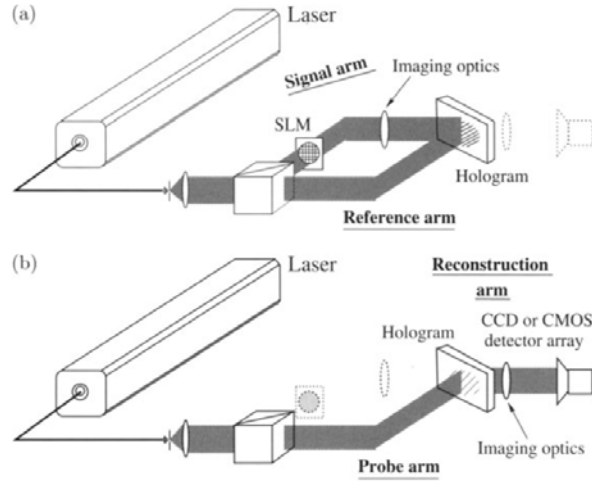


Figure 5.1: Holographic memory architecture: (a)storage arrangement; (b)retrieval arrangement. extracted from reference [120].

duced holograms are a refractive index structure written in three dimensions inside the crystal without any other form of processing. Since this physical process appears for very low optical powers ( $\mu W$ ), photorefractive media is a promising candidate for low power consumption optical information processing. Figure 5.1 shows a schematic of the experimental setup to store (a) and retrieve (b) information inside a PR crystal. In figure 5.1(a) the information is coded on a spatial light modulator (SLM). A laser beam is divided into two beams using a beam splitter. One of the two beams is modulated by the SLM and the other is the reference beam. Then, both beams illuminate the crystal and the resulting interference pattern inside the crystal will depend on the SLM mask. The interference pattern is imprinted inside the crystal by modification of the refractive index in accordance with the light interference pattern due to the Pockels effect. The resulting refractive index variation inside the crystal is referred to as the *hologram*. In figure 5.1(b) the reference beam illuminates the PR crystal and is diffracted by the hologram inside the crystal. After diffraction, the wave-front of the reference beam is that the initial mask image on the SLM, the information has been retrieved. The read and write functions must be operated with the same reference beam in terms of wavelength and angle of incidence. Using different reference beams, multiple images can be stored in the same crystal.

Besides volume holographic data storage [120], PR crystals have been used in applications such as optical amplifiers [121], phase conjugation [122], or the trapping of dielectric particles with light-induced space-charge fields [123]. The ability to imprint and sometimes rewrite information in photorefractive media have made it ideal for

## 5.1. OVERVIEW OF BEAM INTERACTIONS AND INTERCONNECTS IN PHOTOREFRACTIVE MEDIA

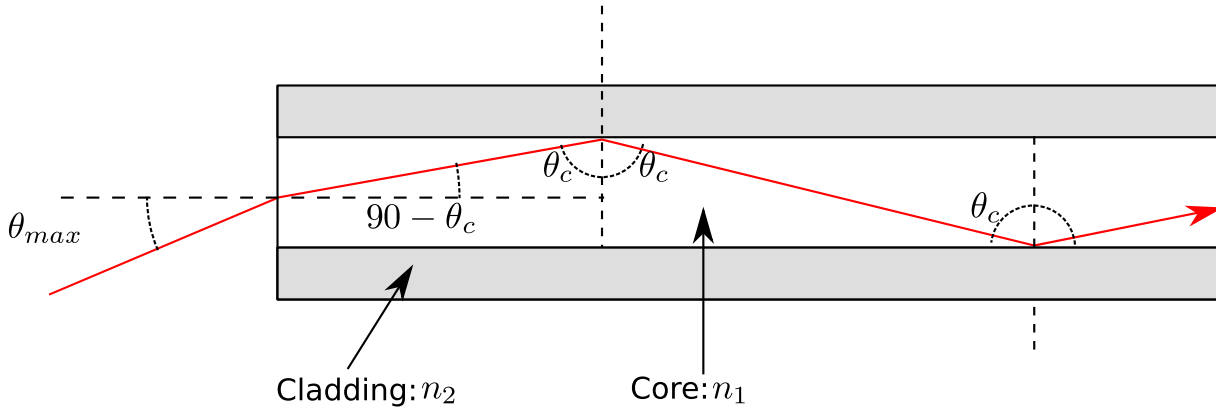


Figure 5.2: Schematic of waveguiding inside an optical fiber. The core refractive index  $n_1$  is greater than the cladding refractive index  $n_2$  causing total internal reflection.

all-optical processing and computing applications; such as neural networks [124] and optical interconnects [9, 11].

We have seen in previous chapters that the natural diffraction of light beams in PR crystals can be compensated by self-induced nonlinear focusing effects when an external bias electric field is applied to the crystal, leading to the propagation of spatial solitons. This is of particular interest for optical interconnects as the soliton creates a waveguide that shares the same properties as the soliton in particular an unchanging profile along propagation [49]. Due to the Pockels effect, the refractive index inside the crystal is proportional to the light intensity quasi-locally. The soliton beam will create a tube of high refractive index contained in lower refractive index that will act as a waveguide similarly to that of an optical fiber shown in figure 5.2. The figure 5.2 shows a beam propagating inside the core of an optical fiber of refractive index  $n_1$ . The core is contained inside a cladding of refractive index  $n_2$ . When reaching the wall separating the core from the cladding, total internal reflection is possible for grazing incidence angles because  $n_1 > n_2$ . The photo-induced waveguides created by beams inside photorefractive medium work similarly to fiber optics. Due to the Pockels effect, a refractive index gradient localized in the lighted region contains the light in those lighted areas.

Furthermore, since photorefractive solitons are very robust and are formed using very low laser power, they are ideal to explore soliton physics and its applications [89].

Originally, the name soliton comes from the particle-like nature of the propagating beam. The optics-particle equivalence possible led to the study of soliton collisions [23]. The interaction of colliding solitons appear to be very similar to that of particles. They can repel or attract each other in function of the distance separating them or their

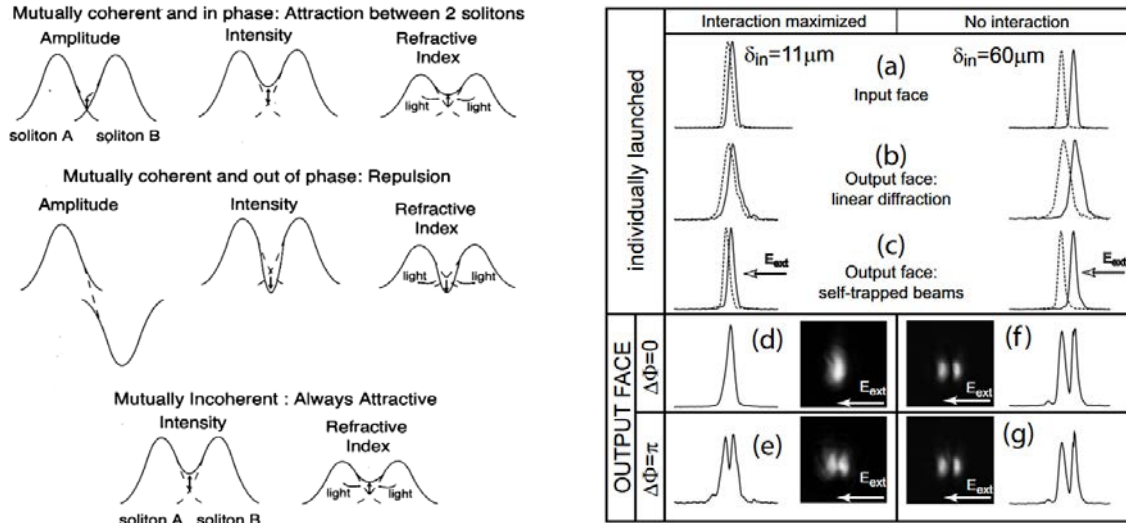


Figure 5.3: (Left) Schematic of the refractive index spatial distribution for a collision between in-phase and out-of-phase coherent spatial solitons or incoherent spatial solitons. Extracted from reference [127]. (Right) Experimental profiles along the c-axis typical of the interaction process. (d) and (f): output for in-phase solitons. (e) and (g): output for out-of phase solitons. (d-e) proximity of propagating solitons allow interaction. (f-g) distance between propagating solitons prevent interaction. Extracted from reference [9].

phase-matching and size [27, 125, 126]. Theoretical and experimental studies have been done in different types of nonlinear media, particularly in photorefractive media, where different interactions have been observed [9, 30, 127].

The schematics of figure 5.3(Left) show three different types of interaction. For coherent beams, the two solitons relative phase is of importance. The schematic illustrates the in-phase and out-of-phase cases. The third case depicted is for two incoherent solitons. For coherent solitons, in-phase solitons will attract each other whereas out-of phase solitons will repulse each other. The difference is due to the constructive (respectively destructive) interference that increases (respectively decreases) the light intensity between the solitons and the resulting refractive index change inside the nonlinear media. A positive (respectively negative) refractive index change between the soliton beams will attract (respectively repel) light and therefore attract (respectively repel) the solitons. In the incoherent case, there is no interference and the intensities always add up resulting in a positive refractive index change systematically and an attractive interaction.

Experimental results are shown on figure 5.3(Right). Two parallel coherent Gaussian beams are launched in a PR (semiconductor InP:Fe). They propagate along the same direction, and have identical waists of  $25 \mu m$ . When no externally applied electric field is applied, both beams diffract (b), however when a bias electric field is applied the beams

self-trap and a soliton propagation is observed. With sufficient proximity of the two propagating solitons (first column), attraction (respectively repulsion) can be observed for in-phase (respectively out-of-phase) solitons. If the distance between the solitons is too great ( $\approx$  four diameter size) no interaction takes place (second column). This example illustrates the diverse particle-like interactions that can be observed with photorefractive soliton collisions. These interactions can help create more waveguiding possibilities inside photorefractive materials such as y junctions when two distinct solitons attract and fuse into one beam [128].

Additionally, the photorefractive effect inside a given crystal is optimal for a precise combination of parameters such as the wavelength of the optical beam. In the case of the SBN crystal used in our experiments, the photorefractive effect is optimal for a wavelength  $\lambda$  of 532 nm. At this wavelength, nonlinear self-focusing solitonic effects can be observed and induced waveguiding structures created. At another wavelength, for example infrared at  $\lambda = 1.55 \mu\text{m}$ , the crystal's response is quasi-linear and there is no change in the refractive index structure. The different sensitivity response of the crystal to wavelengths enables a low power soliton beam at  $\lambda = 532 \text{ nm}$  to induce a waveguiding structure that a high power probe beam at  $\lambda = 1.55 \mu\text{m}$  will use to propagate [49, 128, 129]. This also permits directional couplers to be created by adapting the distance between two non-interacting solitons with the wavelength of a secondary propagating probe beam [130]. Therefore, photorefractive solitons appear as an ideal candidate for waveguiding applications.

Instead of using Gaussian soliton beams to imprint waveguides in photorefractive medium, other non-conventional beams such as Airy beams can be used. The waveguiding structure can then present interesting properties of the Airy beam, such as a multilobed structure or a curved trajectory. In 2013, Airy beams were presented as a possibility for optical routing [38]. The Airy beam's main lobe was used as the waveguiding structure and different output position were obtained by varying the Airy beam's acceleration. Figure 5.4(Left) shows the waveguiding structure from the experiment in reference [38]. Figure 5.4(Right) shows the guided probe beam for different routing configuration. Figure 5.4(Left)(a) shows the input beam and Figure 5.4(Left)(b) the 16 designated output positions. Figures 5.4(Left)(c-f) shows the output of the crystal for different accelerating Airy beams. Each Airy beam of different accelerating will correspond to a different waveguiding configuration. The Airy beam with the least (c) (respectively most (f)) acceleration will create a waveguiding structure with an output closest (respectively farthest) from the center of the output face. Figure 5.4(Right)(a)

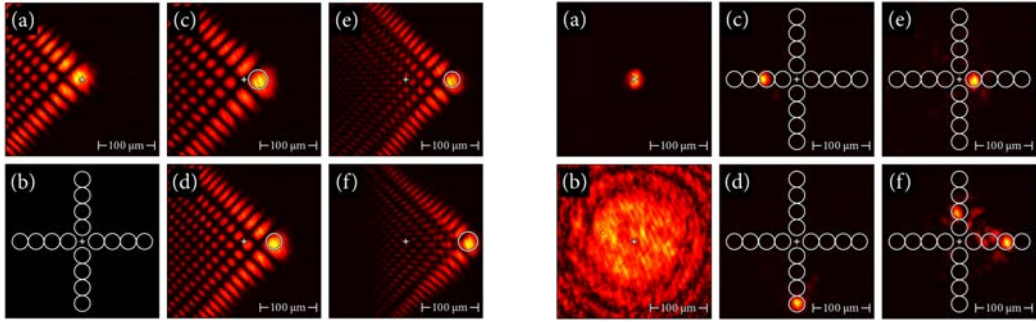


Figure 5.4: (Left) Output scheme of the Airy beam induced optical router. (a) Input position of the Airy beam at the front face of the crystal, (b) schematic array of 16 output channels given by four  $90^\circ$  beam rotations and four different accelerations. Each, (c), (d), (e), (f) output position of the Airy beam at the back face of the crystal for different accelerations. (Right) Airy beam induced optical routing. (a) Gaussian input beam at the front face of the crystal, (b) diffracted Gaussian output at the back face of the crystal without induced refractive index structure, (c), (d), (e) guided output for different selected channels, (f) optically induced splitter with multiple selected outputs. Extracted from reference [38]

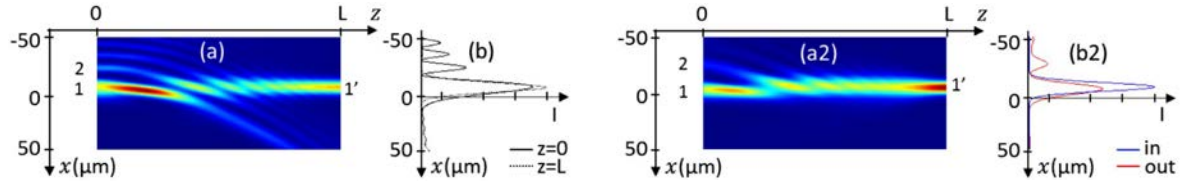


Figure 5.5: (Left) (a) Normalized intensity distribution of a self-focused Airy beam propagating in a PR and (b) corresponding transverse intensity profiles. (a2) Intensity distribution of linear probe beam propagation in the waveguide structure and (b2) transverse profiles of Gaussian beam guided along  $(1') \rightarrow (1, 2)$ . Extracted from reference [11]

shows the input Gaussian beam and figure 5.4(Right)(b) the diffracted Gaussian beam without any waveguiding structure. Figures 5.4(Right)(c-f) shows the output position of the Gaussian probe beam for different waveguiding structures. Figure 5.4(Right)(f) shows an optically induced splitter obtained by switching between two waveguiding configurations at a quicker speed than the response time of the crystal thus enabling two or more waveguiding structures to superimpose themselves. These results show that Airy beams can be used in all-optical routing setups and enable multiple channel configurations.

We have seen in previous chapters that the Airy beam in nonlinear media under strong focusing conditions sheds an off-shooting soliton (OSS). The coexistence of an OSS with a residual Airy beam can enable more complex waveguiding possibilities

## 5.1. OVERVIEW OF BEAM INTERACTIONS AND INTERCONNECTS IN PHOTOREFRACTIVE MEDIA

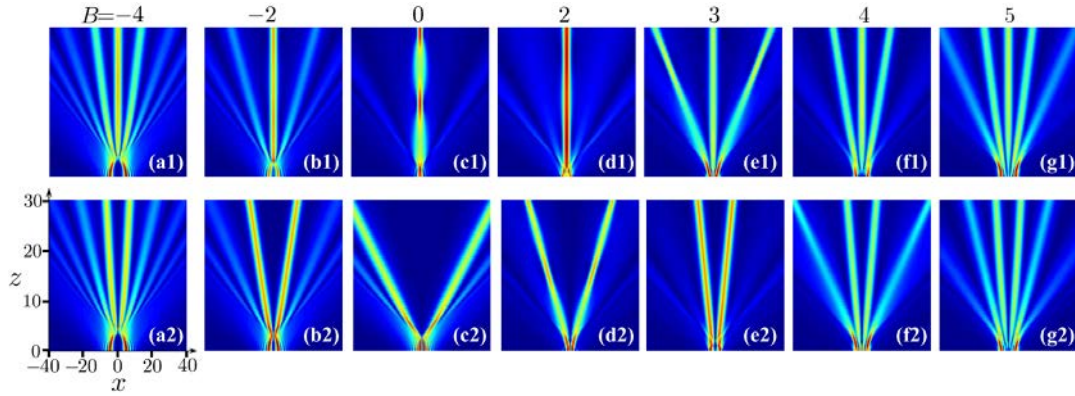


Figure 5.6: Interactions of two in-phase ((a1)-(g1)) and out-of-phase ((a2)-(g2)) Airy beams in saturable medium.  $B$  is the transverse position shift of each beam. Extracted from reference [101].

without having to switch between different input Airy beams. An Airy beam with a given acceleration can present properties of optical splitters as can be seen in figure 5.5. The induced waveguiding structure is shown in figure 5.5(a). The linear Airy beam propagation coexists with the OSS structure leading to a complex waveguide structure that presents different input/output possibilities. These input/output possibilities are numbered 1, 2 and 1' and correspond respectively to the input Airy beam's main lobe, the input Airy beam's secondary lobe and the Airy beam's output OSS. Figure 5.5(a2) shows the propagation behavior of a Gaussian probe beam injected in position 1', the Airy beam's OSS. The probe beam propagates from right to left. The main output of the probe beam is the position 1, but a secondary output in position 2 is also observed. This configuration is similar to that of an optical splitter without the use of a secondary beam revealing more waveguiding possibilities that Airy beams in nonlinear media withholds.

Additionally, by using multiple propagating Airy beams in nonlinear media the possible waveguiding structures are increased and more complex. Co-propagating Airy beams and their interactions have been studied in different medias ranging from nematic liquid crystals [131] to photonic lattices [132] or three-wave systems [133]. Similarly to solitons, in Kerr or photorefractive media, the solitonic structures of two co-propagating coherent Airy beams will exhibit attraction when in-phase and repulsion when out-of-phase [39, 101, 134] whereas two incoherent Airy beams will always exhibit attraction [135].

Figure 5.6 shows the propagation behavior of two co-propagating Airy beams in saturable nonlinear media such as photorefractive media. The first line corresponds to two in-phase Airy beam propagating and the second line corresponds to the out-of-phase

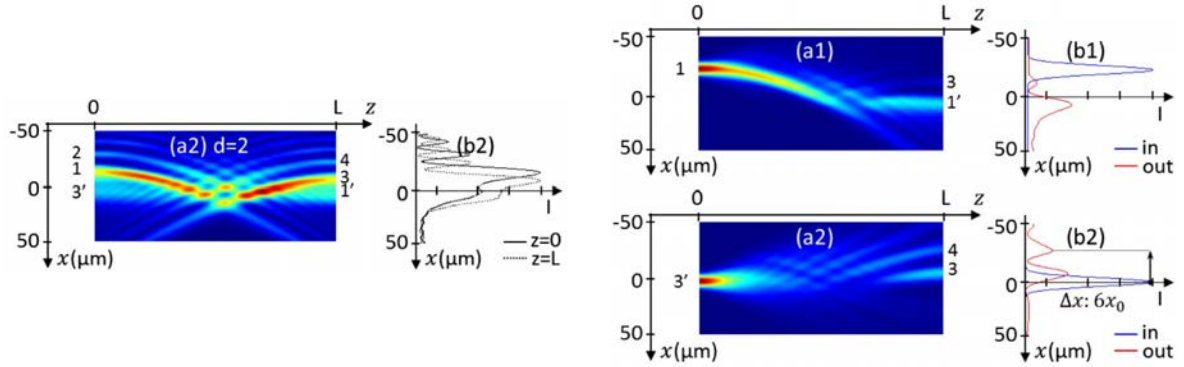


Figure 5.7: (Left) (a2) Normalized intensity distribution inside a  $L=1$  cm PR resulting of the interaction of self-focused counterpropagating Airy beams,  $d$  is the transverse shift between the forward propagating Airy beam and the backward propagating beam. (b2) corresponding transverse intensity profile. (Right) Linear probe beam propagating in the waveguide structure (a1) intensity distribution and (b1) transverse profiles of a Gaussian beam guided along  $1 \rightarrow (1', 3)$ , (a2)-(b2) guided along  $3' \rightarrow (3, 4)$ . Extracted from reference [11]

configuration. The greater the shift between the two input Airy beams ( $|B|$ ), the greater the number of off-shooting beams (OSB): up to three (respectively four) for the in-phase (respectively out-of-phase) configuration and  $|B| = 4$ . When the two Airy beams are in-phase (respectively out-of-phase) the number of OSB is uneven (respectively even).

Other research on the propagation dynamics have shown that by using linear external potentials or harmonic potentials to weaken or strengthen the self-focusing effect, the accelerating trajectory of Airy beam like structures can be further controlled [100, 136]. The interaction of co-propagating Airy beams and solitons in nonlinear media can even reproduce gravitational dynamics [137].

Similarly to studies with two co-propagating Airy beams, two counterpropagating Airy beams in a saturable nonlinear media will shed off-shooting solitons given enough nonlinearity strength [11], furthermore the off-shooting solitons tend to be attracted by the lobes of the counterpropagating Airy beam [40]. However, by contrast to studies with two co-propagating Airy beams, a counterpropagating configuration combined with the large transverse dimension of the Airy shape and their curved trajectory allow several interaction schemes where one or several lobes of the two counterpropagating beams can overlap over relatively short propagation distances [11, 40, 41]. The interaction of such counterpropagating Airy beams introduce new dynamics and open new interesting fields for optical interconnections. Figure 5.7(Left) shows a waveguide constructed by two contra-propagating beams of symmetrical configuration in nonlinear self-focusing condi-

## 5.1. OVERVIEW OF BEAM INTERACTIONS AND INTERCONNECTS IN PHOTOREFRACTIVE MEDIA

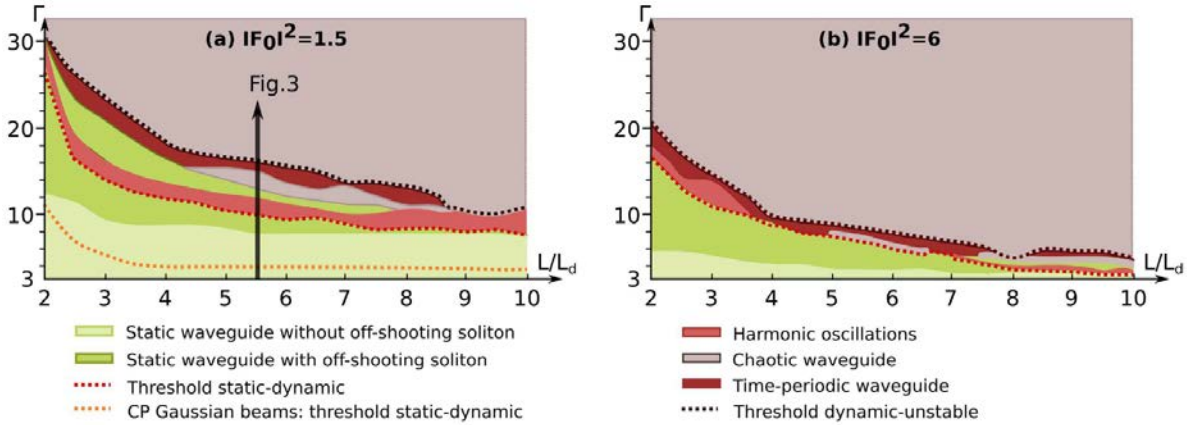


Figure 5.8: Typical dynamical behavior of counterpropagating Airy beams in the parameter plane (nonlinear strength  $\Gamma$ , crystal length  $L$ ): (a) with low input intensities (b) with higher input intensities.

tions. Figure 5.7(Right) shows the propagating Gaussian probe beam for two possible inputs: the Airy beam's main lobe (1) and the Airy beam's OSS (3'). The second case is of particular interest as it allows an output to input shift of 6 beam waist over a relatively short propagation distance of  $L=1\text{cm}$  which is greater than one can be achieved using Gaussian beams and solitons. Using two counterpropagating Airy beams allows multiple input to output waveguiding possibilities with greater shifts than using conventional Gaussian beams. Furthermore, strong nonlinear strength inside the crystal can cause dynamical interactions of the two counterpropagating beams. Figure 5.8 shows the type of interactions between two counterpropagating Airy beams in symmetric configuration. For low nonlinear values, both beams act as a static waveguide with no OSS, when the nonlinearity is increased, the Airy beams form OSS enabling more complex waveguiding structure, finally when the nonlinear strength is increased greatly, the interactions are dynamic. In the case of dynamic interactions, the waveguiding structure can evolve in a harmonic fashion or chaotic fashion. This is of particular interest for optical logic gates, clocks or chaos-based computing.

Interestingly, both multiplexing (combining light beams in a single waveguide) and demultiplexing (splitting light beams in different waveguides) can be achieved by using Airy beams. Moreover, waveguiding with a greater output-to-input transverse shift can be obtained by using Airy beams rather than with conventional Gaussian beams. Waveguiding possibilities in the case of counterpropagating Airy beams have been studied in a symmetric configuration [11]. In this chapter we focus on an antisymmetric configuration of two contra-propagating incoherent Airy beams.

## 5.2 Numerical Antisymmetric Airy beam propagation in nonlinear self-focusing conditions

In this section we analyze numerically optical waveguiding structures created in photorefractive media by the interactions of two incoherent counterpropagating 1-D Airy beams under nonlinear self-focusing conditions. Similarly to holograms, a waveguide is imprinted inside the crystal so that a conventional Gaussian beam can then be guided to predetermined outputs. In order to create complex waveguides we chose to propagate the Airy beams antisymmetrically i.e. with each Airy beam accelerating towards the counterpropagating beam. This allows a larger overlapping of the Airy beams' secondary lobes than in the symmetric configuration shown in figure 5.7. The overlapping lobes are non-coherent and their mutual intensities therefore add up resulting in a stronger Pockels effect and stronger waveguiding structures. Furthermore, these waveguiding structures have multiple input to multiple output possibilities and transverse input-to-output shifts up to 13 times the guided beam's waist.

### 5.2.1 Antisymmetric Airy beams interactions scheme

The typical scheme of antisymmetric Airy beams is presented in figure 5.9(a). Both beams propagate in a PR crystal along the  $z$ -axis. The forward beam  $F$  propagates from left to right and the backward beam  $B$  propagates from right to left.  $d$  is defined as the shift along the  $x$ -axis between the forward and backward Airy beam's main lobes upon injection at each side of the crystal.  $L$  is the length of the PR crystal. The  $x$ -axis is normalized by  $x_0 = 10\mu m$  i.e. the Airy beam's main lobe waist at  $1/e$  of its maximum intensity. The  $z$ -axis is normalized by the diffraction length  $L_d = 4\pi n_e x_0^2 / \lambda = 5.4mm$ , with  $n_e$  the unperturbed extraordinary refractive index and  $\lambda$  the wavelength. The electric field is applied along the  $c$ -axis, parallel to the  $x$ -axis: this concerns nonlinear self-focusing conditions. The figure 5.9(b-c-d) show the intensity distribution of two counterpropagating antisymmetrical Airy beams in linear conditions for different values of shift  $d$ . In a PR crystal due to the Pockels effect, the intensity distribution induces optically a refractive index distribution which can also be seen as a waveguiding structure. In the case  $d = 1$ , the secondary lobes of the Airy beams greatly overlap resulting in a larger total intensity all along the secondary lobes' trajectory through the crystal and therefore corresponding to stronger variations of the refractive index. The greater the

5.2. NUMERICAL ANTISYMMETRIC AIRY BEAM PROPAGATION IN NONLINEAR SELF-FOCUSING CONDITIONS

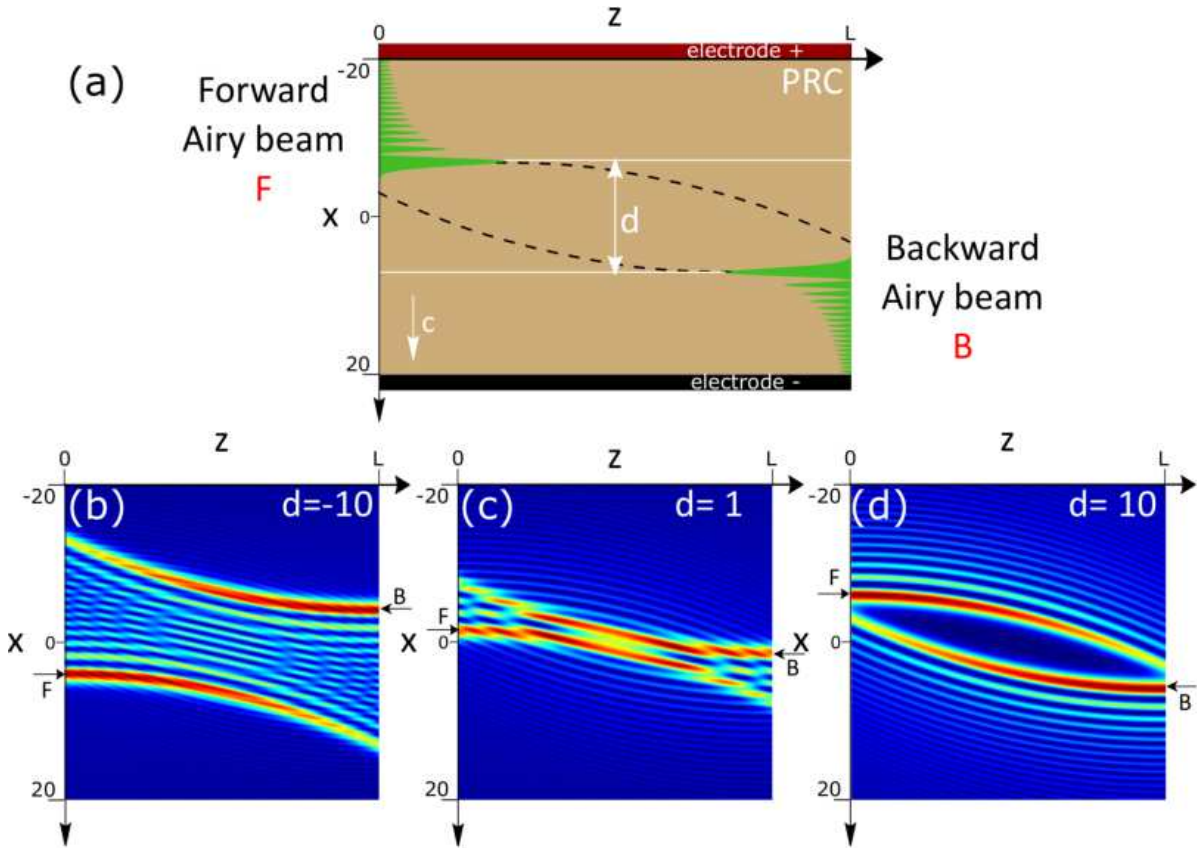


Figure 5.9: (a) Typical scheme of antisymmetric Airy beams' interaction in a PR crystal of length  $L$ . (b-c-d) Intensity distribution obtained for different values of shift  $d = -10$ ,  $d = 1$ ,  $d = 10$ . ( $F_0^2 = B_0^2 = 35$ ,  $x_0 = 10\mu m$ ,  $a = 0.03$ ,  $L = 3 = 1.63cm$ .)

index variation, the better the waveguide. In the case  $d = -10$ , the secondary lobes weakly overlap and the resulting intensity creates weaker waveguiding structures. In the case  $d = 10$ , the copropagating Airy beams don't overlap and do not make use of their interaction. In what follows, we will mainly focus on the configuration  $d = 1$  which allows strong, numerous and complex waveguiding structures to appear.

The truncated Airy beams' input profiles are given by the following equations:

$$(5.1) \quad F(x, z = 0) = F_0 Ai\left(x + \frac{d}{2}\right) \exp\left(a\left(x + \frac{d}{2}\right)\right)$$

$$(5.2) \quad B(x, z = L) = B_0 Ai\left(-x - \frac{d}{2}\right) \exp\left(a\left(-x - \frac{d}{2}\right)\right)$$

where  $F_0$  (respectively  $B_0$ ) is the wave amplitude,  $Ai$  is the Airy function,  $a$  the truncation parameter of the Airy beam.

To simulate the behavior of the propagation of the antisymmetric Airy beams, we use the same theoretical model as in chapter 2 and references [11, 40, 41, 99, 102]. The nonlinear propagation of the two incoherent counterpropagating beams can be expressed as follows:

$$(5.3) \quad i\partial_z F + \partial_x^2 F = \Gamma E_0 F$$

$$(5.4) \quad -i\partial_z B + \partial_x^2 B = \Gamma E_0 B$$

where  $\Gamma = (kn_{ex_0})^2 r_{eff} E_{ext}$  is the nonlinear photorefractive coupling strength,  $r_{eff}$  is the effective component of the electro-optic tensor and  $E_{ext}$  is the external electric field.  $E_0$  is the homogeneous part of the x-component of the photorefractive space-charge field normalized by the external electric field. The temporal evolution of the space-charge field  $E_0$  is considered with a saturable nonlinearity and calculated using a relaxation-type dynamic:

$$(5.5) \quad \tau \partial_t E_0 + E_0 = -\frac{I}{1+I}$$

where the relaxation time of the crystal  $\tau$  is inversely proportional to the total intensity  $\tau = \frac{\tau_0}{1+I}$ , and  $I = |F|^2 + |B|^2$  is the intensity normalized by the effective background intensity.

For small values of  $\Gamma$  ( $< 7$ ), the nonlinear effect is not high enough for producing waveguiding structures; when  $\Gamma > 15$  unstable dynamics are observed [11]. In what follows we present numerical simulations with a nonlinear photorefractive coupling strength  $\Gamma = 9$  which allows the analysis of rich and complex stable waveguiding structures

## 5.2.2 Optical interconnections for a transverse shift $d=1$

In what follows, we focus on the configuration  $d = 1$  and  $\Gamma = 9$  because it has a rich variety of complex and interesting waveguiding structures. We are interested in the number of different outputs for a single input and in the transverse input-to-output shift of the waveguide.

Figure 5.10 shows the intensity distribution of two counterpropagating antisymmetrical Airy beams in non-linear self-focusing conditions for  $d = 1$  and  $\Gamma = 9$ . When the nonlinear self focusing effect compensates the diffractive nature of a light beam, a soliton-like structure appears [99]. The self focusing creates two new waveguiding structures of interest, an off-shooting beam (OSB) and an off-shooting soliton (OSS). The waveguiding structure shows different possible inputs, the OSB and OSS positions

5.2. NUMERICAL ANTISYMMETRIC AIRY BEAM PROPAGATION IN NONLINEAR SELF-FOCUSING CONDITIONS

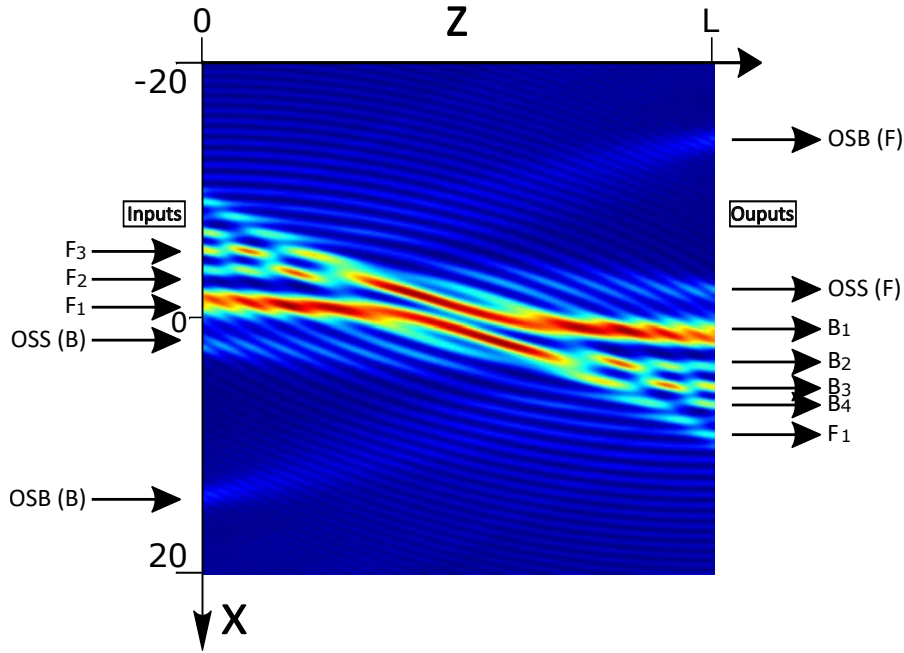


Figure 5.10: Intensity distribution of two counterpropagating antisymmetrical Airy beams in non-linear self-focusing conditions with  $d = 1$ ,  $\Gamma = 9$ ,  $F_0^2 = B_0^2 = 35$ ,  $L = 3 = 1.63cm$ .

created by the backward Airy beam propagation,  $F_1$  the forward Airy beams main lobe position,  $F_2$  and  $F_3$  the forward Airy beams secondary lobes position respectively. The waveguiding structure also shows different possible outputs, the OSB position and OSS position created by the forward Airy beam  $F$ ,  $B_1$  the backward Airy beam's main lobe position,  $B_2$ ,  $B_3$  and  $B_4$  the backward Airy beam's secondary lobes positions respectively, and finally  $F_1$  the forward Airy beam's main lobe position after propagating through the crystal. The forward Airy beam's secondary lobes positions after propagating through the crystal are superimposed with the backward Airy beam's secondary lobe positions.

In order to analyze this waveguiding structure, we propagate a Gaussian probe beam (of waist  $x_0 = 10\mu m$ ) at different input positions of our crystal. The Gaussian probe beam's amplitude represents 10% of the Airy beam's amplitude in order for it's propagation to be considered linear. Figures 5.11(a-e) show the Gaussian beam's propagation in the waveguiding structure. The arrows at the left show the input probe beam's position and the arrows at the right show the output beam's positions. Figures 5.11(f-j) plot the corresponding intensity and position of the input Gaussian beam (dotted line) and the resulting output beams transverse profile (solid line). It is worth mentioning that an output with less than 10% of the amplitude of the input beam is not of interest for

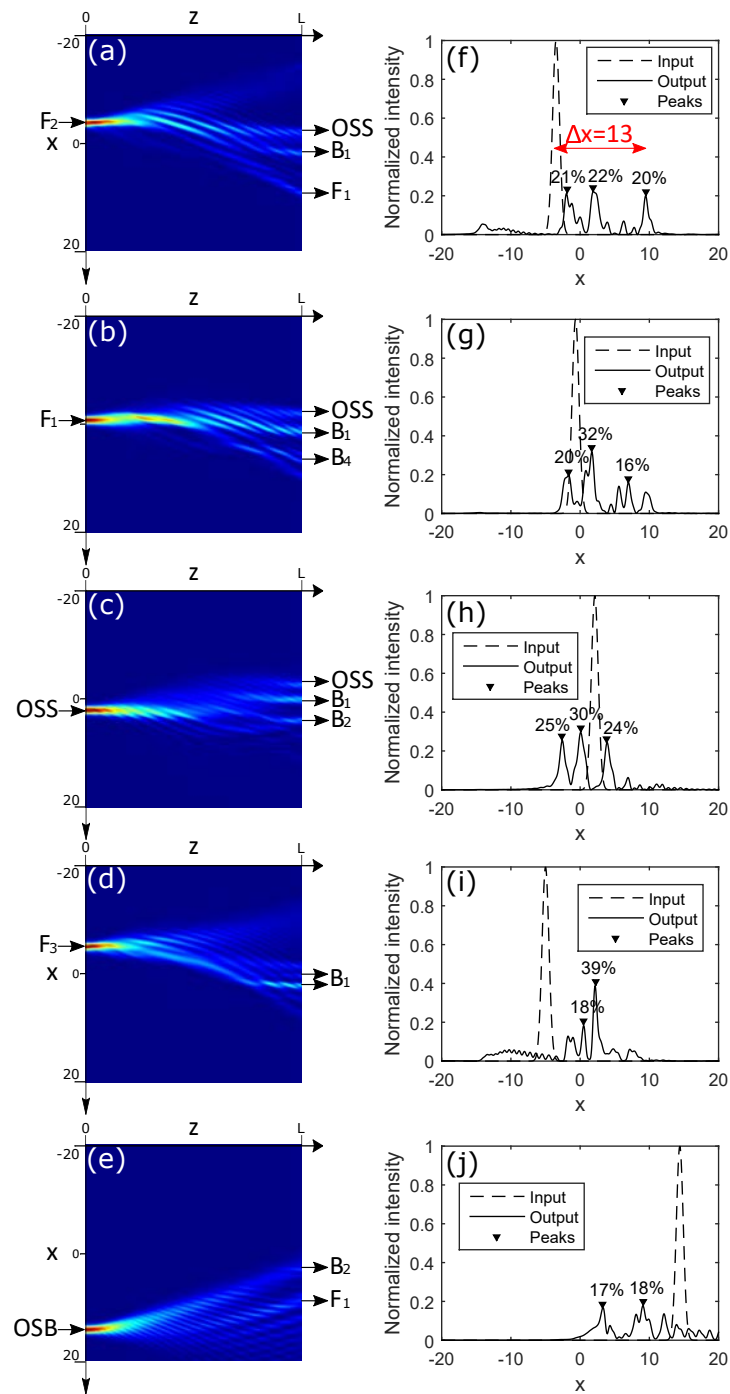


Figure 5.11: Linear probe beam propagation in the waveguide structure of figure 5.10 ( $d = 1$ ,  $\Gamma = 9$ ,  $F_0^2 = B_0^2 = 35$ ,  $L = 33 = 1.63\text{cm}$ .) (a-e) Intensity distribution. (f-j) Transverse intensity profiles of a Gaussian beam guided from different input positions ( $F_2$ ,  $F_1$ , OSS,  $F_3$ , OSB) respectively.

optical interconnects applications. We therefore decided to take into account only the output peaks that are over 15% of the input probe beam's maximum intensity. Some guiding behaviors were already predicted in previous studies of our group in the case of the symmetric Airy beam configuration [11]. By comparison, in this antisymmetrical configuration, we observe a larger number of outputs for all cases. In figure 5.11(a), for a probe beam injected in  $F_2$  we observe simultaneously three outputs (OSS,  $B_1$  and  $F_1$ ) of equal peak intensity (around 20%). The OSS output is an expected output as it is observed even when the waveguide is obtained by injecting a single forward Airy beam [11]. However the two additional outputs called  $B_1$  and  $F_1$  are only obtained because of the interaction with the backward beam and thanks to the antisymmetric configuration. For the symmetric counterpropagating beams interaction, the configuration with  $F_2$  as an input did not yield interesting waveguiding. Similarly in figures 5.11(b-c), injecting in  $F_1$  (respectively in the OSS) yields the expected OSS and  $B_1$  outputs but we also observe an additional  $B_4$  (respectively  $B_2$ ) output. Other inputs give interesting results:  $F_3$  and OSB [figure 5.11(d-e)]. We obtain for both cases two outputs, for the first case in the  $B_1$  area and for the second case in  $B_2$  and  $F_1$  positions. The fact that these inputs did not give any outputs in the previous study [11] shows the effectiveness of overlapping antisymmetric secondary lobes.

The resulting photoinduced waveguiding structure yields more possibilities than what can be observed with counterpropagating Gaussian beams and even with Airy beams in a symmetrical configuration. The resulting waveguiding structure shows interesting features: we observe new optical interconnection schemes such as one input to three outputs with input-output shifts up to  $13x_0$  [figure 5.11(a)] (Shifts of only  $6x_0$  were observed for symmetrically counterpropagating Airy beams [11]).

During our investigation we also found other interesting waveguiding possibilities when the probe beam is not injected in one of the inputs mentioned in figure 5.10 but in between them. In doing so, other configurations are obtained by a coupling of evanescent waves at the different input positions and they are reported in figure 5.12. By injecting the probe beam between  $F_1$  and  $F_2$  [figure 5.12(a)] we combine outputs of the two cases presented in figure 5.11(a-b) ( $B_1$ ,  $B_4$  and  $F_1$ ) while suppressing others (OSS). Similarly by injecting between the OSS and  $F_1$  [figure 5.12(c)], we combine two outputs (OSS and  $B_2$ ) but lose two outputs ( $B_1$  and  $B_4$ ). In figure 5.12(b), by placing the probe beam at the top of guide  $F_1$  we can suppress the topmost output (OSS) while preserving the lobe outputs ( $B_1$  and  $B_4$ ). In figure 5.12(d) by placing the probe beam below the OSS input, we suppress the bottom most outputs ( $B_1$  and  $B_2$ ) and preserve the OSS output. The

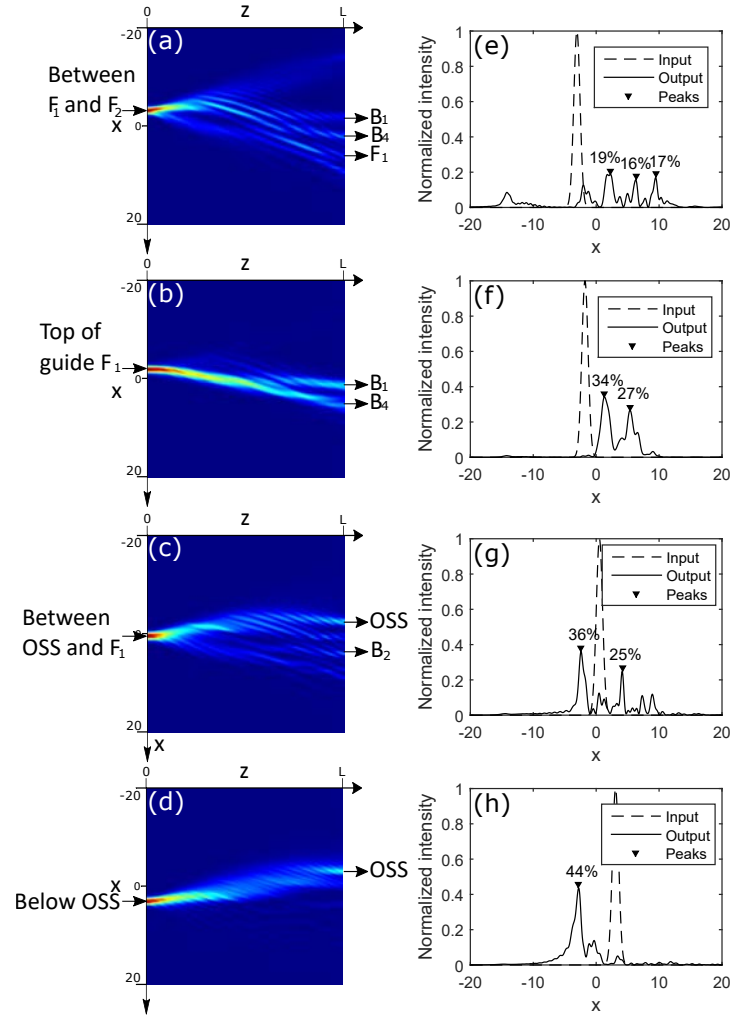


Figure 5.12: Linear probe beam propagation in the waveguide structure of figure 5.10 ( $d = 1$ ,  $\Gamma = 9$ ,  $F_0^2 = B_0^2 = 35$ ,  $L = 3$ )

sensitivity of the waveguiding structure to the input position must be sufficient to allow different outputs for different input positions, however excessive sensitivity to input positions makes the waveguiding configurations difficult to implement, especially for experimental realizations.

The mechanics in Airy beam interactions we have seen in this section can lead to the engineering of complex modular optical waveguides. By varying different parameters such as the shift  $d$  between the beams, the nonlinearity of the medium and the size of the probe beam or its angle of insertion, many more configurations can be obtained. The waveguides using (2+1)D Airy beams could yield another set of possible waveguiding configurations. Finally, similarly to what was done in reference [38] to create an optical splitter, we can imagine switching between different waveguide configurations

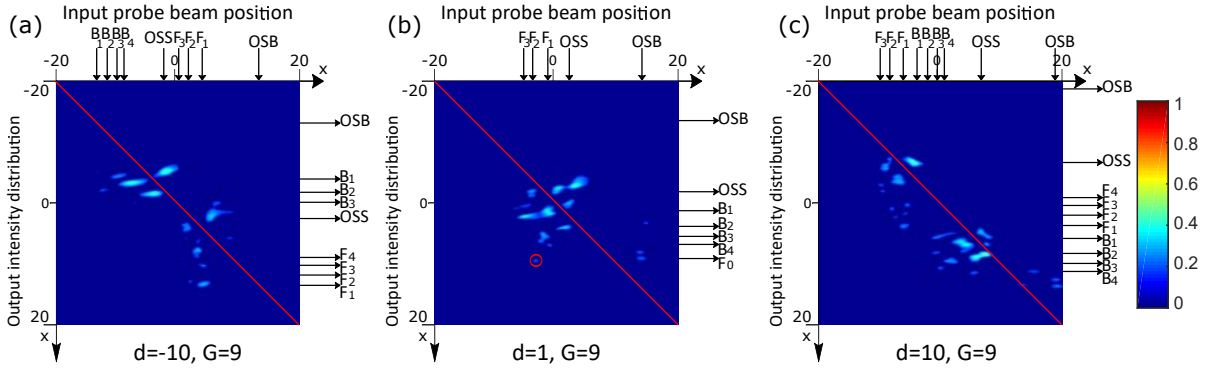


Figure 5.13: Intensity distribution of the probe beam at the output of the PR crystal for different input positions of the probe beam. ( $\Gamma = 9$ ,  $F_0^2 = B_0^2 = 35$ ,  $L = 3$ ). (a) Shift  $d = -10$ . (b) Shift  $d = 1$ . (c) Shift  $d = 10$ .

at a speed greater than the time response of the crystal. This would superimpose the different waveguiding structures and further increase the number of possible waveguide configuration.

### 5.3 Stability of the photoinduced waveguides to input positions

In order to get an overall picture of the different waveguiding possibilities for a given configuration, we want to be able to show all outputs for each possible input probe beams. To do so we scan the entry face of the waveguide and store the output face intensity profile for each input position. By juxtaposing these output profiles we create an image showing the waveguide configurations for every possible entry point. This allows among other things to see if a waveguiding configurations are sensitive to the probe beam's input position. We have plotted a mapping of the output intensity distribution versus different input probe beam positions (figure 5.13). For each input probe beam position, going from  $-20x_0$  to  $20x_0$ , we juxtapose all the output intensity distributions. The arrows on the top of the image show the position of the different entry points of the imprinted waveguiding structure. The arrows on the right of each image shows the position of the outputs of the imprinted waveguiding structure. If the output profile does not change for a certain range of input positions, we observe wide horizontal spots, showing a range

of stability for the waveguide structure. Indeed a large spot means that for different entry position for the probe beam, the intensity at that output position is unchanged, evidencing output stability versus entry position. If there are multiple outputs for a certain position of input we observe vertically multiple and differentiated spots. The cases analyzed in figures 5.11 and 5.12 are reported in the mapping of figure 5.13(b). The most intense spots correspond to the best waveguiding conditions reported previously. From left to right in figure 5.13(b), the first brightest spot corresponds to an entry point ranging from  $F_3$  to  $F_1$  and an output in  $B_1$ . This range of inputs corresponds to the area where the forward and backward beam have superimposed lobes, and every possible entry leads to an output in the backward beams main lobe as can be seen in figures 5.11(a), (b) and (d). Above to the left and below to the right of this first large spot in figure 5.13(b) are smaller spots. These indicate that there will be additional outputs to the  $B_1$  output discussed previously. If we are to the left of the spot with an entry around  $F_2$  the additional output is the OSS, if we are to the right of the spot for an entry point around  $F_1$  the additional outputs rang from  $B_2$  to  $F_0$ . Figure 5.13 is therefore a quick way to see all cases described in figures 5.11 and 5.12. The red diagonal line from the top left corner to the downright corner of the figures in 5.13 show the area where the input to output shift is zero. Indeed, when the input position of the beam scans the input of the crystal for increasing values of  $x$ , the corresponding zero shift output also corresponds to increasing values of  $x$ . Therefore, the spots furthest from the red diagonal reveal the largest shifts from input to output positions. Circled in red is the  $F_1$  output for the  $F_2$  input [figure 5.11(a)] with an input to output shift equal to  $13x_0$ .

Figures 5.13 (a) and (c) show the waveguiding behavior of counterpropagating antisymmetric Airy beams for  $d = -10$  and  $d = 10$  respectively. The configuration differs only by the shift  $d$  between the forward and backward Airy beams, but the resulting waveguiding behaviors are quite different. As can be expected, most spots are close to the diagonal because it corresponds to an input-to-output shift of 0 but multiple outputs are still observed. For example in the case  $d = -10$  [figure 5.13(a)], the probe beam injected in the OSS position has two output positions  $B_1$  and  $B_2$  which is the same result obtained for a single forward beam [11]. The small number of interconnections between the forward and backward beam inputs and outputs show that the overlapping secondary lobes in this configuration (see figure 5.9(b)) are weak waveguiding structures. In the case  $d = 10$  [figure 5.13(b)], the spots seem to aggregate in two groups. A first group pertaining to the forward beam waveguiding structure and a second group pertaining to the backward beam waveguiding structure. This emphasizes the lack of interaction

### 5.3. STABILITY OF THE PHOTOINDUCED WAVEGUIDES TO INPUT POSITIONS

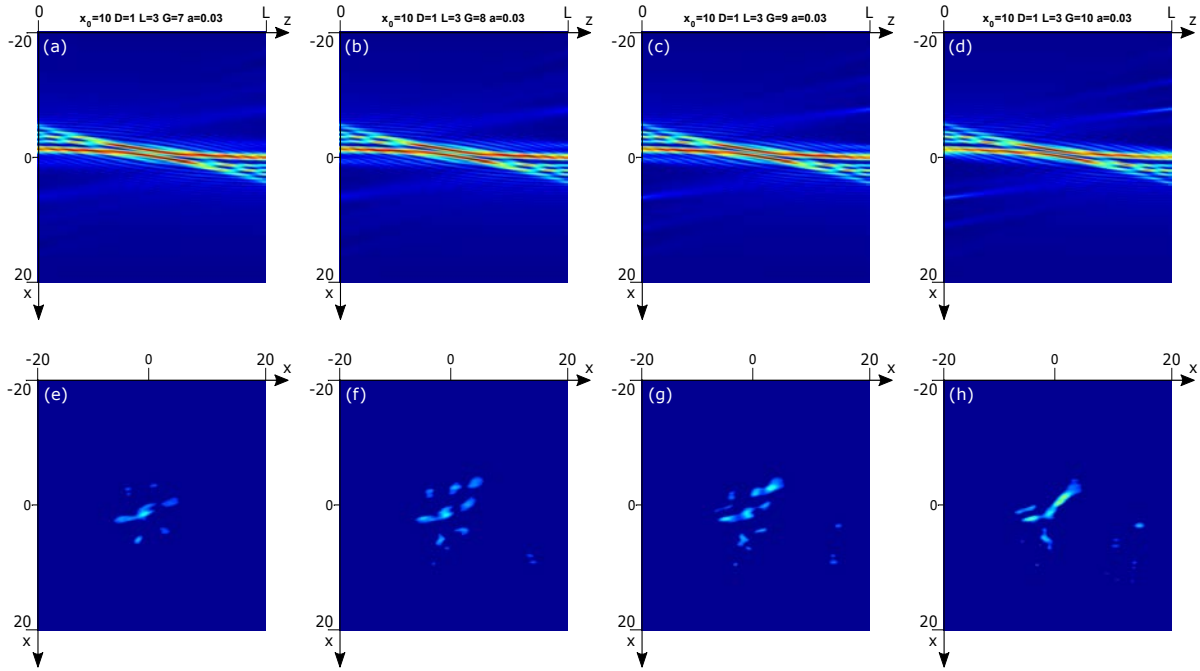


Figure 5.14: Imprinted waveguides (a-d) and propagating Gaussian probe beam mapping (e-h) for different values of nonlinear strength (a,e)  $\Gamma = 7$ , (b,f)  $\Gamma = 8$ , (c,f)  $\Gamma = 9$  and (d,h)  $\Gamma = 10$ .

between the two counterpropagating Airy beams seen in figure 5.9(d). Therefore, these set of figures 5.13 summarize how changing parameters like the transverse shift  $d$  between forward and backward beam can influence the waveguiding structure.

A different waveguiding structure can be obtained for different values of nonlinearity strength  $\Gamma$ . Figure 5.14 shows different waveguide configurations for increasing values of  $\Gamma = 7$  to 10. Figures 5.14(a-d) show the imprinted waveguiding structures for different values of nonlinear strength, (a)  $\Gamma = 7$ , (b)  $\Gamma = 8$ , (c)  $\Gamma = 9$  and (d)  $\Gamma = 10$ . Figures 5.15(e-h) shows the behavior of the propagating Gaussian probe beam in the previously obtained waveguides (e)  $\Gamma = 7$ , (f)  $\Gamma = 8$ , (g)  $\Gamma = 9$  and (h)  $\Gamma = 10$ . The probe Gaussian beam scans the output for increasing values of the transverse dimension  $x$ , and the output transverse intensity distributions are juxtaposed in order to show simultaneously all possible waveguiding configurations. This also allows the evolution of the output for varying input positions to appear. When the nonlinear strength is increased (from (a) to (d)), the OSBs and OSS are narrower and more defined due to stronger focusing effect. The resulting waveguiding in figure 5.14(e-h) show that when  $\Gamma$  is increased, spots appear and become brighter at the bottom right of the mapping. These spots correspond to waveguided outputs when the probe beam is injected in the OSB input. Additionally,

## CHAPTER 5. COUNTER PROPAGATING AIRY BEAMS IN PHOTOREFRACTIVE MEDIUM

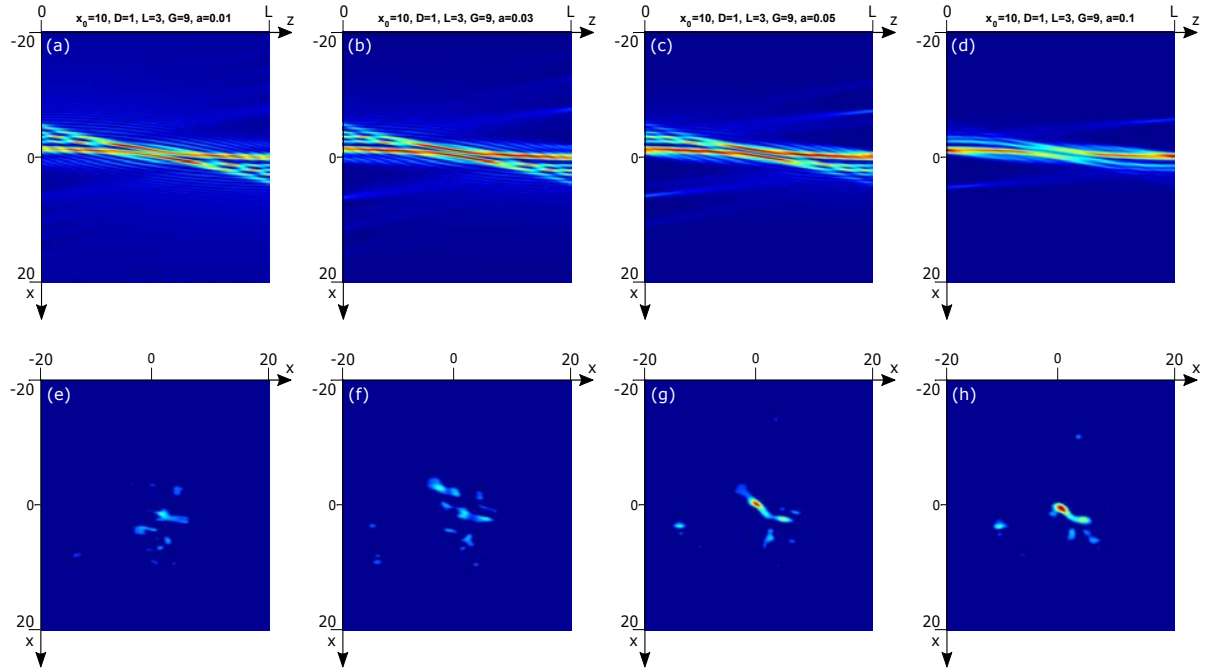


Figure 5.15: Imprinted waveguides (a-d) and propagating Gaussian probe beam mapping (e-h) for different values of truncation parameter (a,e)  $a = 0.01$ , (b,f)  $a = 0.3$ , (c,f)  $a = 0.05$  and (d,h)  $a = 0.1$ .

an increase of nonlinear strengths results in a better imprint of the waveguide. Figures 5.14(e),(f) and (g) show similar mapping in the center but for the stronger nonlinear strength (g) the spots are brighter, testifying stronger waveguides. By further increasing the nonlinear strength in figure 5.14(h), the focusing effect tends to merge different outputs together resulting in a smaller number of stronger waveguides. Furthermore, if the nonlinear strength is over  $\Gamma = 15$ , dynamic interactions occur similarly to the case of two incoherent contra-propagating Airy beams of symmetric configuration (cf. reference [40]). A dynamical interaction could create dynamical waveguiding structure. These kind of time-periodic dynamic structures could enable the distribution of light in an organized way and act as a form of clock in an optical system or a logic gate. For higher nonlinear strength, chaotic dynamics resulting in a chaotic distribution of light could be used in encryption applications and chaos-based computing.

We show in figure 5.15 four different waveguide configurations varying the truncation parameter from 0.1 to 0.01. Figures 5.15(a-d) show the imprinted waveguiding structures for different values of truncation parameter, (a)  $a = 0.01$ , (b)  $a = 0.3$ , (c)  $a = 0.05$  and (d)  $a = 0.1$ . Figures 5.15(e-h) shows the behavior of a propagating Gaussian probe beam in the waveguides obtained above. The probe Gaussian beam scans the output for

increasing values of the transverse dimension  $x$ , and the output transverse intensity distributions are juxtaposed to show the evolution of the output for varying input positions. The interaction of the two contra-propagating Airy beams with a nonlinear strength of  $\Gamma = 9$  yields different waveguiding structure (figure 5.15(a-d)) When the truncation parameter is increased (from (a) to (d)), the linear Airy beam profile of the forward and backward beam present less secondary lobes. Simultaneously we observe less OSBs and a strengthening, in terms of intensity, of the remaining OSS and OSB waveguiding structures. Indeed, the truncation of the linear Airy beam profile reduces the possibilities of interaction and the nonlinear effects will affect the remaining possibilities. The input/output mapping of the Gaussian probe beam to analyze each waveguiding structure (figure 5.15(e-h)) confirm the previous observations. When increasing the truncation parameter (from (e) to (h)) the number of spots reduces and the remaining spots gain in intensity. This means that there are less waveguiding possibilities, but these are stronger waveguiding structures since more intensity make it to the output positions. In the case  $a = 0.01$  in figure 5.15(e), the intensity is distributed in too many waveguiding structures. The output threshold intensity of 15% of the input probe beam intensity is rarely reached, resulting in less waveguiding options. To obtain strong waveguiding structures the truncation parameter must not be too low. To obtain numerous input to output configurations the truncation parameter cannot be too high. Therefore a compromise must be done to obtain the optimal waveguiding structure corresponding to the desired waveguiding system. In other words, multiplying unnecessary outputs can be detrimental to the effectiveness of other desired outputs.

All previous analysis have been done using a Gaussian probe beam of waist  $10\mu m$ , of wavelength  $\lambda = 532$  and average intensity to ensure the probe beam's linear propagation. Further analysis could be done using larger/smaller or more intense probe beams. Notably to guarantee bright outputs in configuration with many output possibilities. Another analysis can be done using a tilted Gaussian probe beam or a light of different wavelength to enable coupling between the waveguiding structures.

## 5.4 Conclusion

We have analyzed the waveguides photoinduced by two counterpropagating antisymmetric Airy beams. We have analyzed the propagation behavior of a Gaussian probe beam in such waveguides. We have found configurations giving multiple outputs for multiple input positions: up to three outputs whereas previous works had up to two

outputs [11]. We have found greater input-to-output shifts (up to 13 beam waists) with counterpropagating antisymmetric Airy beams compared to what was possible with counterpropagating Gaussian beams or even counterpropagating symmetric Airy beams configuration (typically maximum 6 beam waists [11]). We have then seen the influence the transverse shift, nonlinear strength and truncation parameter could have in terms of interaction between the counterpropagating beams and the resulting waveguiding structure. With inadequate transverse shift, the interactions between the counterpropagating Airy beams were nonexistent leading to no added value when compared to solo Airy beam waveguides. With strong nonlinearity the waveguide structure is better because imprinted more strongly. An increase of nonlinear strength can cause outputs to merge together and ultimately lead to dynamic structures resulting in dynamic waveguides. Finally, the truncation parameter helps control the weight of the linear Airy beam waveguiding structures compared to the nonlinear OSS or OSBs waveguiding structures.

Interactions of Airy beams in nonlinear self-focusing conditions yield much broader all-optical waveguiding possibilities than those observed so far with Gaussian beams. The situation discussed here with so-called antisymmetric counterpropagating Airy beams yields to our knowledge the largest variety of all-optical waveguiding: either single input to single output but with possibly large transverse shifts, either single (multiple) inputs to multiple (single) outputs just by varying the initial transverse shift between the counterpropagating Airy beams, the nonlinearity strength or truncation parameter of the Airy beams.

## CONCLUSION AND PERSPECTIVES

### 6.1 Conclusion

This thesis has revolved over three subjects: the Airy beams, solitons and photorefractive crystals. The goal was a better understanding of nonlinear interactions of Airy beams for possible future applications in optical interconnects. This led to the study of the Airy beam's experimental generation, the solitonic characteristics of nonlinear Airy beam propagation and finally the waveguiding possibilities to be expected in a photorefractive crystal illuminated by two counterpropagating Airy beams.

First, we have seen in chapter 2 that Airy beams are generated using a cubic phase mask illuminated by a Gaussian beam, which is then Fourier transformed using an optical lens. We have verified that changing the beam size does not affect the Airy beam's lobe size but its number of lobes through the truncation parameter. Furthermore, we have seen that increasing the phase shift on the mask increases simultaneously the size of the Airy beam lobes and the number of secondary lobes. We have then found the limits of these control parameters analytically and verified these conditions both numerically and experimentally. The conditions rely on an adapted illumination of the phase mask. First, the Gaussian beam illuminating the spatial light modulator (SLM) must not be larger than the phase mask to avoid discontinuities at the edge of the mask. This defines a maximum value for the illuminating Gaussian beam waist. Secondly, lighted area of the modulating cubic phase must have sufficient resolution in order to avoid aliasing. This defines a maximum phase-shift value of the phase mask in function of the illuminating

beam's size. Indeed this spatial light modulator screen resolution issue only concerns pixels illuminated by the Gaussian beam. Finally, the illuminated area of the phase mask must withhold a sufficient amount of information to ensure a properly formed Airy beam. The last conditions sets a bottom limit to maximum phase shift value in function of the Gaussian beams size. This ensures that a sufficient amount of the cubic phase mask is illuminated to form an Airy beam profile. These three conditions allowed us to define a parameter range value to minimize errors when generating a finite Airy beam. Finally we have also looked at the effect of improper illumination due to misalignment or Gaussian beam deformation. These numerical and analytical tools are powerful as they allow us to anticipate, when in the right parameter range, the Airy beam profile and truncation parameter as well as errors due to possible shifts or deformations of the incident Gaussian beam.

Secondly, we have studied nonlinear Airy beam propagation in photorefractive media and evidenced the solitonic properties of Airy beam nonlinear propagation in chapter 3. For a high enough nonlinearity, most of the beam turns into an off-shooting soliton (OSS) while a small fraction of the power remains a self-accelerating linear packet. Differently from Gaussian beams, the OSS coexists with a remaining self-accelerating structure of the Airy beam. Furthermore, additional off-shooting beams (OSB) can be observed that share solitonic properties but propagate at an angle with the initial beam propagation direction. Experimental and numerical profiles of the OSS fit nicely with the theoretical one-dimensional screening soliton profile. Numerical simulations confirm that the OSS propagates invariably on great distances (more than twenty diffraction lengths). Experimental results show that the OSS profile can be formed after a propagation of 2cm. We observed that for fixed nonlinear conditions inside a photorefractive crystal, there exists a range of intensity values for which the OSS property is the closest to the ideal theoretical soliton. Furthermore, we have seen that a single Airy beam profile can yield differently sized OSS in function of the nonlinear strength, by varying either the initial Airy beam intensity or the value of the bias electric field current. We have not only observed stable Airy beam OSS, but also shown that they are flexible and easy to manipulate.

Thirdly, we have seen the propagation behavior of a two dimensional Airy beam in nonlinear photorefractive media in chapter 4.6. These observations allowed us to observe the anisotropic characteristics of photorefractive crystals. The anisotropy of the crystal and asymmetry of the applied electric field along the c-axis of the crystal results in a two-stepped focusing dynamic of the Airy beam into an OSS. Interestingly both

steps can be linked to the soliton existence curve. The first step takes place when the soliton existence curve is decreasing whereas the second step when the soliton existence curve increases after having past the minimum. This two step dynamic allows different types of propagation configurations to take place. For low nonlinear strength we observe unidimensional focusing transforming the 2D Airy beam in a 1D Airy beam profile at the output of the crystal. For medium nonlinearity, the 1D Airy beam undergoes self-focusing and an OSS forms. The residual self-accelerating linear structure is in competition with the OSS structure. For high nonlinearity only the OSS is observed. It is also at higher nonlinearity that the output profile is most unstable as self-bending and over-focusing can occur. This encourages the stable sole OSS configuration to be obtained for the lowest nonlinearity strength possible. In doing so, we were able to obtain a stable OSS for 34 seconds for  $E_{ext} = 2000V/cm$  and  $I = 1.4\mu W$ .

Finally in chapter 5, we have analyzed the waveguides photoinduced by two counter-propagating antisymmetric Airy beams. We have analyzed the propagation behavior of a Gaussian probe beam in such waveguides. We have found configurations giving multiple outputs for multiple input positions: up to three outputs whereas previous works had up to two outputs [11]. We have found greater input-to-output shifts (up to 13 beam waists) with counterpropagating antisymmetric Airy beams compared to what was possible with counterpropagating Gaussian beams or even counterpropagating symmetric Airy beams configuration (typically maximum 6 beam waists [11]). We have then seen the influence that the transverse shift, the nonlinear strength and the truncation parameter has on the interactions between the counterpropagating beams and its resulting waveguiding structure. With an excessive transverse shift, the interactions between the counter-propagating Airy beams are nonexistent leading to little added value when compared to solo Airy beam waveguides. With strong nonlinearity the waveguide structure is more strongly imprinted, and the probe beam loses less energy when propagating. The structure of the nonlinear OSS and OSBs are thinner as well. An increase of nonlinear strength can cause outputs to merge together because of attraction interactions between the two counterpropagating Airy beams and their OSSs. An increase of the nonlinear strength inside the crystal ultimately leads to dynamic structures and dynamic waveguides. Finally, the truncation parameter helps control the weight of the linear Airy beam waveguiding structures compared to the nonlinear OSS or OSBs waveguiding structures. An increased truncation of the Airy beam weakens the linear Airy beam structure allowing refocused structures to emerge more easily resulting in stronger OSS and OSB structures and their waveguides. Interactions of Airy beams in nonlinear

self-focusing conditions yield much broader all-optical waveguiding possibilities than those observed so far with Gaussian beams. The antisymmetric counterpropagating Airy beams yield to our knowledge the largest variety of all-optical waveguiding: either single input to single output but with possibly large transverse shifts, either single (multiple) inputs to multiple (single) outputs just by varying the initial transverse shift between the counterpropagating Airy beams, the nonlinearity strength or truncation parameter of the Airy beams.

## **6.2 Perspectives**

### **6.2.1 The use of nonconventional beams**

Our work has consisted in studying the Airy beams, their generation, their nonlinear propagation and interactions in photorefractive crystal and possible applications such as waveguiding. Similar studies can be done on other nonconventional beams, their derivative or a combination of the two. Vortex, Bessel, Mathieu or "super-Airy" beams can all be generated using a spatial light modulator and can be injected inside a photorefractive crystal using a similar setup as ours. The study of nonconventional beam is threefold. First they offer diverse ways to propagate light, for example inside a nonlinear photorefractive crystal. Secondly they challenge the theoretical and numerical models used in anisotropic photorefractive media. Finally they can help understand the transition dynamics from linear to nonlinear propagation.

#### **6.2.1.1 Diverse ways to propagate light**

The proper illumination of the nonconventional beam phase masks, as in figure 6.1 is of interest. The defects that occur due to improper illumination or misalignment may defer from one beam to the next and can be an indicator to combine or modify different phase masks in order to leverage the most out of different possibilities. Analyzing the critical areas that need illumination can help circumventing problems and offer more flexible modulation capabilities. When they propagate in nonlinear media, these nonconventional beams reorganize as has been seen with vortex beams [115, 116, 138], and their interaction with other nonconventional beams in different co or counterpropagating configurations are still underdocumented. We believe these studies could lead to applications in all-optical waveguiding in bulk material.

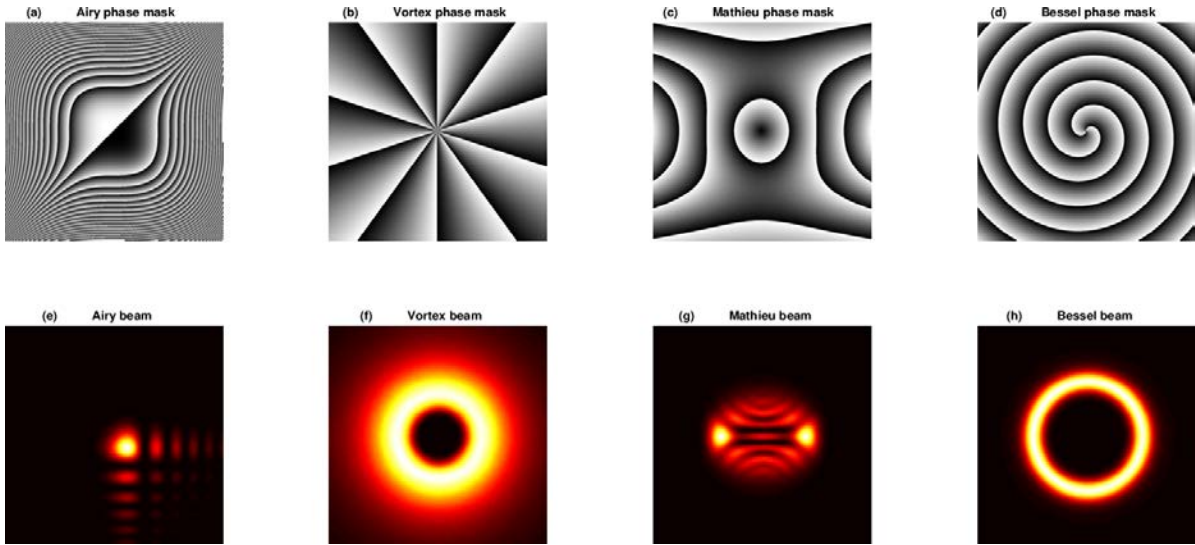


Figure 6.1: Phase masks (a-d) and corresponding beams (e-h) that can be generated using an SLM.

### 6.2.1.2 Challenging the existing theoretical and numerical models

The numerical model we use is one-dimensional and qualitative. It is of interest to develop a better understanding of the photorefractive crystal and other nonlinear saturable media. Further studies, both qualitative and quantitative, of Airy beam propagation in nonlinear saturable media are required to help correct and choose the theoretical and numerical models. Such studies have been led using vortex beams as a mean to compare the anisotropic model to the isotropic model. Indeed, the anisotropic model has been compared to the isotropic model [114–116], and put to the test using nonconventional beams such as vortices [115, 116]. Since the inside of the crystal cannot be properly observed due to refractive index variations, models are important to understand the dynamic and explain what is observed at the output face of the crystal. To explain the photorefractive effect, the set of Kukhtarev equations is generally accepted as valid but the approximations required to solve these equations are still under debate. The most accurate way to solve the equations seems to be Zozulya’s method [109], which solves the electrostatic potential first in order to find the space-charge field afterwards inside the crystal. The accuracy relies on the validity of the approximations made to solve the equations. The approximations using the electrostatic potential are more straightforward than the approximations needed when solving the space charge field directly [115]. In any case, the study of nonconventional beam propagation in photorefractive nonlinear media can only improve the existing model which is yet to be satisfactory in (2+1) dimensions.

### 6.2.1.3 Transition dynamics from linear to nonlinear propagation

We have observed an Airy beam change to an OSS when propagating in nonlinear media and similar transition from linear beam to nonlinear solitonic beams has been observed for vortex beams [102, 138]. The linear Airy beam is a stationary solution of the *linear* Schrödinger equation that is used to describe the evolution of propagating beams in linear media: the stationary nature of the linear Airy beam explains its non-diffracting nature. When a nonlinear effect is applied on the photorefractive crystal the Airy beam propagates through a nonlinear media, and the propagation is described by the *nonlinear* Schrödinger equation. The Airy beam propagation is no longer a stationary solution of this equation. A stationary solution of the *nonlinear* Schrödinger equation is a family of soliton beams. The Airy beam profile injected in nonlinear media changes shape along propagation and converges to a stationary soliton profile. The emergence of the OSS when injecting an Airy beam in nonlinear media can therefore be considered as the transition from the linear Airy solution to the nonlinear soliton one. Interestingly this transition is slow enough for the coexistence of a linear self-accelerating wave packet and an OSS structure allowing interesting interactions and waveguiding possibilities. We have observed that the transition is eased by a longer propagation length, due to the longer distance over which the beam is subject to the nonlinear effect. Similarly, an increase of the linear Airy beam's apodization fragilizes the linear Airy beam profile, and the transition from Airy beam to a nonlinear OSS take place sooner along propagation. An increase of the nonlinear strength will also quicken the transition from linear to nonlinear propagation, but the asymptotic nonlinear soliton profile will also change when the nonlinear strength is changed. If the new asymptotic nonlinear soliton profile is unstable, so will the OSS. This is the case of the sole (2+1)D OSS in chapter 4.6 that becomes unstable after being formed. Since we are interested in complex waveguiding structures, we want the transitional state to be the one at the output of the crystal after propagation. This means we must adapt the truncation of the finite Airy beam and the bias electric field applied on the crystal in order for the transient linear-to-nonlinear propagation behavior to be observed at the output of the crystal for a propagation length equal to the crystal length. It would be of interest to study and compare similar dynamics of other nonconventional beams in similar conditions, to determine if all nonconventional beams change to OSS along propagation, and to determine the characteristic lengths of these transitions in function of nonlinear strength or crystal length.

### 6.2.2 Off-shooting Soliton stability

We have been able to obtain steady state OSSs and off-shooting beams (OSB) in the case of a (1+1)D truncated Airy beam propagating in nonlinear photorefractive media. The (2+1)D soliton is stable for a time (up to 34 seconds for  $E_{ext} = 2000V/cm$  and  $I = 1.4\mu W$ ) but remains transitional and it is unclear if it can be stabilized. As mentioned in chapter 4.6, when the Airy beam refocuses along both transverse dimensions to form an OSS, the newly formed OSS bends and shifts along the preferential c-axis. It is probable that the bending does not occur before due to the residual linear Airy beam profile. What is surprising is the relatively sudden and strong bending effect that occurs after a certain nonlinear strength threshold value. The reason is that when the beam fully changes to an OSS, all the light intensity previously dispersed refocuses into the OSS. The peak intensity of the newly formed OSS is much higher than what was previously observed causing a sudden and strong bending effect. The discontinuity of the phenomena may not allow a stable sole (2+1)D OSS to be observed, even if the bending can be delayed by using low power beams. Due to the complexity of the experimental setup and the multiple parameters at play, a (2+1)D numerical approach taking anisotropy and diffusion effects into consideration would greatly narrow down the effects to consider. In any case, experimental observations of the (2+1)D OSS formation for different parameter ranges close to the transition from one dimensional focusing to two dimensional focusing could answer remaining questions concerning stability.

### 6.2.3 Instability of counterpropagating waveguides

We have been able to stabilize the solitonic structure when one Airy beam propagates. Numerically counterpropagating Airy beams are stable using either short crystals either transversely large Airy beams. However, counterpropagating Airy beam interaction becomes unstable at high nonlinearity or when propagating long distances under nonlinear effect [40]. Figure 6.2 shows a numerical example of unstable nonlinear interactions of two counterpropagating beams. Figure 6.2(a) shows the evolution of the intensity distribution at the output of the crystal and figure 6.2(b) is the intensity distribution inside the crystal at time  $t_f$ . The forward Airy beam propagates along  $z$  and the backward Airy beam propagates in the opposite direction. The intensity distribution at the output crystal seen in figure 6.2(a) is the superposition of the intensities of the forward beam and the backward beam. After traveling through the relatively long crystal (5.4 cm) the forward beam's self-accelerating linear wave packet has lost all energy in favor of

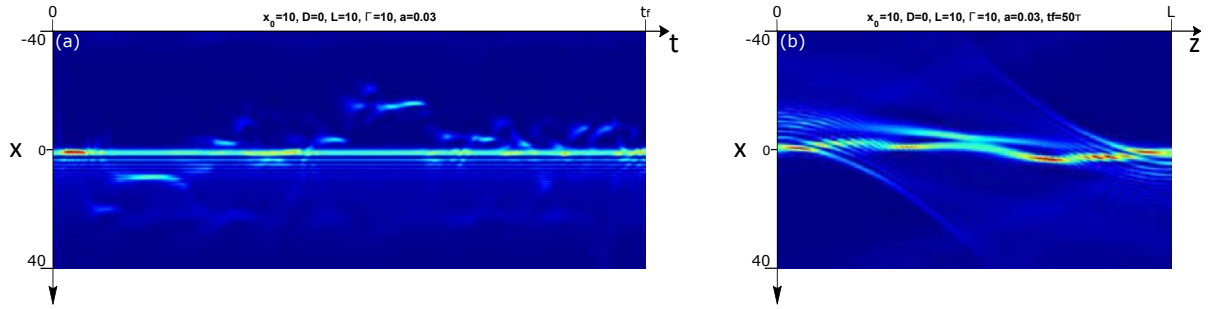


Figure 6.2: Instability of numerical counterpropagating Airy beam interactions. (a) Temporal evolution of the transverse output intensity profile at  $z = L$ . (b) Undergoing nonlinear interaction of two counterpropagating Airy beams in an externally biased photorefractive crystal at  $t = t_f = 50\tau$ .  $\tau$  is the relaxation time of the crystal

the nonlinear OSS. The position of the forward beam OSS changes greatly over time contrarily to the input backward beam that cannot move. This kind of dynamic behavior has been studied in the case of symmetrically injected Airy beams [40], and shown that the forward OSS position tends to be attracted to the backward Airy beam lobe positions. Additionally both OSS are attracted to each other resulting in oscillating or chaotic dynamics [40]. This study has not been done in the anti-symmetric configuration but similar results are expected. The resulting dynamic waveguides imprinted in the photorefractive crystal can be of great interest for optical logic gates and chaos-based computing.

## 6.2.4 Experimental waveguiding of probe beams

We have predicted efficient waveguiding in chapter 5. Those are single (multiple) inputs to multiple (single) outputs, with possibly large transverse shifts. We have identified interesting configurations as well as analyzed their stability to a probe beam's input position. Furthermore, we have identified parameters to observe the stable (1+1)D OSS in chapter 3 and shown that stable (2+1)D Airy beam configurations can be envisioned. In these conditions, an experimental observation of waveguided probe beams using low power Airy beams ( $\approx 3\mu W$ ) to photoinduce the waveguiding structure seems feasible. Ideally, in the imaging system to avoid the superposition of both waveguide and probe beam we need two lasers. Using a probe beam of a different wavelength would allow the observation of the waveguiding structure and the probe beam propagation separately using a filter and/or two cameras. Furthermore, the Airy beams generated using the SLM tend to flicker very rapidly as explained in chapter 2. The time response of the

photorefractive crystal we have used is sufficiently long for the crystal not to "see" the Airy beam flicker. For future applications another generation method may be used to eradicate the flicker such as an engraved phase mask. To speed up the waveguide imprinting, other crystals of shorter time response exist [139] and increasing the intensity can further shorten the response time of the crystal. The flexibility and control of the output profile using either light intensity or applied electric fields makes the use of Airy beams an interesting approach in optical interconnects; enabling different waveguide configurations by controlling the nonlinear strength of the medium. Furthermore, when creating the waveguide, one can control the propagating beams themselves and/or shift between different types of beam quicker than the crystal time response. This allows a great number of waveguiding possibilities to be explored.

An alternative method to study the waveguides formed by Airy beam interaction is to imprint the image of the interaction directly inside the crystal. By illuminating the crystal overhead with a 2D image of the interaction intensity distribution, we can imprint directly inside the crystal a 2D waveguide. The advantage is that the experimental implementation and observation does not require two different wavelengths. Additionally the waveguide would be sturdy and stable letting us focus on the waveguiding behavior of the probe beam. This would however stop dynamic interactions to take place. It would be a first step however and help better understand bulk waveguides.

### 6.2.5 Greater control of the focusing conditions

Applying a bias electric field to the photorefractive crystal allows control of the propagating behavior of the Airy beam inside the crystal. The propagation changes from a linear Airy beam to a nonlinear OSS. The electric field is applied via two plates along the crystal's sides. Illuminating the crystal with a uniform background lighting reduces the nonlinear effect inside the crystal. These two means of control are single valued and uniform, but they could be more complex.

We can imagine applying a parabolic potential to a crystal [100], that would successively switch the nonlinear effect along propagation from focusing conditions to defocusing conditions. Figure 6.3 shows the intensity distribution of an Airy beam propagating (along  $z$ ) in a medium with parabolic potential. The Airy beams' acceleration is periodically reversed along propagation.

The propagation behavior through a medium can also be engineered through control of the refractive index gradient inside the medium. A gradient refractive index can lead to a fine control of the Airy beam acceleration [43], and by using a photoinduced lattice,

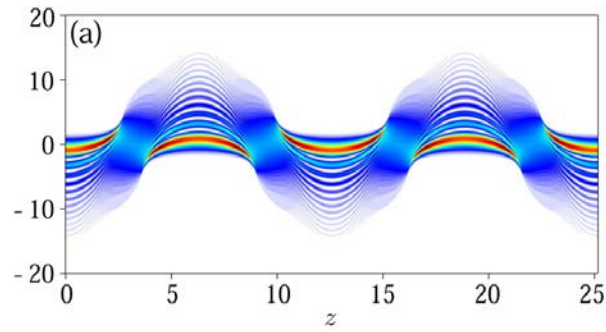


Figure 6.3: Propagation of a finite energy Airy beam in a parabolic potential. Extracted from reference [100]

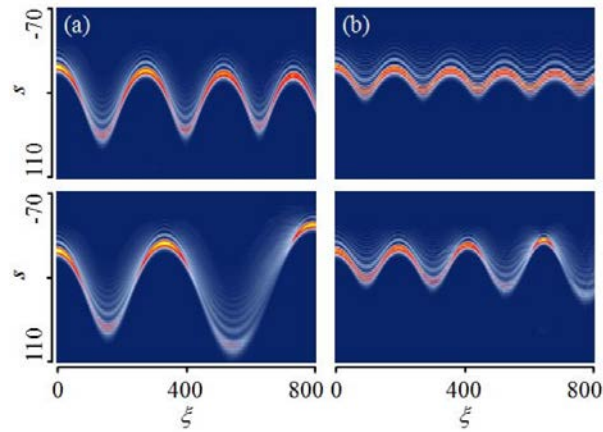


Figure 6.4: Propagation of a finite energy Airy beam in a parabolic potential. Extracted from reference [44]

the Airy beam acceleration can also be periodically reversed [44]. Figure 6.4 shows an Airy beam propagating in a photonic lattice for different index gradient (a) and for different periodicity of the photonic lattice (b).  $s$  is the normalized transverse coordinate and  $\xi$  the normalized propagation axis. The Airy beam is reversed periodically.

It is therefore possible to exert more control over the propagation behavior of Airy beams by a finer control of the applied external field or the background illumination. It is of interest to see if these means of control have the same influence on the linear Airy beam structure and on the nonlinear OSS structure.





## RÉSUMÉ EN FRANÇAIS

Cette thèse porte sur trois sujets : les faisceaux Airy, les solitons et les cristaux photoréfractifs. L'objectif de cette thèse est de mieux comprendre les interactions non-linéaires des faisceaux Airy se propageant dans des cristaux photoréfractifs en vue d'éventuelles applications futures dans le domaine d'interconnexions tout-optiques. Cela a conduit à l'étude de la génération expérimentale du faisceau Airy, des caractéristiques solitoniques de la propagation non linéaire du faisceau Airy et enfin des possibilités de guidage d'ondes auxquelles on peut s'attendre dans un cristal photoréfractif éclairé par deux faisceaux Airy contra-propageant.

### Génération expérimentale de faisceaux Airy

Nous avons généré nos faisceaux Airy à l'aide d'un masque de phase cubique illuminé par un faisceau Gaussien. Grâce à une lentille, qui réalise une transformée de Fourier spatiale, nous obtenons le faisceau Airy au foyer de celle-ci. La figure 6.5 montre les étapes de la génération d'un faisceau Airy. La modification de la taille du faisceau illuminant le masque n'affecte pas la taille des lobes du faisceau Airy. Par contre, elle affecte le nombre

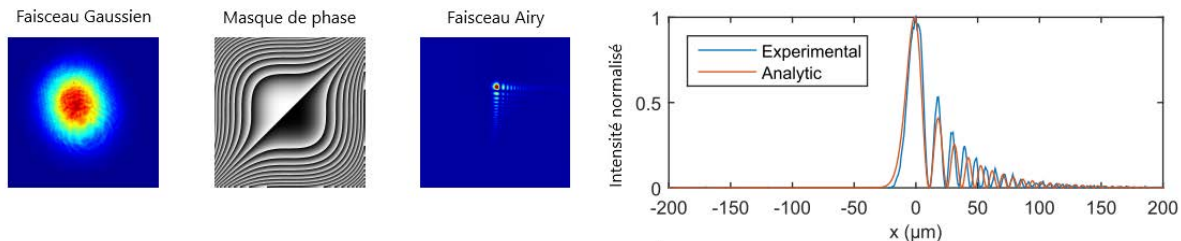


Figure 6.5: De gauche à droite : profil transverse du faisceau Gaussien illuminant le masque de phase, le masque de phase projeté sur le modulateur spatial de phase, le faisceau Airy obtenu au foyer image de la lentille de Fourier, tranche transverse du profil transverse du faisceau Airy obtenu expérimentalement et de celui attendu analytiquement.

de lobes du faisceau Airy dû à un effet de troncature. Quant au masque, une variation de phase plus grande augmente simultanément la taille des lobes du faisceau Airy et le nombre de lobes secondaires observés. Nous avons déterminés analytiquement les limites de ces paramètres de contrôle permettant d'obtenir un faisceau Airy et nous avons vérifié ces conditions à la fois numériquement et expérimentalement. Ces conditions reposent sur un éclairage adapté du masque de phase. Tout d'abord, le faisceau Gaussien éclairant le modulateur spatial de lumière (SLM) ne doit pas être plus grand que le masque de phase pour éviter les discontinuités au bord du masque. Ceci définit une valeur maximale pour la taille du faisceau Gaussien d'éclairage. Deuxièmement, la zone éclairée de la phase cubique modulante doit avoir une résolution suffisante pour éviter les effets de moirage ou de crénelage. Ceci définit une valeur maximale de déphasage sur le masque en fonction de la taille du faisceau d'éclairage. En effet, la résolution du modulateur spatial n'est problématique qu'à condition que les pixels soient éclairés par le faisceau Gaussien. Enfin, la zone illuminée du masque de phase doit contenir une quantité suffisante d'informations pour assurer un faisceau Airy correctement formé. Cette dernière condition fixe une limite inférieure à la valeur du déphasage sur le masque en fonction de la taille du faisceau Gaussien. Cela garantit qu'une quantité suffisante du masque de phase cubique est illuminée pour former un profil de faisceau Airy. Ces trois conditions nous permettent de définir une plage de valeur pour nos paramètres qui minimise les erreurs lors de la génération d'un faisceau Airy. La figure 6.6 représente cette plage de valeur en rouge. Nous avons également étudié l'effet d'un mauvais alignement ou d'une déformation du faisceau Gaussien. Ces outils numériques et analytiques sont puissants car ils nous permettent d'anticiper le profil du faisceau Airy et également les erreurs dues aux éventuels décalages ou déformations du faisceau Gaussien utilisé.

## **Faisceaux Airy dans un milieu photoréfractif**

Nous étudions la propagation non-linéaire du faisceau Airy dans des milieux photoréfractifs et de ses propriétés solitoniques. Si la non-linéarité du milieu est suffisamment élevée, la majeure partie du faisceau se transforme en off-shooting soliton (OSS) tandis qu'une fraction résiduelle du faisceau reste Airy. Contrairement aux faisceaux Gaussiens, l'OSS coexiste avec la structure auto-accélération du faisceau Airy. En outre, on peut observer la formation de faisceaux supplémentaires que l'on appellera off-shooting beams (OSB) et qui possèdent des propriétés typique des solitons à la différence qu'ils se propagent avec un angle par rapport à la direction de propagation initiale du faisceau. Les

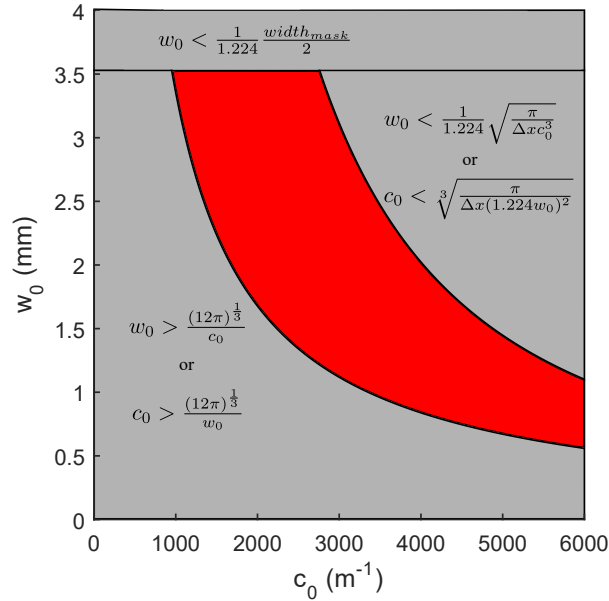


Figure 6.6: Graphique représentant en rouge la plage de paramètres permettant la génération de faisceaux Airy.  $w_0$  est la taille du faisceau Gaussien éclairant le masque de phase et  $c_0$  représente le déphasage maximal au sein du masque.

profils expérimentaux et numériques de l'OSS s'accordent parfaitement avec le profil théorique unidimensionnel de soliton. Les simulations numériques confirment que l'OSS se propage invariablement sur de grandes distances (plus de vingt longueurs de diffraction). Les résultats expérimentaux montrent que le profil de l'OSS peut être formé après une propagation de 2 cm. Nous avons observé que pour un même champ appliqué au cristal photoréfractif, il existe une gamme de valeurs d'intensité du faisceau entrant pour lesquelles la propriété de l'OSS est proche du soliton théorique idéal. En outre, nous avons vu qu'un seul profil de faisceau Airy peut donner des OSS de taille différente en fonction de la non-linéarité. Celle-ci peut être modifiée en faisant varier soit l'intensité du faisceau Airy entrant, soit la valeur du champ électrique appliqué au cristal. Nous avons non seulement observé la stabilité des OSS issues de faisceaux Airy, mais nous avons également montré que leurs profils peuvent être contrôlés grâce à la non-linéarité.

## Faisceaux Airy bidimensionnel dans un milieu photoréfractif

Nous nous sommes intéressés au comportement d'un faisceau Airy bidimensionnel dans un milieu photoréfractif non linéaire. Ces observations nous ont permis de voir les caractéristiques

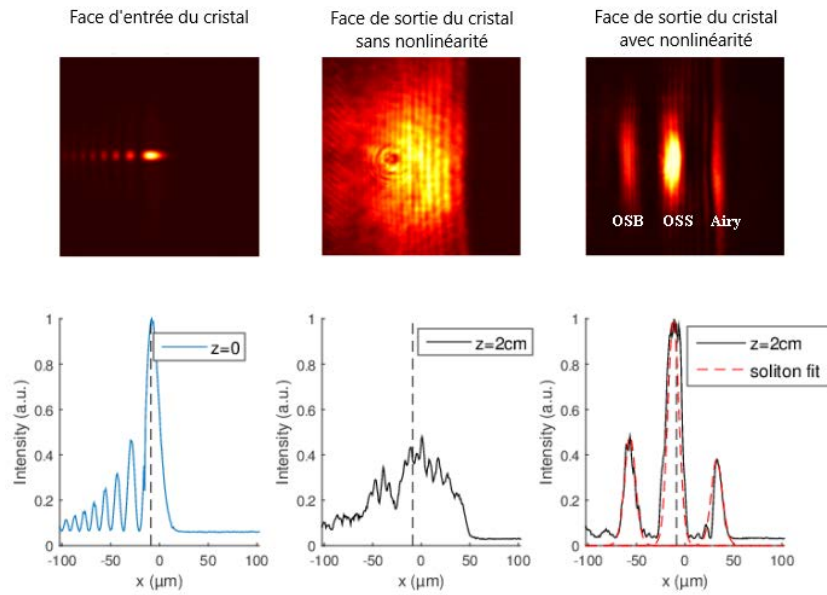


Figure 6.7: De gauche à droite : face d'entrée du cristal où l'on injecte un faisceau Airy unidimensionnel, face de sortie du cristal sans nonlinéarité présentant un faisceau Airy diffus, face de sortie du cristal avec nonlinéarité présentant un OSB, OSS et faisceau Airy résiduel.

téristiques anisotropes des cristaux photoréfractifs. L'anisotropie du cristal et l'asymétrie du champ électrique appliqué le long de l'axe  $c$  du cristal se traduisent par une dynamique de focalisation en deux étapes du faisceau Airy en un OSS. Il est intéressant de noter que les deux étapes peuvent être liées à la courbe d'existence du soliton. La première étape a lieu lorsque la courbe d'existence du soliton est décroissante, tandis que la seconde étape a lieu lorsque la courbe d'existence du soliton a dépassé son minimum. Cette dynamique à deux étapes permet différents types de configurations de propagation. Pour une faible non-linéarité, nous observons une focalisation unidimensionnelle transformant le faisceau Airy 2D en un profil de faisceau Airy 1D à la sortie du cristal. Pour une non-linéarité moyenne, le faisceau Airy 1D subit une autofocalisation et un OSS commence à se former. La structure Airy résiduelle est en concurrence avec la structure OSS. Pour une non-linéarité élevée, seul l'OSS est observé. C'est également à un niveau de non-linéarité élevé que le profil de sortie peut paraître le plus instable, car l'OSS peut se déplacer. Donc l'OSS le plus stable est celui obtenu pour la plus faible non-linéarité. Ainsi, nous avons pu obtenir un OSS stable pendant 34 secondes pour  $E_{ext} = 2000V/cm$  et  $I = 1,4\mu W$ .

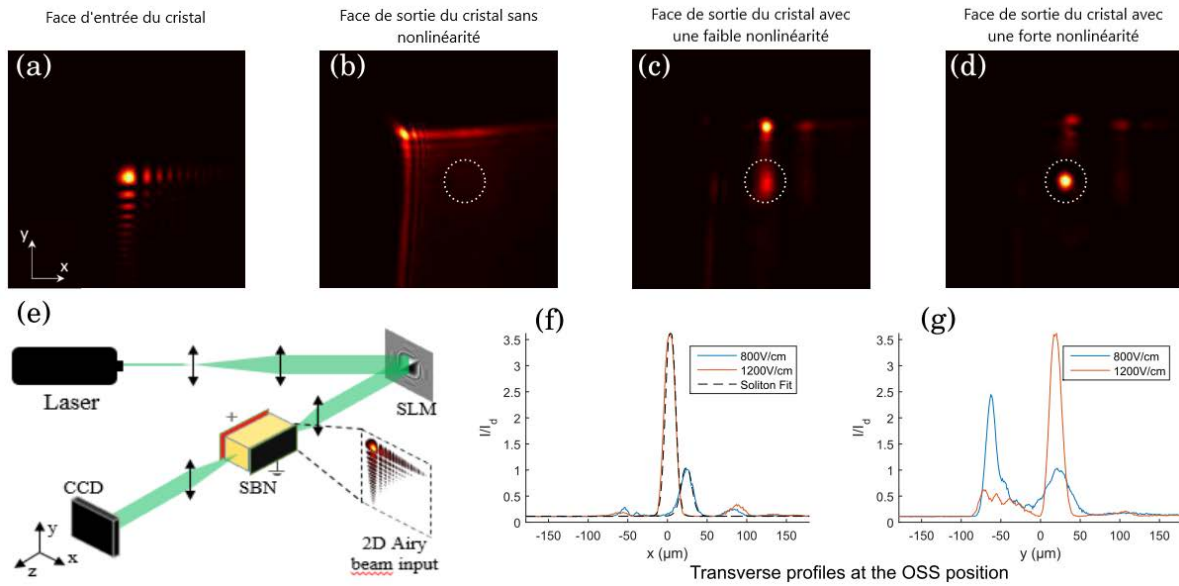


Figure 6.8: (a) Profil d'intensité en entrée du cristal, un faisceau Airy bidimensionnel ( $2,8 \mu\text{W}$ ). (b-d) Profil d'intensité en sortie du cristal pour différents champs électriques appliqués au cristal (b)  $E_{ext} = 0\text{V/cm}$ , (c)  $E_{ext} = 800\text{V/cm}$ , et (d)  $E_{ext} = 1200\text{V/cm}$ , la position de l'OSS est représentée par un cercle blanc en pointillé. (e) Schéma du dispositif expérimental. (f-g) Sections transverse des profils d'intensité en sortie du cristal pour une faible ( $E_{ext} = 800\text{V/cm}$ ) et forte ( $E_{ext} = 1200\text{V/cm}$ ) nonlinéarité (f) le long de l'axe  $x$  et (g) le long de l'axe  $y$ .

## Guides d'ondes photoinduits

Nous avons étudié numériquement les guides d'ondes photoinduits par deux faisceaux Airy contra-propageant antisymétriquement dans un milieu non-linéaire saturable. Nous avons testé les guides d'ondes obtenus en injectant un faisceau Gaussien et en observant sa propagation dans ces guides d'ondes. Nous avons trouvé des configurations donnant de multiples sorties pour de multiples entrées : des guides d'ondes possédant jusqu'à trois sorties alors que ceux des travaux précédents possédaient jusqu'à deux sorties [11]. Nous avons trouvé des décalages entrées-sorties plus importants (jusqu'à 13 fois la taille du faisceau) en utilisant des faisceaux Airy contra-propageant antisymétrique. Cela n'était pas possible avec des faisceaux Gaussiens contra-propageant (décalage de 2 tailles du faisceau) ou avec deux faisceaux Airy contra-propageant symétriques (décalage de 6 tailles de faisceau [11]). Nous avons ensuite observé l'influence de plusieurs paramètres sur les guides d'ondes obtenus. Les trois paramètres étudiés sont le décalage transverse entre les faisceaux contra-propageant, la force de la non-linéarité et le paramètre de troncature des deux faisceaux Airy contra-propageant. Avec un décalage transverse trop

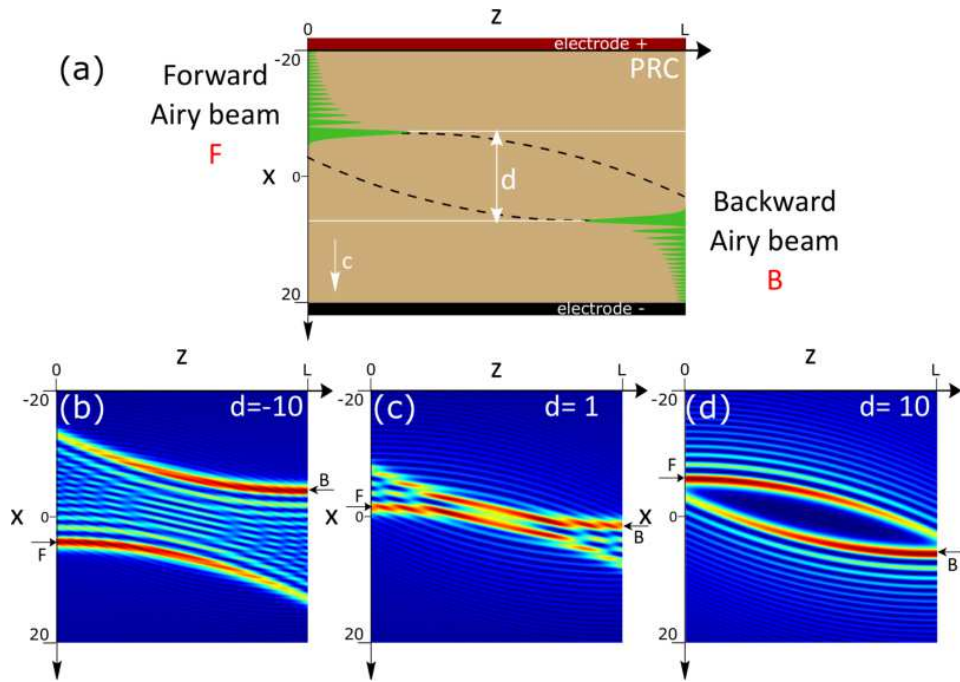


Figure 6.9: (a) Schéma de deux faisceaux Airy contrapropageant antisymétriquement dans un cristal de longueur  $L$ .  $x$  est l'axe transverse et  $z$  l'axe de propagation. (b-c-d) Profil d'intensité à l'intérieur du cristal pour différentes valeurs de décalage transverse entre les deux faisceaux Airy (b)  $d = -10$ , (c)  $d = 1$ , et (d)  $d = 10$ .

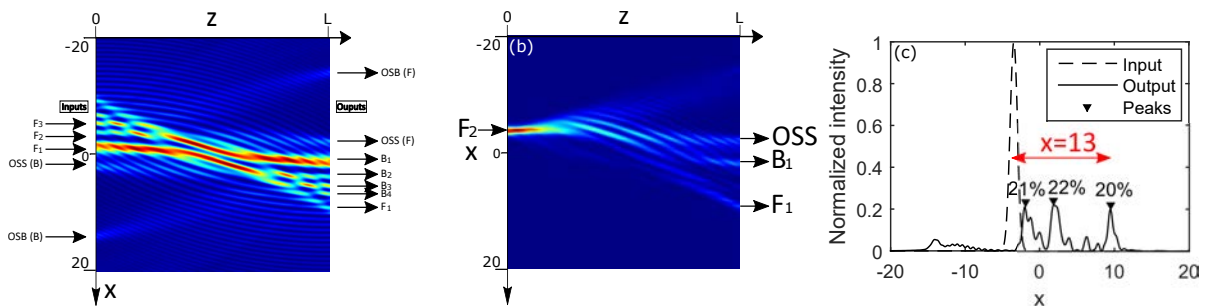


Figure 6.10: (a) Profil d'intensité à l'intérieur du cristal représentant la structure du guide d'onde créée par deux faisceaux Airy contrapropageant antisymétriquement. Les flèches de gauche représentent des entrées et les flèches de droite des sorties. (b) Propagation d'un faisceau Gaussien dans le guide d'onde injecté dans l'entrée  $F_2$ . (c) Profil d'intensité transverse à la sortie du guide d'onde pour un faisceau Gaussien injecté dans l'entrée  $F_2$ , en rouge est représenté le décalage maximal entre la position du faisceau d'entrée et la sortie la plus décalée correspond à 13 tailles de faisceau.

---

important, les interactions entre les faisceaux Airy contra-propageant sont inexistantes, ce qui n'apporte pas de valeur ajoutée par rapport aux guides d'ondes résultant d'un seul faisceau Airy. En cas de forte non-linéarité, la structure du guide d'ondes est plus fortement imprimée dans le cristal et la lumière perd moins d'énergie en se propageant dans les guides. La structure des guides résultants des OSS et des OSB est également plus marquée. Une augmentation de la non-linéarité peut entraîner une fusion des différentes entrées ou différentes sorties en raison de l'attraction qu'exerce entre eux les guides d'onde. Une forte augmentation de la non-linéarité à l'intérieur du cristal peut finalement conduire à des structures dynamiques oscillantes ou chaotiques, de façon similaire à ce qui a été observé pour deux faisceaux contra-propageant symétriques [41]. Enfin, le paramètre de troncature permet de contrôler la quantité de lobe secondaire des faisceaux Airy et ainsi la prépondérance de guide d'onde résultants des faisceaux Airy par rapport aux guides d'ondes résultants des OSS ou des OSB. Une troncature accrue du faisceau Airy affaiblit sa structure multilobe et sa propagation typique en milieu linéaire, ce qui permet aux phénomènes non-linéaire d'émerger plus facilement, d'où des structures et des guides d'ondes OSS et OSB plus forts. Les interactions de faisceaux Airy dans des milieux non-linéaires offrent des possibilités de guidage d'ondes tout-optique beaucoup plus larges que celles observées jusqu'à présent avec les faisceaux Gaussiens.

Les faisceaux Airy contra-propageant antisymétriques offrent, à notre connaissance, la plus grande variété de guides d'ondes tout optique : de multiples entrées et de multiples sorties avec de grands décalages transverses possible entre les entrées et les sorties. De plus il est possible de contrôler la structure de guidage en jouant sur le décalage entre les faisceaux Airy contre-propageant, la force de la réponse nonlinéaire du milieu ou le paramètre de troncature des faisceaux Airy.



## BIBLIOGRAPHY

- [1] J. P. Gordon, H. J. Zeiger, and C. H. Townes: *The Maser—New Type of Microwave Amplifier, Frequency Standard, and Spectrometer*, *Physical Review* **99**, 1264 (1955).
- [2] T. H. Maiman: *Stimulated Optical Radiation in Ruby*, *Nature* **187**, 493 (1960).
- [3] R. N. Hall, G. E. Fenner, J. Kingsley, T. Soltys, and R. Carlson: *Coherent light emission from GaAs junctions*, *Physical Review Letters* **9**, 366 (1962).
- [4] K. Kao and G. Hockham: *Dielectric-fibre surface waveguides for optical frequencies*, *Proceedings of the Institution of Electrical Engineers* **113**, 1151 (1966).
- [5] J. Hecht: *City of light: the story of fiber optics* (Oxford University Press on Demand, Oxford, 2004).
- [6] A. Hasegawa and F. Tappert: *Transmission of stationary nonlinear optical pulses in dispersive dielectric fibers. I. Anomalous dispersion*, *Applied Physics Letters* **23**, 142 (1973).
- [7] L. F. Mollenauer and J. P. Gordon: *Solitons in optical fibers: fundamentals and applications* (Elsevier, London, 2006).
- [8] D. Wolfersberger, N. Khelifaoui, C. Dan, N. Fressengeas, and H. Leblond: *Fast photorefractive self-focusing in InP: Fe semiconductor at infrared wavelengths*, *Applied Physics Letters* **92**, 021106 (2008).
- [9] M. Alonzo, C. Dan, D. Wolfersberger, and E. Fazio: *Coherent collisions of infrared self-trapped beams in photorefractive InP:Fe*, *Applied Physics Letters* **96**, 121111 (2010).
- [10] C. Dan, D. Wolfersberger, and N. Fressengeas: *Experimental control of steady state photorefractive self-focusing in InP: Fe at infrared wavelengths*, *Applied Physics B* **104**, 887 (2011).

## BIBLIOGRAPHY

---

- [11] N. Wiersma, N. Marsal, M. Sciamanna, and D. Wolfersberger: *All-optical interconnects using Airy beams*, Opt. Lett. **39**, 5997 (2014).
- [12] U. Levy, S. Derevyanko, and Y. Silberberg: *Progress in Optics* (Elsevier, Amsterdam, 2016), pp. 237–281.
- [13] G. A. Siviloglou and D. N. Christodoulides: *Accelerating finite energy Airy beams*, Opt. Lett. **32**, 979 (2007).
- [14] G. A. Siviloglou, J. Broky, A. Dogariu, and D. N. Christodoulides: *Observation of Accelerating Airy Beams*, Physical Review Letters **99**, (2007).
- [15] M. V. Berry and N. L. Balazs: *Nonspreading wave packets*, Am. J. Phys **47**, 264 (1979).
- [16] M. A. Bandres, I. Kaminer, M. Mills, B. Rodríguez-Lara, E. Greenfield, M. Segev, and D. N. Christodoulides: *Accelerating optical beams*, Optics and Photonics News **24**, 30 (2013).
- [17] J. Broky, G. A. Siviloglou, A. Dogariu, and D. N. Christodoulides: *Self-healing properties of optical Airy beams*, Optics Express **16**, 12880 (2008).
- [18] A. Chong, W. H. Renninger, D. N. Christodoulides, and F. W. Wise: *Airy–Bessel wave packets as versatile linear light bullets*, Nature Photonics **4**, 103 (2010).
- [19] D. Abdollahpour, S. Suntsov, D. G. Papazoglou, and S. Tzortzakis: *Spatiotemporal Airy Light Bullets in the Linear and Nonlinear Regimes*, Physical Review Letters **105**, (2010).
- [20] D. Bongiovanni, B. Wetzell, Y. Hu, Z. Chen, and R. Morandotti: *Optimal compression and energy confinement of optical Airy bullets*, Optics Express **24**, 26454 (2016).
- [21] W.-P. Zhong, M. R. Belić, and T. Huang: *Three-dimensional finite-energy Airy self-accelerating parabolic-cylinder light bullets*, Physical Review A **88**, (2013).
- [22] F. Deng and D. Deng: *Three-dimensional localized Airy-Hermite-Gaussian and Airy-Helical-Hermite-Gaussian wave packets in free space*, Optics Express **24**, 5478 (2016).
- [23] N. J. Zabusky and M. D. Kruskal: *Interaction of "Solitons" in a Collisionless Plasma and the Recurrence of Initial States*, Physical Review Letters **15**, 240 (1965).

- 
- [24] E. Garmire, R. Y. Chiao, and C. H. Townes: *Dynamics and Characteristics of the Self-Trapping of Intense Light Beams*, Physical Review Letters **16**, 347 (1966).
- [25] A. Barthelemy, S. Maneuf, and C. Froehly: *Propagation soliton et auto-confinement de faisceaux laser par non linearité optique de Kerr*, Opt. Commun. **55**, 201 (1985).
- [26] P. L. Kelley: *Self-Focusing of Optical Beams*, Physical Review Letters **15**, 1005 (1965).
- [27] J. Aitchison, A. Weiner, Y. Silberberg, M. Oliver, J. Jackel, D. Leaird, E. Vogel, and P. Smith: *Observation of spatial optical solitons in a nonlinear glass waveguide*, Optics letters **15**, 471 (1990).
- [28] M. Segev, B. Crosignani, A. Yariv, and B. Fischer: *Spatial solitons in photorefractive media*, Physical Review Letters **68**, 923 (1992).
- [29] G. C. Duree Jr, J. L. Shultz, G. J. Salamo, M. Segev, A. Yariv, B. Crosignani, P. Di Porto, E. J. Sharp, and R. R. Neurgaonkar: *Observation of self-trapping of an optical beam due to the photorefractive effect*, Physical Review Letters **71**, 533 (1993).
- [30] M. Segev and G. Stegeman: *Self-Trapping of Optical Beams: Spatial Solitons*, Physics Today **51**, 42 (1998).
- [31] Z. Chen, M. Segev, and D. N. Christodoulides: *Optical spatial solitons: historical overview and recent advances*, Rep. Prog. Phys. **75**, 086401 (2012).
- [32] M. feng Shih, M. Segev, and G. Salamo: *Three-Dimensional Spiraling of Interacting Spatial Solitons*, Physical Review Letters **78**, 2551 (1997).
- [33] F. Reynaud and A. Barthelemy: *Optically Controlled Interaction Between Two Fundamental Soliton Beams*, Europhysics Letters **12**, 401 (1990).
- [34] A. Lotti, D. Faccio, A. Couairon, D. Papazoglou, P. Panagiotopoulos, D. Abdollahpour, and S. Tzortzakis: *Stationary nonlinear Airy beams*, Physical Review A **84**, 021807 (2011).
- [35] I. Kaminer, M. Segev, and D. N. Christodoulides: *Self-accelerating self-trapped optical beams*, Phys. Rev. Lett. **106**, 213903 (2011).

## BIBLIOGRAPHY

---

- [36] P. Panagiotopoulos, D. Abdollahpour, A. Lotti, A. Couairon, D. Faccio, D. Papazoglou, and S. Tzortzakis: *Nonlinear propagation dynamics of finite-energy Airy beams*, Phys. Rev. A **86**, 013842 (2012).
- [37] S. Jia, J. Lee, J. W. Fleischer, G. A. Siviloglou, and D. N. Christodoulides: *Diffusion-trapped Airy beams in photorefractive media*, Physical review letters **104**, 253904 (2010).
- [38] P. Rose, F. Diebel, M. Boguslawski, and C. Denz: *Airy beam induced optical routing*, Appl. Phys. Lett. **102**, 101101 (2013).
- [39] Y. Zhang, M. Belić, Z. Wu, H. Zheng, K. Lu, Y. Li, and Y. Zhang: *Soliton pair generation in the interactions of Airy and nonlinear accelerating beams*, Opt. Lett. **38**, 4585 (2013).
- [40] N. Wiersma, N. Marsal, M. Sciamanna, and D. Wolfersberger: *Spatiotemporal dynamics of counterpropagating Airy beams*, Sci. Rep. **5**, 13463 (2015).
- [41] N. Wiersma, N. Marsal, M. Sciamanna, and D. Wolfersberger: *Airy beam self-focusing in a photorefractive medium*, Sci. Rep. **6**, 35078 (2016).
- [42] R. Bekenstein and M. Segev: *Self-accelerating optical beams in highly nonlocal nonlinear media*, Optics Express **19**, 23706 (2011).
- [43] Z. Ye, S. Liu, C. Lou, P. Zhang, Y. Hu, D. Song, J. Zhao, and Z. Chen: *Acceleration control of Airy beams with optically induced refractive-index gradient*, O **36**, 3230 (2011).
- [44] F. Xiao, B. Li, M. Wang, W. Zhu, P. Zhang, S. Liu, M. Premaratne, and J. Zhao: *Optical Bloch oscillations of an Airy beam in a photonic lattice with a linear transverse index gradient*, Optics Express **22**, 22763 (2014).
- [45] F. Diebel, B. M. Bokić, M. Boguslawski, A. Piper, D. V. Timotijević, D. M. Jović, and C. Denz: *Control of Airy-beam self-acceleration by photonic lattices*, Physical Review A **90**, (2014).
- [46] Y. Hu, Z. Sun, D. Bongiovanni, D. Song, C. Lou, J. Xu, Z. Chen, and R. Morandotti: *Reshaping the trajectory and spectrum of nonlinear Airy beams*, Opt. Lett. **37**, 3201 (2012).

- [47] A. Ashkin, G. D. Boyd, J. M. Dziedzic, R. G. Smith, A. A. Ballman, J. J. Levinstein, and K. Nassau: *Optically-induced refractive index inhomogeneities in LiNbO<sub>3</sub> AND LiTaO<sub>3</sub>*, Applied Physics Letters **9**, 72 (1966).
- [48] F. S. Chen, J. T. LaMacchia, and D. B. Fraser: *Holographic storage in lithium niobate*, Applied Physics Letters **13**, 223 (1968).
- [49] M. Morin, G. Duree, G. Salamo, and M. Segev: *Waveguides formed by quasi-steady-state photorefractive spatial solitons*, Optics letters **20**, 2066 (1995).
- [50] N. K. Efremidis, Z. Chen, M. Segev, and D. N. Christodoulides: *Airy beams and accelerating waves: an overview of recent advances*, Optica **6**, 686 (2019).
- [51] G. A. Siviloglou, J. Broky, A. Dogariu, and D. N. Christodoulides: *Ballistic dynamics of Airy beams*, Optics Letters **33**, 207 (2008).
- [52] Y. Hu, P. Zhang, C. Lou, S. Huang, J. Xu, and Z. Chen: *Optimal control of the ballistic motion of Airy beams*, Optics letters **35**, 2260 (2010).
- [53] R.-S. Penciu, V. Paltoglou, and N. K. Efremidis: *Closed-form expressions for non-paraxial accelerating beams with pre-engineered trajectories*, Optics letters **40**, 1444 (2015).
- [54] I. M. Besieris and A. M. Shaarawi: *A note on an accelerating finite energy Airy beam*, Optics Letters **32**, 2447 (2007).
- [55] P. Polynkin, M. Kolesik, J. V. Moloney, G. A. Siviloglou, and D. N. Christodoulides: *Curved plasma channel generation using ultraintense Airy beams*, Science **324**, 229 (2009).
- [56] J. Baumgartl, M. Mazilu, and K. Dholakia: *Optically mediated particle clearing using Airy wavepackets*, Nat. Photonics **2**, 675 (2008).
- [57] P. Zhang, S. Wang, Y. Liu, X. Yin, C. Lu, Z. Chen, and X. Zhang: *Plasmonic Airy beams with dynamically controlled trajectories*, Optics Letters **36**, 3191 (2011).
- [58] A. Mathis, F. Courvoisier, L. Froehly, L. Furfaro, M. Jacquot, P. A. Lacourt, and J. M. Dudley: *Micromachining along a curve: Femtosecond laser micromachining of curved profiles in diamond and silicon using accelerating beams*, Applied Physics Letters **101**, 071110 (2012).

- [59] T. Bouchet, N. Marsal, M. Sciamanna, and D. Wolfersberger: *Light-induced interconnects using nonlinear Airy beam interactions*, Journal of Physics: Photonics (2018).
- [60] T. Vettenburg, H. I. Dalgarno, J. Nylk, C. Coll-Lladó, D. E. Ferrier, T. Čížmár, F. J. Gunn-Moore, and K. Dholakia: *Light-sheet microscopy using an Airy beam*, Nat. Methods **11**, 541 (2014).
- [61] N. K. Efremidis and D. N. Christodoulides: *Abruptly autofocusing waves*, Optics Letters **35**, 4045 (2010).
- [62] D. G. Papazoglou, N. K. Efremidis, D. N. Christodoulides, and S. Tzortzakis: *Observation of abruptly autofocusing waves*, Optics Letters **36**, 1842 (2011).
- [63] I. Chremmos, N. K. Efremidis, and D. N. Christodoulides: *Pre-engineered abruptly autofocusing beams*, Optics Letters **36**, 1890 (2011).
- [64] D. McGloin and K. Dholakia: *Bessel beams: Diffraction in a new light*, Contemporary Physics **46**, 15 (2005).
- [65] C. M. Crandall: in *Advanced Imaging Technologies and Commercial Applications*, International Society for Optics and Photonics, Ed.: N. Clark and J. D. Gonglewski (SPIE, Bellingham, 1995), **2566**, pp. 4 – 10.
- [66] G. Porat, I. Dolev, O. Barlev, and A. Arie: *Airy beam laser*, Optics Letters **36**, 4119 (2011).
- [67] H. Deng and L. Yuan: *Two-dimensional Airy-like beam generation by coupling waveguides*, Journal of the Optical Society of America A **30**, 1404 (2013).
- [68] P. Acebal, L. Carretero, S. Blaya, and A. Murciano: *Generation of high-quality tunable one-dimensional Airy beams using the aberrations of a single lens*, IEEE Photonics Journal **4**, 1273 (2012).
- [69] T. Ellenbogen, N. Voloch-Bloch, A. Ganany-Padowicz, and A. Arie: *Nonlinear generation and manipulation of Airy beams*, Nature Photonics **3**, 395 (2009).
- [70] B. K. Singh, R. Remez, Y. Tsur, and A. Arie: *Super-Airy beam: self-accelerating beam with intensified main lobe*, Optics Letters **40**, 4703 (2015).

- 
- [71] O. Solgaard: in *Photonic Microsystems*, Ed.: A. J. R. Stephen D. Senturia, Robert T. Howe (Springer, New York, 2009).
- [72] D. Armitage, I. Underwood, and S.-T. Wu: in *Introduction to Microdisplays*, 1st edition, Ed.: A. C. Lowe (John Wiley & Sons/Society for Information Display, Hoboken, 2006).
- [73] G. Lazarev, A. Hermerschmidt, S. Krüger, and S. Osten: in *Optical Imaging and Metrology: Advanced Technologies*, 1st edition, Ed.: W. Osten and N. Reingand (Wiley-VCH Verlag GmbH & Co. KGaA, Weinheim, 2012), Chap. 1, pp. 1–29.
- [74] P. J. Collings, M. R. Fisch, and M. A. Mooney: *Liquid Crystals: Nature's Delicate Phase of Matter*, American Journal of Physics **60**, 958 (1992).
- [75] N. Wiersma: *Photorefractive self-focusing of Airy beams: nonlinear interactions and all-optical waveguiding*, Physics, Université de Lorraine, 2016.
- [76] J. E. Morris, M. Mazilu, J. Baumgartl, T. Cizmar, and K. Dholakia: *Propagation characteristics of Airy beams: dependence upon spatial coherence and wavelength*, Optics Express **17**, 13236 (2009).
- [77] A. Constantin and D. Henry: *Solitons and Tsunamis*, Zeitschrift für Naturforschung A **64**, (2009).
- [78] A. Menhofer, R. K. Smith, M. J. Reeder, and D. R. Christie: “*Morning-Glory*” *Disturbances and the Environment in which They Propagate*, Journal of the atmospheric sciences **54**, 1712 (1997).
- [79] J. S. Russell: *Report on Waves: Made to the Meetings of the British Association in 1842-43* (Richard and John E. Taylor, Red Lion Court, London, 1845).
- [80] R. K. Bullough: *Solitons* (Springer, Berlin, 1988), pp. 7–42.
- [81] J. Boussinesq: *Essai sur la théorie des eaux courantes* (Impr. nationale, Paris, 1877).
- [82] G. de Vries and D. Korteweg: *On the change of form of long waves advancing in a rectangular canal, and on a new type of long stationary waves*, Phil. Mag **39**, 422 (1895).

## BIBLIOGRAPHY

---

- [83] R. M. Miura: *Korteweg-de Vries Equation and Generalizations. I. A Remarkable Explicit Nonlinear Transformation*, Journal of Mathematical Physics **9**, 1202 (1968).
- [84] C. S. Gardner, J. M. Greene, M. D. Kruskal, and R. M. Miura: *Method for Solving the Korteweg-deVries Equation*, Physical Review Letters **19**, 1095 (1967).
- [85] V. E. Zakharov and A. Shabat: *Exact Theory of TwoDimensional Self-Focusing and OneDimensional Self-Modulation of Waves in Nonlinear Media*, Journal of Experimental and Theoretical Physics **34**, 62 (1972).
- [86] R. Y. Chiao, E. Garmire, and C. H. Townes: *Self-trapping of optical beams*, Phys. Rev. Lett. **13**, 479 (1964).
- [87] F. W. Dabby and J. R. Whinnery: *Thermal self-focusing of laser beams in lead glasses*, Applied Physics Letters **13**, 284 (1968).
- [88] J. Bjorkholm and A. Ashkin: *CW self-focusing and self-trapping of light in sodium vapor*, Physical Review Letters **32**, 129 (1974).
- [89] W. Krolikowski, B. Luther-Davies, and C. Denz: *Photorefractive solitons*, IEEE Journal of Quantum Electronics **39**, 3 (2003).
- [90] M. feng Shih, M. H. Garrett, G. Salamo, G. C. Valley, P. Leach, and M. Segev: *Two-dimensional steady-state photorefractive screening solitons*, Optics Letters **21**, 324 (1996).
- [91] D. L. Staebler and W. Phillips: *Hologram storage in photochromic LiNbO<sub>3</sub>*, Applied Physics Letters **24**, 268 (1974).
- [92] J. F. Lam: *Origin of phase conjugate waves in self-pumped photorefractive mirrors*, Applied Physics Letters **46**, 909 (1985).
- [93] G. Pauliat and G. Roosen: *L'effet photoréfractif*, 1998.
- [94] G. Montemezzani, C. Medrano, M. Zgonik, and P. Günter: *The Photorefractive Effect in Inorganic and Organic Materials*, 2000.
- [95] N. Kukhtarev, V. Markov, S. Odulov, M. Soskin, and V. Vinetskii: *Holographic storage in electrooptic crystals. I. Steady state*, Ferroelectrics **22**, 949 (1978).

- 
- [96] E. DelRe, A. Ciattoni, B. Crosignani, and M. Tamburrini: *Approach to space-charge field description in photorefractive crystals*, Journal of the Optical Society of America B **15**, 1469 (1998).
- [97] E. DelRe and M. Segev: in *Self-focusing and solitons in photorefractive media* (Springer, New York, 2009), pp. 547–572.
- [98] K. Kos, H. Meng, G. Salamo, M.-f. Shih, M. Segev, and G. C. Valley: *One-dimensional steady-state photorefractive screening solitons*, Physical Review E **53**, R4330 (1996).
- [99] T. Bouchet, N. Marsal, M. Sciamanna, and D. Wolfersberger: *Solitonic characteristics of Airy beam nonlinear propagation*, Physical Review A **97**, 051801 (2018).
- [100] Y. Zhang, M. R. Belić, L. Zhang, W. Zhong, D. Zhu, R. Wang, and Y. Zhang: *Periodic inversion and phase transition of finite energy Airy beams in a medium with parabolic potential.*, Optics express **23**, 10467 (2015).
- [101] Y. Zhang, M. R. Belić, H. Zheng, H. Chen, C. Li, Y. Li, and Y. Zhang: *Interactions of Airy beams, nonlinear accelerating beams, and induced solitons in Kerr and saturable nonlinear media*, Optics express **22**, 7160 (2014).
- [102] M. Belić, P. Jander, K. Motzek, A. Desyatnikov, D. Jović, A. Strinić, M. Petrović, C. Denz, and F. Kaiser: *Counterpropagating self-trapped beams in photorefractive crystals*, J. Opt. B: Quantum Semiclassical Opt. **6**, S190 (2004).
- [103] L. Allen, M. Padgett, and M. Babiker: *IV The orbital angular momentum of light*, Progress in optics **39**, 291 (1999).
- [104] D. Faccio, A. Lotti, A. Matijosius, F. Bragheri, V. Degiorgio, A. Couairon, and P. Di Trapani: *Experimental energy-density flux characterization of ultrashort laser pulse filaments*, Opt. Express **17**, 8193 (2009).
- [105] H. Meng, G. Salamo, and M. Segev: *Primarily isotropic nature of photorefractive screening solitons and the interactions between them*, Optics letters **23**, 897 (1998).
- [106] M. feng Shih and M. Segev: *Incoherent collisions between two-dimensional bright steady-state photorefractive spatial screening solitons*, Optics Letters **21**, 1538 (1996).

- [107] B. Crosignani, P. D. Porto, A. Degasperis, M. Segev, and S. Trillo: *Three-dimensional optical beam propagation and solitons in photorefractive crystals*, Journal of the Optical Society of America B **14**, 3078 (1997).
- [108] A. V. Buryak, Y. S. Kivshar, M.-f. Shih, and M. Segev: *Induced coherence and stable soliton spiraling*, Physical review letters **82**, 81 (1999).
- [109] A. A. Zozulya, D. Z. Anderson, A. V. Mamaev, and M. Saffman: *Self-focusing and soliton formation in media with anisotropic nonlocal material response*, Europhysics Letters **36**, 419 (1996).
- [110] A. A. Zozulya, D. Z. Anderson, A. V. Mamaev, and M. Saffman: *Solitary attractors and low-order filamentation in anisotropic self-focusing media*, Physical Review A **57**, 522 (1998).
- [111] F. Devaux, V. Coda, M. Chauvet, and R. Passier: *New time-dependent photorefractive three-dimensional model: application to self-trapped beam with large bending*, JOSA B **25**, 1081 (2008).
- [112] F. Devaux and M. Chauvet: *Three-dimensional numerical model of the dynamics of photorefractive beam self-focusing in InP:Fe*, Physical Review A **79**, (2009).
- [113] C. Dan, D. Wolfersberger, and N. Fressengeas: *Experimental control of steady state photorefractive self-focusing in InP:Fe at infrared wavelengths*, Applied Physics B **104**, 887 (2011).
- [114] S. Gatz and J. Herrmann: *Anisotropy, nonlocality, and space-charge field displacement in  $(2 + 1)$ -dimensional self-trapping in biased photorefractive crystals*, Optics Letters **23**, 1176 (1998).
- [115] M. R. Belić, D. Vujić, A. Stepken, F. Kaiser, G. F. Calvo, F. Agulló-López, and M. Carrascosa: *Isotropic versus anisotropic modeling of photorefractive solitons*, Physical Review E **65**, (2002).
- [116] G. Calvo, F. Agulló-López, M. Carrascosa, M. Belić, and D. Vujić: *Two-dimensional soliton-induced refractive index change in photorefractive crystals*, Optics Communications **227**, 193 (2003).
- [117] F. Diebel, B. M. Bokić, D. V. Timotijević, D. M. J. Savić, and C. Denz: *Soliton formation by decelerating interacting Airy beams*, Optics Express **23**, 24351 (2015).

- [118] J. Petter, C. Weillnau, C. Denz, A. Stepken, and F. Kaiser: *Self-bending of photorefractive solitons*, Optics Communications **170**, 291 (1999).
- [119] D. Christodoulides and M. Carvalho: *Compression, self-bending, and collapse of Gaussian beams in photorefractive crystals*, Optics letters **19**, 1714 (1994).
- [120] *Holographic Data Storage*, Ed.: H. J. Coufal, D. Psaltis, and G. T. Sincerbox (Springer Berlin Heidelberg, Berlin, 2000).
- [121] K. Iizuka: *Wiley Series in Pure and Applied Optics* (John Wiley & Sons, Inc., Hoboken, 2002), Chap. 5, pp. 302–361.
- [122] C. C. Chang: *Photorefractive Multi-Beam Induced Phase Conjugation*, Optical Review **4**, 556 (1997).
- [123] H. A. Eggert, F. Y. Kuhnert, K. Buse, J. R. Adleman, and D. Psaltis: *Trapping of dielectric particles with light-induced space-charge fields*, Applied Physics Letters **90**, 241909 (2007).
- [124] C. Denz: in *Optical Neural Networks*, Ed.: T. Tschudi (Vieweg+Teubner Verlag, Berlin, 1998).
- [125] J. P. Gordon: *Interaction forces among solitons in optical fibers*, Optics Letters **8**, 596 (1983).
- [126] M. Shalaby, F. Reynaud, and A. Barthelemy: *Experimental observation of spatial soliton interactions with a  $\pi/2$  relative phase difference*, Optics Letters **17**, 778 (1992).
- [127] G. I. Stegeman: *Optical Spatial Solitons and Their Interactions: Universality and Diversity*, Science **286**, 1518 (1999).
- [128] Z. Chen, M. Mitchell, and M. Segev: *Steady-state photorefractive soliton-induced Y-junction waveguides and high-order dark spatial solitons*, Optics letters **21**, 716 (1996).
- [129] M. feng Shih, Z. Chen, M. Mitchell, M. Segev, H. Lee, R. S. Feigelson, and J. P. Wilde: *Waveguides induced by photorefractive screening solitons*, Journal of the Optical Society of America B **14**, 3091 (1997).

- [130] S. Lan, E. DelRe, Z. Chen, M.-f. Shih, and M. Segev: *Directional coupler with soliton-induced waveguides*, Optics letters **24**, 475 (1999).
- [131] M. Shen, W. Li, and R.-K. Lee: *Control on the anomalous interactions of Airy beams in nematic liquid crystals*, Optics express **24**, 8501 (2016).
- [132] Z. Shi, J. Xue, X. Zhu, Y. Xiang, and H. Li: *Interaction of Airy-Gaussian beams in photonic lattices with defects*, Physical Review E **95**, 042209 (2017).
- [133] T. Mayteevarunyoo and B. A. Malomed: *The interaction of Airy waves and solitons in a three-wave system*, Journal of Optics **19**, 085501 (2017).
- [134] M. Zhang, G. Huo, H. Zhong, and Z. Hui: *Interactions between self-accelerating beams in photorefractive media*, Optics express **25**, 22104 (2017).
- [135] M. Shen, L. Wu, M. Gao, and W. Li: *Incoherent interactions of Airy beams in nonlocal nonlinear media*, Journal of Physics B: Atomic, Molecular and Optical Physics **51**, 165401 (2018).
- [136] H. Zhong, Y. Zhang, M. R. Belić, C. Li, F. Wen, Z. Zhang, and Y. Zhang: *Controllable circular Airy beams via dynamic linear potential*, Optics express **24**, 7495 (2016).
- [137] R. Bekenstein, R. Schley, M. Mutzafi, C. Rotschild, and M. Segev: *Optical simulations of gravitational effects in the Newton–Schrödinger system*, Nature Physics **11**, nphys3451 (2015).
- [138] Z. Chen, M.-f. Shih, M. Segev, D. W. Wilson, R. E. Muller, and P. D. Maker: *Steady-state vortex-screening solitons formed in biased photorefractive media*, Optics letters **22**, 1751 (1997).
- [139] L. Xue, H. Liu, D. Zheng, S. Saeed, X. Wang, T. Tian, L. Zhu, Y. Kong, S. Liu, S. Chen, *et al.*: *The Photorefractive Response of Zn and Mo Codoped LiNbO<sub>3</sub> in the Visible Region*, Crystals **9**, 228 (2019).

**Solitonic characteristics of Airy beam nonlinear propagation**

Thomas Bouchet, Nicolas Marsal, Marc Sciamanna, and Delphine Wolfersberger  
*Chair in Photonics, LMOPS, CentraleSupélec, Université Paris-Saclay, F-57070 Metz, France*  
*and Chair in Photonics, LMOPS, CentraleSupélec, Université de Lorraine, F-57070 Metz, France*



(Received 27 September 2017; published 17 May 2018)

We analyze the nonlinear propagation of a one-dimensional Airy beam. Under nonlinear focusing conditions, the Airy beam splits into a weak accelerating structure and a beam that has been named an “off-shooting soliton.” Experimental measurements and numerical results related to the off-shooting Airy beam are compared to soliton theoretical profiles and a good agreement is found in terms of transverse shape, width, and amplitude. We identify the different parameters to generate an Airy beam off-shooting soliton and demonstrate that its profile is also preserved through propagation over long distances.

DOI: [10.1103/PhysRevA.97.051801](https://doi.org/10.1103/PhysRevA.97.051801)

Dispersion-free Airy wave packets were first predicted by Berry and Balazs in the context of quantum mechanics [1]. By truncating the ideal Airy wave form, and applying it in optics, the first optical Airy beam was observed in 2007 [2]. Contrary to the ideal Airy solution in quantum mechanics, an optical Airy beam displays a finite energy but it retains a shape-preserving accelerating propagation over a finite distance and self-healing properties. Such unique features offer a large range of applications in a variety of domains, such as optical micromanipulation [3], plasma channel generation [4], all-optical routing [5,6], or light-sheet microscopy [7].

Recently, the self-trapping of Airy beams in biased nonlinear media has suggested interesting dynamics, such as soliton-like behaviors and interactions of co- and counterpropagating Airy beams [8–12]. In particular, under focusing nonlinear conditions, the Airy beam may split into a weak accelerating structure and a structure that has been named an “off-shooting soliton” (OSS) and that propagates along the medium without transverse acceleration [13]. The interactions between the photoinduced OSS and the accelerating beam have been studied recently [14], resulting in attraction, deflection, and tightening effects of the OSS and interesting analogies with gravitational lensing and tidal forces. The OSS has also been studied in the context of optical interconnects, offering more complex all-optical waveguiding possibilities than those achieved with Gaussian beams [6]. These two configurations suggest that the OSSs share properties that are typically attributed to spatial solitons.

In spite of these recent achievements, one question remains of interest: Is the Airy beam OSS a spatial soliton? To answer this question, it is worth reminding what defines a soliton. An optical soliton is a solitary wave packet that propagates at a constant velocity and maintains its shape due to nonlinear effects compensating dispersive effects. Particularly, spatial solitons are self-trapped beams of light that propagate while maintaining their shape due to the nonlinear effect compensating the diffraction of the propagating beam [15]. Optical solitons have been studied extensively for the past three decades in a variety of domains [16], in particular, in

photorefractive media where they appear to be stable in one and two transverse dimensions [17].

In this Rapid Communication, we study and analyze both experimentally and theoretically the nonlinear propagation of a one-dimensional (1D) Airy beam in a  $\text{Sr}_x\text{Ba}_{1-x}\text{Nb}_2\text{O}_6$  (SBN) photorefractive crystal. Under nonlinear focusing conditions, as expected, the Airy beam splits into a weak accelerating structure and an OSS. We demonstrate that the OSS matches with the theoretical soliton profile in terms of width and amplitude. We also prove that its profile remains unchanged during propagation. Finally, we analyze the OSS output position and width behavior versus its amplitude and show that its characteristics match the existence curve of the theoretical spatial soliton.

As depicted in Fig. 1(a), our experiment consists of propagating a one-dimensional Airy beam into a biased photorefractive SBN crystal with dimensions  $5\text{ mm} \times 5\text{ mm} \times 2\text{ cm}$ . The Airy beam is generated using a cubic phase modulation on a spatial light modulator [2]. We observe the profile of the Airy beam OSS at the output face of the crystal using a CCD camera. When a bias external electrical field is applied along the crystal  $c$  axis, the optical Airy beam photoinduces a refractive index variation inside the crystal through the Pockels effect. For high enough nonlinearity strength, most of the beam turns into a so-called off-shooting soliton, while a small fraction of the power remains a self-accelerating linear packet [13,14]. Figures 1(b)–1(d) show the beam output captured on the camera with and without an external electric field applied. The experimental transverse profile of each OSS [Fig. 1(e)] is extracted from the brightest areas of Figs. 1(c) and 1(d). We can note that the OSS width and amplitude can be controlled by changing the voltage applied to the crystal. The analysis of each profile and their comparison to a theoretical soliton profile is done using the following theory described in Ref. [18] that was developed for solitons.

A one-dimensional steady-state bright screening soliton profile is described by the following reduced wave equation [18],

$$\frac{d^2u}{d\xi^2} + \frac{u}{u_0^2} \ln(1 + u_0^2) - \frac{u}{1 + u^2} = 0, \quad (1)$$

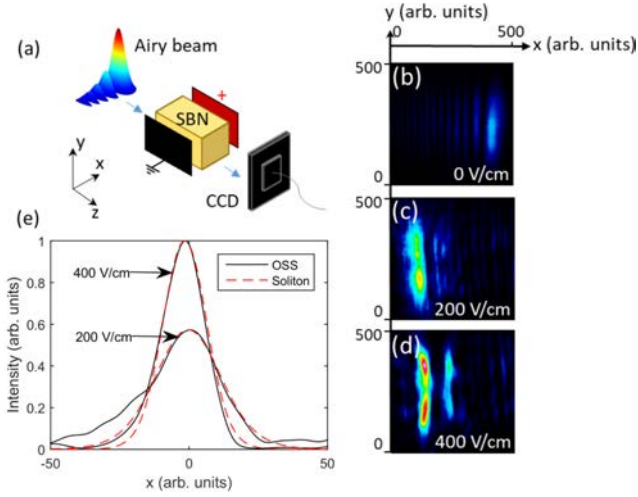


FIG. 1. (a) Schematic of the experimental setup: 1D Airy beam propagating in a 2-cm-long SBN crystal ( $x_0 = 10$ ,  $a = 0, 1$ ). (b) Observation of the Airy beam at the crystal output face on the camera with no electric field  $E_{\text{ext}}$  applied. (c), (d) Observation of the OSS at the crystal output face on the CCD camera ( $E_{\text{ext}} = V/l = 200$  and  $400$  V/cm). (e) Corresponding experimental Airy beam OSS profile extracted from the camera and theoretical classic soliton fit ( $E_{\text{ext}} = 200$  or  $400$  V/cm and  $P_A = 50$   $\mu$ W).

whose first integral is

$$\frac{du}{d\xi} = [\ln(1 + u^2) - (u^2/u_0^2) \ln(1 + u_0^2)]^{1/2}, \quad (2)$$

and where  $u(\xi)$  is the soliton amplitude divided by the square root of the effective background intensity (defined as the sum of the background and dark intensities induced respectively by an external homogeneous illumination of the crystal and the intrinsic thermal excitation of charges inside the crystal),  $\xi = x/d$  is the transverse coordinate normalized by  $d = (k^2 n_b^2 r_{\text{eff}} V/l)^{-1/2}$ ,  $u_0$  is the maximum amplitude of the soliton at  $\xi = 0$ ,  $k = 2\pi n_b/\lambda$  is the wave vector,  $n_b$  is the unperturbed refractive index,  $\lambda$  is the wavelength,  $r_{\text{eff}}$  is the effective component of the electro-optic tensor,  $V$  is the voltage applied onto the crystal, and  $l$  is the crystal's width.

Equation (2) can be solved using a Runge-Kutta method in order to obtain the theoretical soliton profile. In practice, this means that for each different nonlinear condition corresponding to the  $d$  criteria and maximum soliton amplitude  $u_0$ , we obtain a different soliton profile. Once  $d$  and  $u_0$  are determined from our experiment ( $n_b = 2.3$ ,  $r_{\text{eff}} = 235$  pm/V,  $V = 100$  or  $200$  V, and  $l = 0.5$  cm), we therefore have access to the corresponding theoretical soliton profile whose plot is superimposed in Fig. 1(e) with the transverse experimental profiles. We evidence that under a focusing condition, the Airy beam sheds an OSS whose profile matches the theoretical soliton profile.

Although the experimental profile of the OSS fits with the theoretical soliton profile, it is worth mentioning that experimentally we only image the output and input faces of the crystal due to the nonhomogeneous refractive index that alters the imaging system inside the medium. In order to observe the formation and evolution of the OSS inside the crystal

versus different parameters (crystal length or beam intensity, for example), we use a numerical model to simulate the OSS propagation. In what follows, we numerically propagate a 1+1D Airy beam in a photorefractive medium. The model is similar to the one presented in Refs. [6,12,14,19]. The normalized nonlinear Schrödinger equation reads

$$i\partial_z F + \partial_x^2 F = \Gamma E_0 F, \quad (3)$$

where  $F$  is the beam's electric field amplitude,  $\Gamma = (kn_0 x_0)^2 r_{\text{eff}} E_e$  is the nonlinear photorefractive coupling strength, and  $E_e$  is the external electric field.  $E_0$  is the homogeneous part of the  $x$  component of the photorefractive space-charge field normalized by the external electric field applied. The temporal evolution of the space-charge field  $E_0$  is considered with saturable nonlinearity and calculated using a relaxation-type dynamic,

$$\tau \partial_t E_0 + E_0 = -\frac{I}{1+I}, \quad (4)$$

where the relaxation time of the crystal  $\tau$  is inversely proportional to the total intensity  $\tau = \frac{\tau_0}{1+I}$ , and  $I = |F|^2$  is the intensity normalized by the effective background intensity.

The beam propagates along the  $z$  axis, and has a truncated Airy beam transverse profile upon injection at  $z = 0$ ,

$$F(x, z = 0) = F_0 \text{Ai}\left(\frac{x}{x_0}\right) e^{a \frac{x}{x_0}}, \quad (5)$$

where  $F_0$  is the total amplitude of the Airy beam, Ai is the Airy function,  $x_0$  is the Airy beam's main lobe waist at  $1/e$  of its maximum intensity, and  $a$  is the truncation parameter.

Based on this model, we numerically propagate a 1+1D Airy beam in a photorefractive medium using a beam propagation method within a temporal loop that recalculates the electric field inside the crystal at each time iteration. The study is done once steady state is reached (more than  $50\tau$ ).

Figure 2(a) shows the linear propagation at steady state of the 1D Airy beam along the  $z$  axis of a photorefractive medium. Similar to Ref. [6] and in order to fit to the experiment presented here, the truncation and waist parameters are  $x_0 = 10$   $\mu$ m and  $a = 0.1$ . As expected, we observe a curved trajectory for a 2-cm propagation length inside the medium.

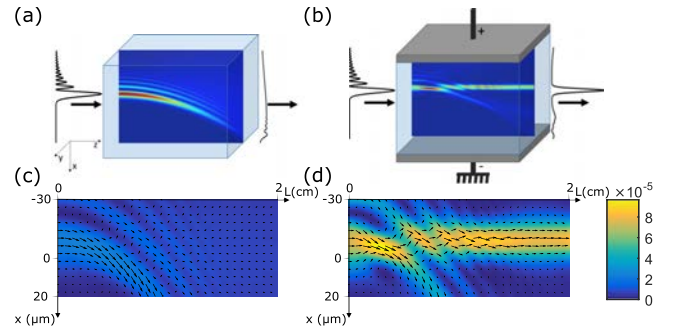


FIG. 2. Propagation of a 1D Airy beam in a 2-cm-long photorefractive crystal at steady state. (a) Linear propagation ( $\Gamma = 0$ ). (b) Nonlinear propagation in the presence of an external electric field leading to an OSS ( $\Gamma = 10$ ,  $F_0 = 1.95$ ,  $x_0 = 10$   $\mu$ m,  $a = 0.1$ ). (c), (d) Distribution of the refractive index change vs  $x$  and  $z$  at steady state. Arrows represent the Poynting vector. (c)  $\Gamma = 3$ . (d)  $\Gamma = 10$ .

Moreover, our numerical simulation reproduces qualitatively well our experimental result since, similarly to the experiment in Fig. 1, when an external electric field is applied ( $\Gamma > 0$ ), we numerically observe the shedding of an OSS from the original Airy beam [Fig. 2(b)]. It is worth noting that for a smaller apodization factor we observe several off-shooting beams in different directions of propagation (similar to Ref. [9] in Kerr media). In our study we decided to focus on the OSS which does not deviate from the propagation axis.

Figure 2(c) [respectively Fig. 2(d)] represents the photoinduced distribution of the refractive index change  $\Delta n = -\frac{n_0^3}{2} r_{\text{eff}} E_{sc}$  inside the crystal for  $\Gamma = 3$  (respectively  $\Gamma = 10$ ) versus  $x$  and  $z$ . To gain further insight, we superimpose the time-averaged Poynting vector  $\langle \vec{S} \rangle$  using the following equation from Refs. [20,21],

$$\langle \vec{S} \rangle = i\omega \frac{\epsilon_0}{2} \left( F_x \frac{\partial F_x^*}{\partial x} - F_x^* \frac{\partial F_x}{\partial x} \right) \vec{u}_x + \omega k \epsilon_0 |F|^2 \vec{u}_z, \quad (6)$$

where  $\epsilon_0$  is the vacuum permittivity and  $\omega = ck$  with  $c$  the speed of light. Increasing the nonlinearity  $\Gamma$  leads to the creation of a photoinduced waveguide that modifies the beam's propagation. The arrows show how energy is transferred from the main lobe to the second lobe which is then transferred to the next lobes, hence explaining the creation of the OSS.

We now propose to compare the numerical OSS with the theoretical soliton and analyze its behavior versus  $u_0$ . We therefore link the two models using

$$d = \frac{x_0}{\sqrt{\Gamma}}, \quad (7)$$

and fix the maximum amplitude of the Airy beam OSS as  $u_0$ . Then we can solve Eq. (2) and compare the different profiles.

Figure 3(a) shows the OSS numerical amplitude profile versus  $x$  corresponding to Fig. 2(b) after a propagation of 2 cm at steady state. The amplitude does not reach the zero value in the tails of the solitonlike profile because the diffraction of the Airy beam multilobe structure creates residual lighting on the numerical simulation [Fig. 3(b)]. The OSS numerical

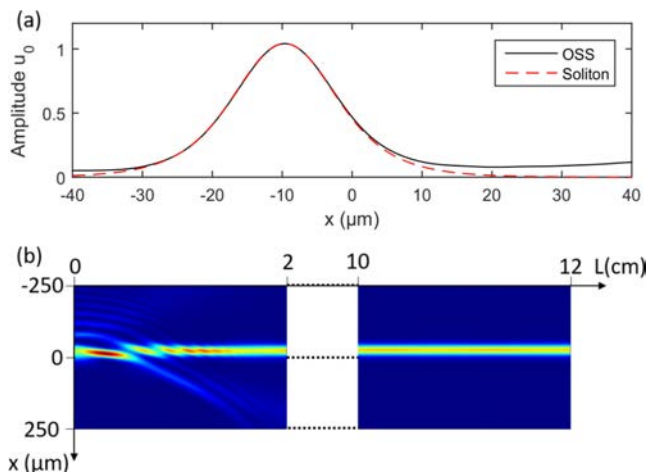


FIG. 3. (a) Numerical profile of the Airy beam OSS in Fig. 2(b) and corresponding theoretical soliton at  $L = 2$  cm. (b) Propagation of the OSS over long distances at steady state ( $\Gamma = 10$ ,  $F_0 = 1.95$ ,  $x_0 = 10 \mu\text{m}$ ,  $a = 0.1$ ,  $u_0 = 1.04$ ).

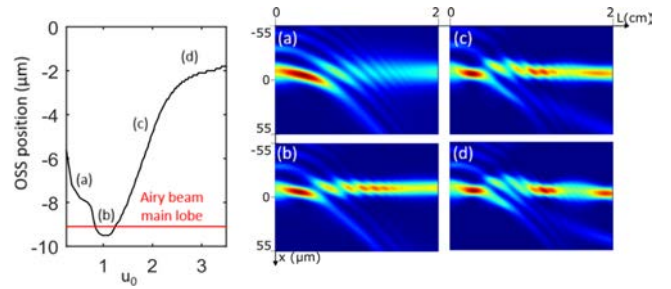


FIG. 4. Position of the Airy beam OSS as function of OSS maximum amplitude for  $\Gamma = 10$ ,  $F_0 = 1-7.5$  or  $u_0 = 0.25-3.5$ ,  $x_0 = 10 \mu\text{m}$ ,  $a = 0.1$ , and  $t_f = 20\tau_0$ . (a)–(d) Corresponding numerical simulation inside the crystal for (a)  $u_0 = 0.5$ , (b)  $u_0 = 1.04$ , (c)  $u_0 = 1.9$ , (d)  $u_0 = 2.9$ .

profile shows a transverse profile that matches a solitonlike profile. By using the model from Ref. [18] [Eqs. (1) and (2)] and expression (7), we can link our numerical simulations with the theoretical soliton model. We draw the theoretical soliton profile that would propagate in the crystal under the same conditions as our numerical simulation. Figure 3(a) demonstrates that the theoretical soliton profile fits nicely with the numerical profile of the OSS.

Is the solitonlike profile of the OSS stable over long distances? To answer this question, we numerically propagate the OSS up to 12 cm inside the nonlinear medium (corresponding to more than 20 diffraction lengths). The profile illustrated in Fig. 3(b) shows a constant behavior over the 12-cm propagation length. The maximum amplitude between the OSS at 2 cm and the one at 12 cm of propagation differs by only 1%, unveiling its solitonlike nature.

We can now fairly consider the Airy beam OSS as a spatial soliton even after 2 cm of propagation inside the crystal. But as observed in Ref. [14], it is important to note that the output position of the OSS varies slightly with the intensity of the Airy beam sent into the nonlinear medium. Figure 4 shows at steady state the evolution of the OSS position at the output face of the crystal as a function of the off-shooting beam's maximum amplitude. This curve is drawn by increasing numerically the total amplitude of the input Airy beam  $F$  from 1 to 7.5, which corresponds to the maximum amplitude  $u_0$  of the OSS going from 0.25 to 3.5. We notice that the OSS position is correlated to different propagation behaviors. For  $0.5 < u_0 < 2$  [Figs. 4(a)–4(c)] the position of the OSS at steady state is close ( $< 5 \mu\text{m}$ ,  $< x_0/2$ ) to the position of the Airy beam's main lobe at the input of the crystal (red line in Fig. 4). We also checked that the OSS beam profile corresponds to that of a theoretical soliton in this region. When  $u_0 > 2$  [Fig. 4(d)], the OSS trajectory is no longer perpendicular to the input face of the crystal, the solitonic profile is lost, and we observe spatial breathing along the propagation axis. For Figs. 4(a) and 4(c) the trajectory of the OSS is not perpendicular to the input face of the crystal and the position of the OSS shifts along the  $x$  axis over greater distances, whereas in the area close to the extremum of the curve [Fig. 4(b)], the position of the soliton no longer changes over greater distances.

Referring to Figs. 4(a)–4(d) we can observe variations of the intensity and width of the OSS at the output face

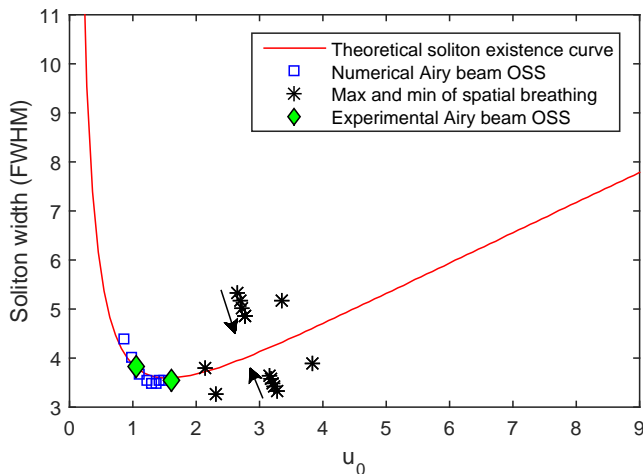


FIG. 5. Full width at half maximum (FWHM) in dimensionless units ( $\xi$ ) versus of soliton amplitude ( $u_0$ ). In red, the theoretical curve from Ref. [18]; in blue squares, the Airy beam OSS at 2-cm propagation from our numerical model; in black stars, the maximum and minimum of the observed spatial breathing; and the arrows show the evolution when propagating over greater distances. In green diamonds, the experimental OSS observed in Fig. 1.

of the medium. The theory of one-dimensional steady-state screening solitons in bulk material states that a relation exists between the width and the intensity of the soliton: Fig. 5 depicts the theoretical existence curve of the soliton full width at half maximum (FWHM) as a function of  $u_0$  from Ref. [18]. The green diamonds represent the experimental Airy OSS seen in Fig. 1 for the two different applied electric fields (200 and 400 V/cm). These experimental points are on the existence curve and confirm that the obtained OSS is indeed a soliton. Also represented in this figure is the Airy beam off-shooting FWHM for different values of  $u_0$ , all selected close to the extrema in Fig. 4, and obtained by solely modifying the amplitude of the input Airy beams. The values of  $u_0$  go from 0.8 to 1.5 and we measure the corresponding FWHM of the OSS. We see that our numerical OSS width and theoretical curve are in good agreement, further corroborating the similarity between OSS and a classical soliton. At greater values of  $u_0$ , where spatial breathing takes place, the maximum and minimum of the FWHM and corresponding  $u_0$  are included in Fig. 5 as black stars. These points are

on either side of the existence curve. Therefore, the beam's profile oscillates around the soliton profile. Furthermore, the amplitude and FWHM of these spatial oscillations tend to converge towards the theoretical soliton existence curve over greater distances (arrows in Fig. 5).

The two experimental profiles are obtained using the same Airy beam but different applied electric fields on the crystal. Therefore, we can control the output width and amplitude of the OSS by changing the electric field applied on the crystal. For a given Airy beam input profile, the OSS fits with the theoretical plot for values of  $u_0$  from 0.8 to 1.5. The values of  $u_0$  from 0.8 to 1.5 correspond to the extrema in position of the OSS as a function of  $u_0$  (seen in Fig. 4). We conclude that the extrema in position versus  $u_0$  indicates the area for which the OSS is closest to a theoretical soliton (blue squares in Fig. 5). Furthermore, since there is a quasilinear relation between the Airy beam amplitude and the OSS amplitude, we can also control the output OSS width and amplitude by changing the amplitude of the Airy beam. Therefore, unlike Gaussian beams, with one Airy beam we can create solitons of different widths when we change the nonlinearity in the crystal by modifying either the light intensity or the applied electric field.

In summary, we have evidenced the solitonic properties of Airy beam nonlinear propagation. Differently from Gaussian beams, the OSS coexists with a remaining self-accelerating structure. Experimental and numerical profiles of the OSS fit nicely with the theoretical soliton profile. Numerical simulations confirm that the OSS propagates invariably over great distances (more than 20 diffraction lengths). We observed that for fixed nonlinear conditions inside a photorefractive crystal, there exists a range of intensity values for which the OSS property is the closest to an ideal theoretical soliton. Our work motivates further studies of 2D Airy beams propagating in a photorefractive medium for testing the properties and the stability of the 2D OSS. Furthermore, since the OSS profile is quite similar to previously observed solitons such as those arising from Gaussian beams, our study is thought to be of interest for a large community and, in particular, those analyzing interactions and applications of spatial solitons.

We acknowledge the support of AIRBUS-GDI Simulation, Metz Métropole, Conseil Départemental de Moselle, Conseil Régional Grand-Est, Préfecture de Région Grand-Est, CentraleSupélec, Fondation Supélec and FEDER through the funding of the Chair in Photonics.

- [1] M. V. Berry and N. L. Balazs, *Am. J. Phys.* **47**, 264 (1979).
- [2] G. A. Siviloglou and D. N. Christodoulides, *Opt. Lett.* **32**, 979 (2007).
- [3] J. Baumgartl, M. Mazilu, and K. Dholakia, *Nat. Photonics* **2**, 675 (2008).
- [4] P. Polynkin, M. Kolesik, J. V. Moloney, G. A. Siviloglou, and D. N. Christodoulides, *Science* **324**, 229 (2009).
- [5] P. Rose, F. Diebel, M. Boguslawski, and C. Denz, *Appl. Phys. Lett.* **102**, 101101 (2013).
- [6] N. Wiersma, N. Marsal, M. Sciamanna, and D. Wolfersberger, *Opt. Lett.* **39**, 5997 (2014).
- [7] T. Vettenburg, H. I. Dalgarno, J. Nyk, C. Coll-Lladó, D. E. Ferrier, T. Čížmár, F. J. Gunn-Moore, and K. Dholakia, *Nat. Methods* **11**, 541 (2014).
- [8] A. Lotti, D. Faccio, A. Couairon, D. G. Papazoglou, P. Panagiotopoulos, D. Abdollahpour, and S. Tzortzakis, *Phys. Rev. A* **84**, 021807(R) (2011).
- [9] P. Panagiotopoulos, D. Abdollahpour, A. Lotti, A. Couairon, D. Faccio, D. G. Papazoglou, and S. Tzortzakis, *Phys. Rev. A* **86**, 013842 (2012).
- [10] I. Kaminer, M. Segev, and D. N. Christodoulides, *Phys. Rev. Lett.* **106**, 213903 (2011).

- [11] Y. Zhang, M. Belić, Z. Wu, H. Zheng, K. Lu, Y. Li, and Y. Zhang, *Opt. Lett.* **38**, 4585 (2013).
- [12] N. Wiersma, N. Marsal, M. Sciamanna, and D. Wolfersberger, *Sci. Rep.* **5**, 13463 (2015).
- [13] Y. Hu, Z. Sun, D. Bongiovanni, D. Song, C. Lou, J. Xu, Z. Chen, and R. Morandotti, *Opt. Lett.* **37**, 3201 (2012).
- [14] N. Wiersma, N. Marsal, M. Sciamanna, and D. Wolfersberger, *Sci. Rep.* **6**, 35078 (2016).
- [15] R. Y. Chiao, E. Garmire, and C. H. Townes, *Phys. Rev. Lett.* **13**, 479 (1964).
- [16] Z. Chen, M. Segev, and D. N. Christodoulides, *Rep. Prog. Phys.* **75**, 086401 (2012).
- [17] E. DelRe and M. Segev, *Self-Focusing and Solitons in Photorefractive Media* (Springer, New York, 2009), pp. 547–572.
- [18] K. Kos, H. Meng, G. Salamo, M.-f. Shih, M. Segev, and G. C. Valley, *Phys. Rev. E* **53**, R4330(R) (1996).
- [19] M. Belić, P. Jander, K. Motzek, A. Desyatnikov, D. Jović, A. Strinić, M. Petrović, C. Denz, and F. Kaiser, *J. Opt. B: Quantum Semiclassical Opt.* **6**, S190 (2004).
- [20] L. Allen, M. Padgett, and M. Babiker, *Prog. Opt.* **39**, 291 (1999).
- [21] D. Faccio, A. Lotti, A. Matijosius, F. Bragheri, V. Degiorgio, A. Couairon, and P. Di Trapani, *Opt. Express* **17**, 8193 (2009).

PAPER • OPEN ACCESS

## Light-induced interconnects using nonlinear Airy beam interactions

To cite this article: T Bouchet *et al* 2019 *J. Phys. Photonics* **1** 025001

View the [article online](#) for updates and enhancements.



## PAPER

## Light-induced interconnects using nonlinear Airy beam interactions

## OPEN ACCESS

RECEIVED  
12 July 2018REVISED  
8 December 2018ACCEPTED FOR PUBLICATION  
12 December 2018PUBLISHED  
18 January 2019

Original content from this work may be used under the terms of the [Creative Commons Attribution 3.0 licence](#).

Any further distribution of this work must maintain attribution to the author(s) and the title of the work, journal citation and DOI.

T Bouchet<sup>1,2</sup> , N Marsal<sup>1,2</sup>, M Sciamanna<sup>1,2</sup> and D Wolfersberger<sup>1,2</sup><sup>1</sup> Chair in Photonics, LMOPS, CentraleSupélec, Université Paris-Saclay, F-57070, Metz, France<sup>2</sup> Chair in Photonics, LMOPS, CentraleSupélec, Université de Lorraine, F-57070, Metz, FranceE-mail: [thomas.bouchet@centralesupelec.fr](mailto:thomas.bouchet@centralesupelec.fr)

Keywords: Airy beam, nonlinear dynamics, soliton, photorefractive effect, photorefractive medium

## Abstract

We analyze numerically optical waveguiding structures created in photorefractive media by two incoherent counter-propagating 1D Airy beams under nonlinear self-focusing conditions. We then inject a Gaussian probe beam to test our waveguiding structure. By using an anti-symmetric Airy beam configuration in stationary conditions, we find rich and complex waveguiding structures with multiple input to multiple output configurations and transverse input-to-output shifts up to 13 times the guided beam's waist.

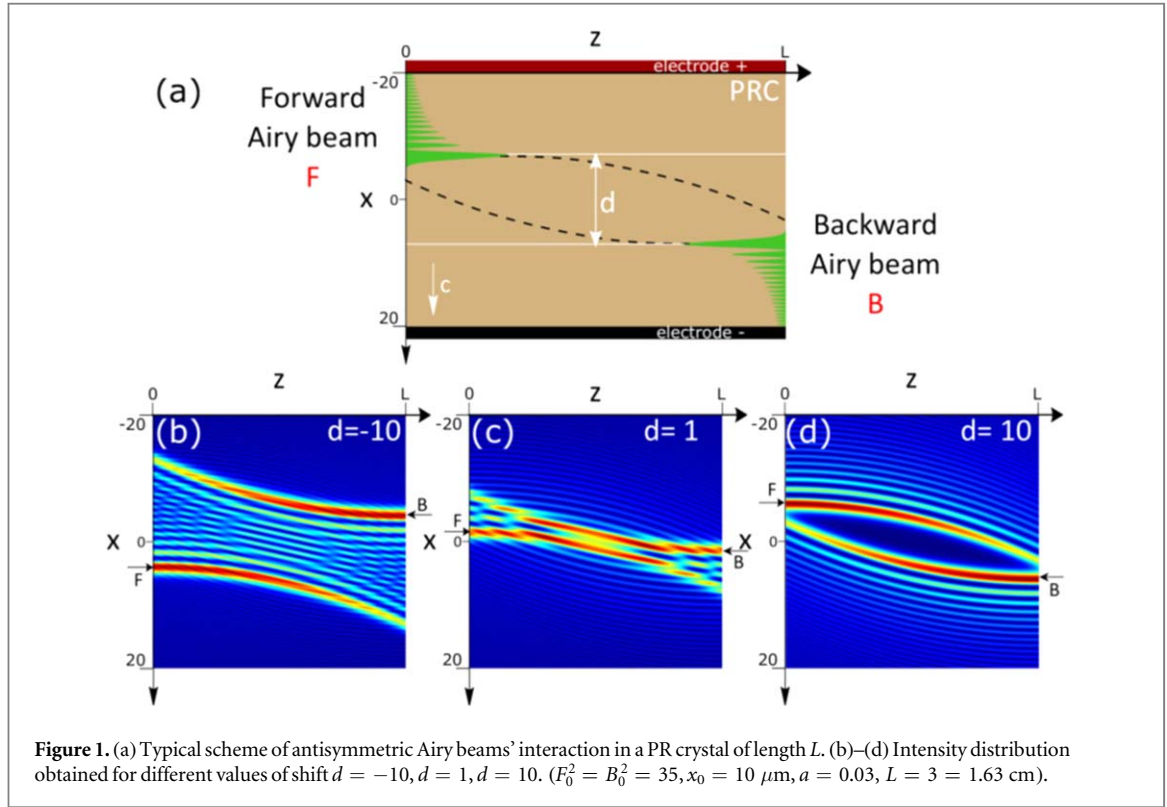
## 1. Introduction

In 1979, in the context of quantum mechanics, Berry and Balazs predicted a new solution to the Schrödinger equation [1], the Airy wave packets. In 2007, by truncating the ideal Airy waveform the first optical Airy beam was observed in free space [2]. This self-healing, shape-preserving, accelerating beam has multiple applications from manipulating microparticles [3] and plasma channel generation [4] to all-optical routing [5], or light-sheet microscopy [6]. Recently, the self trapping character of Airy beams in biased nonlinear media has suggested interesting dynamics such as soliton-like behaviors [7–11]. Co-propagating Airy beams and their interactions have been studied in different medias ranging from nematic liquid crystals [12] to photonic lattices [13] or three-wave systems [14]. In Kerr or photorefractive (PR) media, the solitonic structures of two co-propagating coherent Airy beams will exhibit attraction when in-phase and repulsion when out-of-phase [15–17] whereas two incoherent Airy beams will always exhibit attraction [18]. Other research on the propagation dynamics have shown that by using external potentials and weakening or strengthening of the autofocussing effect, the accelerating trajectory of Airy beam like structures can be controlled [19, 20]. The interaction of Airy beams and solitons in nonlinear media can even reproduce gravitational dynamics [21].

Similarly to studies with two co-propagating Airy beams, two counter-propagating Airy beams in a saturable nonlinear media will shed OSSs given enough nonlinearity strength [22], furthermore the OSSs tend to be attracted by the lobes of the counter-propagating Airy beam [23]. However, by contrast to studies with two co-propagating Airy beams, a counter-propagating configuration combined with the large transverse dimension of the Airy shape and their curved trajectory allow several interaction schemes where one or several lobes of the counter-propagating beams can overlap [10, 22, 23]. The interaction of such counter-propagating Airy beams introduce new dynamics and open new interesting fields for optical interconnections. Interestingly, both multiplexing (combining light beams in a single waveguide) and demultiplexing (splitting light beams in different waveguides) can be achieved using Airy beams. Moreover, waveguiding with a greater output-to-input transverse shift can be obtained by using Airy beams rather than with conventional Gaussian beams.

Waveguiding possibilities in the case of counter-propagating Airy beams have been studied in a symmetric configuration [22], but to our knowledge no study exists on an anti-symmetric configuration.

In this letter we analyze numerically optical waveguiding structures created in PR media by two incoherent counter-propagating 1-D Airy beams under nonlinear self-focusing conditions. In order to create complex waveguides we chose to propagate the Airy beams anti-symmetrically i.e. with each Airy beam accelerating towards the counter-propagating beams. This allows a larger overlapping of the Airy beams' secondary lobes.



The overlapping results in stronger waveguiding structures with multiple input to multiple output configurations and transverse input-to-output shifts up to 13 times the guided beam's waist.

## 2. Antisymmetric Airy beams interactions scheme

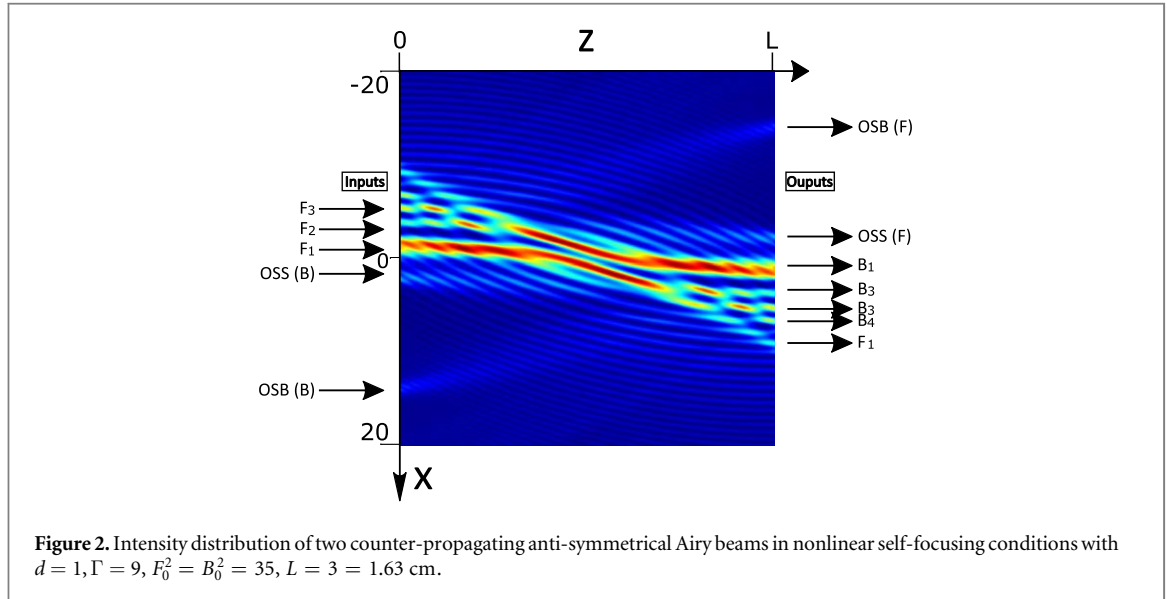
The typical scheme of antisymmetric Airy beams is presented in figure 1(a). Both beams propagate in a PR crystal along the  $z$ -axis. The forward beam  $F$  propagates from left to right and the backward beam  $B$  propagates from right to left.  $d$  is defined as the shift along the  $x$ -axis between the forward and backward Airy beam's main lobes upon injection at each side of the crystal.  $L$  is the length of the PR crystal. The  $x$ -axis is normalized by  $x_0 = 10 \mu\text{m}$  i.e. the Airy beam's main lobe waist at  $1/e$  of its maximum intensity. The  $z$ -axis is normalized by the diffraction length  $L_d = 4\pi n_b x_0^2 / \lambda = 5.4 \text{ mm}$ , with  $n_b$  the unperturbed refractive index and  $\lambda$  the wavelength. The electric field is applied along the  $c$ -axis, parallel to the  $x$ -axis: this concerns nonlinear self-focusing conditions. The figures 1(b)–(d) show the intensity distribution of two counter-propagating anti-symmetrical Airy beams in linear conditions for different values of  $d$ . In a PR crystal due to the Pockels effect, the intensity distribution induces optically a refractive index distribution which can also be seen as a waveguiding structure. In the case  $d = 1$ , the secondary lobes of the Airy beams greatly overlap resulting in a larger total intensity all along the secondary lobes' trajectory through the crystal and therefore corresponding to stronger variations of the refractive index. In what follows, we will mainly focus on this configuration which allows strong, numerous and complex waveguiding structures to appear.

The truncated Airy beams' input profiles are given by the following equations:

$$F(x, z = 0) = F_0 \text{Ai}\left(x + \frac{d}{2}\right) \exp\left(a\left(x + \frac{d}{2}\right)\right) \quad (1)$$

$$B(x, z = L) = B_0 \text{Ai}\left(-x - \frac{d}{2}\right) \exp\left(a\left(-x - \frac{d}{2}\right)\right), \quad (2)$$

where  $F_0$  (respectively  $B_0$ ) is the wave amplitude,  $\text{Ai}$  is the Airy function,  $a$  the truncation parameter of the Airy beam.



To simulate the behavior of the propagation of the antisymmetric Airy beams, we use the same theoretical model as in [10, 11, 22–24]. The nonlinear propagation of the two incoherent counter-propagating beams can be expressed as follows:

$$i\partial_z F + \partial_x^2 F = \Gamma E_0 F \quad (3)$$

$$-i\partial_z B + \partial_x^2 B = \Gamma E_0 B, \quad (4)$$

where  $\Gamma = (kn_b x_0)^2 r_{\text{eff}} E_c$  is the nonlinear PR coupling strength,  $r_{\text{eff}}$  is the effective component of the electro-optic tensor and  $E_c$  is the external electric field.  $E_0$  is the homogeneous part of the  $x$ -component of the PR space-charge field normalized by the external electric field. The temporal evolution of the space-charge field  $E_0$  is considered with a saturable nonlinearity and calculated using a relaxation-type dynamic:

$$\tau \partial_t E_0 + E_0 = -\frac{I}{1 + I}, \quad (5)$$

where the relaxation time of the crystal  $\tau$  is inversely proportional to the total intensity  $\tau = \frac{\tau_0}{1 + I}$ , and  $I = |F|^2 + |B|^2$  is the intensity normalized by the effective background intensity.

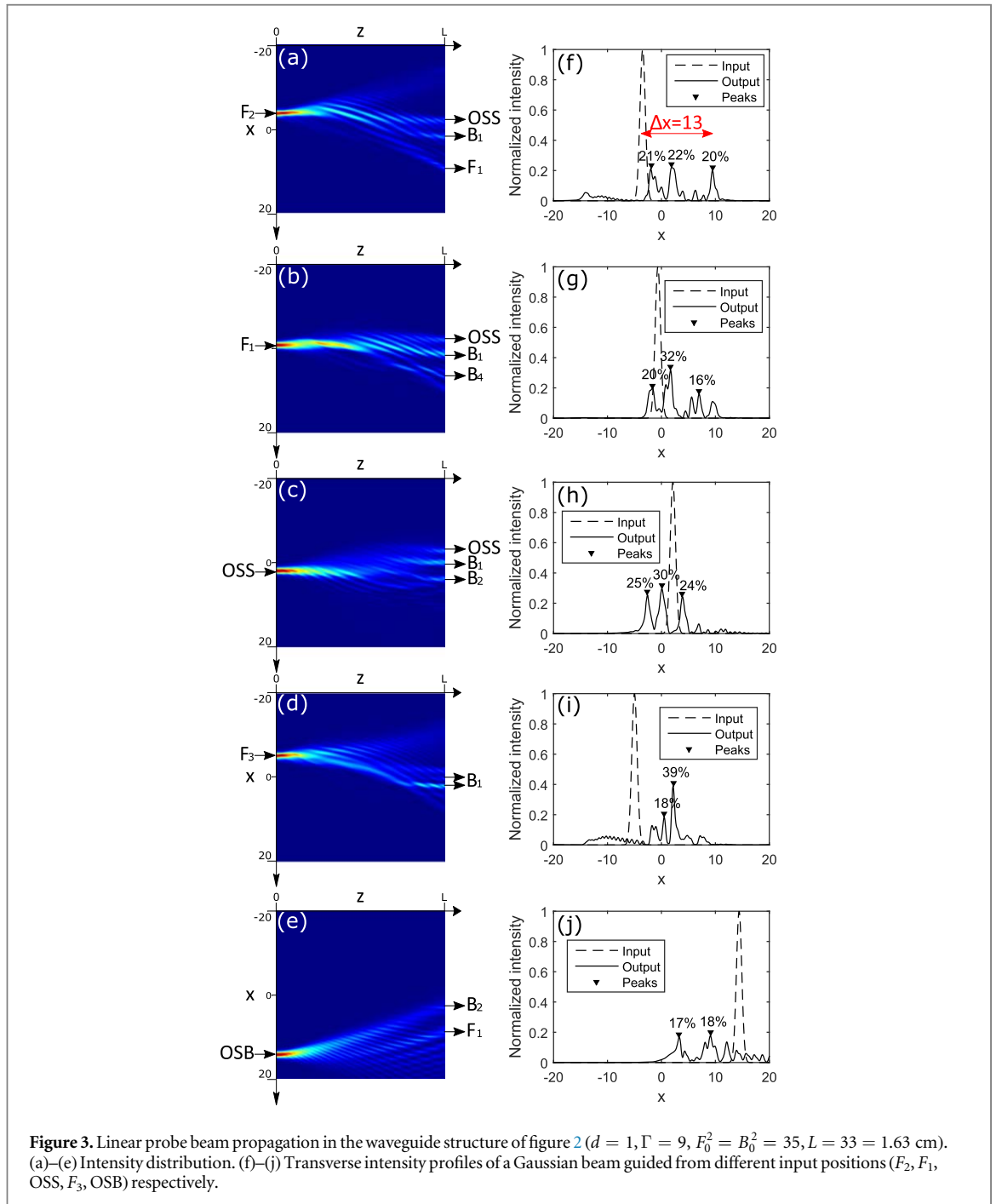
For small values of  $\Gamma$  ( $< 7$ ), the nonlinear effect is not high enough for producing waveguiding structures; when  $\Gamma > 15$  unstable dynamics are observed [22]. In this paper we present numerical simulations with a nonlinear PR coupling strength  $\Gamma = 9$  which allows the analysis of rich and complex stable waveguiding structures.

### 3. Optical interconnections for a transverse shift $d = 1$

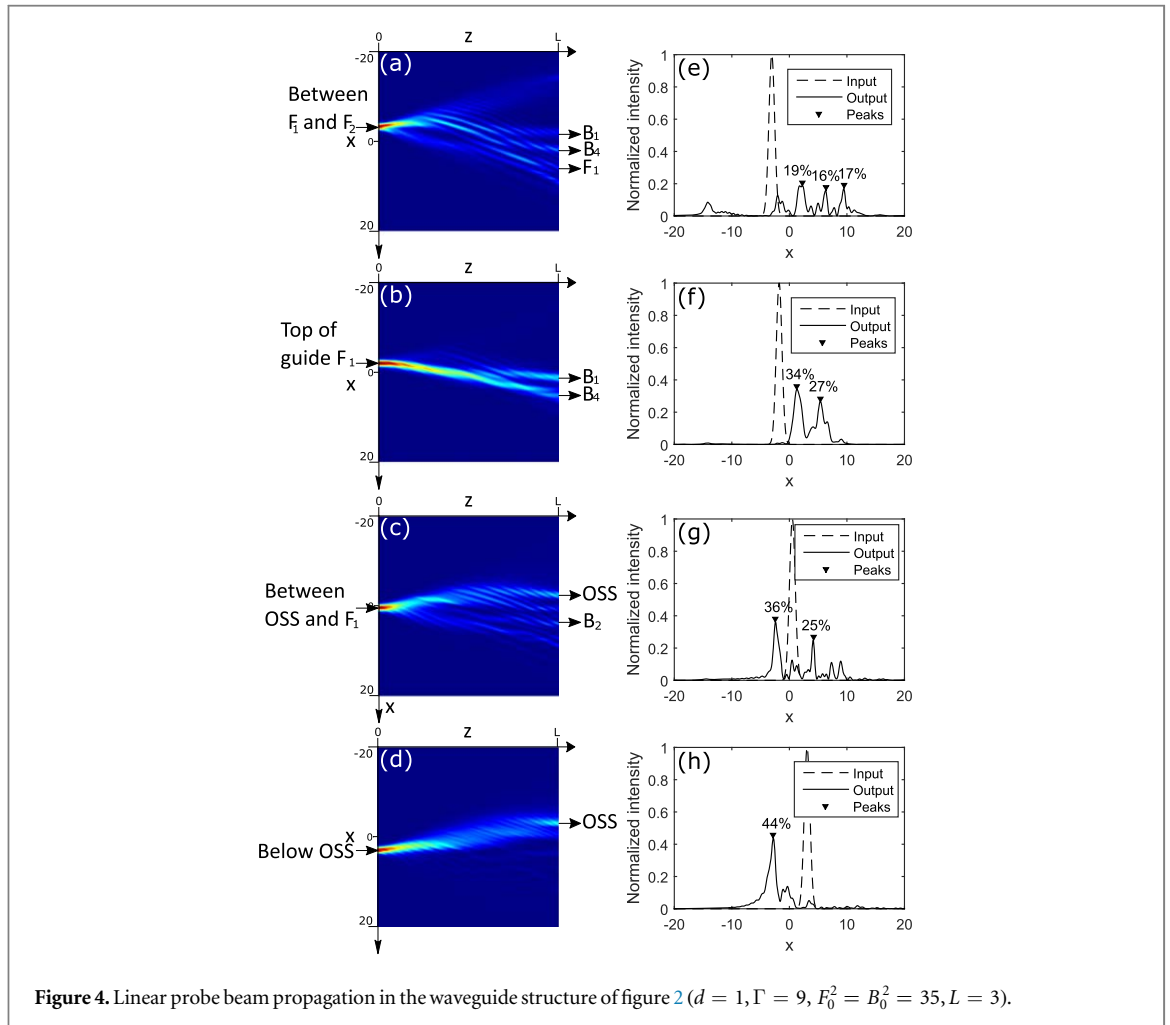
In what follows, we focus on the configuration  $d = 1$  and  $\Gamma = 9$  because it has a rich variety of complex and interesting waveguiding structures. We are interested in the number of different outputs for a single input and in the transverse input-to-output shift of the waveguide.

Figure 2 shows the intensity distribution of two counter-propagating anti-symmetrical Airy beams in nonlinear self-focusing conditions for  $d = 1$  and  $\Gamma = 9$ . When the nonlinear self focusing effect compensates the diffractive nature of a light beam, a soliton-like structure appears [11]. The self focusing creates two new waveguiding structures of interest, an off-shooting beam (OSB) and an off-shooting soliton (OSS). The waveguiding structure shows different possible inputs, the OSB and OSS positions created by the backward Airy beam propagation,  $F_1$  the forward Airy beams main lobe position,  $F_2$  and  $F_3$  the forward Airy beams secondary lobes position respectively. The waveguiding structure also shows different possible outputs, the OSB position and OSS position created by the forward Airy beam  $F$ ,  $B_1$  the backward Airy beam's main lobe position,  $B_2, B_3$  and  $B_4$  the backward Airy beam's secondary lobes positions respectively, and finally  $F_1$  the forward Airy beam's main lobe position after propagating through the crystal. The forward Airy beam's secondary lobes positions after propagating through the crystal are superimposed with the backward Airy beam's secondary lobe positions.

In order to analyze this waveguiding structure, we propagate a Gaussian probe beam (of waist  $x_0 = 10 \mu\text{m}$ ) at different input positions of our crystal. The Gaussian probe beam's amplitude represents 10% of the Airy beam's amplitude in order for its propagation to be linear. Figures 3(a)–(e) show the Gaussian beam's propagation in



the waveguiding structure. The arrows at the left show the input probe beam's position and the arrows at the right show the output beam's positions. Figures 3(f)–(j) plot the corresponding amplitude and position of the input Gaussian beam (dotted line) and the resulting output beams transverse profile (solid line). It is worth mentioning that an output with less than 10% of the amplitude of the input beam is not of interest for optical interconnects applications. We therefore decided to take into account only the output peaks that are over 15% of the input probe beam's maximum intensity. Some guiding behaviors were already predicted in previous studies of our group in the case of the symmetric Airy beam configuration [22]. By comparison, in this anti-symmetrical configuration, we observe a larger number of outputs for all cases. In figure 3(a), for a probe beam injected in  $F_2$  we observe simultaneously three outputs (OSS,  $B_1$  and  $F_1$ ) of equal peak intensity (around 20%). The OSS output is an expected output as it is observed even when the waveguide is obtained by injecting a single forward Airy beam [22]. However the two additional outputs called  $B_1$  and  $F_1$  are only obtained because of the interaction with the backward beam and thanks to the anti-symmetric configuration. For the symmetric counter-propagating beams interaction, the configuration with  $F_2$  as an input did not yield interesting waveguiding. Similarly in figures 3(b)–(c), injecting in  $F_1$  (respectively in the OSS) yields the expected OSS and  $B_1$  outputs but



**Figure 4.** Linear probe beam propagation in the waveguide structure of figure 2 ( $d = 1, \Gamma = 9, F_0^2 = B_0^2 = 35, L = 3$ ).

we also observe an additional  $B_4$  (respectively  $B_2$ ) output. Other inputs give interesting results:  $F_3$  and OSB (figures 3(d)–(e)). We obtain for both cases two outputs, for the first case in the  $B_1$  area and for the second case in  $B_2$  and  $F_1$  positions. The fact that these inputs did not give any outputs in the previous study [22] shows the effectiveness of overlapping anti-symmetric secondary lobes.

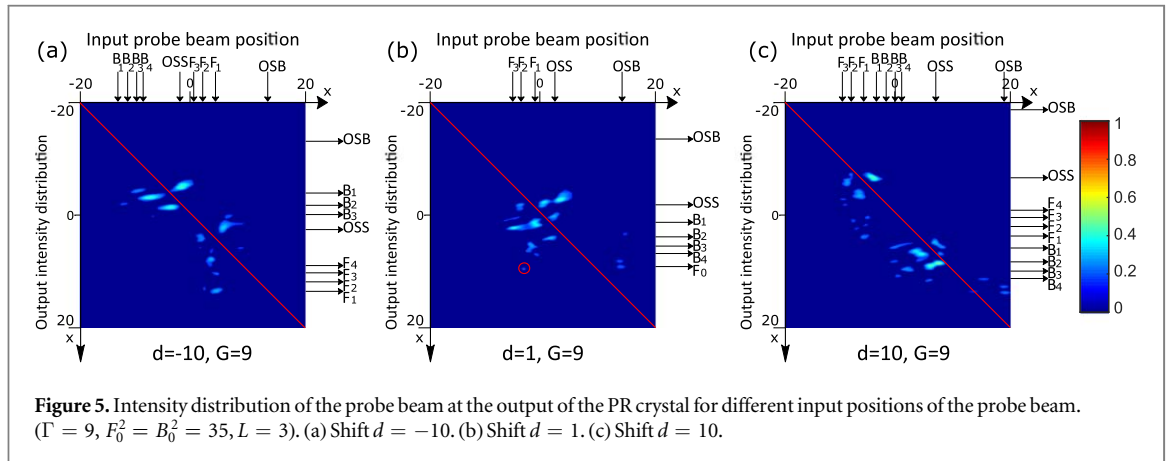
The resulting photoinduced waveguiding structure yields more possibilities than what can be observed with counter-propagating Gaussian beams and even with Airy beams in a symmetrical configuration. The resulting waveguiding structure shows interesting features: we observe new optical interconnection schemes such as one input to three outputs with input-output shifts up to  $13x_0$  (figure 3(a)) (shifts of only  $6x_0$  were observed for symmetrically counter-propagating Airy beams [22]).

During our investigation we also found other interesting waveguiding possibilities when the probe beam is not injected in one of the inputs mentioned in figure 2 but in between them. In doing so, other configurations are obtained by a coupling of evanescent waves at the different input positions and they are reported in figure 4. By injecting the probe beam between  $F_1$  and  $F_2$  (figure 4(a)) we combine outputs of the two cases presented in figures 3(a) and (b) ( $B_1, B_4$  and  $F_1$ ) while suppressing others (OSS). Similarly by injecting between the OSS and  $F_1$  (figure 4(c)), we combine two outputs (OSS and  $B_2$ ) but lose two outputs ( $B_1$  and  $B_4$ ). In figure 4(b), by placing the probe beam at the top of guide  $F_1$  we can suppress the topmost output (OSS) while preserving the lobe outputs ( $B_1$  and  $B_4$ ). In figure 4(d) by placing the probe beam below the OSS input, we suppress the bottommost outputs ( $B_1$  and  $B_2$ ) and preserve the OSS output.

Such mechanics in Airy beam interactions can lead to the engineering of complex modular optical waveguides by varying different parameters such as the shift  $d$  between the beams, the nonlinearity of the medium and the size of the probe beam compared to the Airy beam.

#### 4. Stability of the photoinduced waveguide

In order to get an overall picture of the different waveguiding possibilities, we have plotted a mapping of the output intensity distribution versus  $x$  for different input probe beam positions (figure 5). For each input probe



beam position, going from  $-20x_0$  to  $20x_0$ , we draw the output intensity distribution. If the output profile does not change for a certain range of input positions, we observe wide horizontal spots, showing a range of stability for the waveguide structure. If there are multiple outputs for a certain position of input we observe vertically multiple spots. The cases analyzed in figures 3 and 4 are reported in the mapping of figure 5(b). The most intense spots correspond to the best waveguiding conditions reported previously. The spots furthest from the topleft to downright diagonal (red) reveal the largest shifts from input to output positions. The spots circled in red is the  $F_1$  output for the  $F_2$  input (figure 3(a)) with an input to output shift equal to  $13x_0$ . Figures 5(a) and (c) show the waveguiding behavior of counter-propagating anti-symmetric Airy beams for  $d = -10$  and  $d = 10$  respectively. The configuration differs only by the shift  $d$  between the forward and backward Airy beams, but the resulting waveguiding behaviors are quite different. As expected, most spots are close to the diagonal because it corresponds to an input-to-output shift of 0 but multiple outputs are still observed. For example in the case  $d = -10$  (figure 5(a)), the probe beam injected in the OSS position has two output positions  $B_1$  and  $B_2$  which is the same result obtained for a single forward beam [22]. In the case  $d = 10$  however (figure 5(b)), the probe beam injected in the OSS position has three output positions  $F_1$ ,  $B_1$  and  $B_2$ . Therefore, figure 5 summarizes how changing parameters like the transverse shift  $d$  between forward and backward beam or the nonlinearity of the medium can give new waveguiding possibilities in comparison to the situation of photoinduced waveguiding from a single Airy beam or even two symmetric counter-propagating Airy beam.

## 5. Conclusion

We have analyzed the waveguides photoinduced by two counter-propagating anti-symmetric Airy beams. We have analyzed the propagation behavior of a Gaussian probe beam in such waveguides. We have found configurations giving multiple outputs for multiple input positions: up to three outputs whereas previous works had up to two outputs [22]. We have found greater input-to-output shifts (up to 13 beam waists) with counter-propagating anti-symmetric Airy beams compared to what was possible with counter-propagating Gaussian beams or even counter-propagating symmetric Airy beams configuration (typically maximum 6 beam waists [22]). Interactions of Airy beams in nonlinear self-focusing conditions yield much broader all-optical waveguiding possibilities than those observed so far with Gaussian beams. The situation discussed here with so-called anti-symmetric counter-propagating Airy beams yields to our knowledge the largest variety of all-optical waveguiding: either single input to single output but with possibly large transverse shifts, either single (multiple) inputs to multiple (single) outputs just by varying the initial transverse shift between the counter-propagating Airy beams or the nonlinearity strength.

## Acknowledgments

We acknowledge the support of AIRBUS-GDI Simulation, Metz Métropole, Conseil Départemental de Moselle, Conseil Régional Grand-Est, Préfecture de Région Grand-Est, FEDER, CentraleSupélec, Fondation Supélec through the funding of the Chair in Photonics.

## ORCID iDs

T Bouchet  <https://orcid.org/0000-0001-6873-9133>

## References

- [1] Berry M V and Balazs N L 1979 Nonspreading wave packets *Am. J. Phys.* **47** 264–7
- [2] Siviloglou G A and Christodoulides D N 2007 Accelerating finite energy Airy beams *Opt. Lett.* **32** 979–81
- [3] Baumgartl J, Mazilu M and Dholakia K 2008 Optically mediated particle clearing using Airy wavepackets *Nat. Photon.* **2** 675–8
- [4] Polynkin P, Kolesik M, Moloney J V, Siviloglou G A and Christodoulides D N 2009 Curved plasma channel generation using ultraintense Airy beams *Science* **324** 229–32
- [5] Rose P, Diebel F, Boguslawski M and Denz C 2013 Airy beam induced optical routing *Appl. Phys. Lett.* **102** 101101
- [6] Vettenburg T, Dalgarno H I C, Nylk J, Coll-Lladó C, Ferrier D E K, Čizmar T, Gunn-Moore F J and Dholakia K 2014 Light-sheet microscopy using an Airy beam *Nat. Methods* **11** 541–4
- [7] Kaminer I, Segev M and Christodoulides D N 2011 Self-accelerating self-trapped optical beams *Phys. Rev. Lett.* **106** 213903
- [8] Diebel F, Bokić B M, Timotijević D V, Savić D M J and Denz C 2015 Soliton formation by decelerating interacting Airy beams *Opt. Express* **23** 24351–61
- [9] Shen M, Gao J and Ge L 2015 Solitons shedding from Airy beams and bound states of breathing Airy solitons in nonlocal nonlinear media *Sci. Rep.* **5** 9814
- [10] Wiersma N, Marsal N, Sciamanna M and Wolfersberger D 2016 Airy beam self-focusing in a photorefractive medium *Sci. Rep.* **6** 35078
- [11] Bouchet T, Marsal N, Sciamanna M and Wolfersberger D 2018 Solitonic characteristics of Airy beam nonlinear propagation *Phys. Rev. A* **97** 051801
- [12] Shen M, Li W and Lee R-K 2016 Control on the anomalous interactions of Airy beams in nematic liquid crystals *Opt. Express* **24** 8501–11
- [13] Shi Z, Xue J, Zhu X, Xiang Y and Li H 2017 Interaction of airy-gaussian beams in photonic lattices with defects *Phys. Rev. E* **95** 042209
- [14] Maytevarunyoo T and Malomed B A 2017 The interaction of Airy waves and solitons in a three-wave system *J. Opt.* **19** 085501
- [15] Zhang Y, Belić M, Wu Z, Zheng H, Lu K, Li Y and Zhang Y 2013 Soliton pair generation in the interactions of Airy and nonlinear accelerating beams *Opt. Lett.* **38** 4585–8
- [16] Zhang Y, Belić M R, Zheng H, Chen H, Li C, Li Y and Zhang Y 2014 Interactions of Airy beams, nonlinear accelerating beams, and induced solitons in Kerr and saturable nonlinear media *Opt. Express* **22** 7160–71
- [17] Zhang M, Huo G, Zhong H and Hui Z 2017 Interactions between self-accelerating beams in photorefractive media *Opt. Express* **25** 22104–12
- [18] Shen M, Wu L, Gao M and Li W 2018 Incoherent interactions of Airy beams in nonlocal nonlinear media *J. Phys. B: At. Mol. Opt. Phys.* **51** 165401
- [19] Zhong H, Zhang Y, Belić M R, Li C, Wen F, Zhang Z and Zhang Y 2016 Controllable circular Airy beams via dynamic linear potential *Opt. Express* **24** 7495–506
- [20] Zhang Y, Belić M R, Zhang L, Zhong W, Zhu D, Wang R and Zhang Y 2015 Periodic inversion and phase transition of finite energy Airy beams in a medium with parabolic potential *Opt. Express* **23** 10467–80
- [21] Bekenstein R, Schley R, Mutzafi M, Rotschild C and Segev M 2015 Optical simulations of gravitational effects in the Newton–Schrödinger system *Nat. Phys.* **11** nphys3451
- [22] Wiersma N, Marsal N, Sciamanna M and Wolfersberger D 2014 All-optical interconnects using Airy beams *Opt. Lett.* **39** 5997–6000
- [23] Wiersma N, Marsal N, Sciamanna M and Wolfersberger D 2015 Spatiotemporal dynamics of counterpropagating Airy beams *Sci. Rep.* **5** 13463
- [24] Belić M, Jander P, Motzek K, Desyatnikov A, Jović D, Strinić A, Petrović M, Denz C and Kaiser F 2004 Counterpropagating self-trapped beams in photorefractive crystals *J. Opt. B: Quantum Semiclass. Opt.* **6** S190